DTU Library

Convex Reformulations of Security and Uncertainty Constraints for Power System Optimization.

Halilbasic, Lejla

Publication date:
2019

Document Version
Publisher's PDF, also known as Version of record

[Link back to DTU Orbit](#)

Technical University of Denmark

Convex Reformulations of Security and Uncertainty Constraints for Power System Optimization

Lejla Halilbašić

Ph.D. Thesis

Kgs. Lyngby, Denmark 2019

DTU Center for Electric Power and Energy
Department of Electrical Engineering

DANMARKS TEKNISKE UNIVERSITET
Center for Electric Power and Energy (CEE)
DTU Electrical Engineering

Convex Reformulations of Security and Uncertainty Constraints for Power System Optimization

Ph.D. Thesis, by Lejla Halilbašić

Supervisors:

Associate Professor Spyros Chatzivasileiadis, Technical University of Denmark

Professor Pierre Pinson, Technical University of Denmark

Convex Reformulations of Security and Uncertainty Constraints for Power System Optimization

This thesis was prepared by:
Lejla Halilbašić

Supervisors:
Associate Professor Spyros Chatzivasileiadis, Technical University of Denmark
Professor Pierre Pinson, Technical University of Denmark

Dissertation Examination Committee:
Associate Professor Jalal Kazempour (Chairman)
Department of Electrical Engineering, Technical University of Denmark, Denmark

Professor Ian A. Hiskens
Department of Electrical Engineering and Computer Science, University of Michigan, United States of America

Associate Professor Anthony Papavasiliou
Department of Mathematical Engineering, Université catholique de Louvain, Belgium

Center for Electric Power and Energy (CEE)
DTU Electrical Engineering
Elektrovej, Building 325
DK-2800 Kgs. Lyngby
Denmark

Tel: (+45) 4525 3500
Fax: (+45) 4588 6111
E-mail: cee@elektro.dtu.dk

To my grandparents Ahmed, Nezira, Meho and Šaha

Preface

This thesis was prepared at the Department of Electrical Engineering of the Technical University of Denmark (DTU) in partial fulfillment of the requirements for acquiring a Ph.D degree.

The thesis is based on six scientific papers, five of which have been peer-reviewed and published, whereas one of them is a working paper to be submitted for a journal publication.

Lejla Halilbašić
March 2019

Acknowledgements

Table of Contents

List of Figures

List of Tables

Abstract

A sustainable future with continuing technological and economic progress can only be achieved based on a renewable, reliable and affordable electricity supply. Renewable generation such as wind and solar power is inherently uncertain. Integrating it efficiently without compromising reliability is a key challenge to modern power system operations. To address this issue, system operators and electricity markets increasingly rely on the optimal power flow (OPF), an optimization tool for identifying cost-efficient and secure dispatch decisions. To this end, various formulations of the OPF with different levels of modeling accuracy and complexity are used. They differ in their representation of the nonlinear AC power flow equations and in the operational requirements they address. Most OPF algorithms include only parts of the numerous aspects of power system security and adequacy. As a result, there is still a lack of consensus on a fundamental definition of the *target operating region* (i.e., the feasible space), ensuring both power system security and adequacy. There have been only few attempts to derive a comprehensive and tractable constraint set capturing the *true* target operating region for the various power flow modeling frameworks. This is primarily due to the immense complexity of the numerous requirements imposed on power system operations.

Many power system security requirements such as dynamic security criteria cannot be directly expressed as linear or nonlinear constraints. Static security constraints are in theory tractable. However, they often lead to a computationally prohibitive problem complexity. At the same time, higher shares of partially unpredictable renewable generation further call for modeling approaches that account for uncertainty. Additionally, the nonconvexity of the power flow equations still challenges current solution algorithms. As a result, the electricity industry generally relies on linear approximations, which are computationally more robust. However, these approximations can be prone to severe errors. This in turn has prompted the development of more accurate *relaxations* and *approximations*. They preserve convexity and provide increased levels of computational robustness. This thesis builds on these advancements and develops convex reformulations of security and uncertainty constraints with the aim of defining the target operating region for a wide range of OPF formulations.

First, we address the challenge of translating static and dynamic security requirements to tractable constraints suitable for any OPF framework. We derive decision trees to partition the nonconvex security region into subspaces and subsequently incorporate them in the optimization through integer programming and disjunctive constraints. This is the first work to combine decision tree based security assessments with integer programming, allowing us to bridge the gap between machine learning and traditional mathematical optimization. We preserve the nonconvex reality of power systems in an efficient and robust way, even when using convex relaxations and approximations of the power flow equations. Larger regions of the secure operating region are accessible in the optimization, resulting in less conservative solutions than current approaches. We

show how the security constraints can be combined with linear and nonlinear formulations of the power flow equations, depending on their application in market or system operations.

To address the uncertainty of renewable generation, we develop the first formulation of a chance-constrained AC-OPF based on the convex second-order cone formulation of the power flow equations. Second-order cone programming is one of the computationally most efficient methods for nonlinear systems. We leverage extended formulations of quadratic chance constraints to approximate the nonconvex *confidence region* more accurately – the portion of the operating region secure against the impact of forecast errors with a desired probability. Coupled with an ex-post AC feasibility recovery, our method identifies lower cost solutions in the confidence region which are not represented in current nonconvex formulations of the chance-constrained AC-OPF. To consider both security and uncertainty, we provide a unified definition of the target operating region of power systems. For this purpose, we formulate the problem as a security- and chance-constrained OPF and propose two tractable and efficient approximations suitable for any OPF algorithm.

Compared to solely considering preventive control actions, corrective control actions allow to enlarge the target operating region, thereby substantially reducing system costs. They can be provided by controllable and fast-acting system components, such as high voltage direct current (HVDC) transmission lines. To this end, we develop optimization tools for incorporating and optimizing corrective control in response to forecast errors. We focus on HVDC lines as well as HVDC grids, which are very likely to emerge from already existing point-to-point links. In both cases, optimized corrective control actions allow for a better coordination of generation resources and reduce the cost associated with an uncertain system operation.

Resumé

En bæredygtig fremtid med fortsat teknologisk og økonomisk udvikling kan kun opnås hvis den baseres på vedvarende og pålidelig elforsyning til en overkommelig pris. Vedvarende energi er i sig selv usikker og effektiv integration heraf uden at gå på kompromis med pålidelighed og omkostningseffektivt er en stor udfordring for det moderne energisystem. For at imødekomme dette benytter systemoperatører og elektricitetsmarkeder sig i stigende grad af optimal effektflow (OPF), et optimeringsværktøj til at identificere omkostningseffektive og sikre fordelingsbeslutninger. Her benyttes en række formuleringer af OPF med forskellige niveauer af nøjagtighed og kompleksitet. De adskiller sig i deres repræsentation af de ikke-lineære effektflowligninger og i de operationelle krav, de adresserer. De fleste OPF algoritmer inkluderer kun dele af de talløse aspekter af energisystemets sikkerhed og tilstrækkelighed. Som et resultat heraf er der stadig ikke en konsensus blandt nuværende OPF-formuleringer på en fundamental definition af måldriftsområdet (dvs. rummet af mulige løsninger) som sikrer både energisystemets sikkerhed og tilstrækkelighed. Som konsekvens heraf har der været få forsøg på at udlede et omfattende og bearbejdeligt bibetingelsessæt, som fanger det sande måldriftsområde for forskellige effektflowmodelleringsrammer.

Mange af energisystemets sikkerhedskrav som for eksempel dynamiske sikkerhedskriterier kan ikke direkte udtrykkes som lineære eller ikke-lineære bibetingelser. Statiske sikkerhedsbibetingelser er i teorien bearbejdelige, men de leder ofte til en uoverkommelig kompleksitet af problemet. Større andele af delvis uforudsigelige vedvarende energi i systemet stiller et krav til modellering, som tager højde for usikkerhed. Derudover, udfordrer den høje kompleksitet af effektflowligningerne nuværende løsningsalgoritmer. Derfor er elindustrien generelt afhængig af de beregningsmæssigt mere robuste lineære approksimationer. Disse approksimationer har dog en tendens til alvorlige fejl og har derfor ført til udviklingen af mere nøjagtige relakseringer og approksimationer. Disse bevarer konveksitet og bidrager med højere niveau af beregningsmæssig robusthed. Denne afhandling bygger på disse fremskridt og udvikler konvekse omformuleringer af sikkerheds- og usikkerhedsbibetingelser med det formål at definere et måldriftsområde for en bred række af OPF-formuleringer.

Først, adresserer vi udfordringen ved at omformulere statiske og dynamiske krav til bearbejdelige bibetingelser egnet til enhver OPF-ramme. Vi definerer beslutningstræer, som opdeler det ikke-konvekse sikkerhedsområde i underrum og dernæst inkorporeres de i optimeringen ved brug af heltalsprogrammering og disjunkte bibetingelser. Kombinationen af beslutningstræer og blandet heltalsprogrammering gør det muligt at bygge bro mellem maskinlæring og traditionel matematisk optimering. Dette bevarer den ikke-konvekse realitet af energisystemer på en effektiv og robust måde selv ved brug af konvekse formuleringer af effektflowligningerne. Større områder af det sikre driftsområde er tilgængelige i optimeringen og resulterer i en mindre konservativ løsning end nuværende fremgangsmåder. Vi viser hvordan sikkerhedsbibetingelserne kan blive kombineret med lineære og ikke-lineære formuleringer af effektflowligningerne afhængig af deres anvendelse i markeds- eller systemdrift.

For at adressere usikkerheden af vedvarende energi udvikler vi først en formulering af tilfældigheds-betinget AC-OPF baseret på den konvekse anden ordens kegle formulering af effektflowligningerne. Vi udnytter udvidede formuleringer af kvadratiske tilfældighedsbibetingelser for bedre at approksimere det ikke-konvekse konfidensområde – den del af driftsområdet, der er sikker mod indvirkning af forudsigelsesfejl med en ønsket sandsynlighed. Sammen med en efterfølgende AC mulig genopretning identificerer vores metode løsninger med lavere omkostninger, som opfylder konfidensniveauet og som ikke er repræsenteret i nuværende ikke-konvekse formuleringer af tilfældighedsbetinget AC-OPF. For at kunne betragte både sikkerhed og usikkerhed bidrager vi med en generel definition på måldriftsområdet for energisystemmer. Til dette formål formulerer vi problemet som en sikkerheds- og tilfældighedsbetinget OPF og foreslår to bearbejdelige og effektive approksimationer velegnet til enhver OPF-algoritme.

Korrigerende kontrolhandlinger tillader sammenlignet med udelukkende at betragte forebyggende kontrolhandlinger en forstørrelse af måldriftsområdet og derved en betydelig reduktion af syste-momkostningerne. Disse kan blive leveret af kontrolbare og hurtigt reagerende komponenter som for eksempel højspændingjævnstrøms (HVDC) transmissionslinjer. Hertil udvikler vi optimeringsværktøjer til at inkorporere og optimere forebyggende kontrol som reaktion på forudsigelsesfejl. Vi fokuserer på HVDC linjer og HVDC-netværk, som sandsynligvis vil forekomme fra allerede eksisterende punkt til punkt forbindelser.

Acronyms

AC	alternating current
AC-OPF	AC optimal power flow
CoS	cost of security
ATC	available transfer capacity
BG	best guess
DA-SC-CC-OPF	data-driven security- and chance-constrained optimal power flow based on analytical reformulations
DC	direct current
DC-OPF	DC optimal power flow
DD-SC-CC-OPF	purely data-driven security- and chance-constrained optimal power flow
DT	decision tree
FACTS	flexible AC transmission system
FBMC	flow-based market coupling
HVDC	high-voltage direct current
ISO	independent system operator
LP	linear programming
MIP	mixed integer programming
MILP	mixed integer linear programming
MINLP	mixed integer nonlinear programming
MISOCP	mixed integer second order cone programming
NTF	notified transmission flow
OPF	optimal power flow
PSC-OPF	preventive security-constrained optimal power flow
PST	phase-shifting transformer
PTDF	power transfer distribution factor

RAM   remaining available margin

SC-OPF   security-constrained optimal power flow

SOC   second-order cone

TRM   transmission reliability margin

TSO   transmission system operator

TTC   total transfer capacity

CHAPTER 1

Introduction

1.1 Background and motivation

Over the last two decades, power systems have undergone significant changes, unlocking new opportunities but also introducing additional challenges. Increasing amounts of renewable electricity production from e.g., inverter-based wind and solar generators, more flexible demand and higher consumer engagement have led to a reduced predictability of both supply and demand. In combination with the liberalization of electricity markets, which has led to larger cross-border flows and more volatile operation due to short-term trading, the system is exposed to larger deviations of power injections and flows from their planned schedules. As a result, transmission system operators (TSOs) are often required to interfere with the market outcome and perform expensive redispatching actions to maintain power balance and system security. In Germany, redispatched energy volumes grew by a factor of more than 60 from $306\,\mathrm{GWh}$ to $20\,439\,\mathrm{GWh}$ in the period between 2010 and 2017 while the associated costs increased 30-fold from €13 million to €396.5 million [1, 2]. The system is increasingly operated closer to its limits, leading to an observed reduction in power system reliability, and thus compromising security and adequacy [3–5].

The electric power system is the backbone of modern life and key enabler of technological and economic development. Interruptions of its services such as blackouts are particularly onerous and costly, incurring immediate direct and indirect damages as well as long-term economic losses. Extreme weather events can lead to long lasting and severe power outages such as the 2003 North American blackout, whose economic losses the US Department of Energy estimates at $6 billion [6]. While such extreme events are rare, less severe interruptions recur due to poor system planning and operation, aging infrastructure, occasional faults, system overloading and insufficient generation [7]. Despite usually being less severe, their associated losses accumulate to several billions of dollars annually in the US alone and are projected to increase under the current planning and operational paradigm [3]. In order to reverse this trend, the system needs to be operated at any time with sufficient margin to maintain security while simultaneously compensating for the inherent uncertainty of modern power system operations. However, current tools and strategies for system and market operations do not adequately address the growing degree of uncertainty that power systems are exposed to.

In addition to reliability, the provision of electricity at the lowest possible cost is another basic requirement. Considering the capital intensity of the power industry, even small efficiency gains can have profound impacts on the overall social welfare. A 1% improvement in dispatch can annually save $4 to $20 billion worldwide [8]. To this end, the optimal power flow (OPF) problem is widely used in various forms for both market and system applications to optimize costs at planning and operational stages [9]. In its most common application, the OPF aims at minimizing the total cost of electricity production under consideration of the power flow equations and various system limits. The electricity industry usually relies on simplified approximation models for the power

flow equations (i.e., the DC approximation). However, the standard OPF as introduced in [10] accounts for their true nonlinear and nonconvex nature (i.e., the AC power flow) and accurately models the relationship between active and reactive power injections and complex nodal voltages. Regardless of the power flow formulation, the basic OPF problem is considered to be of limited use. The resulting dispatch is not guaranteed to be secure against potential contingencies, instability or forecast errors of uncertain system parameters [11]. This has led to the development of many different extensions to the basic OPF problem. Most of them aim at incorporating security or uncertainty constraints. Some rely on an extensive mathematical model designed to be solved in a one-shot optimization; therefore, they often constitute a computational burden. Others employ iterative algorithms to ensure computational efficiency, alternating between an optimization and a contingency or uncertainty analysis [11]. These extensions tackle some deficiencies of the OPF. However, they still rely on the basic OPF formulation and neglect more fundamental issues related to its algorithmic reliability, which under the nonlinearity of the power flow equations remains highly questionable. In other cases, convex approximations of the power flow equations are used instead to allow for more robust solution procedures. Here, the feasibility of the solution, which is indispensable to a reliable system operation, is usually left unaddressed. Additionally, current security-constrained OPF algorithms tend to focus on static security limits and neglect system dynamics, potentially imposing stricter security limits [12]. A feasible and reliable system operation can, however, only be guaranteed if both static and dynamic security requirements are met.

1.2 Modern challenges in OPF problems

In general, a comprehensive framework that addresses the major shortcomings of the OPF simultaneously and efficiently is still missing, namely: (i) reformulating static and dynamic security requirements to tractable constraints for an optimization environment, the latter of which is a particular challenge and remains tailored to specific systems and problems only [9]; (ii) accounting for the inherent uncertainty in power system operations; (iii) dealing with the high complexity of the power flow equations. In addition to (i) – (iii), more volatile system operation renders the traditional paradigm for preventive security obsolete and often requires fast corrective actions in real-time. Thus, any OPF algorithm needs to be adaptable to the required control framework. Additionally, the generation dispatch is dictated by electricity markets, calling for algorithms tailored to the modeling and time frames demanded by market clearing processes.

To deal with (i), many security-constrained optimal power flow (SC-OPF) algorithms have been proposed. The majority focuses on static security criteria and ensures that for a set of pre-defined contingencies all equipment and voltage ratings are met [13]. In theory, these constraints are tractable but often lead to prohibitive problem sizes. Less focus has been put on dynamic security criteria (i.e., stability criteria). They ensure that after a disturbance the system can return to a secure operating point. Stability metrics (e.g., for small-signal stability) are based on differential algebraic equations and eigenvalue sensitivity analyses. The eigenvalues are highly nonlinear functions of the system parameters and can lead to tractability issues even for small systems [14]. Indeed, current OPF algorithms including dynamic security criteria remain a huge computational burden [15]. Additionally, an increasing deployment of power electronics and inverter-based generation means that the definition of security itself – in particular with regard to stability – is bound to change [11]. This calls for SC-OPF frameworks which are adaptable and do not rely on the security definition.

As for the uncertainty, many probabilistic versions of the OPF have been proposed. They explicitly model the impact of deviations in uncertain system parameters on the OPF decision variables and are based on stochastic programming or robust optimization. Stochastic programming optimizes over a set of discrete uncertainty realizations in the form of samples. Robust formulations account for a continuous range of the uncertainty and either aim at the worst case scenario or allow for an adjustable level of robustness with a priori guarantees through chance constraints. Choosing the right framework for modeling the uncertainty generally boils down to determining an adequate trade-off between accuracy, conservatism and computational complexity [16]. On top of that, the uncertainty modeling has to be compatible with the security constraints such that together they represent the *target operating region* of power systems. The operating points in the *target operating region* fulfill all security requirements and are guaranteed to remain within the secure region with sufficient confidence even when deviating from their forecasted position.

The nonconvex nature of the AC power flow equations challenges the robustness of existing solution algorithms. They highly depend on an appropriate initialization (i.e., warm start), are not guaranteed to converge, particularly for large networks [17, 18], and can only provide guarantees for locally optimal solutions. To address these challenges, several convex approximations and relaxations of the AC power flow equations are widely used for OPF algorithms today, benefiting from convex programming to provide globally optimal solutions of the problems solved and computational efficiency. They range from fully linearized DC approximations, neglecting reactive power, voltage magnitudes and losses, to more accurate relaxations and approximations, leveraging the quadratic dependency of the AC power flow equations on the nodal voltages. Despite their increased robustness and efficiency, all AC-OPF relaxations and approximations share the major drawback of potentially leading to solutions which are either physically meaningless or not located in the *target operating region*. This is a result of inaccurately mapping the desired AC feasible space to the constraint set of the underlying OPF formulation. Even though the AC-OPF is considered to be the most accurate one, as it fully represents the power flow physics, it can also suffer from inaccuracies if the *target operating region* is not properly defined and embedded in the optimization.

The scope of the *target operating region* is further determined by the underlying control framework and whether it allows for only preventive or preventive-corrective control actions. Under increasingly stressed conditions, secure operation after a contingency or a deviation in power injections cannot always be maintained without resorting to corrective adjustments in real-time [4]. Being able to control power flows and quickly react to changes in the expected operating conditions, flexible system components, such as high voltage direct current (HVDC) transmission lines, phase-shifting transformers (PSTs) and FACTS devices, allow enlarging the *target operating region*. Since changing the setpoints of, e.g., HVDC converters does not incur any costs as such (in contrast to expensive generation redispatch [19]), corrective control actions allow maintaining security at reduced system costs. In order to align the operation of flexible components in a cost-optimal and secure way, their corrective control strategies need to be accounted for in the OPF.

Existing OPF algorithms cover only parts of the numerous requirements on power system security and adequacy. Regardless of the underlying power flow environment, they still lack a comprehensive and fundamental definition on (i) the desired nonconvex *target operating region* ensuring both power system security and adequacy and (ii) a tractable constraint set able to capture the full *target operating region* for the required power flow modeling framework. In practice, the definition of the *target operating region* is a result of TSOs' reliability assessment and prone to

inaccuracies. First, it depends on TSOs' estimates of the eventual market outcome and the future operating conditions. Predictions of this kind are increasingly difficult to determine with sufficient accuracy. Second, it usually captures one convex subspace of the true nonconvex operating region and might neglect feasible regions which could contain more cost-efficient OPF solutions. The identified subspace further constitutes the limits for both market and system operations. Thus, decision-makers at all levels are deprived of choices that in fact would be feasible. As a result, regulating authorities and market stakeholders often perceive these limits as intransparent, restricting trades and counteracting the primary objective of maximizing social welfare [4, 20]. As the OPF is at the core of market and increasingly of system operations, its boundaries, constraining the social welfare for the sake of system reliability, and their derivation need to be comprehensible and accessible to all parties involved, system and market operators alike as well as regulating authorities.

1.3   Research objectives and contributions

This thesis addresses the challenges described above with the primary objective of developing efficient, scalable and adaptable methods to model security and uncertainty in the OPF problem. We focus on short-term operational planning with time horizons spanning from day-ahead up to a few minutes prior to the actual physical delivery of electricity.

Specifically, the contributions of this thesis can be summarized by the four main research questions we address:

I. How can we develop a tractable optimization framework for any type of static and dynamic security constraints?

In [**Paper A**] and [**Paper B**], we introduce a data-driven approach to reformulate static and dynamic security requirements to tractable constraints suitable for any OPF, regardless of the underlying power flow modeling framework. The *secure operating region* (i.e., the feasible space of the proposed data-driven SC-OPF) is defined for the N-1 criterion with static security and small-signal stability as part of the dynamic security [13]. The data-driven approach is, however, agnostic to the criteria representing the secure operating region and could also include alternative definitions. We use a large database of operating points to derive conditional decision rules in the form of decision trees (DTs). The DT partitions the nonconvex security region and essentially represents conditional security margins, which we formulate in the form of conditional transfer limits. The resulting subspaces can then be efficiently incorporated into the optimization using mixed integer programming (MIP) and disjunctive constraints. This work is the first one to combine decision tree based security assessments with MIP in an optimization framework. Whenever the OPF is based on the full nonlinear power flow equations, the problem turns into a nonconvex mixed integer nonlinear program (MINLP). In general, nonconvex MINLPs are very difficult to solve even for small problems. [**Paper A**] therefore explores alternative formulations of the power flow equations to derive efficient convex approximations, which achieve significant speed-ups. As such, the data-driven SC-OPF can be used by both system and market operators for, e.g., optimizing redispatch or AC based market-clearing auctions. However, electricity markets are traditionally cleared based on the DC approximation of the power flow equations. In [**Paper B**], we demonstrate how the data-driven SC-OPF can also be adapted to a DC power flow modeling framework and made suitable for the current market paradigm. The MIP approach allows to preserve the nonconvex reality of power systems in a robust and efficient way even when using linear or convex formulations of the power flow equations. Larger regions of the feasible space are accessible in the optimization, resulting in more cost-efficient solutions than current approaches.

II. How can we develop a tractable optimization framework to consider the uncertainty in system conditions and what is the impact of the required approximations?

[**Paper C**] addresses both the uncertainty inherent to modern power system operations and the shortcomings of nonconvex programming. In this context, we develop the first formulation of a chance-constrained second order cone OPF (CC-SOC-OPF). Chance constraints ensure that all constraints are satisfied with a desired probability over a continuous uncertainty range. They are well aligned with the preventive security framework from [**Paper A**] and [**Paper B**], as they can be reformulated to deterministic constraints. Thereby, they introduce an uncertainty margin [21], which reduces the feasible space of the OPF to the *confidence region* and preventively secures the system against the uncertainty impact. As the confidence region of nonlinear problems is unknown, even when the statistical properties of the uncertain input parameters are exactly known, efficient approximations are required. We use extended formulations of convex quadratic chance constraints from [22] in the CC-SOC-OPF to more accurately approximate the original nonconvex confidence region. Coupled with an ex-post feasibility recovery, we identify an entire lower cost area within the confidence region which is not represented in current nonconvex formulations of the chance-constrained AC-OPF.

III. How can we give decision-makers access to the entire decision space and reduce costs while maintaining secure operation under increasing uncertainty?

In [**Paper D**], we introduce a framework to give decision-makers access to the entire permissible decision space. It reduces the role of system operators in determining its limits and eliminates the dependency on their estimates of the eventual market outcome and future system conditions. Specifically, we provide the first unified definition of the target operating region of power systems, accounting for both security and uncertainty. We formulate the problem as a security- and chance-constrained OPF and propose two efficient approximations. The first is based on purely data-driven techniques. The second uses a combination of data-driven and analytical reformulations and can act as an alternative in case of lower information availability. In combination with mixed integer programming, both of them give access to the entire nonconvex decision space, irrespective of how the power flow equations are modeled. We show for both methods how the target operating region can be approximated with very high accuracy even in a DC-OPF. Our method is easily adaptable to the current operational framework and can significantly improve decision-making processes across the industry.

IV. How can we enlarge the decision space in order to access more cost-efficient solutions?

Improved controllability and additional means for flexibility allow to change the scope of the target operating region. Vast potential for renewable electricity generation in remote locations reinforces the installation of new HVDC lines, which have become the preferred technology for transporting large amounts of electricity over long distances. HVDC converters can independently control active and reactive power injections and introduce additional degrees of flexibility for both preventive and corrective control. Therefore, we move from the previous framework for preventive control in [**Paper A**] – [**Paper D**] and develop in [**Paper E**] an optimization tool for system operators that accounts for the ability of HVDC lines to react to wind power forecast errors. HVDC control policies are incorporated and optimized in a chance-constrained AC-OPF. Eventually, DC grids are very likely to emerge from already existing point-to-point links. They will interact with the underlying AC infrastructure and span multiple areas under the jurisdiction of different system

and market operators. Appropriate tools and mechanisms will be required to optimally coordinate the interaction between AC and DC transmission assets as well as among different operators. In [**Paper F**], we therefore propose a decentralized DC-OPF algorithm, incorporating meshed DC grids. It preserves computational efficiency of the OPF in large interconnected systems and allows to share flexibility resources between areas while only requiring a moderate exchange of sensitive information. Decentralized algorithms will gain in importance as regulations on data privacy become more stringent, requiring also the OPF to adapt accordingly.

1.4   Thesis outline

This thesis presents the contributions of the papers published during this Ph.D. project. Chapter 2 introduces the OPF problem and gives an overview of various OPF approximations as well as security and uncertainty modeling approaches relevant to the work in this thesis. It further outlines how security and uncertainty considerations are currently accounted for in practice. Chapter 3 presents the data-driven SC-OPF for different power flow modeling frameworks. It discusses the database generation, the knowledge extraction using DTs and the implementation of the conditional decision rules defined by the DT in the OPF. The formulation of the CC-SOC-OPF is presented in Chapter 4. Chapter 5 discusses the unified framework for considering security and uncertainty in OPF algorithms. The benefits of corrective control to enlarge the target operating region are explored in Chapter 6. It focuses on the flexibility provided by HVDC lines to quickly react to changes in the forecasted system conditions, alleviating the impact of uncertain system parameters. Additionally, a decentralized market clearing algorithm for eventual multi-area AC and DC grids is presented in Chapter 7. Finally, Chapter 8 concludes and discusses possible directions for future work.

1.5   List of publications

The relevant publications which are the core of this thesis are listed as follows:

[**Paper A**] L. Halilbašić, F. Thams, A. Venzke, S. Chatzivasileiadis, and P. Pinson, "Data-driven security-constrained AC-OPF for operations and markets," in *Proceedings of 20th Power Systems Computation Conference*, Dublin, Ireland, 2018.

[**Paper B**] F. Thams, L. Halilbašić, P. Pinson, S. Chatzivasileiadis, and R. Eriksson, "Data-driven security-constrained OPF," in *Proceedings of 10th Bulk Power Systems Dynamics and Control Symposium - IREP*, Espinho, Portugal, 2017.

[**Paper C**] L. Halilbašić, P. Pinson, and S. Chatzivasileiadis, "Convex relaxations and approximations of chance-constrained AC-OPF problems," *IEEE Transactions on Power Systems*, vol. 34, no. 2, pp. 1459-1470, March 2019.

[**Paper D**] L. Halilbašić, F. Thams, P. Pinson, and S. Chatzivasileiadis, "Security and uncertainty in power systems operations and markets: A unified framework," *Working paper*.

[**Paper E**] A. Venzke, L. Halilbašić, A. Barré, L. Roald, and S. Chatzivasileiadis, "Chance-constrained AC optimal power flow integrating HVDC lines and controllability," in *Proceedings of the 11th Mediterranean Conference on Power Generation, Transmission, Distribution and Energy Conversion*, Dubrovnik, Croatia, 2018.

[**Paper F**] L. Halilbašić, S. Chatzivasileiadis, and P. Pinson, "Coordinating flexibility under uncertainty in multi-area AC and DC grids," in *Proceedings of IEEE PowerTech Conference*, Manchester, UK, 2017.

Other work not included in the thesis:

[**Paper G**] L. Halilbašić, F. Thams and S. Chatzivasileiadis, "BEST PATHS Deliverable 13.1: Technical and economical scaling rules for the implementation of demo results," Technical Report, Technical University of Denmark, 2018.

CHAPTER 2

Security and uncertainty in power system optimization today

This chapter provides an overview of basic power system modeling aspects relevant to the work in this thesis and reviews various applications of optimization methods in power systems. It introduces the power flow equations. They constitute the fundamental component of many power system tools ensuring reliable and economic operation. One such tool is the optimal power flow (OPF), an optimization problem widely used across the entire industry in various forms to optimize e.g., costs or losses. The OPF is introduced and various requirements for the OPF relevant to real-life applications are discussed, such as extensions to and more robust approximations of the basic problem. Finally, this chapter defines the target operating region of power systems and reviews issues and current practices related to its implementation in optimization algorithms.

For a more extensive analysis focusing on power flow based studies and optimization algorithms, the reader is referred to [23–25].

2.1 The power flow equations

The electrical grid is a large-scale network, which connects electricity producers (generators) and customers (loads), and consists of a set of network nodes $\mathcal{N}$ and network lines $\mathcal{L}$. Each line $l \in \mathcal{L}$ is associated with a tuple (i, j) defining its sending and receiving node. The AC power flow equations model the complex, steady-state network flows of a power system and determine the nonlinear relationship between complex voltages $\underline{\mathbf{V}}$ and complex/apparent power injections $\underline{\mathbf{S}}$, both of which are defined for each node $i \in \mathcal{N}$,

$$\underline{\mathbf{S}} = \underline{\mathbf{S}}_{\mathrm{G}} - \underline{\mathbf{S}}_{\mathrm{L}} = \mathrm{diag}(\underline{\mathbf{V}})(\underline{\mathbf{Y}}\underline{\mathbf{V}})^{*}. \tag{2.1}$$

$\underline{\mathbf{Y}}$ represents the complex ($|\mathcal{N}| \times |\mathcal{N}|$) network admittance matrix [26]. Subscript G and L refer to the contributions of generators and loads to the nodal apparent power injection, respectively. The complex conjugate of a quantity is denoted with an asterisk.

Alternatively, the complex nodal voltages $\underline{V}_i$ are often represented in polar coordinates, while the complex nodal power injections $\underline{S}_i$ are expressed in rectangular coordinates with their real and imaginary parts denoting active and reactive power injections, respectively. The most common notation of the AC power flow equations is given by

$$P_i = P_{\mathrm{G}_i} - P_{\mathrm{L}_i} = V_i \sum_{j \in \mathcal{N}} V_j \Big(\mathbf{G}_{ij} \cos(\theta_i - \theta_j) + \mathbf{B}_{ij} \sin(\theta_i - \theta_j) \Big), \qquad \forall i \in \mathcal{N}, \tag{2.2}$$

$$Q_i = Q_{\mathrm{G}_i} - Q_{\mathrm{L}_i} = V_i \sum_{j \in \mathcal{N}} V_j \Big(\mathbf{G}_{ij} \sin(\theta_i - \theta_j) - \mathbf{B}_{ij} \cos(\theta_i - \theta_j) \Big), \qquad \forall i \in \mathcal{N}, \tag{2.3}$$

where P denotes the active power injection, Q the reactive power injection, V the voltage magnitude and θ the voltage angle. Analogously to (2.1), they are defined for each node $i \in \mathcal{N}$. $\mathbf{G}$ and $\mathbf{B}$ are the real and imaginary part of $\underline{\mathbf{Y}}$. Hence, the relationship between the $4|\mathcal{N}|$ variables $\mathbf{x} := \{\mathbf{P}, \mathbf{Q}, \mathbf{V}, \boldsymbol{\theta}\}$ is described through $2|\mathcal{N}|$ equations (2.2) – (2.3). In order to be able to apply appropriate solution techniques, two variables are typically specified per node according to the corresponding nodal characteristics. *PQ* buses are usually load buses and have known active and reactive power injections. Generators are equipped with voltage regulators, and can adjust their reactive power outputs to keep their desired active power injections and voltage magnitudes constant. Therefore, generator buses are usually classified as *PV* buses. At all times, total power generation must equal the sum of total power demand and total power losses. As power losses are not known in advance, active and reactive power injections of at least one generator need to remain unspecified. This so-called *slack* or *reference* bus has a pre-defined voltage magnitude and angle ($\theta = 0$), the latter of which serves as a reference for all other angles in the system.

The system of equations (2.2) – (2.3) represents a set of nonlinear equations, for which no closed-form solution exists. AC power flow tools therefore rely on iterative numerical techniques, such as the Newton-Raphson or Gauss-Seidel method, to determine all unknown voltage magnitudes and angles for a given dispatch. Once all voltage magnitudes and angles, and thus the power flows are known, all remaining unknown power injections are determined.

2.2   The optimal power flow problem

AC power flow tools determine the nodal voltage quantities for a given dispatch and do not take into account any equipment ratings or other system limitations. Although some tools can integrate more considerations, such as generator reactive power limits through heuristic bus type switching [27], the generator active power dispatch itself always has to be provided as an input to the power flow analysis. The optimal power flow problem, on the other hand, is an optimization problem. It seeks an optimal solution of all $4|\mathcal{N}|$ variables, and thus an optimal operating point $\mathbf{x} := \{\mathbf{P}, \mathbf{Q}, \mathbf{V}, \theta\}$ for a given objective function. The general problem formulation is given by

$$\min_{\mathbf{x}} \quad f(\mathbf{x}) \tag{2.4}$$

$$\text{s.t.} \quad g_i(\mathbf{x}) = 0, \quad i = 1, \dots, \mathrm{n}, \tag{2.5}$$

$$h_i(\mathbf{x}) \leq 0, \quad i = 1, \dots, \mathrm{m}, \tag{2.6}$$

where the objective function (2.4) can be either linear or nonlinear. It is usually formulated in terms of the active power generation cost to ensure economic operation of the system, i.e., $f(\mathbf{x}) = \mathbf{c}_{\mathrm{G}}^{\mathsf{T}} \mathbf{P}_{\mathrm{G}}$ in case of a linear cost function. Vector $\mathbf{c}_{\mathrm{G}}$ contains the marginal cost of all generators. The set of equations in (2.5) refers to the $2|\mathcal{N}|$ power balance equations (2.2) – (2.3) as well as an additional equality constraint which sets the angle of the reference bus to zero, i.e., $\theta_{\mathrm{ref}} = 0$. The set of inequalities $\mathbf{h}(\mathbf{x}) := \{h_i(\mathbf{x}) \leq 0 \mid i = 1, \dots, \mathrm{m}\}$ comprises upper and lower limits on active and reactive power generation, voltage magnitudes and angles, as well as upper limits on apparent

power branch flows for both flow directions (i, j) and (j, i):

$$\mathbf{h}(\mathbf{x}) = \begin{cases} \mathbf{P}_{\mathrm{G}}^{\min} \leq \mathbf{P}_{\mathrm{G}} \leq \mathbf{P}_{\mathrm{G}}^{\max} \\ \mathbf{Q}_{\mathrm{G}}^{\min} \leq \mathbf{Q}_{\mathrm{G}} \leq \mathbf{Q}_{\mathrm{G}}^{\max} \\ \mathbf{V}^{\min} \leq \mathbf{V} \leq \mathbf{V}^{\max} \\ \boldsymbol{\theta}^{\min} \leq \boldsymbol{\theta} \leq \boldsymbol{\theta}^{\max} \\ (\mathbf{P}_{\mathbf{ij}})^2 + (\mathbf{Q}_{\mathbf{ij}})^2 \leq (\mathbf{S}^{\max})^2 \\ (\mathbf{P}_{\mathbf{ji}})^2 + (\mathbf{Q}_{\mathbf{ji}})^2 \leq (\mathbf{S}^{\max})^2. \end{cases} \tag{2.7}$$

$\mathbf{P}_{\mathbf{ij}}$ and $\mathbf{Q}_{\mathbf{ij}}$ denote vectors of active and reactive power branch flows for all lines $l \in \mathcal{L}$ from their sending to their receiving node. $\mathbf{P}_{\mathbf{ji}}$ and $\mathbf{Q}_{\mathbf{ji}}$ analogously define the reversed flow direction. The OPF based on the full AC power flow equations (2.2) – (2.3) is termed AC-OPF [10]. The nonlinearity of (2.2) – (2.3) and of the apparent power flow limits in (2.7) renders the AC-OPF nonlinear and nonconvex. Potentially many local minima, saddle points and very flat regions make nonconvex optimization very hard (in general, NP-hard [28, 29]) and still challenge existing solution algorithms. Significant advances in nonconvex optimization have been achieved, though, and many *local* solution techniques exist for efficiently computing feasible solutions, such as interior point methods, or sequential quadratic programming [30]. Nevertheless, none of them is guaranteed to converge. Even if they do, the solution quality is determined by the initialization of the solution algorithm (i.e., the input/starting operating point) and there is no proof that the obtained solution is the global optimum. Thus, computational robustness remains the biggest challenge for both AC power flow and OPF algorithms, which, particularly for large networks, often fail to succeed [17, 18, 31, 32].

To increase the reliability of solution algorithms and foster widespread application of optimization tools to improve decision-making in the electricity industry, several convex approximations of the AC power flow equations are widely used for the OPF today. They leverage the benefits of convex programming to provide globally optimal solutions of the approximated problems they solve as well as computational robustness and efficiency. They range from fully linearized DC approximations, neglecting reactive power, voltage magnitudes and losses, to more accurate relaxations and approximations, leveraging the quadratic voltage dependency of the AC power flow equations.

2.2.1 OPF approximations

Two approximations relevant to this thesis are outlined in the following.

The DC optimal power flow

The DC optimal power flow (DC-OPF) is a simplification of the full AC-OPF and based on a linearization of the AC power flow equations. It neglects reactive power and exploits typical power system properties observed in transmission networks under "normal" operating conditions [33]. The DC power flow model is based on the following assumptions:

- voltage magnitudes at all buses are close to their nominal values, such that $V_i = 1$ p.u.;

- voltage angle differences across transmission lines are small, such that $\sin(\theta_i - \theta_j) \approx \theta_i - \theta_j$ and $\cos(\theta_i - \theta_j) \approx 1$;

- transmission lines are lossless (i.e., their resistances are ignored) and their shunt elements are neglected; this assumption stems from the fact that the resistance of a transmission line is usually much smaller than its reactance (i.e., $R \ll X$).

Under these assumptions, the set of optimization variables in the DC-OPF reduces to $\mathbf{y} := \{\mathbf{P}, \theta\}$, the set of equality constraints (2.5) to $|\mathcal{N}|$ linear active power balance equations,

$$P_i = P_{G_i} - P_{L_i} = \sum_{j \in \mathcal{N}} \mathbf{B}^{\mathrm{dc}}_{ij} \theta_j, \quad \forall i \in \mathcal{N}, \tag{2.8}$$

and the set of inequality constraints (2.6) to

$$\mathbf{h}(\mathbf{y}) = \begin{cases} \mathbf{P}^{\mathrm{min}}_{\mathrm{G}} \le \mathbf{P}_{\mathrm{G}} \le \mathbf{P}^{\mathrm{max}}_{\mathrm{G}} \\ -\mathbf{P}^{\mathrm{max}} \le \mathbf{P}_{\mathbf{ij}} \le \mathbf{P}^{\mathrm{max}}. \end{cases} \tag{2.9}$$

$\mathbf{B}^{\mathrm{dc}}$ denotes the bus susceptance matrix. $\mathbf{P}^{\mathrm{max}}$ represents the limits on active power flows (i.e., "MW-only" line ratings). They are usually lower than the apparent power flow limits $\mathbf{S}^{\mathrm{max}}$ to account for the neglected reactive power flows [34–36]. The DC-OPF is a linear program (LP) and can be extended to include integer variables resulting in a mixed integer linear program (MILP), which is suitable for a wide range of power system optimization applications, such as unit commitment, transmission line switching, or expansion planning to name a few. Solution techniques for both problem classes are highly efficient and reliable, even for large-scale problems. Due to the numerous benefits of linear programming, many extensions of the DC-OPF have been proposed to include reactive power, voltage magnitudes and losses. A comprehensive review of linear approximations for the OPF problem is provided in [37]. Operators usually rely on one of the DC-OPF variants to clear electricity markets and only use the AC power flow to evaluate the feasibility of the solution ex-post [33]. The accuracy of any DC approximation can vary significantly depending on the system conditions (e.g., system loading) and the number of dimensions it captures from the original problem [34]. Therefore, all DC-OPF variants are prone to approximation errors and can result in physically meaningless solutions. The impact of the linearization for approximating the nonconvex feasible space of the AC-OPF is visualized in Fig. 2.1. The extent of the polyhedral feasible space of the DC-OPF is controlled by the reduced "MW-only" line ratings $\mathbf{P}^{\mathrm{max}}$. Their quality and conservatism highly depends on the system conditions and prior knowledge on the eventual operating region, i.e., generator dispatch and associated system losses. For a better approximation, losses need to be included as additional loads in the DC-OPF [34]. However, the dispatch with its associated losses is in itself an outcome of the optimization. Given the limited a priori information on the final operating region, the polyhedral feasible space of the DC-OPF might be either very conservative or include parts of the originally infeasible region. In order to recover the feasibility in case the objective function steers the solution towards the originally infeasible region, operators rely on metaheuristic approaches. They can be highly suboptimal and costly.

The application of optimization methods in power systems has already resulted in millions of dollars in savings annually [38], despite being based on usually rather conservative linear approximations. Therefore, significant research effort has been invested in developing more accurate approximations of the AC-OPF. Recently, the major focus has been on convex relaxations, as for certain test systems and conditions, they have proven to provide globally optimal solutions of the original problems [29]. Convex relaxations *outer* approximate the AC-OPF with a general
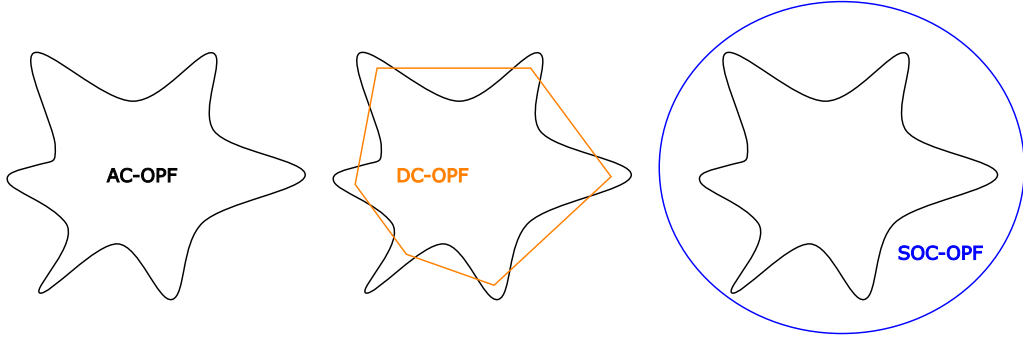
Figure 2.1: From left to right: Illustration of the feasible spaces of the nonconvex AC-OPF, its linearization (e.g., DC-OPF), and its relaxation (e.g., SOC-OPF).

convex program rather than an LP (see Fig. 2.1). They leverage equivalent reformulations of the AC power flow equations to transfer the nonconvexities to constraints, which can then be relaxed or dropped. Convex AC-OPF relaxations are based on semidefinite (SDP) [39], quadratic convex [40], or second-order cone (SOC) [41, 42] programming. Out of those, the SDP relaxation has proven to *dominate* the other two (i.e., it is tighter) and is shown to be exact for many test cases. Still, numerous instances remain, where the SDP relaxation fails to provide AC feasible solutions. In these cases, moment relaxations proposed in [43] can strengthen the relaxation at the expense of larger semidefinite programs. Solvers for SDP have not yet reached the same level of maturity as for general nonlinear problems (and specifically, for convex quadratically constrained problems) [44]. Another major obstacle in SDP are integer variables [45]. Solvers for mixed integer SDP are still in their infancy, which severely limits the application of SDP relaxations.

The second-order cone optimal power flow

SOC relaxations are computationally less demanding and can be extended to mixed integer second order cone programs (MISOCP), which belong to the more general problem class of convex mixed integer nonlinear programs (MINLP). Solvers for convex MINLPs have reached a high level of maturity and exact methods for their solution exist, which combine advances in solution techniques developed separately for MILPs and general nonlinear programming [28]. The SOC relaxation was first proposed in [41, 46]. It is based on an alternative reformulation of the AC power flow equations (2.2) – (2.3), represented by an extended set of $(2|\mathcal{N}| + 2|\mathcal{L}|)$ equations,

$$P_i = \mathbf{G}_{ii}u_i + \sum_{l=(i,j)} \Big(\mathbf{G}_{ij}c_l - \mathbf{B}_{ij}s_l\Big) + \sum_{l=(j,i)} \Big(\mathbf{G}_{ij}c_l + \mathbf{B}_{ij}s_l\Big), \qquad \forall i \in \mathcal{N}, \qquad (2.10)$$

$$Q_i = -\mathbf{B}_{ii}u_i - \sum_{l=(i,j)} \Big(\mathbf{B}_{ij}c_l + \mathbf{G}_{ij}s_l\Big) - \sum_{l=(j,i)} \Big(\mathbf{B}_{ij}c_l - \mathbf{G}_{ij}s_l\Big), \qquad \forall i \in \mathcal{N}, \qquad (2.11)$$

$$0 = c_l^2 + s_l^2 - u_i u_j, \qquad \forall l \in \mathcal{L}, \qquad (2.12)$$

$$0 = \theta_j - \theta_i - \mathrm{atan}\Big(\frac{s_l}{c_l}\Big), \qquad \forall l \in \mathcal{L}. \qquad (2.13)$$

It uses an extended set of optimization variables $\mathbf{z} := \{\mathbf{P}, \mathbf{Q}, \mathbf{u}, \boldsymbol{\theta}, \mathbf{c}, \mathbf{s}\}$, where the new variables $u_i := V_i^2$, $c_l := V_i V_j \cos(\theta_{ij})$ and $s_l := -V_i V_j \sin(\theta_{ij})$ partially capture the nonlinearities of the standard AC-OPF. The power balance equations (2.10) – (2.11) are linearized and the nonlinearities

are transferred to (2.12) – (2.13). The set of inequality constraints is given by

$$\mathbf{h}(\mathbf{z}) = \begin{cases} \mathbf{P}_{\mathrm{G}}^{\min} \leq \mathbf{P}_{\mathrm{G}} \leq \mathbf{P}_{\mathrm{G}}^{\max} \\ \mathbf{Q}_{\mathrm{G}}^{\min} \leq \mathbf{Q}_{\mathrm{G}} \leq \mathbf{Q}_{\mathrm{G}}^{\max} \\ (\mathbf{V}^{\min})^2 \leq \mathbf{u} \leq (\mathbf{V}^{\max})^2 \\ \boldsymbol{\theta}^{\min} \leq \boldsymbol{\theta} \leq \boldsymbol{\theta}^{\max} \\ -\mathbf{V}_{\mathbf{i}}^{\max}\mathbf{V}_{\mathbf{j}}^{\max} \leq \mathbf{c} \leq \mathbf{V}_{\mathbf{i}}^{\max}\mathbf{V}_{\mathbf{j}}^{\max} \\ -\mathbf{V}_{\mathbf{i}}^{\max}\mathbf{V}_{\mathbf{j}}^{\max} \leq \mathbf{s} \leq \mathbf{V}_{\mathbf{i}}^{\max}\mathbf{V}_{\mathbf{j}}^{\max} \\ (\mathbf{P}_{\mathbf{ij}})^2 + (\mathbf{Q}_{\mathbf{ij}})^2 \leq (\mathbf{S}^{\max})^2 \\ (\mathbf{P}_{\mathbf{ji}})^2 + (\mathbf{Q}_{\mathbf{ji}})^2 \leq (\mathbf{S}^{\max})^2. \end{cases} \tag{2.14}$$

$\mathbf{V}_{\mathbf{i}}^{\max}$ and $\mathbf{V}_{\mathbf{j}}^{\max}$ represent $(|\mathcal{L}| \times 1)$ vectors of upper limits on voltage magnitudes for all lines' sending and receiving nodes, respectively. Note that the linearization of the power balance equations renders active and reactive power flows ($\mathbf{P}_{\mathbf{ij}}$, $\mathbf{P}_{\mathbf{ji}}$, $\mathbf{Q}_{\mathbf{ij}}$, $\mathbf{Q}_{\mathbf{ji}}$) linear. Thus, the apparent power flow limits in (2.14) are convex quadratic. The OPF based on (2.10) – (2.14) is an exact reformulation of the original AC-OPF and still nonlinear and nonconvex. To obtain the convex SOC-OPF in its original form as introduced in [46], (2.12) is relaxed through a second order cone constraint (i.e., $c_l^2 + s_l^2 \leq u_i u_j$), while the arctangent constraint (2.13) is dropped. Under certain conditions [47], the SOC relaxation is exact for radial networks and the optimal voltage angles can be recovered by solving $\theta_j^* - \theta_i^* = \operatorname{atan}(\frac{s_l^*}{c_l^*})$, where $(.^*)$ indicates the optimal solution obtained from the SOC-OPF. For meshed networks, it is a strict relaxation, potentially resulting in solutions, which are infeasible to the original problem. To this end, various approaches have been proposed to reintroduce (2.13) while maintaining the convexity of the problem. The author in [42] proposes a sequential conic procedure based on a Taylor series approximation, resulting in an AC-OPF approximation. Other approaches preserve the relaxation and introduce convex envelopes on either the arctangent function [48] or the polar representation of the voltage variables [40, 44] (i.e., the so-called QC relaxation). The main difference lies in whether the final problem represents an approximation (as the DC-OPF) or a relaxation of the AC-OPF (see Fig. 2.1) [25].

This thesis focuses on the original SOC formulation of the power flow equations from [46] and uses the approximation procedure from [42], resulting in an AC-OPF approximation. However, the basic formulation based on [46] is general enough to allow for extensions along the line of [40, 44, 48, 49], which preserve the relaxation.

2.2.2 OPF extensions

The general OPF algorithm, including its convex approximations and relaxations, as presented above, whose feasible set is bounded by usual power system equipment and voltage ratings, is considered to be of limited use. It neither reflects the probabilistic nature of the power injections nor incorporates any security constraints to ensure safe operation [11, 15]. Transmission system operators (TSOs) are responsible for securing the system against sudden disturbances (contingencies) and define criteria to maintain both static (steady-state) and dynamic security after a fault. Static security ensures that after a disturbance no equipment ratings or voltage constraints are violated, whereas dynamic security involves different categories of system stability [13]. In practice, the N-1 criterion is widely used as a preventive measure to ensure that the system can withstand the loss of any of its major system components from both a static and dynamic

security perspective. Errors in nodal power injection forecasts $\boldsymbol{\xi}$ (e.g., renewable energy or load forecasts) lead to deviations from the forecasted operating point and might lead to violations of the security requirements. This raises the need to operate in a region which is also secure against the uncertainty impact with sufficient confidence, termed *confidence region* in this thesis. As a result, many extensions to the standard OPF problem for different power flow modeling frameworks have been proposed. Their basics and outstanding challenges are discussed in the following.

Security-constrained OPF

Security-constrained OPF (SC-OPF) algorithms have primarily focused on static security requirements. They ensure that for a specified set of contingencies $\mathcal{C}$ (i.e., N-1 criterion) all equipment and voltage ratings are within limits. The variable vector and the constraint set of the optimization problem are simply replicated for all contingencies. The standard static SC-OPF is formulated as

$$\min_{\mathbf{x}_c} \quad f(\mathbf{x}_0) \tag{2.15}$$

$$\text{s.t.} \quad g_i(\mathbf{x}_j) = 0, \qquad i = 1, \ldots, \text{n}, \quad j = 0, \ldots, \text{c}, \tag{2.16}$$

$$\qquad h_i(\mathbf{x}_j) \leq 0, \qquad i = 1, \ldots, \text{m}, \quad j = 0, \ldots, \text{c}, \tag{2.17}$$

where $c = |\mathcal{C}|$ denotes the number of contingencies. The objective function (2.15) minimizes the total generation cost for the faultless base case indicated with subscript 0. In a preventive security framework, control variables (e.g., generator active power, generator terminal voltages etc.) are not allowed to change from pre- to post-contingency state, as opposed to frameworks that permit corrective control actions in real-time after a fault has occurred. Regardless of the control framework, the major challenges of conventional SC-OPF algorithms are [9] (i) the inclusion of dynamic security constraints and (ii) their problem size, particularly for large networks with many considered contingencies. For a comprehensive review on SC-OPF algorithms, the reader is referred to [9, 15].

OPF under uncertainty

Optimization problems contain more often than not parameters which are inherently uncertain and require decisions to be made with only partial information on their actual realizations. In the OPF problem, these parameters primarily refer to renewable energy and load forecasts. Both are increasing in significance with the growing share of variable and only partially predictable renewable electricity generation and a higher consumer engagement. To this end, several methods for optimization under uncertainty have been adopted for the OPF problem to secure the system against the impact of forecast errors. These include stochastic programming and robust optimization. Common to both of them is that they explicitly model the impact of the uncertainty $\boldsymbol{\xi}$ (i.e., forecast error) on the optimization variables,

$$\tilde{\mathbf{x}}(\boldsymbol{\xi}) = \mathbf{x} + \boldsymbol{\Delta}\mathbf{x}(\boldsymbol{\xi}). \tag{2.18}$$

Here, $\tilde{\mathbf{x}}$ represents the actual realizations of the optimization variables, modeled as the sum of their optimal value for the forecasted operating point $\mathbf{x}$ and their reaction to a forecast deviation $\boldsymbol{\Delta}\mathbf{x}(\boldsymbol{\xi})$. Note that $\boldsymbol{\xi}$ denotes a multidimensional vector of uncertain parameters.
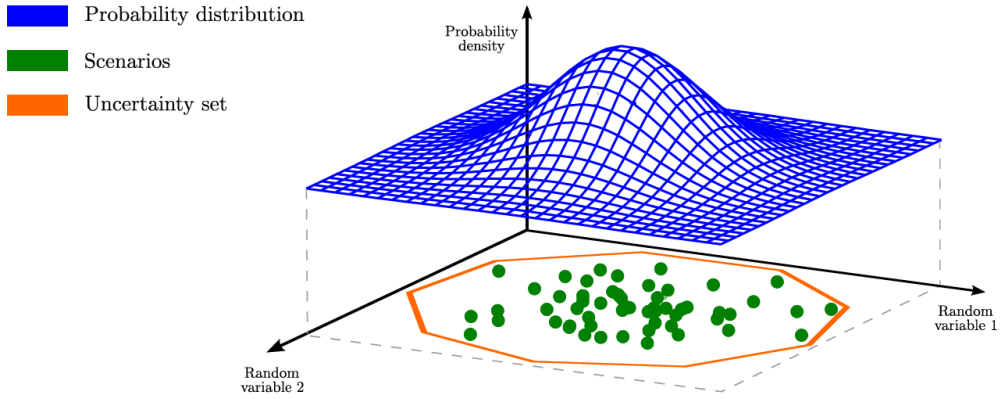
Figure 2.2: Uncertainty representation in the form of scenarios (stochastic programming), uncertainty sets (robust optimization), and continuous probability distributions (chance constraints). Figure from [50].

Stochastic programming

Stochastic programming optimizes over a set of potential uncertainty realizations $\boldsymbol{\Xi} := \{\boldsymbol{\xi}_i \mid i = 1, \ldots, s\}$ in the form of scenarios [51], sampled from a pre-assumed probability distribution. The number of scenarios is denoted with s. The stochastic program may involve a number of temporal *stages*, where information of uncertain parameters is gradually revealed and decisions are made. In the OPF literature, the most frequently applied framework is the two-stage stochastic program. The first stage represents the day-ahead stage, where *here-and-now* decisions $\mathbf{x}$ need to be taken for the forecast values of the uncertain parameters before their actual realizations are disclosed. The real-time or second stage involves *wait-and-see* or *recourse* actions for each scenario, $\boldsymbol{\Delta}\mathbf{X}(\boldsymbol{\Xi}) := \{\boldsymbol{\Delta}\mathbf{x}_i(\boldsymbol{\xi}_i) \mid i = 1, \ldots, s\}$. Those are corrective measures to ensure feasibility once the uncertainty is revealed. Similar to the SC-OPF (2.15) – (2.17), where contingencies are the equivalent of scenarios, the stochastic OPF is given by

$$\min_{\mathbf{x}, \boldsymbol{\Delta}\mathbf{X}(\boldsymbol{\Xi})} \quad f(\mathbf{x}) + \sum_{i=1}^{s} \pi_i q_i(\boldsymbol{\Delta}\mathbf{x}_i(\boldsymbol{\xi}_i)) \tag{2.19}$$

$$\text{s.t.} \quad g_i(\mathbf{x} + \boldsymbol{\Delta}\mathbf{x}_j(\boldsymbol{\xi}_j)) = 0, \qquad i = 1, \ldots, n, \quad j = 0, \ldots, s, \tag{2.20}$$

$$h_i(\mathbf{x} + \boldsymbol{\Delta}\mathbf{x}_j(\boldsymbol{\xi}_j)) \leq 0, \qquad i = 1, \ldots, m, \quad j = 0, \ldots, s. \tag{2.21}$$

The objective function (2.19) minimizes the total *expected* cost, which is typically modeled as the sum of first-stage cost $f(\mathbf{x})$ and recourse cost $q_i(\boldsymbol{\Delta}\mathbf{x}_i(\boldsymbol{\xi}_i))$ of all scenarios weighted by their respective probabilities π_i [50]. The recourse cost function of scenario i is denoted with q_i. Scenario $\boldsymbol{\xi}_0$ refers to the forecasted operating point, where $\boldsymbol{\Delta}\mathbf{x}_0(\boldsymbol{\xi}_0) = 0$. Hence, all equality and inequality constraints are enforced for both the forecasted operating conditions and all scenarios.

Robust optimization

Robust optimization represents an alternative framework to deal with uncertainty in optimization problems. In its general definition, it refers to problems, in which decision-makers seek a desired level of robustness against the uncertainty. Contrary to stochastic programming, robust optimization considers a continuous range of the uncertainty and aims at ensuring feasibility for all realizations within. It is therefore well aligned with the strict requirements for power

system reliability, where feasibility at all times is most fundamental. The uncertainty in robust optimization is represented through so-called *uncertainty sets*. They are usually bounded and constructed around a collection of data points in the uncertainty space. In a one-dimensional uncertainty space for example, the uncertainty set is determined by the minimum and maximum values of the uncertainty realization, i.e., $\Xi := [\xi^{min}, \xi^{max}]$. An illustrative comparison of the uncertainty representation for different programming frameworks is depicted in Fig. 2.2. Chance-constrained programming can be considered a subclass of robust optimization. Some sources do not assign it to robust optimization but rather classify it as a distinct optimization framework (e.g., *probabilistic programming* [52]). Still, it shares the same goal of providing decision makers with guarantees for robustness. The robustness guarantees in chance-constrained programming are probabilistic and allow for constraint violations with very low probability [53].

Chance-constraints are very versatile. They can be reformulated to classical robust problems with bounded uncertainty sets, where the bounds are derived from assumptions on the probability distribution [54]. Alternatively, chance constraints can be substituted with a finite number of hard constraints corresponding to random samples of the uncertainty. This so-called *scenario approach* does not require any assumptions on the probability distribution. It can, under certain conditions and with a finite number of random samples, provide a priori guarantees for the solution to satisfy the probabilistic constraints with a desired confidence level [55]. As it completely disregards the likelihood of the uncertainty realizations, the scenario approach usually results in very conservative solutions. Analytical reformulations of chance constraints as proposed in [56] allow to leverage the knowledge on the statistical properties of the uncertainty and (can but) do not necessarily need to consider the full probability distribution [57], if it cannot be estimated. A major benefit is that probabilistic constraints are directly transformed into equivalent deterministic constraints, keeping the problem size unchanged and the computational complexity low.

This thesis primarily focuses on chance-constrained programming as an intermediate approach between stochastic and classical robust optimization. The general chance-constrained OPF formulation is given by

$$\min_{\mathbf{x}, \mathbf{\Delta x}(\boldsymbol{\xi})} \quad f(\mathbf{x}) \tag{2.22}$$

$$\text{s.t.} \quad g_i(\mathbf{x} + \mathbf{\Delta x}(\boldsymbol{\xi})) = 0 \qquad i = 1, \dots, \mathrm{n}, \quad \boldsymbol{\xi} \in \Xi, \tag{2.23}$$

$$\mathbb{P}\Big(h_i(\mathbf{x} + \mathbf{\Delta x}(\boldsymbol{\xi})) \leq 0, \quad i = 1, \dots, \mathrm{m}, \quad \boldsymbol{\xi} \in \Xi \,\Big) \geq 1 - \epsilon. \tag{2.24}$$

The objective function (2.22) minimizes the total cost for the forecasted operating point. The equality constraints (2.23) are formulated for all realizations $\boldsymbol{\xi}$ in the considered uncertainty set Ξ. The *joint* chance constraint (2.24) limits the joint violation probability of all inequality constraints to a pre-determined tolerance ϵ and ensures a desired confidence level $1 - \epsilon$. Constraint (2.24) can also be approximated through *single* or *univariate* chance constraints, defined for each constraint individually. Single chance constraints are particularly suited for application in power system optimization as they allow to consider individual system constraints with different levels of robustness. This accounts for the fact that there are usually only few active constraints [58], which could compromise system security and need to be treated more cautiously.

Problem (2.22) – (2.24) is however intractable. First, Ξ describes a continuous uncertainty set with infinitely many uncertainty realizations, rendering (2.23) semi-infinite [59]. Second, the chance-constraint (2.24) needs to be reformulated to tractable constraints suitable for current

solution techniques. The major difficulty in chance-constrained programming, particularly when dealing with nonlinear problems, lies in determining a priori the probability distribution of $h_i(\tilde{\mathbf{x}}(\boldsymbol{\xi}))$, and thus of the output variables. Exact deterministic reformulations of (2.24) exist only for very few instances with Gaussian distributions [60]. In all other cases, chance constraints can only be reformulated through tractable approximations using the robust approach, the scenario approach or single chance constraints with analytical reformulations.

2.3   The target operating region

2.3.1   Defining the target operating region

The inclusion of security and uncertainty constraints in the OPF leads to a reduction of the feasible space as compared to the standard deterministic OPF, which is illustrated in Fig. 2.3. The true nonconvex feasible space of the standard AC-OPF is represented by the black boundary. Fig. 2.3 further depicts (a) the *secure operating region* and (b) the *confidence region*. The secure operating region constitutes the intersection of the statically and dynamically secure regions for all considered contingencies. The confidence region contains only operating points that under any realization of the uncertainty (i.e., forecast error $\boldsymbol{\xi}$) remain within the allowable operating region with sufficient confidence $1 - \epsilon$. While many approaches have been proposed, which model either security or uncertainty constraints in the OPF, little work exists that combines both, the majority of which has focused on applications in the DC-OPF with static security [19, 21, 57, 61]. Those implicitly assume a "safe" linear approximation of the nonconvex feasible space and do not question the feasibility of the resulting dispatch. The few proposed methods for the AC-OPF – or more accurate approximations of it considering the solution feasibility [62, 63] – integrate uncertainty with static security constraints only. Hence, they do not accurately represent the secure region (a) in Fig. 2.3.
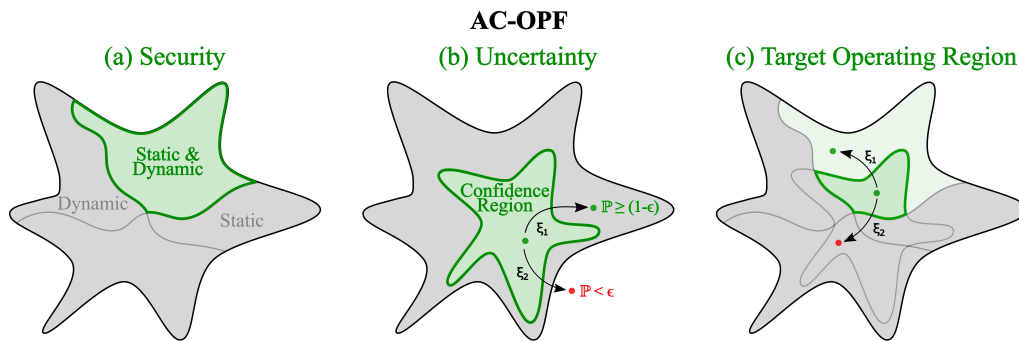
Figure 2.3: Illustration of the target operating region and its components.

The *target operating region* of power system operations (c) is however built up by the intersection of the statically and dynamically secure regions with the confidence region. To the author's knowledge, the works in [64–66] are the only ones which aim at approximating the true target operating region. In [64, 65], the authors derive an approximation of the small-signal and voltage stability boundary considering the distribution of the uncertain parameters. The boundary is directly included in the OPF. This approach is promising as the computationally intensive approximations of the boundary and the uncertainty impact are performed offline, keeping the optimization complexity fairly low. However, the boundary approximation is local and already requires a good estimate of the forecasted operating point as an input, around which to construct

it. Thus, the approximation quality of the boundary is determined by the forecast accuracy. The authors therefore suggest to use the proposed OPF only for re-dispatching generators close to real-time provided that the updated forecasts are close to the initial estimate to ensure sufficient accuracy of the boundary approximation.

The authors in [66] propose an iterative probabilistic transient stability constrained OPF, which alternates between a probabilistic transient stability assessment (PTSA) and an optimization based on a group search algorithm. Despite improvements in the PTSA, the algorithm is still computationally very expensive, as it requires a PTSA at each iteration. Additionally, the approaches presented in [64–66] are tailored to the nonlinear AC power flow equations. However, their solution is not guaranteed as nonlinear solution procedures continue to suffer from convergence issues. The adaptability of any OPF algorithm to linear or convex power flow modeling frameworks, and thus to more robust solution procedures, is a crucial consideration for its real-life deployment.

2.3.2 Modeling the target operating region

Current practice

In order for electricity markets to identify a safe generation dispatch compatible with operational reliability standards (i.e., a dispatch located in the target operating region), system operators first need to determine physical transfer limits. They capture all security and uncertainty requirements and are suitable for a DC modeling framework. After that, the physical transfer limits need to be adjusted to the market environments and translated to limits on commercial transactions. The relationship between physical transfer limits and commercial transaction limits is determined by the congestion management scheme underlying the specific electricity market. The two main approaches in use are based on either *nodal* or *zonal* system models [67], which differ in their granularity of network representation.

In nodal electricity markets, e.g., in the U.S. and New Zealand, a DC model of the entire transmission network with all physical transmission constraints is taken into account. MW limits on physical flows are therefore directly translated to limits on commercial transactions. They are based on the physical line capacities, adjusted for the pre-assumed target operating conditions and the associated security requirements [20].

In zonal electricity markets, such as the integrated European day-ahead market, hundreds of nodes are aggregated into bidding zones. There, market participants can exchange electric power without considering transmission constraints (i.e., "copper plate"). Bidding zones are further linked to each other through constrained interconnectors (i.e., tie-lines), which allow for commercial exchanges between zones. Due to the reduced network representation, commercial transactions no longer correspond to physical flows, which increases the complexity in determining appropriate transaction limits. The two main methods employed in practice are based on *available transfer capacities* (ATCs) or *flow-based market coupling* (FBMC) [68]. In both cases, system operators carry out extensive security assessments prior to the day-ahead market clearing. Those are based on a combination of AC power flow analyses and heuristic methods to derive so-called *total transfer capacities* (TTCs) for all zonal interconnections. The TTC represents the maximum active power that can be transferred between two bidding zones without compromising system reliability [69, 70]. It is highly dependent on the system conditions (i.e., network topology, demand, generation dispatch, considered contingencies etc.), and therefore difficult to evaluate ex-ante before the actual operating

(a) ATC.   (b) FBMC.

(c) Flow domains of ATC and FBMC.
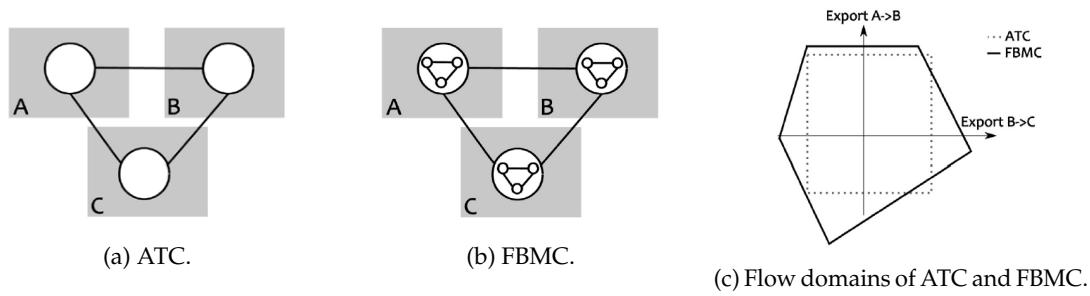
Figure 2.4: Comparison of ATC and FBMC in terms of zonal network representation (a) and (b) as well as flow domains (c). Figure adapted from [20].

conditions are known. The pre-assumed system state determines which limiting condition is most restrictive – thermal, voltage or stability limits. Thus, a TTC is defined as follows,

$$\text{TTC} = \min\{\text{thermal limit, voltage limit, stability limit}\}. \tag{2.25}$$

TSOs additionally determine transmission reliability margins (TRMs), which aim at compensating for the inherent uncertainty in the system conditions. The final cross-border transfer capacity available for commercial use in the day-ahead market is termed *available transmission capacity* (ATC) and is given by

$$\text{ATC} = \text{TTC} - \text{TRM} - \text{NTF}. \tag{2.26}$$

NTF denotes the *notified transmission flow* and represents the already committed long-term capacity nominations (i.e., accepted transfer contracts) [68]. In Europe, long-term interconnector capacity continues to be allocated in *explicit* auctions, where electricity and transmission capacity are traded separately. After the introduction of *market coupling* at the day-ahead level, electricity and the remaining interconnector capacity (i.e., ATC) are cleared jointly in *implicit* auctions after TSOs inform all participating power exchanges on the ATC values of their interconnectors.

In order to ensure a feasible market dispatch, ATCs need to capture all security and uncertainty requirements of the entire interconnected power system. Hence, the originally high-dimensional, large-scale and nonconvex problem has to be approximated with a dramatically reduced low-dimensional set of static ATC parameters. Besides that, ATCs are independent of the flows on other cross-border links and tend to be very conservative. Their calculation procedures are considered by regulators and market participants to be opaque and overly conservative [20].

As a result, an alternative transmission capacity allocation mechanism has been proposed as an intermediate approach between the ATC method and the nodal market clearing. After a two years offline testing period demonstrating an increase in social welfare as compared to the ATC method, FBMC was introduced in the Central Western European day-ahead market in 2015. The remaining part of the European day-ahead market continues to use ATCs [20]. Both methods can be incorporated alongside each other in Euphemia, the optimization algorithm that clears the European day-ahead market [71]. The key difference lies again in the network representation, which is visualized in Fig. 2.4a and 2.4b. An increased amount of physical transmission constraints is taken into account, where not only cross-border interconnectors but also other critical intrazonal lines are explicitly accounted for. In the FBMC framework, the commercial transaction along a

critical line is constrained by the *remaining available margin* (RAM). The mutual impact of the commercial flows is modeled through zonal power transfer distribution factors (PTDFs). RAMs and zonal PTDFs constitute the FBMC parameters, which are determined by the participating TSOs and provided to the day-ahead market prior to its clearing. Since FBMC considers the interdependence of flows on critical lines through PTDFs, its *flow domain* (i.e., its feasible space) tends to be larger and thus less conservative than the ATC domain (see Fig. 2.4c).

Note that also across the U.S., similar concepts to ATCs and FBMC are used for managing power exchanges on interconnections between neighboring ISOs and balancing authorities [69, 72]. While most ISOs' internal electricity markets use a nodal network representation, imports and exports across interconnectors are managed and priced using a proxy bus for each system. As such, the coupling of various US electricity markets can also be regarded to rely on a zonal network representation. Similar to the European case, the selection of the proxy bus and the calculation of the transfer capacities available for trade on the interconnectors is often considered to be opaque and inefficient.

Challenges

Nodal, ATC and FBMC methods differ in their accuracy for approximating the target operating region. The nodal approach tends to be the least conservative and most accurate as it allows to capture more dimensions of the original problem. However, all three methods are based on polyhedral approximations of the original feasible space as visualized in Fig. 2.5. In the best case, the polyhedrons represent convex inner approximations (left column (a) in Fig. 2.5), such that infeasible results outside the target operating region are avoided. This is usually the case when TSOs' forecasts on the eventual market outcome and the associated system conditions, around which the flow domain is constructed, are sufficiently accurate. However, the increasing uncertainty in power system operations makes it gradually more difficult to estimate the future conditions. In the worst case, unexpected system conditions might lead to the point, where flow domains fail at adequately representing the target operating region. In this case, the risk for physically infeasible market outcomes increases (right column (b) in Fig. 2.5). Additionally, a single polyhedral approximation does not sufficiently represent the nonconvex reality of power system operations and ultimately leads to the loss of "valuable" feasible space, which might contain more efficient solutions.

In the following chapters, this thesis introduces modular and computationally efficient methods to better approximate the target operating region in OPF algorithms. They are adaptable to various power flow modeling frameworks and as such, suitable for both market and system operations.
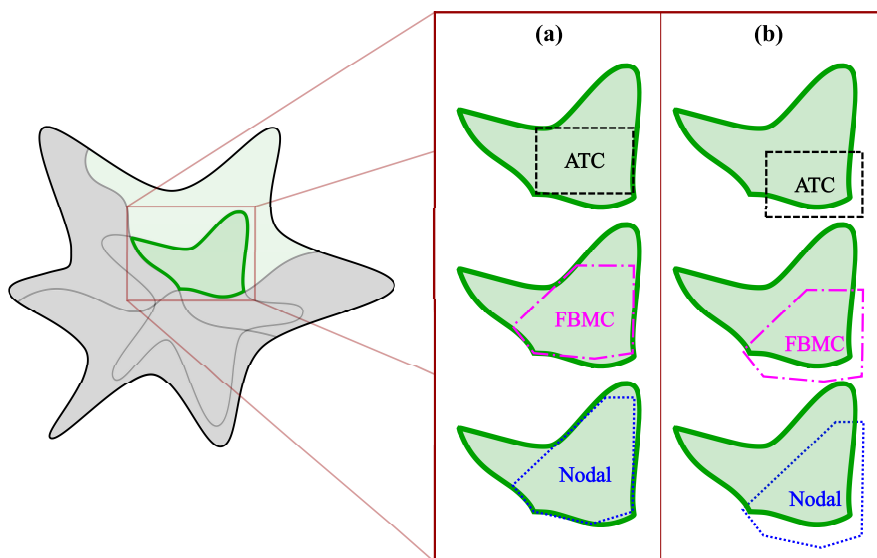
Figure 2.5: Illustration of the target operating region and its approximation with different flow domains. The approximations on the left represent cases with accurate estimates of the eventual operating conditions, where the flow domains do not intrude into the insecure space surrounding the target operating region. The approximation on the right depicts a case in which the estimates on the eventual system conditions are not sufficiently accurate.

CHAPTER 3

Approximating the security region: A data-driven SC-OPF

*This chapter focuses on the secure operating region as a major constituent part of power systems' target operating region. In order to include the secure operating region in an optimization, we propose a data-driven security-constrained OPF (SC-OPF) in [**Paper A**] and [**Paper B**], which unifies machine learning and traditional mathematical optimization. Our approach integrates both static and dynamic security, remains computationally efficient, and is adaptable to various power flow modeling frameworks. Therefore, it is suitable for both market-clearing processes and close to real-time operations. We use decision trees to capture the nonconvex secure operating region and translate them to an optimization framework through mixed integer programming and disjunctive constraints. This allows us to efficiently preserve the nonconvex reality of power systems, even when using convex formulations of the power flow equations. We present specific examples for an AC and DC formulation and demonstrate how the secure operating region represented in the OPF can be significantly enlarged compared to current approaches.*

3.1 Introduction

The security-constrained optimal power flow (SC-OPF) is a fundamental tool for power system operation and planning, as it is used to assess and enhance power system security. It can be applied at different planning stages to either determine an optimal and secure dispatch or to identify optimal redispatching actions closer to real-time operation. The SC-OPF identifies optimal preventive control actions and ensures that the system can withstand the loss of any major component without violating system constraints. This criterion, commonly known as N-1 criterion, is the prevailing security requirement currently employed by most TSOs. In this context, system constraints refer to both static and dynamic security limits. Static security limits include usual power system equipment and voltage ratings, whereas dynamic security constraints refer to various categories of system stability [13]. Dynamic security limits can be stricter than static limits [12]. They are gradually imposing tighter restrictions on power system operations due to the increasing deployment of inverter-based renewable electricity generation and other power electronic devices. Power electronic dynamics are faster than those occurring in predominantly synchronous machine-based systems and their interactions give rise to more complex dynamic system behavior. At the same time, power electronic devices provide better control capabilities, which, in turn, can improve system security if they are adequately accounted for in operational tools.

Despite the increasing impact of dynamics on system security, SC-OPF algorithms have primarily focused on static security requirements. Dynamic security constraints (i.e., stability constraints) are based on differential algebraic equations and are, therefore, difficult to incorporate in an optimization problem. The traditional SC-OPF, as discussed in Chapter 2, extends the constraint

set of the conventional OPF and replicates it for all considered contingencies to ensure that static ratings are always met under any scenario. This highlights two major drawbacks of the SC-OPF: (i) its large problem size and high complexity due to the large number of contingencies and nonlinear power flow equations, and (ii) the negligence of dynamic security requirements. In practice, these challenges are addressed by using computationally more efficient linear DC approximations of the power flow equations and decoupling static from dynamic security assessments. Transmission system operators (TSOs) often rely on iterative procedures, which alternate between (i) a security-constrained DC-OPF for the static security and (ii) a feasibility recovery and dynamic security assessment [73]. The goal of (ii) is to determine tighter constraints for (i) in order to yield AC feasible and secure solutions. These metaheuristic procedures are, however, suboptimal and intransparent.

Additionally, market-clearing processes and security assessments are separated in most electricity markets [14]. Market operators determine the generator dispatch in auctions based on DC-OPFs considering only a few physical limitations, such as generation limits and selected line flow limits. TSOs, in charge of a secure and reliable system operation, determine the actual physical bounds through metaheuristic approaches and carry out necessary redispatching measures. In order to optimally establish secure system operation and avoid expensive redispatching actions, market-clearing processes need to account for all security considerations. Today, this is done by imposing overly conservative constraints on commercial transactions, which TSOs determine a priori based on their assumptions on the eventual market outcome. However, growing uncertainty in power system operations gradually impedes accurate predictions, requiring even more conservative security strategies. Furthermore, current commercial transactions are constrained to a convex security domain and do not sufficiently represent the nonconvex reality of power system operations. To this end, comprehensive SC-OPF algorithms are required, which capture the entire nonconvex static and dynamic security domain and can be used by both market and system operators to identify cost-efficient dispatch and redispatch decisions while avoiding complicated metaheuristic approaches. As such, they need to be adaptable to an AC and DC environment depending on their application, scalable and rapidly deployable in market-clearing processes and close to real-time operations.

Several methods to include more extensive security considerations have been proposed. The authors in [14] and [74] use eigenvalue sensitivities with respect to OPF decision variables to maintain tractability of small-signal stability constraints. However, both papers conclude that the required computational effort is a major challenge and the methods perform poorly when applied to larger systems. Additionally, as opposed to our work, the method developed in [14] determines only the optimal redispatching action of the TSO and does not incorporate small-signal stability constraints in market-clearing mechanisms. An online preventive control strategy accounting for contingencies and transient stability was developed in [75]. The security considerations are translated to generator capacity limits of the most critical generators, which are included as hard constraints in the OPF. This approach, however, does not allow the market participants to bid all their available capacity and imposes very conservative bounds, which can prevent the deployment of cheaper generation capacity. In [76] a security boundary-constrained DC-OPF ensuring voltage and small-signal stability is proposed, where hyperplanes are used to linearly approximate the security boundary. However, operating points outside the convex space constructed by the hyperplanes are neglected, increasing the likelihood of missing the optimal solution. In general,

SC-OPF frameworks including dynamic security remain computationally very expensive and tailored to specific problems [9].

In this chapter, we address the challenges described above and propose a data-driven SC-OPF, which

- efficiently incorporates static and dynamic security for the base case and all considered contingencies;

- avoids the complex reformulation of dynamic constraints and the explicit modeling of all contingencies in the OPF;

- is adaptable to any power flow modeling framework, and therefore suitable for market and system applications;

- reflects the true nonconvex security region, regardless of how the power flow equations are formulated, potentially revealing more cost-efficient solutions;

- is applicable to large systems and allows for a fast online computation, as all computations related to the N-1 criterion and dynamic security are carried out offline.

The data-driven SC-OPF relies on a large database of operating points classified according to their security assessment. The database essentially captures a discrete representation of the whole potential operating region and distinguishes between secure and insecure instances within. We use decision trees to derive conditional decision rules that capture the full nonconvex security region. The decision tree partitions the security region into subspaces, which can be incorporated in any OPF through mixed integer programming (MIP), using binary variables and disjunctive constraints. Although the integrality restriction renders the problem nonconvex, solution techniques for MIP have significantly improved since the 1990s and become very efficient, which has fostered its widespread application across various industries. This continually reinforces further development of MIP approaches.

We demonstrate how the data-driven SC-OPF can be applied in both AC and DC environments and discuss specific challenges and solutions in the corresponding sections.

3.2 Framework for the data-driven SC-OPF

The framework for deriving the proposed data-driven SC-OPF is depicted in Fig. 3.1. Our approach consists of two major parts: (i) an offline construction of the discretized secure operating region and its subsequent partitioning using linear decision rules, and (ii) an online SC-OPF incorporating the partitions through mixed integer programming (MIP). The data-driven SC-OPF ensures static and dynamic security of the solution for the faultless base case and all considered contingencies. The constituent parts of the approach are explained in the following.
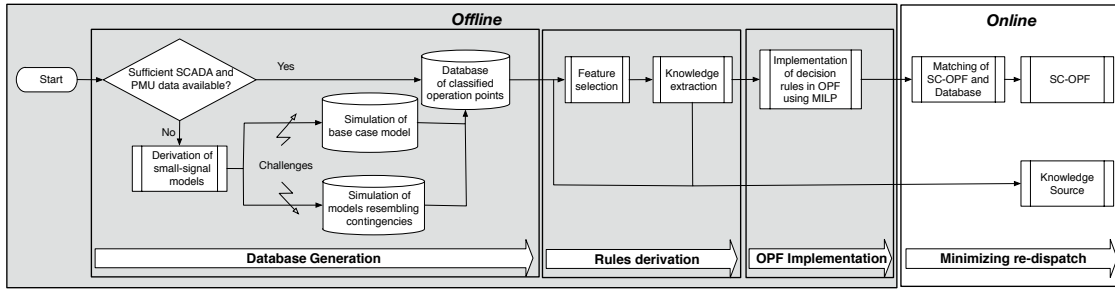
Figure 3.1: Framework for the data-driven SC-OPF. Figure adapted from [**Paper B**].

3.3   Offline approximation of the secure operating region

The offline part (i) consists of a *database generation* followed by a *feature selection and knowledge extraction*. During the *database generation*, we first create a large collection of operating points and then perform a security assessment of each of them for the desired security criteria. Once all operating points in the database are classified according to their security performance, the *feature selection and knowledge extraction* uses appropriate machine learning tools to derive decision rules based on selected features suitable for the desired classification (i.e., secure or not secure) and the subsequent application. The decision rules aim at determining the security performance (i.e., the *target variable*) of any operating point (regardless of whether it is already represented in the database or not) based on some of its selected features, which can correspond to either one of its nodal state/control variables $\{P_i, Q_i, V_i, \theta_i\}$ or combinations of them.

3.3.1   Database generation

In order to generate the required operating points for the database $\mathbf{\Psi} := \{\boldsymbol{\psi} \mid \psi_i = (\mathbf{P}_i, \mathbf{Q}_i, \mathbf{V}_i, \boldsymbol{\theta}_i)\}$, each of which is characterized by the common nodal variables, we use standard AC power flow calculations. The AC power flows are initialized by "all" possible generator dispatch combinations for various load levels. We vary the output of each generator using a specified step size α and thereby, discretize the space of possible dispatch combinations. Thus, depending on the number of generators in the grid N_G, their minimum and maximum production limits $\mathbf{P}_G^{\min}$ and $\mathbf{P}_G^{\max}$, the number of considered load patterns Λ and the chosen discretization interval α, the number of operating points in $\mathbf{\Psi}$ is given by

$$|\mathbf{\Psi}| = \Lambda \prod_{i=1}^{N_G-1} \left(\frac{P_{G_i}^{\max} - P_{G_i}^{\min}}{\alpha} + 1 \right). \tag{3.1}$$

Obviously, this is only one among the possible data generation approaches. The study of how to define and determine the entire space of operating points is equally important and needs to be addressed. We will discuss some challenges of the database generation at the end of this section.

In case that sufficient historical data is available from phasor measurement units (PMUs) or SCADA systems, a portion of the necessary database can be constructed from the recorded measurements. Noise reduction and data correction methods as well as additional security assessments of the measured operating points might also be necessary, in order to accurately project them onto the required domain of $\mathbf{\Psi}$. Nevertheless, given that power systems operate with a very high level of reliability, it is very likely that not enough historical data related to contingency situations have been collected. This makes additional simulations indispensable. Our work in [**Paper A**] and [**Paper B**] relies on simulation data only as we do not have access to adequate PMU or SCADA data.

Security assessment

Once the database $\mathbf{\Psi}$ is created, all operating points need to be examined for their security performance under the faultless base case and all considered contingencies. The results of the evaluation are added to the database, thereby classifying each operating point i according to its security performance κ_i, which is defined for the desired security criteria, i.e., $\mathbf{\Psi} := \{\boldsymbol{\psi} \mid \psi_i = (\mathbf{P}_i, \mathbf{Q}_i, \mathbf{V}_i, \boldsymbol{\theta}_i, \kappa_i)\}$. We define κ_i as a Boolean parameter, which takes the value 1 if the operating point ψ_i is located in the secure operating region and 0 otherwise. The boundary separating the secure $\boldsymbol{\kappa} = \mathbf{1}$ from the insecure $\boldsymbol{\kappa} = \mathbf{0}$ operating region can either correspond to a specific security boundary (e.g., a specific stability boundary or the boundary enclosing the intersection of the static and dynamic security regions for the base case and all contingencies) or represent a required security margin (i.e., a safe distance to the actual security boundary) [77].

In this work, we focus on the N-1 criterion with static security and small-signal (or small disturbance) stability for the dynamic security. We therefore define the secure operating region as the intersection between the static and small-signal stable regions for the base case and all considered faults.

Small-signal stability refers to the ability of a power system to maintain synchronism after small disturbances [78]. It depends on the initial operating point and is nowadays usually a result of insufficient damping of oscillations. The damping ratio ζ describes how system oscillations decay after a disturbance occurs, and therefore serves as a metric for small-signal stability. It can also be interpreted as a margin to the stability boundary and TSOs typically require a minimum damping ratio at any time (e.g., $5\,\%$ in Ireland [79] or $3\,\%$ in Sweden) to ensure sufficient damping and a secure system operation. Although power system stabilizers and other damping controllers have been proposed and shown to be effective in improving small-signal stability, the authors of [80] argue that it is usually not possible to design a damping controller for all possible operating conditions. Hence, if a system's damping controllers are not appropriately tuned to the operating conditions, remedial measures become necessary to maintain small-signal stability. An OPF considering small-signal stability constraints preventively is therefore an efficient way to compensate for the limited operating range of damping controllers and by that, avoid small-signal stability problems.

Besides ensuring that all equipment and voltage ratings are met through a static security evaluation, the security assessment needs to include a small-signal stability assessment of the operating points in $\mathbf{\Psi}$ for all considered network conditions. To this end, we derive $|\mathcal{C}| + 1$ small-signal models, one for each contingency and the base case, where $|\mathcal{C}|$ denotes the number of contingencies. Each small-signal model explicitly incorporates the corresponding fault (e.g., the outage of a transmission line) and describes the dynamic behavior of the power system for the current network conditions through a set of nonlinear differential algebraic equations

$$\dot{\mathbf{x}} = \mathbf{f}(\mathbf{x}, \mathbf{y}) \tag{3.2}$$

$$\mathbf{0} = \mathbf{g}(\mathbf{x}, \mathbf{y}), \tag{3.3}$$

where (3.2) and (3.3) represent the differential and algebraic equations, respectively. Vector $\mathbf{x}$ contains the state variables, while $\mathbf{y}$ represents the algebraic variables. The total number of equations in the *multi-machine model* (3.2) – (3.3) depends on the dynamic order (i.e., the level of detail) of the model used. Several different synchronous machine models have been proposed and a comprehensive review can be found in [81]. In this study, we use a sixth-order synchronous machine model [82] with an automatic voltage regulator (AVR) Type I. The model is based on the following assumptions commonly applied throughout the literature:

- stator and network transients are neglected;

- turbine governor dynamics are neglected allowing to assume a constant mechanical torque;

- the damping torque is assumed to be linear.

Small-signal stability analysis focuses on disturbances, which are small enough to allow for the nonlinear functions $\mathbf{f}(\mathbf{x}, \mathbf{y})$ and $\mathbf{g}(\mathbf{x}, \mathbf{y})$ describing the dynamic and static system responses, respectively, to be linearized around an equilibrium through a first-order Taylor series expansion, i.e.,

$$\mathbf{\Delta \dot{x}} = \mathbf{A \Delta x} + \mathbf{B \Delta y} \tag{3.4}$$

$$\mathbf{0} = \mathbf{C \Delta x} + \mathbf{D \Delta y}. \tag{3.5}$$

Under these conditions, the small-signal stability of the nonlinear dynamic system (3.2) – (3.3) can be determined by the eigenvalues of the characteristic system matrix $\mathbf{A}^{\text{sys}}$, which is derived from the matrices $\mathbf{A}$, $\mathbf{B}$, $\mathbf{C}$, and $\mathbf{D}$ of the linearized system (3.4) – (3.5). According to Lyapunov's first method, a linearized model $\mathbf{A^{sys}}$ is asymptotically stable if all its complex eigenvalues $\lambda_i = a_i + jb_i$ have negative real parts. Each eigenvalue is associated with a *dynamic mode* and the linear combination of all modes describes the final system response to a perturbation. The real component a_i determines the damping, where $a_i < 0$ represents a damped oscillation – the larger the magnitude of a_i the faster its decay – and $a_i > 0$ an oscillation with increasing amplitude. The damping ratio of the ith mode is defined as

$$\zeta_i = \frac{-a_i}{\sqrt{a_i^2 + b_i^2}}. \tag{3.6}$$

In this work, the $|\mathcal{C}| + 1$ small-signal models are derived symbolically. This enables us to initialize each model through the input vector $\mathbf{u}$ with every simulated dispatch and load combination, such that we can derive the characteristic system matrix $\mathbf{A}^{\text{sys}}$ for each contingency and data point in $\mathbf{\Psi}$. Thus, the small-signal stability assessment essentially consists of an eigenvalue analysis of all $|\mathbf{\Psi}|(|\mathcal{C}| + 1)$ system matrices. An operating point ψ_i is considered to be small-signal stable, if all of its associated eigenvalues for all considered network conditions have negative real parts. Its overall damping ratio is determined as the minimum damping ratio ζ_i^{min} associated with all eigenvalues. Note that our approach can also be extended to include other stability or security criteria by incorporating an appropriate evaluation procedure in the security assessment of the operating points.

All equations of the multi-machine model relevant to this thesis and the expression for the characteristic system matrix $\mathbf{A}^{\text{sys}}$ are listed in the appendix of [**Paper B**]. A detailed description of the linearization procedure to obtain (3.4) – (3.5) can be found in e.g., [78].

Challenges

The database generation is one major challenge of this approach and although carried out offline, is an obstacle for scalability if the available historical data is insufficient. Grids with many generators lead to very large databases, even when considering only one load level, if all possible operating points were evaluated as indicated in (3.1). In fact, for grids containing more than a few generators, evaluating all combinatorial dispatch configurations quickly becomes computationally intractable. Specifically, two partially contradicting goals exist: (i) keeping the size of the database as small as

(a) Impact of the discretization interval.

(b) High information content region.
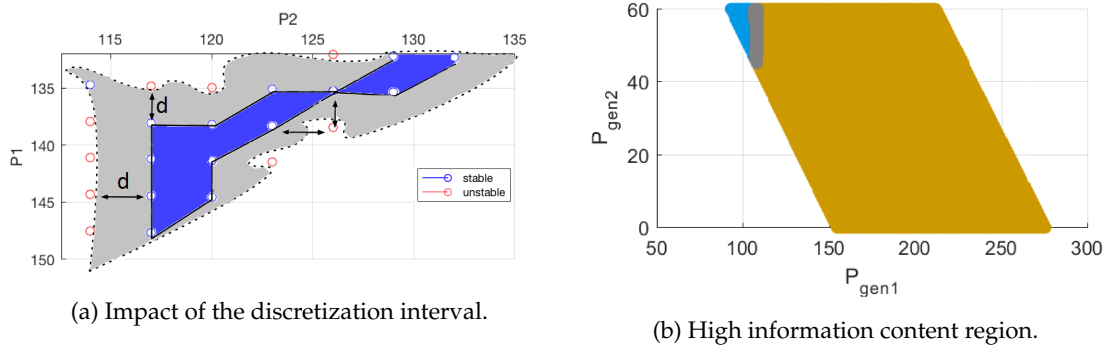
Figure 3.2: The discretization interval α (denoted with d in (a)) needs to be chosen in a way, such the grey area between known secure/stable (blue) and known insecure/unstable (red) operating points, where the security boundary passes through, is minimized. Focusing on the grey high information content region surrounding the boundary in Fig. 3.2b significantly reduces the computational effort. This allows discarding large parts of the operating space, whose security can be inferred if the course of the boundary is approximately known. Fig. 3.2a from [**Paper B**], Fig. 3.2b from [77].

possible to minimize computational demand associated with its generation, while (ii) determining the security boundary as accurately as possible.

The discretization of the operating space leads naturally to a loss of information between the discrete data samples as visualized in Fig. 3.2a. The circles represent samples from the database, whose security/stability is known. Red circles mark insecure/unstable points, whereas blue ones are secure/stable instances. The security performance of the operating points located in the grey area in-between, where the security boundary passes through, is unknown and would require an infinitesimal discretization interval to be accurately determined. Smaller discretization intervals lead to a larger data sample though and are computationally more demanding, whereas larger distances incur inaccuracies and more conservative boundaries.

Fig. 3.2b highlights that applying a uniform discretization interval over the entire potential operating space is counterproductive and will always come at the expense of at least one of the two goals (i) and (ii). More specifically, Fig. 3.2b depicts the scatter plot of all possible operating points of two generators for a certain load level. Blue and yellow mark secure and insecure operating points, respectively. It becomes obvious that large areas of the potential operating space, particularly far away from the boundary, can actually be neglected and do not need to be explicitly represented in the database. The local security level can be inferred when the outline of the security boundary is approximately known. Therefore, focusing on the security boundary and the *high information content* (HIC) region around it significantly reduces the size of the database. In this regard, a nonuniform discretization interval would allow to coarsely sample operating points far away from the region of interest and to increase granularity close to it, which decreases the computational requirements for generating the database but still maintains a sufficient level of accuracy.

Motivated by the work in [**Paper A**] and [**Paper B**], the authors in [77] have recently proposed a highly scalable and computationally efficient method for generating databases for power system security assessment. As the focus lies on identifying and exploring the HIC region, which constitutes only a fraction of the entire potential operating space, the computation time is

substantially decreased. Using convex relaxation techniques and complex network theory, large infeasible regions are discarded, which drastically reduces the search space. The remaining space is explored by *directed walks*, which besides being parallelizable, quickly traverse through large parts of feasible (or infeasible) space using a variable step size, focusing on the HIC region instead. The method accommodates numerous definitions of power system security, has proven to determine the security boundary with very high accuracy, and reduces the computational time to a fraction of the time required by other approaches (over 90% decrease). Creating or enriching already existing databases through an efficient method like this can eliminate the obstacles for large-scale applications of the proposed data-driven SC-OPF.

3.3.2   Feature selection and knowledge extraction

After the database has been created, *features* of the data points need to be selected, which the decision rules will be based upon. The chosen features represent a subset $\hat{\psi}$ of the data's attributes, which are relevant to the security performance κ and well suited for distinguishing between secure and insecure operating points. An appropriate feature selection is crucial, as it determines the accuracy of the decision rules for predicting an operating point's security level. Additionally, the feature selection is constrained by the intended use of the decision rules, requiring $\hat{\psi}$ to be explicitly represented in the target environment.

Since we focus on the application of the decision rules in an OPF environment, the selected features have to be compatible with the required power flow modeling framework, which might not represent all data attributes (e.g., the DC approximation does not model voltage magnitudes and reactive power). One of the most obvious and effective attributes recurring in all OPF formulations would be the active power injection of generators. Imposing limits on the generation dispatch, however, directly targets electricity producers and constrains their ability to fully participate in the electricity market, which does not conform to the current market paradigm that promotes competition and open access. Furthermore, in order to be able to substitute simulation data with PMU or SCADA data in the future, only easily accessible variables should be considered as inputs. We, therefore, focus on line limits or transfer limits, which can be computed based on nodal voltage quantities and are also in line with current industry practices (see Section 2.3.2).

Feature selection for the AC-OPF

In an AC-OPF and more accurate approximations of it, where all data attributes are explicitly represented in the optimization, transfer limits can be directly derived for active, reactive as well as apparent power flows or any combination of them using both voltage magnitudes and angles. In this work, we use voltage angle differences along transmission lines as proxies for the transfer limits,

$$\hat{\psi} := \left\{ \boldsymbol{\Delta\theta} \mid \Delta\theta_l = \theta_i - \theta_j, \ \forall l = (i,j) \in \mathcal{L} \right\}. \tag{3.7}$$

Feature selection for the DC-OPF

Another benefit of using voltage angle differences is that they can be directly incorporated in a DC-OPF or translated to active power line flow limits suitable for a market environment,

$$\hat{\psi} := \left\{ \mathbf{F} \mid F_l = \frac{\theta_i - \theta_j}{x_{ij}}, \ \forall l = (i,j) \in \mathcal{L} \right\}. \tag{3.8}$$

F is used to denote the features for determining the active power transfer limits for a DC environment. DC power flows can however significantly differ from AC power flows [33], such that $\frac{\theta_i - \theta_j}{x_{ij}}$ based on results for θ_i and θ_j from an AC analysis might not well represent the corresponding DC power flows. Since the accuracy of the DC approximation is very application and system specific, no statistical patterns on the DC error have been identified [34] to allow for general guidelines on improving the approximation. Therefore, the main challenge lies in achieving a good mapping between (i) the AC power flow results from the database and the transfer limits derived from them, and (ii) the DC power flows in the optimization, i.e., a mapping from the AC space to the DC space $AC \rightarrow DC$. The standard DC approximation (3.8) represents one approach. However, considering more dimensions and variable interactions of the original problem when computing the transfer limits for the DC-OPF, such as voltage magnitudes and the sine of the angle differences, can yield more accurate approximations,

$$\hat{\psi} := \left\{ \mathbf{F} \mid F_l = \frac{V_i V_j \sin(\theta_{ij})}{x_{ij}}, \ \forall l = (i,j) \in \mathcal{L} \right\}. \tag{3.9}$$

However, the most significant improvements of the DC approximation can be achieved, when including an estimate of the active power losses [34]. We also observed that the most precise $AC \rightarrow DC$ mapping has been achieved, when incorporating a *loss matching* directly into the database generation. To do this, we first determined the MW losses for all operating points in the database and included them as additional loads $\mathbf{P}_{\text{loss}}$ in a subsequent DC power flow. This allows us to determine the exact DC flows $\mathbf{P}^{\text{dc}}$ corresponding to each AC operating point in $\mathbf{\Psi}$. We consider the losses of a line as evenly distributed onto its sending and receiving nodes,

$$P_{\text{loss}_i} = \frac{1}{2} \sum_{j \in \mathcal{L}_i} \left(P_{ij} + P_{ji} \right), \quad \forall i \in \mathcal{N} \tag{3.10}$$

where $\mathcal{L}_i$ represents the set of lines connected to node i and P_{ij}/P_{ji} the active AC power flows. Each sample in the database is thus extended by an additional attribute $\mathbf{P}^{\text{dc}}$, which allows us to select features for the DC environment directly derived from DC power flows,

$$\hat{\psi} := \left\{ \mathbf{F} \mid F_l = P_{ij}^{dc}, \ \forall l = (i,j) \in \mathcal{L} \right\}. \tag{3.11}$$

In other words, we project the discrete AC space from the database onto the loss augmented DC space, from which the features are selected. In our DC-OPF case study in Section 3.6.3, we compare all three approaches (3.8), (3.9) and (3.11) to evaluate the quality of the $AC \rightarrow DC$ mapping. Note that in (3.8) and (3.9) the selected features, and thus the transfer limits for them, are computed from the results of the AC power flow analyses used to generate the database, whereas in (3.11) results from the DC power flow analyses are used.

Knowledge extraction

The knowledge extraction (i.e., the derivation of the decision rules) based on the selected features represents the last part of the offline analysis. In this work, we employ decision trees as the knowledge extraction method, as they are easy to interpret for the user (e.g., the operator), and can be directly incorporated in an optimization problem, which will be discussed in the next Section.

A classification tree is a subset of decision trees (DTs) where the final decision outcome, called *target variable*, can take a finite and discrete set of values. A complete introduction to DT theory for

power systems can be found in [83]. In the generated database, we distinguish between secure ($\kappa = 1$) and insecure ($\kappa = 0$) operating points, such that our target variable takes either 0 or 1 to classify an operating point. The classification tree reveals patterns in the relationships between observation attributes and target variables with the goal of using these patterns as decision rules to predict the decision outcome of new observations. The observation attributes/features used as decision variables are called *predictors*. A simple example of a DT is shown in Fig. 3.3. It contains nodes, branches and terminal decisions. At each node a test of a predictor splits the data set into subsets according to the test result. The branches connecting this node with the nodes one level below represent the possible test outcomes. The leaf nodes with terminal decisions constitute the final classification of the input observation. We use DTs instead of other data mining or machine learning techniques, as they can provide a better understanding of the entire system's security behavior and reveal, which parts of the system are most critical to a secure operation.
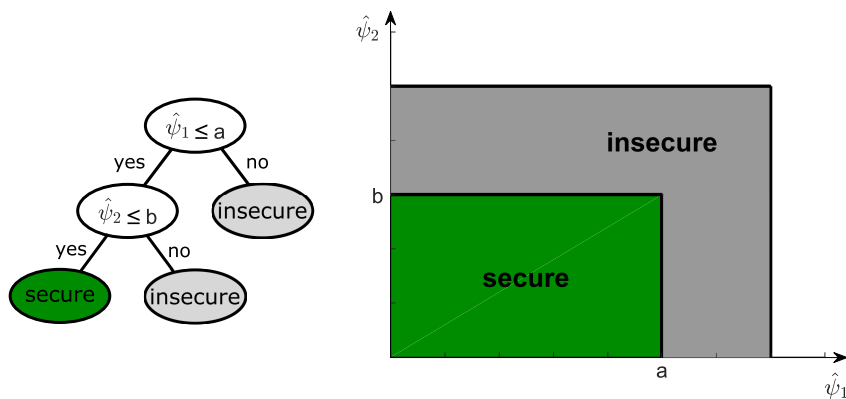
Figure 3.3: Simple example of a decision tree.

Note that before training the DT, the database should be analyzed with respect to the potential problem of skewed classes, i.e. it needs to be examined whether one class ($\kappa = 0$ or $\kappa = 1$) is significantly overrepresented compared to the other. If this is the case, three options exist: (i) limiting the number of the overrepresented class by neglecting an appropriate amount of samples, (ii) oversampling the minority class or (iii) raising the cost of misclassifying the minority class. While option (i) might leave out exactly the most important information close to the security boundary, option (ii) degrades the learning speed due to duplicate instances. Finally, option (iii) allows to introduce risk aversion, which might lead to more conservative and less cost-efficient transfer limits. Though, the consequences of option (iii) can be alleviated through smaller discretization intervals α during the database generation described in Section 3.3.1. The DT is trained using a subset of the whole database, called training set A. The derived rules are tested using another subset B of the database with $A \cap B = \emptyset$. It is worth mentioning that although DTs achieve very high accuracies, there will always be misclassifications, which in theory could lead to insecure solutions of the proposed data-driven SC-OPF. To minimize, if not completely avoid this risk, we took a set of additional actions. First, by increasing the cost for misclassifications of unstable cases we reduce the misclassifications in this direction. Second, by requiring a certain security margin and differentiating between *fulfilling the security margin* and *not fulfilling the security margin*, rather than *secure* and *insecure*, we can reduce the risk even further, since misclassifications do not necessarily lead to insecure instances, but just to operating points with lower margins than

formally required. Finally, in order to avoid overfitting, where the decision rules are fitted too closely to the training data degrading the DT's ability to reliably classify new data points, the obtained trees need to be pruned appropriately. This work applies a manual approach for pruning specific nodes according to the test results of the OPF.

3.4 Online data-driven SC-OPF

The DT essentially represents conditional decision rules. Each full DT path $p \in \mathcal{P}$ from the root node to each terminal decision node comprises a set of upper and lower limits for the selected predictor variables $\hat{\psi}$ and represents linear cuts that partition the operating region. As such, the DT can capture nonconvex and even discontinous feasibility spaces. Each branch leads to a different region of the feasible space, one of which contains the least-cost, optimal solution. An illustration is depicted in Fig. 3.4. Instead of defining bounds that contain only one of the three stable regions depicted in the shades of green, conditional rules defined by DTs allow to capture the entire feasible region within the black frame.
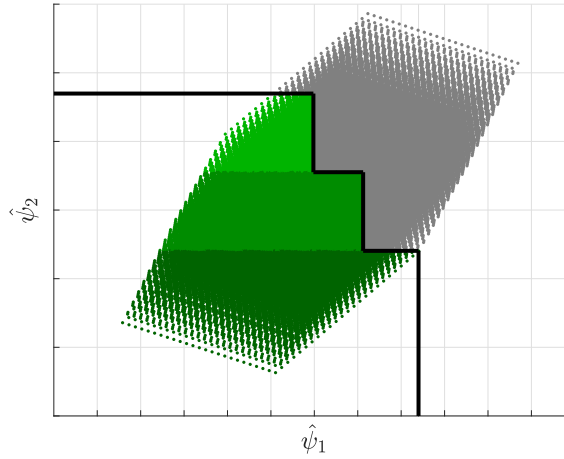
Figure 3.4: Illustrative example of the nonconvex feasible space represented by a decision tree.

The major benefit of using DTs is that they can be easily incorporated in an optimization problem using mixed integer programming (MIP), which allows us to bridge the gap between machine learning and traditional mathematical optimization without loss of accuracy. Each full branch p of the DT is associated with a binary variable b_p, which if chosen, activates the corresponding upper and lower bounds, $\hat{\Psi}_p^{\max}$ and $\hat{\Psi}_p^{\min}$, on the predictor variables. As we are only interested in the secure operating region, all DT paths leading to insecure regions (i.e., with terminal decisions $\kappa = 0$) are discarded, such that $\mathcal{P}$ only contains branches with secure decisions. The proposed data-driven SC-OPF simply extends the standard OPF (2.4) – (2.6) through the additional set of disjunctive constraints

$$\hat{\Psi}^{\min}\mathbf{b} \leq \hat{\psi} \leq \hat{\Psi}^{\max}\mathbf{b}. \tag{3.12}$$

$\mathbf{b}$ is a ($|\mathcal{P}| \times 1$) vector of binary variables, while $\hat{\Psi}^{\min}$ and $\hat{\Psi}^{\max}$ are matrices, where the number of rows corresponds to the number of predictor variables and the number of columns to $|\mathcal{P}|$. Note that not all selected predictor variables are decisive for system security and might therefore, not occur in the DT at all. When using e.g., active power line flows as predictor variables, the DT

identifies the set of lines critical to system security and primarily determines decision rules along their dimensions, while the remaining less significant lines remain unaffected by the decision rules. In this case, their corresponding entries in $\hat{\boldsymbol{\Psi}}^{\min}$ and $\hat{\boldsymbol{\Psi}}^{\max}$ are set to their default limits (i.e., the usual thermal limits) or high values that do not unnecessarily constrain the problem. To ensure that only one DT branch is selected, which provides the bounds on the optimal solution, all binary variables must add up to 1,

$$\sum_{p \in \mathcal{P}} b_p = 1. \tag{3.13}$$

The constraints (3.12) and (3.13) representing the DT capture all static and dynamic security requirements for the base case and all contingencies. As they do not require each contingency to be explicitly modeled in the optimization, the problem size can be significantly reduced compared to conventional SC-OPF approaches discussed in Section 2.2.2. The combination of DTs and integer programming allows to fully reflect the nonconvex nature of power system operations. This renders the approach less conservative than current practices, which usually consider a convex region of operation (see Section 2.3.2).

Additionally, the decision rules can be derived for various predictor variables and are therefore suitable for all OPF formulations irrespective of how the power flow equations are modeled. Different applications and formulations of the data-driven SC-OPF are discussed and demonstrated in the following.

3.5 Data-driven security-constrained AC-OPF

3.5.1 Formulation and challenges

The security-constrained AC-OPF has been identified as the "ultimate goal" for market software to be used by independent system operators (ISOs) across the US [8]. The authors in [8] outline the oversimplification of current software, often requiring operator intervention and resulting in suboptimal solutions due to inaccurate ISO models, which solely use estimates for reactive power and voltage constraints. Improved modeling of voltage and stability constraints can lead to more realistic dispatch decisions and better market signals, resulting in up to 10% cost savings worldwide [84]. The relative amount of potential savings will increase over the course of the coming decades due to the ongoing electrification of the entire energy industry. From a system operations perspective, efficient and fast algorithms for the security-constrained AC-OPF are required to, e.g., optimize redispatch close to real-time, when better estimates on the operating conditions are available.

However, as discussed in previous chapters, current AC-OPF tools, commonly considering only static security, are already a huge computational burden and often computationally intractable, let alone extensions to them, which additionally incorporate aspects of dynamic security. Capturing all security aspects with disjunctive linear inequalities ((3.12) and (3.13)) allows to increase computational efficiency and at the same time include more security considerations. In an AC-OPF framework, the data-driven SC-OPF is thus formulated as a nonconvex mixed integer nonlinear problem (MINLP). We use voltage angle differences across transmission lines as predictor variables and proxies for transfer limits, such that the exact formulation of (3.12) is given by

$$\Delta \boldsymbol{\theta}^{\min} \mathbf{b} \leq \Delta \boldsymbol{\theta} \leq \Delta \boldsymbol{\theta}^{\max} \mathbf{b}, \tag{3.14}$$

where $\mathbf{\Delta\theta}$ denotes the vector of voltage angle differences across all transmission lines and $\mathbf{\Delta\theta}^{\min}/\mathbf{\Delta\theta}^{\max}$ the matrices of conditional DT limits. Nonconvex MINLPs constitute the most challenging class of optimization problems with two levels of nonconvexities: one referring to the integrality of the binary decisions and another one concerning the AC power flow equations. As a consequence, current solvers struggle even with small nonconvex MINLP instances.

3.5.2 Solutions

We therefore propose to relax the nonconvex AC power flow equations using the second-order cone (SOC) relaxation as discussed in Section 2.2.1. The obtained data-driven SC-OPF is thus formulated as a mixed integer SOC problem (MISOCP), which is a convex mixed integer program that can be solved efficiently by already existing solvers. However, the original SOC relaxation as introduced in [46] drops the angle variables and all constraints associated with them, which prevents us from directly incorporating the limits imposed by the DT (3.14). Various convex approximations have been proposed to reintroduce the angle constraint (2.13) (i.e., $\theta_j - \theta_i = \text{atan}(\frac{s_l}{c_l})$) [40, 42, 48]. In this work, we use the sequential conic procedure from [42], where the arctangent function is linearized using a Taylor series expansion. The convergence of the resulting iterative conic procedure is determined by the change in $\mathbf{c}$ and $\mathbf{s}$ variables, e.g. $||\mathbf{c}^\nu - \mathbf{c}^{\nu-1}||_\infty$, where ν denotes the iteration counter.

Known limits on angle differences can also be used to define bounds on the SOC variables $\mathbf{c}$ and $\mathbf{s}$,

$$\left(c_l \tan(\mathbf{\Delta\theta}_l^{\min}) \right) \mathbf{b} \leq s_l \leq \left(c_l \tan(\mathbf{\Delta\theta}_l^{\max}) \right) \mathbf{b}, \quad \forall l = (i, j) \in \mathcal{L}, \tag{3.15}$$

where $\mathbf{\Delta\theta}_l^{\min}/\mathbf{\Delta\theta}_l^{\max}$ refers to the l-th row of matrix $\mathbf{\Delta\theta}^{\min}/\mathbf{\Delta\theta}^{\max}$. Otherwise, the SOC variables $c_l = V_i V_j \cos\theta_{ij}$ and $s_l = -V_i V_j \sin\theta_{ij}$ are constrained by their implied upper and lower bounds $\pm V_i^{\max} V_j^{\max}$, which in practice, can be very loose.

Although the integrality restriction is a nonconvex constraint, convex MINLPs have desirable characteristics that distinguish them from general nonconvex optimization. Specifically, the nonconvex constraints are of a discrete nature. In theory, a convex MINLP can be solved to global optimality through an exhaustive search, which is not true for general nonconvex optimization [85]. In our case, this is particularly straightforward by enumerating all possible DT outcomes. General SOCP has already gained increased attention for power system applications, as it is computationally less demanding than other relaxations, such as semidefinite programming (SDP). MISOCP, on the other hand, has largely remained overlooked by the power systems community. As of the state-of-the art, the only applications of MISOCPs have been proposed in [49, 86] for OPF problems incorporating optimal transmission switching and capacitor placement. Nevertheless, MISOCPs have demonstrated significant potential for real-life applications including among others portfolio optimization, network design, and design and control of chemical processes [28]. In this work, we introduce MISOCP for the security-constrained OPF.

3.5.3 Case study

We evaluate the performance of the proposed data-driven SC-OPF ensuring static security and small-signal stability (i.e., dynamic security) for the base case and all N-1 contingencies on a modified version of the IEEE 14 bus test system [87]. In this section, we focus on the implementation in an AC power flow environment. Our case study consists of three parts. First, we compare the

MISOCP formulation of the algorithm to a data-driven MINLP implementation and a standard (i.e., not data-driven) preventive SC-OPF as formulated in (2.15) – (2.17). Its low computational effort makes the proposed MISOCP suitable for AC based market-clearing auctions as envisaged in the US. In Europe, however, electricity markets will probably continue to rely on DC approximations. To this end, we show how the proposed method can also be used by TSOs for optimizing redispatching actions in order to ensure N-1 security and small-signal stability after the market-clearing. Finally, we analyze how the data-driven approach coupled with MIP notably extends the feasible space of the OPF. Note that the standard preventive SC-OPF (PSC-OPF) does not incorporate stability considerations, but only extends the constraint set to account for the defined N-1 contingencies.

The network data is given in [88]. Bus 1 with generator 1 has been chosen as the slack bus for the base case and all N-1 contingencies. The considered contingencies include all line and bus faults, except for faults at buses 1, 2 and 6. These would lead to either instability/AVR limit violations or operating points, which are unstable for the remaining contingencies. The voltage setpoints of generators 4 and 5 are changed to 1.02 p.u. and 1.01 p.u., respectively, and the reactive power of generator 1 is limited within ± 990 Mvar. The reactive power limits had to be adjusted, as the IEEE 14 bus system would not have been stable for most N-1 contingencies. A step size of 1.5 MW was chosen for discretizing the possible operating range and generating the database of operating points used to derive the decision tree. The minimum damping ratio of an operating point over the base case and all N-1 cases is used as a metric for small-signal stability. As usual in power system operation, we define a security margin by requiring a minimum damping ratio of 3%, which is required for the base case as well as for the steady states obtained after a contingency during the N-1 security analysis. However, this could also be chosen differently by e.g. allowing lower damping ratios after certain faults. As such, the secure operating region $\kappa = 1$ is defined for a 3% damping ratio, such that the insecure region $\kappa = 0$ does contain generally secure operating points but with lower damping ratios than required.

The derived DT contains 136 leaf nodes, out of which 74 point to operating regions, which are small-signal stable for the base case and all considered contingencies. Thus, 74 binary variables are used to define conditional constraints on voltage angle differences along lines and incorporate the stable regions in the data-driven SC-OPF. Note that 1.34 million operating points have been evaluated for this case study, from which more than 88 000 fulfill the required minimum damping ratio. We derive the DT based on three different load levels (base case, $\pm 20\%$). The data-driven SC-OPF was performed for all three levels separately. Given that they showed very similar results, we present our results for the base case only. The voltage magnitude at generator buses is set to the corresponding generator voltage setpoint in order to ensure an appropriate voltage profile, which is fundamental to a secure system operation.

The small-signal models were derived using Mathematica, the initialization and small-signal analysis were carried out using Matlab and Matpower 6.0 [88]. All parameters of the small-signal model for the security assessment are given in the appendix of [**Paper B**]. The MISOCP was implemented in Python using the Gurobi Optimizer. The standard PSC-OPF (i.e., NLP) and the MINLP implementation of the data-driven SC-OPF were carried out in GAMS. BONMIN and COUENNE were used for solving the MINLPs, while CONOPT was used for the NLP (i.e., the PSC-OPF).

Table 3.1: Results of standard PSC-OPF and data-driven SC-OPF implemented as MINLP and MISOCP. Table from [**Paper A**].

		Standard PSC-OPF	Data-driven SC-OPF		
		NLP	MINLP		MISOCP
			COUENNE	BONMIN	
Cost	(€/h)	3022.83	3445.09	3381.21	3365.95
Runtime	(s)	10.06	1000.16	96.16	5.58
Iterations*	(-)	-	-	-	4
Min. damping ratio	(%)	unstable	3.27	2.97	2.53
Leaf node	(-)	-	31	133	104

* The number of iterations refers to the sequential conic algorithm used to approximate constraint (2.13) with a chosen convergence tolerance of 10^{-6}.
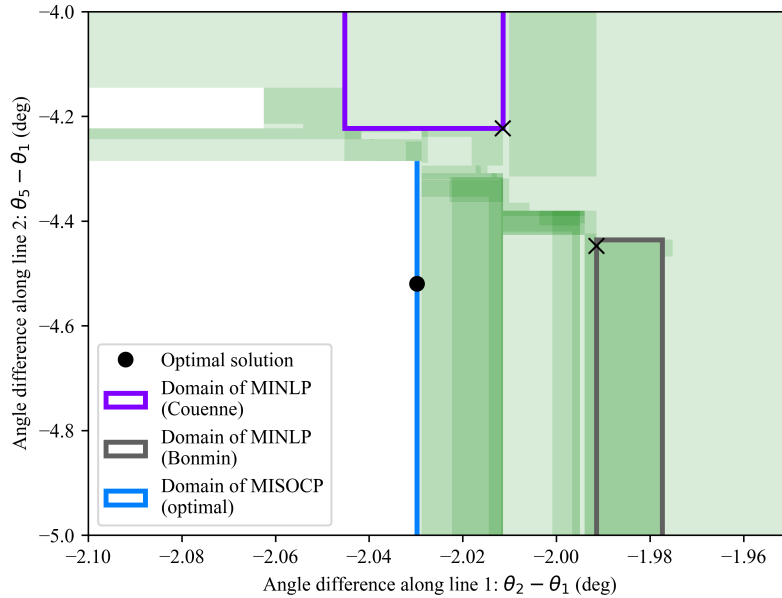
Figure 3.5: Nonconvex security domain of the DT as a function of the angle differences along lines 1 and 2. The green shaded areas represent the stable regions defined by all DT branches. The darker the color, the more domains of different DT branches overlap. Note that the actual security domains covered by the different leaf nodes do not overlap and might even be disjoint, which however cannot be depicted by only two dimensions. Figure from [**Paper A**].

Comparison of preventive and data-driven SC-OPFs

Table 3.1 lists the results of all three SC-OPF implementations. It can be observed that all implementations based on decision trees result in operating points, which exhibit minimum damping ratios that are non-negative, and are thus stable for the base case and all considered N-1 contingencies. The solution of the standard PSC-OPF however is unstable for a fault at bus 5 and line 1-2, respectively. Thus, the identified preventive control actions do not fullfill the system's security requirements and would call for redispatching measures. As the PSC-OPF results in an operating point which does not reflect the small-signal stability requirements, its total cost is lower than the other solutions. All three data-driven implementations result in different leaf nodes of the DT and thus in different regions of the feasible space with various degrees of conservatism.

Higher damping ratios are also reflected by higher costs. All solutions include a stability margin, but only the most conservative result achieves a minimum damping ratio of more than 3%. This can be explained by the fact that (i) the OPF is not limited to the specified discretization intervals of 1.5 MW, as used for the database generation and (ii) DTs are not 100% accurate leading to missclassifications. For cases, where the minimum damping ratio is a hard constraint, higher values can be required when deriving the DT in order to avoid violations. Fig. 3.5 illustrates the stable domain covered by all DT leaf nodes as a function of the angle differences along lines 1 and 2. The rectangles indicate the domains covered by the three different leaf nodes obtained from the data-driven SC-OPF implementations with the location of the corresponding solution pointed out. It can be seen that the stable domain is nonconvex and that safer operating points exhibiting higher damping ratios are located further away from the stability boundary.

The known scalability issues of COUENNE [86], which is a global optimization solver, lead to significantly higher execution times compared to BONMIN, which employs heurisitic methods for nonconvex MINLPs. Also, the default settings for both solvers include a relative tolerance gap of 10% terminating the computation as soon as a solution is found, which lies within 10% of the true objective value. This explains the choice of different leaf nodes. However, even reducing the tolerance value does not change the outcome indicating that neither of the solvers is able to provide the best integer solution. The MISOCP is able to find the optimal integer solution, which has been verified by an exhaustive search. Specifically, we solved 74 AC-OPFs consecutively, one for each DT branch, with the corresponding DT bounds imposed on the angle differences. Thereafter, we determine the DT branch which contains the least-cost, optimal NLP solution. Leaf node 104 actually contains the bounds, which result in the least-cost NLP solution. Notably, in this test case, the MISOCP approximation is exact, i.e. its solution is feasible to the nonlinear and nonconvex AC-OPF and corresponds to the optimal integer outcome. Nonetheless, given that the MISOCP formulation is still an approximation, identified solutions can be infeasible for the original problem. Therefore, we propose to use the MISOCP primarily to identify the optimal DT branch and hence the linear bounds on the feasible space, such that the optimal solution is included. Once these are known and the feasible space has been reduced, the integer variables can be omitted and a common AC-OPF (i.e., NLP) with the previously identified bounds on angle differences imposed as linear constraints can be performed to identify feasible and secure preventive control actions.

Table 3.1 also outlines the savings in online computation time of the proposed SC-OPF method. The data-driven approach outperforms the usual PSC-OPF by more than 40%, while at the same time incorporating more security requirements. Naturally, the computation time depends on the size of the DT and the number of binary variables used to represent it. Even though introducing binaries increases the OPF complexity, this side effect is offset by a significantly reduced overall size of the SC-OPF. While the PSC-OPF increases 32-fold when considering 31 contingencies, the proposed data-driven approach increases only by a fraction for the same amount of contingencies. As indicated by constraint (3.14), $(|\mathcal{L}|+1)$ additional constraints are added, i.e., $|\mathcal{L}|$ linear inequality constraints, where $|\mathcal{L}|$ denotes the number of network lines, and one equality constraint (3.13), which ensures that the binary variables add up to 1. Hence, the complexity of the resulting MISOCP is primarily determined by the $|\mathcal{L}|$ SOC constraints $c_l^2 + s_l^2 \leq u_i u_j$ and the $|\mathcal{P}|$ binary variables.

Furthermore, given that the problem is a convex MIP, which can be solved efficiently by already existing solvers that are able to handle up to a few thousand binaries, the amount of discrete variables is not expected to be an obstacle. Indeed, solvers for MISOCPs have not yet reached the
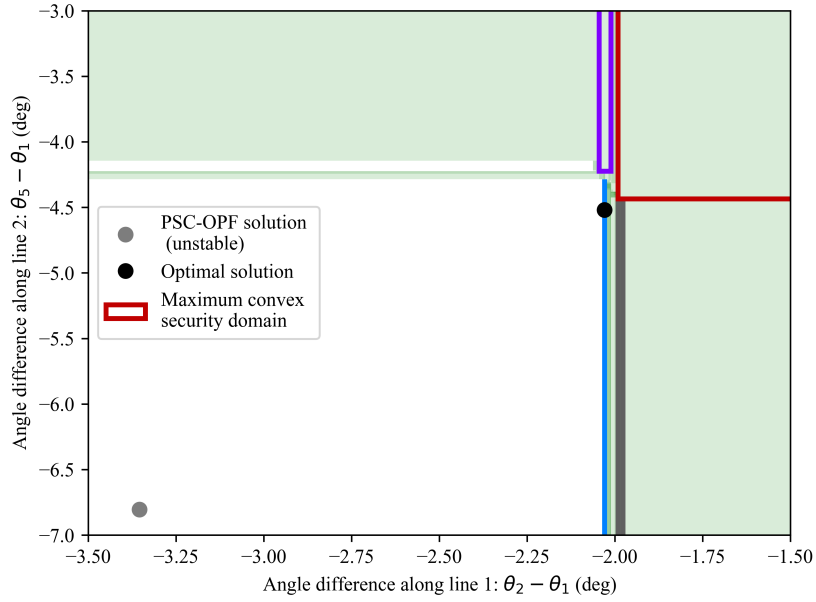
Figure 3.6: Visualization of redispatch and maximum convex security domain, which can be covered by one leaf node only. Figure from [**Paper A**].

maturity of MILP solvers. However, recent work has demonstrated how general convex MIPs can be solved to global optimality by a sequence of MILPs using polyhedral outer approximations and continuous convex programs [89]. Large-scale instances of a similar type of problem class with up to 3000 binary variables and quadratic constraints have successfully been solved in [90] using state-of-the-art solvers and employing heuristic methods. The size of the DT is directly determined by the size of the dataset, which it is derived from. Hence, a more efficient method to generate the database of operating points, appropriate pruning of the DT and techniques to decompose the data-driven optimization are aspects that require a deeper analysis and are promising approaches to enhance the scalability performance of the method.

Optimizing Redispatch

The method can be used by TSOs to identify optimal redispatching actions, where for example the market-based day-ahead dispatch, if identified as insecure, is redirected through the DT to a secure domain. We have reformulated the MISOCP in order to optimize redispatching actions, assuming that the costs of generator up- and down-regulation correspond to its marginal cost. Generators are assumed to be paid for up-regulation and charged for savings resulting from down-regulation. We have used the unstable solution of the standard PSC-OPF listed in Table 3.1 as an input to the redispatch and successfully shifted the operating point to leaf node 104. The cost of redispatch amounts to 343.12€, which corresponds to the original difference in objective values between the PSC-OPF and MISOCP. The MISOCP, if implemented at the market stage, could result in more than 10% cost savings for the system operator and better reflects the locational impact of stability requirements.

Enlarging the Feasible Space

The generated database contains 1.34 million operating points, out of which 6.57% fulfill the 3% minimum damping ratio and define the feasible space of operation. We have evaluated how much of the entire stable region is covered by each individual leaf node, i.e. how many operating points fulfill the constraints imposed by the corresponding DT branch. All leaf nodes cover in total 99.91% of the considered stability region, where leaf node 7 accounts for most of it, capturing 77.78% of the entire feasible space. The implied bounds of leaf node 7 are depicted in Fig. 3.6. If we had considered the stability requirements in the OPF only by imposing bounds which define a convex space, as it is currently done in practice, we would have been able to capture at most 77.78% of the feasible space, thereby also missing the optimal solution as can be seen in Fig. 3.6. Thus, our approach to incorporate the information provided by the database in the optimization problem through binary variables allows us to enlarge the feasible space by more than 28%, enclosing the remaining 22.13%, which are covered by the DT.

3.6 Data-driven security-constrained DC-OPF

3.6.1 Formulation

Applications of the OPF in the electricity industry are mainly limited to the DC approximation, such as the transmission-constrained economic dispatch in electricity markets or linear SC-OPF algorithms used by system operators. This is mainly due to the lower levels of robustness and the scalability issues of nonlinear solvers as compared to linear solvers. In this section, we therefore demonstrate how the data-driven SC-OPF can also be applied in a DC power flow environment and what additional aspects need to be considered.

As discussed in Section 3.3.2, we derive decision rules for the DC-OPF based on various features/predictor variables. Two of the selected features are derived directly from the results of the AC power flow analyses used for generating the database (i.e., (3.8) and (3.9)). The third feature is based on the results of a DC power flow, which essentially projects all AC operating points in the database to the DC domain. The DTs for all of them ultimately define conditional transfer limits, which are summarized in the matrices $\mathbf{F}^{\min}$ and $\mathbf{F}^{\max}$. Both are of size $(|\mathcal{L}| \times |\mathcal{P}|)$, where $|\mathcal{L}|$ is the number of network lines, and thus predictor variables, and $|\mathcal{P}|$ the number of decision tree paths leading to secure outcomes. The number of secure DT paths corresponds also to the number of binary variables. In the data-driven security-constrained DC-OPF, the DT constraints (3.12) are formulated as

$$\mathbf{F}^{\min}\mathbf{b} \leq \mathbf{PTDF}\Big(\mathbf{P}_\mathrm{G} - \mathbf{P}_\mathrm{L}\Big) \leq \mathbf{F}^{\max}\mathbf{b}. \tag{3.16}$$

$\mathbf{PTDF}$ denotes the matrix of power transfer distribution factors, which are derived from the line susceptances and relate nodal power injections to active power flows. Their derivation can be found in [91].

Note that from an algorithmic perspective, the data-driven SC-OPF is well aligned with current software for electricity market-clearing. MIP is already widely applied in electricity markets for e.g., the clearing of block orders in the European day-ahead market [71], or the modeling of unit commitment decisions in various day-ahead and real-time markets across the US.

3.6.2 Incorporation of active power losses

In contrast to the operating points saved in the database, losses are not inherently considered in the DC-OPF or the data-driven security-constrained DC-OPF described above. The authors in [34] note that incorporating losses in a DC power flow is essential for it to provide a good estimate of the actual AC power flows and to reduce the approximation error to a *reasonable* level. However, the losses are dependent on the operating point, which is not known a priori and only available after the optimization. This is a circular problem, in which the losses are needed for the optimization, and the optimization outcome is in return needed for determining the losses.

We therefore seek an initial *best guess* (BG) of the optimal operating point in the database (assuming generator costs are known a priori), which complies with the security requirements and meets the considered load level. The losses of the *best guess* solution are then added as additional loads to the DC-OPF and SC-OPF according to (3.10).

3.6.3 Case study

We evaluate the performance of the data-driven SC-OPF in a DC power flow environment based on the 14 bus test system from Section 3.5.3. The case study consists of two parts. First, we compare the results of the data-driven security-constrained DC-OPF, when using different features for deriving the conditional transfer limits and thus, different strategies for mapping the power flows from an AC to a DC environment. Then, we investigate the impact of various discretization intervals for generating the database on the results of the data-driven SC-OPF, the DT accuracy and database size. Finally, we discuss some benefits of the proposed data-driven approaches.

Comparison of DC-OPF and data-driven SC-OPF using different mapping strategies

For the comparison of the data-driven SC-OPFs based on different mapping strategies, we use a database with a 2.5 MW discretization interval. Note that we derive three different DTs for the three mapping strategies (3.8), (3.9) and (3.11). Table 3.2 lists the results of both the standard DC-OPF and all data-driven SC-OPFs. Additionally, it lists the best guess operating point, which we use for the loss augmentation of the linearized OPFs. Table 3.2 shows that the standard DC-OPF fails to ensure N-1 security, as for this generation dispatch the most critical pair of eigenvalues for a fault at bus 5 has a negative damping ratio and is therefore, unstable. Fig. 3.7 depicts the most critical eigenvalues and the contingencies they belong to, which violate the minimum required stability margin of 3%. It shows that all data-driven SC-OPFs ensure N-1 security of the system through a generation redispatch, which shifts the most critical eigenvalues into the safe area in the left-half plane, where the real parts of the eigenvalues become negative and the minimum damping ratio is larger than the required 3%.

Fig. 3.7 also shows the impact of the feature selection and thus, of the different mapping strategies. All of them ensure a result compliant with the 3% damping ratio but they differ in their levels of conservatism. The most conservative transfer limits are derived with (3.8) depicted in red, where only voltage angle differences resulting from the AC power flow analysis are selected as features. Considering additionally voltage magnitudes and the sine of the voltage angle differences in the computation of the transfer limits reduces the minimum damping ratio and thus, the conservatism (in pruple). The best mapping is achieved with transfer limits based on features from results of the DC power flow, which more accurately capture the projection of the AC operating points in

Table 3.2: Results of the standard DC-OPF and the data-driven security-constrained DC-OPF using different mapping strategies. Table adapted from [**Paper B**].

Feature	BG	DC-OPF	Data-driven SC-OPF					
	-	-	(3.8)		(3.9)		(3.11)	
P_G (MW)			1st run	2nd run	1st run	2nd run	1st run	2nd run
g_1	183.73	275.55	165.96	165.26	176.54	176.30	184.11	184.13
g_2	55.00	0	60.00	60.00	60.00	60.00	60.00	60.00
g_3	27.50	0	26.60	26.67	22.51	22.62	24.63	24.91
g_4	2.50	0	16.17	15.69	9.69	9.58	0	0
g_5	0	0	0	0	0	0	0	0
Cost* (€)	2981	2756	3092	3077	3023	3020	2961	2965
ζ^{min} (%)	4.07	-20.33	9.73	9.59	6.59	6.57	2.98	3.05
CoS* (€)	226	-	336	322	267	264	205	209

* Cost is rounded to the closest integer.
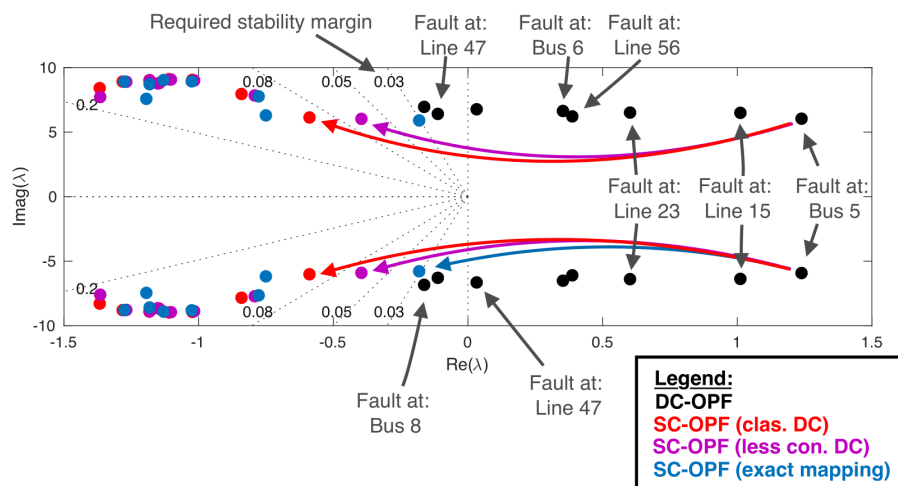
Figure 3.7: Visualization of the most critical eigenvalues from the N-1 security analysis for the standard DC-OPF (black) and the data-driven SC-OPF using: (i) the classic DC approximation (3.8) in red, (ii) the less conservative DC approximation (3.9) in purple, and (iii) the "exact" mapping approach from (3.11) in blue. Figure from [**Paper B**].

the database to a DC environment. More conservative line flow limits also yield a higher cost of security (CoS), as indicated in Table 3.2.

Finally, Table 3.2 also outlines the importance of having a good loss estimate. We perform two runs of each data-driven SC-OPF. The 1st run includes the losses of the data based best guess operating point, while the 2nd run uses the result of the 1st run for the loss estimate. Specifically, the 1st result is used to initialize an AC power flow, from which the losses are determined for the 2nd run. In this case, the loss distribution and therefore the line flows are more accurate and better aligned with the power flows obtained during the data generation. Thus, the matching of operating points is improved leading to better results in all cases.

Table 3.3: Database analysis for different discretization intervals α. Table adapted from [**Paper B**].

α		**1 MW**	**2.5 MW**	**5 MW**
$|\mathbf{\Psi}|$		2.5 million	75'625	6'084
Simulation time		8.17 h	15.11 min	1.29 min
Training set				
Tree accuracy	(%)	99.86	99.77	98.90
# FP		55	1	0
$\frac{FP}{FP+FN}$	(%)	1.54	0.57	0
ζ^{min} of FP	(%)	2.89	2.76	-
Using database of other α as test set				
Tree accuracy	(%)	99.79	99.03	97.64
# FP		36	9'111	13'298
$\frac{FP}{FP+FN}$	(%)	23.08	37.34	22.44
ζ^{min} of FP	(%)	2.73	1.37	0.82

Comparison of different discretization intervals

Table 3.3 compares the databases and DTs created with different discretization intervals α. We use a uniform discretization interval over the entire possible operating range, such that the size of the database $|\mathbf{\Psi}|$ for $\alpha = \{1\,\mathrm{MW}, 2.5\,\mathrm{MW}, 5\,\mathrm{MW}\}$ ranges from 2.5 million operating points to approximately 6'000. The time for generating the database reduces from 8.17 hours for a 1 MW discretization interval to 1.29 minutes for 5 MW. The database was generated using 20 cores in parallel on the high performance computing farm at DTU.

The tree accuracy is also related to the available database size. In general, it should be easier to differentiate between secure and insecure instances (or in our case between operating points that meet the 3% minimum damping ratio and those that do not), if the discretization interval is higher. This is reflected in Table 3.3 by a decreasing number of *false positives* (FPs) with increasing values for α. FPs are those predictions, which wrongly classify insecure operating points as secure, whereas *false negatives* (FNs) wrongly predict secure instances as insecure. As discussed in Section 3.3.2, DTs allow to impose a cost on misclassifications in order to adjust the risk level in either the direction of FPs or FNs. We increase the penalty for FPs, which however comes at the expense of less cost-efficient transfer limits, such that the majority of false predictions corresponds to FNs. From a system operations perspective FNs are tolerable, whereas FPs constitute a greater threat to system security. The higher penalty on FPs is reflected in the low share of FPs in the total number of false predictions FP + FN.

While the number of FPs decreases with an increasing discretization interval when testing the DT on its own training set, the trend reverses when using data sets other than the training set for verification. This is reflected by an increasing number of FPs, when the DTs are tested with the other two database using different discretization intervals. Here, the DTs of 2.5 MW and 5 MW are tested on the 1 MW database, while the 1 MW DT is tested on the 2.5 MW database. A larger value of α leads to more and unsafer false positives, as indicated by the increasing number of FPs and the decreasing minimum damping ratio of those false predictions.

Smaller database sizes result in less data being available for training the DT, which may decrease its accuracy as indicated in Table 3.3. This also leads to potentially shorter trees reflected by a smaller

Table 3.4: Results of the data-driven SC-OPF for different discretization intervals α. Table adapted from [**Paper B**].

Data-driven SC-OPF			
α	1 MW	2.5 MW	5 MW
$|\mathcal{P}|$	616	35	28
Time (s)	26.64	1.08	0.98
Cost (€)	2965.4	2964.9	2959.2
ζ^{min} (%)	3.03	3.05	3.42
P_G (MW)			
g_1	187.00	193.50	183.32
g_2	60.00	42.72	58.04
g_3	18.70	24.73	27.46
g_4	3.70	0	0
g_5	0	0	0

number of binary variables $|\mathcal{P}|$ and a faster execution time of the OPF as shown in Table 3.4. Here, we perform again two runs using the 1st run for initializing the 2nd run as described previously. All tested SC-OPFs for $\alpha = \{1\,\text{MW}, 2.5\,\text{MW}, 5\,\text{MW}\}$ lead to points that meet the required minimum damping ratio. Note that the tree accuracy should not be confused with the cost efficiency of the transfer limits. Table 3.4 shows that the SC-OPF using the largest discretization interval yields the cheapest operating point. This is due to the wider uncertain area in between the analyzed operating points (see Fig. 3.2a) resulting in more relaxed transfer limits. However, the difference is very small. It is important to emphasize that although the largest discretization interval achieves the best performance in this particular case study, smaller step sizes are safer as discussed before and indicated in Table 3.3 with the number of FPs and their associated minimum damping ratios.

Additional benefits of the data-driven approach

Besides the possibility of delivering cost-efficient transfer limits, the data-driven approach provides the additional benefit of serving as an easily accessible source of knowledge for TSOs, which can be useful in operations but in particular for training new employees. First, similar to the visualization in Fig. 3.7, the database provides an overview of which faults are most critical for any operating point. Second, the use of DTs instead of other knowledge extraction methods allows to identify the line flows decisive for system security. By just visualizing the tree as e.g. in Fig. 3.3, the user is able to access this valuable comprehensive information, which would not be possible with most other knowledge extraction methods that generally work like a black-box from the outside.

3.7 Summary

In this chapter, we introduced a data-driven approach for approximating the secure operating region of power systems in the OPF, which accounts for both static and dynamic security. We proposed a framework that unifies machine learning and traditional mathematical optimization by coupling decision trees (DTs) with mixed integer programming (MIP). Our method leverages the benefits of data analytics, MIP and convex AC-OPF approximations to efficiently capture the true nonconvex and possibly disjoint area of operation in the optimization problem. This significantly increases the security region represented in the OPF – by 28% in our case study – and can reveal

more cost-efficient solutions compared to current approaches, which usually consider one convex subspace.

Specifically, we focus on the N-1 criterion with static security and small-signal stability as part of the dynamic security. The data-driven approach is, however, agnostic to the security criteria and could also be extended to include other security considerations (e.g., voltage stability). We derive DTs from data that operators often already have available and which we generate in offline simulations. The DTs define conditional decision rules that capture all security considerations and partition the nonconvex area of operation. Thus, they can be efficiently integrated in an optimization problem through binary variables and disjunctive constraints. We avoid the need to explicitly incorporate all contingencies and stability requirements in the OPF, which significantly reduces the overall problem size compared to conventional SC-OPF algorithms.

The decision rules can be based on any desired feature depending on the target optimization environment. We demonstrate how the data-driven SC-OPF can be applied to different power flow modeling frameworks in line with both market and system operations. The combination of convex AC-OPF approximations and MIP makes the SC-OPF scalable, computationally very efficient, and therefore well suited for the time frames required by market-clearing processes and close to real-time operations.

The database generation used in this work is a major challenge and the only obstacle to scalability. Promising approaches have recently been proposed in [77], which focus on the security boundary rather than on the entire possible operating range. They require less than 10% of the computation time compared to other methods. Additionally, the database generation could be extended by time-domain simulations to account for transient and large-disturbance voltage stability. This would not only ensure a pre- and post-contingency equilibrium, as is currently the case, but also a safe transition in-between, completely characterizing the secure operating region of power system operations.

In this chapter, we have focused on preventive security, which does not rely on additional control actions after a contingency and is still the prevailing security paradigm in power system operations. This framework was justifiable in the past, when operating conditions were fairly well predictable and the pressure for economic efficiency was limited given that state-owned, vertically-integrated utilities were in charge of the generation dispatch and competition was virtually nonexistent. Today, system operation is more volatile than ever and increasingly difficult to predict due to the growing share of renewable electricity generation and market liberalization. As a result, corrective control has substantially increased over the past years and become indispensable for maintaining system security under stressed conditions [4]. Thus, there is a growing need to optimally coordinate remedial actions calling for SC-OPF algorithms that account for corrective control. Including corrective control in the proposed data-driven SC-OPF is a natural extension and an important direction for future work.

Approximating the confidence region: A chance-constrained SOC-OPF

*After the approximation of the secure operating region for the optimal power flow (OPF) problem in Chapter 3, this chapter focuses on the confidence region, the second major constituent part of power systems' target operating region. Specifically, it deals with the impact of linear approximations for the unknown nonconvex confidence region of chance-constrained AC-OPFs, which is the focus of [**Paper C**]. Such approximations are required for the formulation of tractable chance constraints. In this context, we introduce the first formulation of a chance-constrained second-order cone (SOC) OPF, a convex problem providing increased levels of robustness compared to previous approximations, which maintain the nonlinearity of the power flow equations. Combined with an AC feasibility recovery, it is able to better approximate the confidence region. Thereby, it identifies more cost-efficient solutions than chance-constrained nonconvex AC-OPF formulations.*

4.1 Introduction

Power system operations increasingly rely on the AC-OPF to identify optimal decisions [11]. Higher shares of intermittent renewable generation add an additional layer of complexity and call for modeling approaches that account for uncertainty. The literature considers uncertainty either in the form of stochastic formulations, optimizing over several possible realizations (i.e. scenario-based), or in the form of robust formulations, accounting for a continuous uncertainty range (see Chapter 2). This chapter focuses on chance-constrained optimization.

Chance constraints define the maximum allowable violation probability ϵ of inequality constraints and reduce the nonconvex feasible space of the AC-OPF to a desired confidence region, which is also nonconvex as depicted in green in Fig. 4.1. This confidence region includes only operating points which under any realization of the uncertainty $\boldsymbol{\xi}$ are guaranteed to remain within the feasible space of the original AC-OPF (in black in Fig. 4.1) with a probability of at least $(1 - \epsilon)$. The notion of preventively securing the system against uncertainty by restricting the feasible space is also in line with the concept of transmission reliability margins used for the cross-border capacity management in the ENTSO-E region [92]. Additionally, chance constraints offer the benefit of being relatively easily adaptable to a wide range of uncertainty behavior and safety requirements. Their application ranges from robust formulations – such as targeting joint chance constraints [63, 93], not relying on the assumption of any distribution [57, 94] or accounting for a family of possible distributions (i.e., distributionally robust) [57, 95–97] – to less conservative frameworks, considering single system constraints with different levels of robustness [21, 59]. The
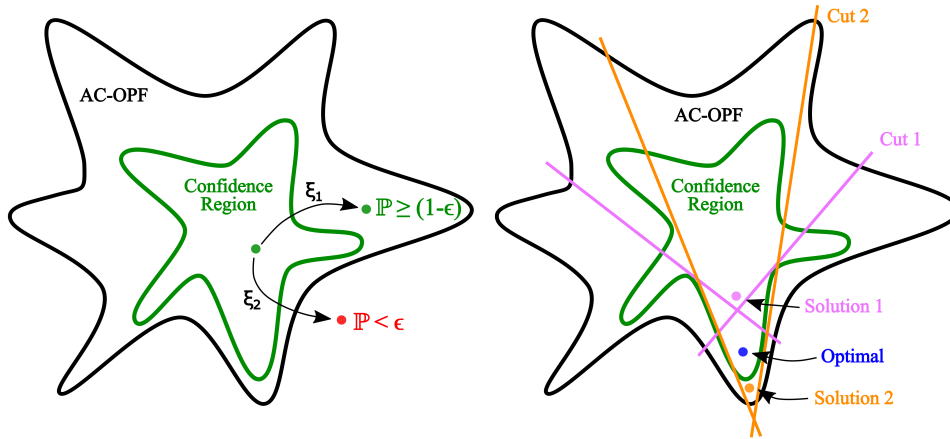
Figure 4.1: Left: Illustration of the feasible space of the AC-OPF and the chance-constrained AC-OPF (confidence region). Right: Illustration of the approximation of the confidence region using linear cuts.

latter accounts for the fact that there are usually only few active constraints [58], which could compromise system security and need to be treated more cautiously.

As the AC-OPF is a nonlinear and nonconvex problem, it is impossible to formulate tractable chance constraints able to cover the whole continuous uncertainty space. Instead, the literature has proposed tractable approximations. Recent research has focused on developing formulations of the chance-constrained AC-OPF based on either partial or full linearizations, and analytical reformulations of single chance constraints [59, 94, 98–101]. Other works propose a combination of convex relaxations for the power flow equations based on semidefinite programming (SDP) and a scenario-based reformulation of the joint chance constraint [63, 93].

The main challenge of the chance-constrained AC-OPF lies in approximating the unknown nonconvex confidence region. Common to all approaches in [21, 57–59, 63, 93–96, 98–101] is that they approximate the impact of the uncertainty by a linearization, allowing to reformulate the chance constraints to tractable deterministic constraints. These are tighter than the original AC-OPF constraints and represent linear cuts to the original feasible space in order to approximate the confidence region. As visualized in Fig. 4.1, depending on the quality of the cuts, the identified operating points may either lie outside the confidence region (solution 2) [59] or are too conservative (solution 1), as in the case of sample-based reformulations [63, 93] and the distributionally robust case in [95]. A less conservative distributionally robust OPF has recently been proposed in [97], considering ambiguity sets of distributions based on historical forecast error data and the Wasserstein metric. Data-driven DRO frameworks are a promising intermediate approach between stochastic optimization, which rely on the assumption of a certain distribution, and robust optimization for the worst-case uncertainty realization. They leverage the knowledge from observed historical data and other statistical information to provide robustness for the uncertainty distribution. However, several challenges remain such as the choice of an appropriate radius for the ambiguity set and maintaining computational efficiency under the necessary sample based reformulations.

The authors in [59, 98, 99] develop an iterative framework for approximating the chance-constrained AC-OPF. The algorithm alternates between an AC-OPF and a computation of the constraint

tightenings (i.e., the linear cuts) based on a first-order Taylor series expansion around the forecasted operating point. This partial linearization of the uncertainty impact is more accurate than the full linearization in [94]. However, due to the nonconvex nature of the AC-OPF, the algorithm is not guaranteed to converge. Convergence and robustness are still challenges even for the standard AC-OPF, which often fails to succeed, particularly for large networks [17, 18]. The authors in [101] use a first-order Taylor expansion to linearize the AC power flow equations around the forecasted operating point and to model the uncertainty impact. The resulting approximation of the chance-constrained AC-OPF achieves a high computational efficiency due to its convexity and an improvement in system costs by optimizing over affine response policies. Despite its increased robustness, the method still relies on the availability of an AC-OPF solution at the forecasted operating point to allow for the linearization of the power flow equations. Otherwise, the method's solution quality is determined by the quality of the input AC-OPF solution, which can be highly suboptimal [18]. The SDP relaxation of the chance-constrained AC-OPF developed in [63] improves on the approximation of the confidence region by optimizing over affine control policies. In [93], we additionally aim at providing AC feasible solutions and global optimality guarantees. However, as SDP solvers are still under development it can be computationally challenging.

As in Chapter 3, we focus on the second-order cone (SOC) relaxation of the power flow equations as a good trade-off between approaches for two reasons. First, compared with the original AC-OPF formulation, SOC relaxations define a convex problem which is guaranteed to converge. Second, they are computationally more efficient than SDP relaxations. However, the SOC relaxation is very loose for meshed networks and requires either strengthening procedures [40, 44, 48, 49] or additional approximations [42] to improve its accuracy. In this work, we use approximations as an intermediate approach between the AC-OPF and its SOC relaxation. It must be noted that any relaxation or approximation can result in physically meaningless solutions, requiring procedures to recover an AC feasible point.

SOC-OPF algorithms considering uncertainty have been proposed in [102–104], where the authors develop convex formulations of the robust two-stage AC-OPF problem focusing on the worst-case uncertainty realization. Specifically, in [103] and [104] SOC relaxations are used within the framework of an affinely adjustable robust OPF (first proposed in [105] for a DC-OPF). However, both papers consider only affine policies for active power generation neglecting the impact of the uncertainty on all other control and state variables. A very extensive framework for relaxations of robust AC-OPFs is provided in [102], where the authors develop three methods using conic duality to obtain tractable formulations of the robust AC-OPF based on SOC-, SDP-, and DC-OPFs. To guarantee AC feasible solutions, the conic OPF models are used to approximate the second stage of the two-stage robust optimization problem and are then solved alternately with an AC-OPF that represents the first stage problem. However, as in [59] this results in a nonconvex iterative program, which is not guaranteed to converge. None of the papers mentioned address the issue of AC infeasibility of the SOC-OPF solutions.

The main contributions of this work are:

- the first formulation of a chance-constrained SOC-OPF (CC-SOC-OPF), able to provide both convergence guarantees and high computational efficiency; coupled with an AC feasibility recovery it can identify better solutions than the chance-constrained nonconvex AC-OPF formulation;

- the approximation of quadratic apparent power flow chance constraints with linear chance constraints using results proposed in [22];

- the introduction of new parameters able to reshape the approximation of the confidence region, along with a rigorous analysis of the linear approximations; these parameters offer a high degree of flexibility for the robustness of the solution.

4.2 Chance-constrained optimal power flow

The chance-constrained OPF (2.22) – (2.24) as introduced in Chapter 2 restricts the feasible space of the basic OPF to a desired confidence region (CR). It aims at identifying optimal decisions in the CR, such that for any realization of the uncertainty and appropriate remedial actions all constraints are satisfied with a desired probability. Remedial or corrective control actions can be either pre-determined or embedded as optimization variables in the chance-constrained OPF. In this chapter, we focus on *preventive security* against the uncertainty impact, which is aligned with current industry practices and the security framework from Chapter 3. The only control assumed to be acting in real-time in response to deviations from the day-ahead schedule are adjustments of the active power output of generators participating in the automatic generation control (AGC).

As pointed out in Chapter 2, the general formulation of the chance-constrained OPF (2.22) – (2.24) is intractable. The equality constraints cannot be enforced for all possible uncertainty realization in the continuous uncertainty space and the distribution of $h_i(\tilde{\mathbf{x}}(\boldsymbol{\xi}))$ in the chance constraint $\mathbb{P}(h_i(\tilde{\mathbf{x}}(\boldsymbol{\xi})) \leq 0) \geq 1 - \epsilon$ is not known, thus, preventing a tractable reformulation. In the following, we will outline our assumptions to achieve a tractable convex approximation of the chance-constrained AC-OPF.

4.2.1 Uncertainty modeling

Similar to the literature, we assume wind power generation $\tilde{\mathbf{P}}_W$ to be the only source of uncertainty. The actual wind realization $\tilde{P}_{W_i}$ is modeled as the sum of forecasted value P_{W_i} and deviation (i.e., forecast error) ξ_i,

$$\tilde{P}_{W_i} = P_{W_i} + \xi_i, \qquad \forall i \in \mathcal{W}. \tag{4.1}$$

$\mathcal{W} \subseteq \mathcal{N}$ denotes the set of nodes containing wind generators, while subscript W refers to the contribution of wind power to the nodal power injection at node i. $\boldsymbol{\xi} := \{\xi_i \mid \text{for } i = 1, \ldots, |\mathcal{W}|\}$ defines the uncertainty space. Recently, grid codes also require renewable energy generators to be able to provide reactive power [106]. We include the reactive power generation of wind farms as optimization variables and assume that the reactive power output follows the deviation of the active power output according to the optimal power factor $\cos \phi$ at the forecasted operating point. Thus, the actual realization of the reactive wind power output is modeled as follows

$$\tilde{Q}_{W_i} = \lambda(P_{W_i} + \xi_i), \qquad \forall i \in \mathcal{W}, \tag{4.2}$$

where $\lambda = \sqrt{\frac{1-\cos^2 \phi}{\cos^2 \phi}}$ is an optimization variable and denotes the ratio between reactive and active wind power generation.

We model all decision variables $\tilde{\mathbf{z}}(\boldsymbol{\xi})$ of the OPF as functions of the uncertainty $\boldsymbol{\xi}$,

$$\tilde{\mathbf{z}}(\boldsymbol{\xi}) = \mathbf{z} + \boldsymbol{\Delta}\mathbf{z}(\boldsymbol{\xi}), \tag{4.3}$$

where $\mathbf{z}$ represents the optimal setpoint at the forecasted operating point and $\boldsymbol{\Delta}\mathbf{z}(\boldsymbol{\xi})$ the system response to a change in active power injection (i.e., wind power deviation $\boldsymbol{\xi}$).

4.2.2 Chance-constrained AC-OPF

We formulate the chance-constrained AC-OPF in the space of $\mathbf{z} := \{\mathbf{P}, \mathbf{Q}, \mathbf{u}, \boldsymbol{\theta}, \mathbf{c}, \mathbf{s}\}$ variables as

$$\min_{\mathbf{z}} \mathbf{c}_G^T \mathbf{P}_G \tag{4.4}$$

$$\text{s.t. } P_i = \mathbf{G}_{ii}u_i + \sum_{l=(i,j)} \left(\mathbf{G}_{ij}c_l - \mathbf{B}_{ij}s_l \right) + \sum_{l=(j,i)} \left(\mathbf{G}_{ij}c_l + \mathbf{B}_{ij}s_l \right), \qquad \forall i \in \mathcal{N}, \tag{4.5}$$

$$Q_i = -\mathbf{B}_{ii}u_i - \sum_{l=(i,j)} \left(\mathbf{B}_{ij}c_l + \mathbf{G}_{ij}s_l \right) - \sum_{l=(j,i)} \left(\mathbf{G}_{ij}c_l - \mathbf{B}_{ij}s_l \right), \quad \forall i \in \mathcal{N}, \tag{4.6}$$

$$0 = c_l^2 + s_l^2 - u_i u_j, \qquad \qquad \forall l \in \mathcal{L}, \tag{4.7}$$

$$0 = \theta_j - \theta_i - \text{atan}\left(\frac{s_l}{c_l}\right), \qquad \qquad \forall l \in \mathcal{L}, \tag{4.8}$$

$$\theta_{ref} = 0, \tag{4.9}$$

$$\mathbb{P}\left(\tilde{z}_i(\boldsymbol{\xi}) \leq z_i^{\max} \right) \geq 1 - \epsilon, \qquad \qquad \forall \tilde{z}_i(\boldsymbol{\xi}) \in \tilde{\mathbf{z}}(\boldsymbol{\xi}), \tag{4.10}$$

$$\mathbb{P}\left(\tilde{z}_i(\boldsymbol{\xi}) \geq z_i^{\min} \right) \geq 1 - \epsilon, \qquad \qquad \forall \tilde{z}_i(\boldsymbol{\xi}) \in \tilde{\mathbf{z}}(\boldsymbol{\xi}), \tag{4.11}$$

$$\mathbb{P}\left(\tilde{S}_{ij}^2(\boldsymbol{\xi}) \leq (S_l^{\max})^2 \right) \geq 1 - \epsilon, \qquad \qquad \forall l \in \mathcal{L}, \tag{4.12}$$

$$\mathbb{P}\left(\tilde{S}_{ji}^2(\boldsymbol{\xi}) \leq (S_l^{\max})^2 \right) \geq 1 - \epsilon, \qquad \qquad \forall l \in \mathcal{L}. \tag{4.13}$$

In order to ensure tractability of the equality constraints (2.23), we enforce (4.5) – (4.9) for the forecasted operating, where the forecast error is zero $\boldsymbol{\xi} = \mathbf{0}$. The objective function (4.4) minimizes the total generation cost for the forecasted operating point. $\epsilon \in (0,1)$ represents the allowed constraint violation probability. Thus, the CR (i.e., the restricted feasible space) of the chance-constrained OPF is defined by the confidence level $(1 - \epsilon)$. The chance constraints (4.10) – (4.11) refer to the inequality constraints of the OPF. They maintain each lower and upper limit of the decision variables, $z_i^{\min}$ and $z_i^{\max}$, with probability $(1 - \epsilon)$ over the uncertainty range. (4.12) and (4.13) constrain the apparent power flow in both directions of the line, where S_{ij}^2 (and analogously S_{ji}^2) is defined as

$$\begin{aligned} S_{ij}^2 &= P_{ij}^2 + Q_{ij}^2 \\ &= \left(-\mathbf{G}_{ij}u_i + \mathbf{G}_{ij}c_l - \mathbf{B}_{ij}s_l \right)^2 + \left((\mathbf{B}_{ij} - \mathbf{B}_{ij}^{sh})u_i - \mathbf{B}_{ij}c_l - \mathbf{G}_{ij}s_l \right)^2, \forall l \in \mathcal{L}. \end{aligned} \tag{4.14}$$

Note that in this formulation, we assume a π-model of the transmission lines with reactive shunt elements $\mathbf{B}_{ij}^{sh}$ only.

Constraints (4.10) – (4.13) represent separate chance constraints, i.e., the probability of satisfying the inequality constraints – see (2.14) in Chapter 2.2.1 – is enforced for each constraint individually and not jointly. We use separate chance constraints as they (i) do not significantly change the computational complexity of the problem as opposed to joint formulations and (ii) have proven to also effectively reduce the joint violation probability while remaining less conservative than approaches which explicitly target joint chance constraints and usually overly satisfy them [16, 93]. Separate chance constraints are also used to approximate joint chance constraints [56]. They offer the flexibility to identify and target individual constraints which are decisive for the system's security while avoiding to unnecessarily limit the solution space along other dimensions that are of minor significance to security but could have a substantial impact on costs.

4.2.3   Chance-constrained SOC optimal power flow

Problem (4.4) – (4.13) represents the chance-constrained formulation of the exact (i.e., nonconvex) AC-OPF based on the variables $\mathbf{z} := \{\mathbf{P}, \mathbf{Q}, \mathbf{u}, \boldsymbol{\theta}, \mathbf{c}, \mathbf{s}\}$ and can be relaxed as described in Chapter 2.2.1 to obtain the convex CC-SOC-OPF. The quadratic equality (4.7) is replaced by $c_l^2 + s_l^2 \leq u_i u_j$, while (4.8) can be approximated through various approaches that maintain the convexity. Analogous to Chapter 3, we use a sequential conic procedure based on a first-order Taylor series expansion [42]. Its convergence is determined by the change in $\mathbf{c}$ and $\mathbf{s}$ variables, e.g., $||\mathbf{c}^\nu - \mathbf{c}^{\nu-1}||_\infty$, where ν denotes the iteration counter. Given that we reintroduce the angle constraint (4.8) through a Taylor series, the OPF no longer represents a pure relaxation but an approximation of the original problem. We refer to the OPF based on relaxations and approximations as *second-order cone OPF* (SOC-OPF). Note that the apparent power flow limits in (4.12) – (4.13) are already convex quadratic constraints. As the SOC-OPF is an approximation of the AC-OPF, identified solutions might not be feasible to the original problem. We address this issue in Section 4.2.7, where we propose an ex post AC feasibility recovery based on an AC power flow analysis. In Section 4.3, we demonstrate in our case study how the proposed procedure is not only able to recover the AC-OPF solution of a nonlinear solver but can also identify more cost-efficient solutions.

4.2.4   Control policies: Modeling the system response

In order to model the system response to a change in wind power injection $\boldsymbol{\xi}$, we use linear policies for all variables concerned.

Reserve deployment

Fluctuations in active power generation are balanced by conventional generators. They are assumed to provide up- and down-reserves according to their generator participation factors $\boldsymbol{\gamma}$. The participation factors are pre-determined and proportional to each generator's share in the total installed capacity of conventional generation. The generator output is adjusted according to the total power mismatch $\Xi = \sum_{i \in \mathcal{W}} \xi_i$ [21]. Hence, the sum of all generator contributions to the reserve deployment needs to balance the total power mismatch Ξ, which implies the following condition: $\sum_{i \in \mathcal{G}} \gamma_i = 1$. Thus, the total contribution of all generators equals the total power mismatch $\sum_{i \in \mathcal{G}} \gamma_i \sum_{i \in \mathcal{W}} \xi_i = \Xi$. Similar to (4.1), the actual dispatch of a conventional unit is modeled as the sum of its optimal dispatch at the expected wind infeed and its reaction to the wind power deviation,

$$\tilde{P}_{\mathrm{G}_i}(\boldsymbol{\xi}) = P_{\mathrm{G}_i} + \Delta P_{\mathrm{G}_i}(\boldsymbol{\xi})$$
$$= P_{\mathrm{G}_i} - \gamma_i \Xi + \Delta P_{\mathrm{U}_i}(\boldsymbol{\xi}), \quad \forall i \in \mathcal{G}. \tag{4.15}$$

$\Delta P_{\mathrm{U}_i}(\boldsymbol{\xi})$ represents the unknown nonlinear changes in active power losses, usually compensated by the generator at the reference bus. Thus, this term is equal to zero for all other generators. As for the other variables $\mathbf{Q}, \mathbf{u}, \mathbf{c}, \mathbf{s}, \theta$, which vary nonlinearly with the wind power injection, we approximate ΔP_{U_i} through a linearization around the forecasted operating point, which is described in the next section. Note that the participation factors can also be included as optimization variables and defined for each wind infeed individually. However, a higher number of optimization variables and additional second-order cone constraints in that case also increase the computational burden.

Linear decision rules

We derive linear sensitivities of each variable with respect to the uncertainty based on a Taylor series expansion around the forecasted operating point. We model the response as follows: $\Delta\mathbf{z}(\boldsymbol{\xi}) = \frac{\partial\mathbf{z}}{\partial\boldsymbol{\xi}}\boldsymbol{\xi} = \boldsymbol{\Upsilon}\boldsymbol{\xi}$, such that $\tilde{\mathbf{z}}(\boldsymbol{\xi}) = \mathbf{z} + \Delta\mathbf{z}(\boldsymbol{\xi})$ represents a linear decision rule (LDR) with respect to the uncertainty. The authors in [59, 98, 107] have derived the linear sensitivity factors from the Jacobian matrix at the forecasted operating point of the original AC power flow equations. The detailed derivation can be found in [16]. In this work, we derive the linear sensitivity factors $\boldsymbol{\Upsilon}$ based on the Jacobian matrix of the alternative load flow equations (4.5) – (4.8), such that we can directly use them as input to the convex chance-contrained SOC-OPF,

$$
\begin{bmatrix} \Delta\mathbf{P} \\ \Delta\mathbf{Q} \\ \mathbf{0} \\ \mathbf{0} \end{bmatrix} = \left[\mathbf{J}^{\mathrm{SOC}}\right]\Big|_{\mathbf{z}} \begin{bmatrix} \Delta\mathbf{u} \\ \Delta\mathbf{c} \\ \Delta\mathbf{s} \\ \Delta\boldsymbol{\theta} \end{bmatrix}.
\tag{4.16}
$$

The derivation of $\boldsymbol{\Upsilon}$ is presented in Appendix A. The left-hand side of equation (4.16) can also be expressed in terms of the uncertain wind infeed, the generator participation factors, the optimal ratio between reactive and active wind power generation and the unknown nonlinear changes in active and reactive power. We replace the entries for $\Delta\mathbf{P}$ and $\Delta\mathbf{Q}$ accordingly and modify the system of equations considering the following assumptions, aligned with current practices in power system operations:

- the change in active power losses is compensated by the generator at the reference bus: $\Delta\mathbf{P}_{\mathrm{U_{PV}}} = \mathbf{0}$ and $\Delta\mathbf{P}_{\mathrm{U_{PQ}}} = \mathbf{0}$;

- changes in reactive power generation are compensated by generators at PV and reference buses, as PQ buses are assumed to keep their active and reactive power injection constant: $\Delta\mathbf{Q}_{\mathrm{PQ}} = \mathbf{0}$;

- generators at PV and reference buses regulate their reactive power output to keep the voltage magnitude and thus the square of the voltage magnitude constant: $\Delta\mathbf{u}_{\mathrm{PV}} = \mathbf{0}$ and $\Delta u_{\mathrm{ref}} = 0$;

- the voltage angle at the reference bus is always zero: $\Delta\theta_{\mathrm{ref}} = 0$.

Rearranging the resulting system of equations allows us to define the changes in all variables of interest (i.e., $\Delta\mathbf{z} \setminus \{\Delta\mathbf{P}_{\mathrm{U_{PV}}}, \Delta\mathbf{P}_{\mathrm{U_{PQ}}}, \Delta\mathbf{Q}_{\mathrm{PQ}}, \Delta\mathbf{u}_{\mathrm{PV}}, \Delta u_{\mathrm{ref}}, \Delta\theta_{\mathrm{ref}}\}$) as a function of $\boldsymbol{\xi}$. The changes in active and reactive power flows due to fluctuations in wind infeed can be represented by a linear combination of the changes in u, c and s variables, as shown in Eq. (4.17) for active branch flows.

$$
\Delta P_{ij}(\boldsymbol{\xi}) = -\mathbf{G}_{ij}\Delta u_i + \mathbf{G}_{ij}\Delta c_l - \mathbf{B}_{ij}\Delta s_l, \quad \forall l \in \mathcal{L}.
\tag{4.17}
$$

The chance-constrained apparent power flow limits are thus formulated as quadratic chance constraints for all lines $l := (i,j)$ (and analogously for the reversed power flow direction (j,i)),

$$
\mathbb{P}\left[\left(P_{ij} + \Delta P_{ij}(\boldsymbol{\xi})\right)^2 + \left(Q_{ij} + \Delta Q_{ij}(\boldsymbol{\xi})\right)^2 \le \left(S_l^{\mathrm{max}}\right)^2\right] \ge 1 - \epsilon.
\tag{4.18}
$$

4.2.5   Reformulating the linear chance constraints

The LDR approach coupled with the assumption that the wind deviations $\boldsymbol{\xi}$ follow a multivariate distribution with known mean and covariance allows us to analytically reformulate the single chance constraints in (4.10) – (4.13) to deterministic constraints [21]. We choose the analytical approach based on a Gaussian distribution with zero mean given that previous work in [59] has shown that (i) it is reasonably accurate, even when the uncertainty is not normally distributed, and (ii) it performs better than sample-based reformulations based on Monte Carlo simulations and the so-called scenario approach [53]. Using the properties of the Gaussian distribution, the linear chance constraint $\mathbb{P}[z_i + \boldsymbol{\Upsilon_i}\boldsymbol{\xi} \leq z_i^{\max}] \geq 1 - \epsilon$ is reformulated to

$$z_i + \Phi^{-1}(1-\epsilon)\sqrt{\boldsymbol{\Upsilon}_i\boldsymbol{\Sigma}\boldsymbol{\Upsilon}_i^{\mathrm{T}}} \leq z_i^{\max}, \tag{4.19}$$

where Φ^{-1} denotes the inverse cumulative distribution function of the Gaussian distribution and $\boldsymbol{\Sigma}$ the $(|\mathcal{W}|\times|\mathcal{W}|)$ covariance matrix. Note that $\boldsymbol{\Upsilon}_i$ denotes the i-th row of matrix $\boldsymbol{\Upsilon}$ and is a $(1\times|\mathcal{W}|)$ vector containing the sensitivity of the considered variable w.r.t. $\boldsymbol{\xi}$ at each node in $\mathcal{W}$. The derivation of how the chance constraint is reformulated to its deterministic form can be found in e.g., [16]. It can be observed that introducing uncertainty results in a tightening of the original constraint $z_i \leq z_i^{\max}$ and thus, a reduction of the feasible space to the CR defined by the confidence level $(1 - \epsilon)$. The introduced margin $\Omega_i = \Phi^{-1}(1 - \epsilon)\sqrt{\boldsymbol{\Upsilon}_i\boldsymbol{\Sigma}\boldsymbol{\Upsilon}_i^{\mathrm{T}}}$ secures the system against uncertain infeeds and was termed *uncertainty margin* in [21].

4.2.6   Reformulating the quadratic chance constraints

The apparent power flow constraint inside (4.18) is indeed convex but nonlinear, which prevents a straightforward analytical reformulation of the chance constraint similar to the linear one in (4.19). We therefore approximate the quadratic chance constraint by a set of probabilistic absolute value constraints and a nonprobabilistic quadratic constraint as proposed in [22] and recently applied in [101]. Constraint (4.18) is replaced by the following set of constraints,

$$\mathbb{P}\Big[|P_{ij} + \Delta P_{ij}(\boldsymbol{\xi})| \leq k_{ij}^{\mathrm{P}}\Big] \geq 1 - \beta\epsilon, \tag{4.20}$$

$$\mathbb{P}\Big[|Q_{ij} + \Delta Q_{ij}(\boldsymbol{\xi})| \leq k_{ij}^{\mathrm{Q}}\Big] \geq 1 - (1 - \beta)\epsilon, \tag{4.21}$$

$$(k_{ij}^{P})^2 + (k_{ij}^{Q})^2 \leq (S_l^{\max})^2. \tag{4.22}$$

k_{ij}^{P} and k_{ij}^{Q} are optimization variables introduced to enable the reformulation. The absolute value constraints (4.20) and (4.21), also called two-sided linear chance constraints, are a special type of joint chance constraints. They can be approximated by two single linear chance constraints, e.g. $\mathbb{P}[P_{ij} + \Delta P_{ij}(\boldsymbol{\xi}) \leq k_{ij}^{\mathrm{P}}] \geq 1 - \beta\epsilon$ and $\mathbb{P}[P_{ij} + \Delta P_{ij}(\boldsymbol{\xi}) \geq -k_{ij}^{\mathrm{P}}] \geq 1 - \beta\epsilon$. In this form, the constraints can be reformulated analytically as desribed in Section 4.2.5. $\beta \in (0, 1)$ is a parameter, which balances the trade-off between violations in the two constraints (4.20) and (4.21) and ensures that the union of the constraints still satisfies the desired confidence level, i.e., $\mathbb{P}[(4.20) \cup (4.21)] \geq 1 - \epsilon$. Note that without β, i.e., when enforcing (4.20) and (4.21) with $(1 - \epsilon)$, respectively, the union $\mathbb{P}[(4.20) \cup (4.21)]$ only holds with $(1 - 2\epsilon)$ [22].

The major benefit of using an approach combining LDRs and analytical reformulations lies in its adaptability to a wide range of uncertainty behavior. The authors in [57, 99] thoroughly discuss how different assumptions on the statistical behavior of the uncertainty can be incorporated into

the analytical reformulation. To this end, (4.19) can be generalized by replacing $\Phi^{-1}(1-\epsilon)$ with a more general function $f_{\mathcal{P}}^{-1}(1-\epsilon)$, whose value can be determined for any distribution if the mean μ and variance Σ of the uncertainty are known. The exact expressions of $f_{\mathcal{P}}^{-1}(1-\epsilon)$ for different distributions are derived in [57]. Different values for $f_{\mathcal{P}}^{-1}(1-\epsilon)$ and thus different assumptions on the distribution are simply reflected in the optimization through different values for the uncertainty margins $\Omega_i = f_{\mathcal{P}}^{-1}(1-\epsilon)\sqrt{\mathbf{\Upsilon}_i \mathbf{\Sigma} \mathbf{\Upsilon}_i^{\mathsf{T}}}$.

4.2.7 Modeling inaccuracies

The linearization of the uncertainty impact and the approximation of both the quadratic chance constraints and the angle constraint are sources of inaccuracies. As a result, the CC-SOC-OPF solution might still lie outside the feasible space of the AC-OPF and the CR (i.e., the chance-constrained AC-OPF) despite the constraint tightenings as depicted in Fig. 4.2. This highlights the need for appropriate back-mapping procedures to project the CC-SOC-OPF solution back into the AC feasible space. One option could include ex ante "approximation tightenings" similar to the reduced MW line ratings used for improving the accuracy of a DC-OPF [34]. They could improve the approximation but can still not guarantee AC feasibility of the solution. Therefore, we propose to use the solution of the (CC-)SOC-OPF as a warm start to an ex post AC power flow analysis. To ensure that the CC-SOC-OPF solution is not only projected back into the AC feasible space but into the CR, increased levels of conservatism are required in the CC-SOC-OPF modeling. β provides an additional degree of freedom to improve the approximation along the dimension of the corresponding quadratic chance constraint. Note that the CC-SOC-OPF solution might still not be AC feasible due to loose bounds along other dimensions, but can be made so through the feasibility recovery. How to appropriately choose β has to our knowledge not been addressed in previous work. Performing a rigorous investigation in our case studies, we find that for $\mathbb{P}[(4.20) \cup (4.21)] \geq 1-\epsilon$ to hold while keeping the additional cost incurred by the uncertainty as low as possible, β needs to be tuned for each quadratic chance constraint individually. Alternatively, choosing a value for β of 0.5, as done in [101], provides a convex inner approximation of the quadratic chance constraint and thus, a robust approximation of the constraint [22]. This is aligned with the classical Bonferroni approximation, which uses the union bound to approximate the violation probability ϵ of K jointly considered chance constraints by K single chance constraints, each of which is enforced by $(1 - \frac{\epsilon}{K})$ [56].

4.2.8 Critical line screening

In order to reduce both the effort associated with the parameter tuning and the number of new variables and constraints required to reformulate (4.18), we propose to perform a pre-screening based on the forecasted operating point to identify the most critical lines. Specifically, we evaluate the vertices $\boldsymbol{\kappa}$ of the polyhedral outer approximation of the ellipsoidal uncertainty set given by the multivariate Gaussian distribution [93]. One of the vertices includes the worst-case realization of the ellipsoidal uncertainty set. We then use a linearization based on power transfer distribution factors (PTDF) to approximate the change in active power line flows at each vertex, i.e., $\mathbf{\Delta PF}^{\kappa_i} = \mathbf{PTDF} \times \mathbf{\Delta P}^{\kappa_i}$. The change in active power injection $\mathbf{\Delta P}^{\kappa_i}$ is defined w.r.t. the forecasted operating point. The final active power flows at each vertex show which lines could be overloaded, and thus have a high risk of exceeding the allowable violation probability. These lines are classified as *critical* and their capacity constraints are included as chance constraints. The branch flows on all other lines are constrained by their usual limits and do not consider an uncertainty margin. This procedure takes place iteratively after every solution of a CC-SOC-OPF until no new critical lines are identified.
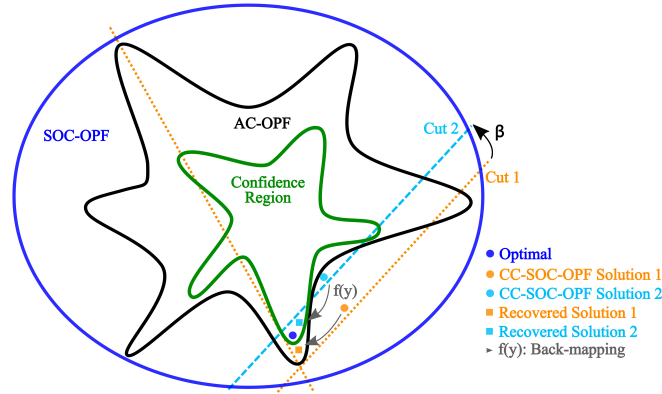
Figure 4.2: Illustration of how modeling inaccuracies might affect the CC-SOC-OPF and visualization of the AC feasibility recovery (back-mapping).

4.2.9 Solution algorithm

The sensitivity factors $\boldsymbol{\Upsilon}$ depend nonlinearly on the operating point and would render the problem nonconvex if they were introduced as optimization variables. Therefore, we define $\boldsymbol{\Upsilon}$ and the uncertainty margins $\boldsymbol{\Omega}$ outside the optimization problem and adopt the iterative solution algorithm from [98]. We apply it in the context of a SOC-OPF, which allows us to maintain the convexity of the CC-SOC-OPF. We improve on the work in [98] and [59] by avoiding nonconvexities in the optimization, and thus provide convergence guarantees for the iterative solution algorithm. The algorithm converges as soon as the change in $\boldsymbol{\Omega}$ between two consecutive iterations is lower than a pre-defined tolerance value ρ and is defined in Algorithm 1. This allows us to fully exploit the

---

Algorithm 1 Iterative chance-constrained SOC-OPF

1: Set iteration count: $\nu \leftarrow 0$
2: **while** $||\boldsymbol{\Omega}^\nu - \boldsymbol{\Omega}^{\nu-1}||_\infty > \rho$ **do**
3:    **if** $\nu = 0$ **then**
4:       solve the SOC-OPF for the forecasted wind infeed without considering uncertainty and obtain the operating point $\mathbf{z}^0$
5:       evaluate $\boldsymbol{\Upsilon}^0$ and $\boldsymbol{\Omega}^0$ at $\mathbf{z}^0$
6:    **end if**
7:    perform critical line screening based on $\mathbf{z}^\nu$ and $\boldsymbol{\kappa}$ and append the *critical* line list
8:    include $\boldsymbol{\Omega}^\nu$ according to (4.19) for all variables $\mathbf{z}(\boldsymbol{\xi})$ and (4.20)-(4.22) for all *critical* lines
9:    solve CC-SOC-OPF to obtain $\mathbf{z}^{\nu+1}$
10:   evaluate $\boldsymbol{\Upsilon}^{\nu+1}$ and $\boldsymbol{\Omega}^{\nu+1}$ at $\mathbf{z}^{\nu+1}$
11:   $\nu \leftarrow \nu + 1$
12: **end while**.

---

efficiency of solvers for convex programming. Note that the iterative solution algorithm for the chance constraints adds an additional outer iteration loop to the iterative conic procedure for approximating the angle constraint (4.8).

4.2.10 Robustness and extensions of the algorithm

In this Section, we discuss several aspects and possible extensions of the algorithm which are not only limited to the examples mentioned here. Other possible extensions include the consideration of security requirements (e.g., N-1 and stability criteria) and distributionally robust formulations.

The need for robustness

The efficiency of the iterative algorithm to handle large dimensions of the uncertainty has been demonstrated in [59], where the full AC power flow equations and the Polish test case of 2383 buses with 941 uncertain loads are used. The example also proves the good performance of the iterative approach even for nonconvex problems, if it converges. This is emphasized by the work in [99], where the authors analyze the impact of perturbations of the initial operating point on the final solution. Despite having large differences in cost and uncertainty margins in the first iteration, the results quickly converge to solutions sharing the same cost and uncertainty margins. Nevertheless, several instances were also identified in [99], where the iterative algorithm failed to converge as a result of the nonconvexities. Some cases encountered infeasibility of the OPF at intermediate iterations and failed to recover subsequently. Others exhibited a cycling behavior (e.g., the five bus case from [108]). There the algorithm oscillated between two different local optima, which had large differences in their corresponding uncertainty margins and were located in two disjoint regions of the feasible space.

The recent work in [17] compares the performance of several convex solvers with three nonlinear solvers. The nonprobabilistic AC-OPF relaxation based on SDP and the standard AC-OPF are solved for 133 different test cases of up to 25 000 buses, respectively. Contrary to the SDP solvers, even the most efficient nonlinear AC-OPF solver failed to converge to a solution for 20 out of the 133 systems tested, including all test cases over 10 000 buses. All the examples mentioned highlight the need for more robust solution approaches and the ability of convex programming to provide them. The results from [17] are proof that robustness is not only an issue for more sophisticated AC-OPF algorithms, which include functionalities beyond the usual ones from the standard AC-OPF. Robustness is already a challenge for the standard AC-OPF, whose convergence and success is fundamental to the functioning of any other algorithm that builds on top of it.

Uncertainty dimension

Besides maintaining convexity, another benefit of combining the iterative approach, where Υ is computed outside the OPF, and the analytical reformulation is the independence from the size of the uncertainty set $|\mathcal{W}|$. $|\mathcal{W}|$ solely has an impact on the dimensions of Υ, Σ and ξ. Operations on these matrices are only conducted at steps 5 and 10 of each iteration and are decoupled from the optimization in steps 4 and 9. The computational complexity of the approach is mainly determined by the size of the optimization problem, which remains unchanged with an increasing number of uncertainty sources. It only changes if more *critical lines* are detected during the critical line screening, whose reformulated chance constraints need to be added to the constraint set. However, this is not expected to be an obstacle, as the number of active constraints is usually low, even in large systems [58].

Large uncertainty ranges

The linearization of the uncertainty impact performs better close to the forecasted operating point and might lead to inaccuracies, when considering large ranges of the uncertainty. Given that we operate in a nonlinear space, some type of affine approximation is necessary to keep the chance constraints tractable. However, we do not expect that this poses a significant limitation for this method. Our approach is expected to be used for power system operations, which usually require

short-term forecasts (e.g. usually days/hours instead of months or years). The forecast uncertainty range associated with such time intervals is expected to be reasonable for our method.

Integer variables

The resulting optimization problem solved at each iteration is formulated in almost the same way as the deterministic SOC-OPF with the only difference of having tighter variable limits to represent the uncertainty impact. Therefore, the problem can also be extended to include integer variables accounting for e.g., shunt elements or tap changers. Once the optimal integer decisions at one iteration have been determined, the uncertainty margins can still be derived as described above by a linearization around the optimal integer solution. However, different integer solutions throughout the iteration process could also result in constantly changing values for Ω leading to convergence issues. Similar to what has been proposed in [99], one possible solution approach could be a branching algorithm. Specifically, the initial uncertainty margins of each integer solution are used to obtain a new integer solution (i.e., a new branch). At the same time, the CC-SOC-OPF algorithm described above is applied to each integer solution with the discrete variables fixed to their optimal values in order to obtain the final uncertainty margins of the corresponding branch. The associated operating point is added to the list of candidate solutions. The branching algorithm would be considered to converge as soon as it does not identify any new integer solutions, which have not been explored yet. The most cost-efficient candidate solution would constitute the final solution.

4.3 Case study

We evaluate the performance of the proposed CC-SOC-OPF on the IEEE 118 bus test system [109]. We assume the MW line ratings given in [109] as MVA line ratings and reduce them by 30% to obtain a more constrained system. We add wind farms to node 5 and 64 with expected production levels of 300 MW and 600 MW, respectively. We assume a standard deviation of 10% and a power factor between 0.95 capacitive and 0.95 inductive for each wind farm. Minimum and maximum voltage limits are set to 0.94 p.u. and 1.06 p.u.. Generator cost functions are assumed to be linear.

We first demonstrate how an SOC-OPF coupled with an AC feasibility recovery is able to approach the solution of a nonlinear solver for the exact AC-OPF problem. Afterwards, we show how the convex CC-SOC-OPF coupled with the AC feasibility recovery is able to identify even better solutions in terms of operation cost than the CC-AC-OPF from [59]. We evaluate the constraint violation probabilities in all cases empirically using Monte Carlo simulations of AC power flow calculations based on $10\,000$ scenarios drawn from a multivariate Gaussian distribution. All simulations related to SOC-OPFs were carried out in Python using the Gurobi Optimizer. The nonconvex CC-AC-OPF was implemented in Matlab, where the OPF at each iteration was solved using Matpower and its internal MIPS solver [88]. All AC power flow analyses, i.e., the AC feasibility recovery and the Monte Carlo simulations, were also carried out with Matpower.

4.3.1 Recovering the SOC-OPF solution

We evaluate the SOC-OPF at the forecasted operating point without considering wind power uncertainty and compare the outcome to the standard AC-OPF solution. We assume a convergence tolerance of 10^{-6} for the sequential conic procedure to approximate the angle constraint (4.8). The objective function value of the SOC-OPF is identical to the one obtained with the exact problem

(37 692.03 €), providing a seemingly exact approximation. However, when evaluating the full AC power flow equations at the operating point identified by the SOC-OPF, we observe a mismatch of active and reactive power injections at nodes 37 and 38. Despite being fairly small (i.e., 0.06 MW and 0.98 Mvar), this indicates that the operating point is not AC feasible. The infeasibility is also reflected in the SOC constraint of line 50 connecting nodes 37 and 38, which is the only one that fails to maintain the equality constraint (4.7) at the SOC-OPF solution. Even though we use an AC-OPF approximation, this still highlights the inadequacy of defining the relaxation gap of OPF relaxations solely based on differences in objective function values. The OPF objective function only considers costs on active power generation, and thus, neglects the fact that one $\mathbf{P}$ solution might be associated with numerous $\{\mathbf{Q}, \mathbf{V}, \boldsymbol{\theta}\}$ solutions, not all of which might be feasible.

Therefore, we use the SOC-OPF solution as a warm start to an AC power flow analysis in order to recover a feasible AC power flow solution. However, given that power flow calculations do not consider any variable limits, we need to enforce generator reactive power limits, slack bus active power limits (by e.g. changing the slack bus if necessary), and check for voltage and branch flow limits. The final power flow solution results in a dispatch with slightly lower generation cost (37 691.97 €) as a result of numerical discrepancies.

The results of the Monte Carlo simulations are listed in Table 4.1 showing the maximum violation probabilities for generator active power, bus voltage, and apparent power flow limits. Table 4.1 also shows the joint violation probability, which represents the probability of at least one constraint being violated (i.e., the number of samples with at least one constraint violation out of the 10 000 tested). A joint violation probability of 100% for the standard AC-OPF and SOC-OPF indicates that neither OPF algorithm results in an operating point, which is able to maintain feasibility for any other wind power realization if uncertainty in wind power infeed is not explicitly accounted for. The maximum violation probability of single constraints in that case lies around 50%.

4.3.2 Critical line screening

The critical line screening shows that line 100, which is already congested at the forecasted operating point $\mathbf{z}^0$, violates its power flow limits in both directions of the line. Furthermore, the limits of line 37, which is not congested at $\mathbf{z}^0$, are also estimated to be violated in the positive flow direction (i.e., from node 8 to node 30). Thus, we include three quadratic chance constraints: two for line 100 defining both flow directions and one for line 37 defining only the positive flow direction. The weighting factors are denoted with $\beta_{100}^{\leftrightarrow}$ and $\beta_{37}^{\rightarrow}$ with the arrows indicating the direction of the constrained flow.

4.3.3 Chance-constrained SOC-OPF

We first determine the optimal parameters β for the CC-SOC-OPF and then compare it to the CC-AC-OPF algorithm proposed in [59]. We assume an acceptable violation probability ϵ of 5% for all chance constraints. The convergence tolerance ρ of the uncertainty margins for the iterative CC-SOC-OPF and CC-AC-OPF is set to 10^{-5}. Both algorithms converge after 4 iterations demonstrating the suitability of the iterative solution algorithm for both OPFs. However, the algorithm is more robust in case of the SOC-OPF due to the convexity of the problem solved at each iteration step [110].

Table 4.1: Results of the Monte Carlo simulations: Comparison of maximum violation probabilities between AC-OPF, SOC-OPF*, CC-SOC-OPF* and CC-AC-OPF. The results of the CC-SOC-OPF* include the ones obtained without β and with the final optimal values for β.

AC-OPF	SOC-OPF*	CC-AC-OPF	CC-SOC-OPF*	
			$\beta = \emptyset$	$\beta \neq \emptyset$
Generator active power limits				
48.74%	48.74%	5.00%	4.96%	4.96%
Bus voltage limits				
43.86%	56.89%	3.26%	1.30%	0.25%
Apparent power line flow limits				
50.22%	50.12%	4.07%	7.72%	5.00%
Joint violation probability				
100%	100%	14.85%	17.35%	15.60%

* The Monte Carlo simulations were carried out with the recovered (i.e., AC feasible) SOC solution.

Quadratic chance constraints without weighting factors $\beta = \emptyset$

First, we analyze the solution without considering the weighting factors $\beta_{100}^{\leftrightarrow}$ and $\beta_{37}^{\rightarrow}$, i.e., we enforce the two separate absolute value constraints (4.20) – (4.21) for each quadratic chance constraint with the usual confidence level $(1 - \epsilon)$. The results are listed in Table 4.1. It can be observed that the chance constraints for active power generation and voltage magnitudes are satisfied. However, the maximum violation probability of the apparent power flow limits exceeds the allowable threshold of 5% and indicate that the recovered solution is not located within the CR. Specifically, this violation is caused by the flow in the positive flow direction on line 37 and confirms that the union of the two separate constraints (4.20) and (4.21) only holds with $1 - 2\epsilon$, as described in Section 4.2.6. In case of line 100, the level of conservatism for enforcing the two separate constraints is already sufficient. The violation probabilities are reduced to 4.47% and 4.17% in the positive and negative flow directions, respectively.

Quadratic chance constraints with weighting factors $\beta = \{\beta_{37}^{\rightarrow}, \beta_{100}^{\leftrightarrow}\}$

In order to evaluate the impact of different values of the weighting factors on the CC-SOC-OPF, we perform a sensitivity analysis varying $\beta_{100}^{\leftrightarrow}$ uniformly in both flow directions from 0.1 to 0.9 in 0.1 increments and add 0.01 and 0.99 as the approximate endpoints of the interval $\beta \in (0, 1)$ (i.e., in total 11 samples). As line 37 has proven to be more critical, we use a finer sampling of $\beta_{37}^{\rightarrow}$ between 0.02 and 0.98 in 0.02 increments (i.e., 49 samples). Hence, we perform the sensitivity analysis based on 539 simulations of the CC-SOC-OPF with a subsequent AC feasibility recovery.

The performance of the resulting 539 operating points when subjected to wind infeed variations is evaluated through Monte Carlo simulations based on 2000 samples drawn from a Gaussian distribution. The results are visualized in Fig. 4.3. The top plot shows the maximum violation probability of the apparent power flow constraints, which in all 539 cases is due to the flow on line 37. It can be seen that lower values of $\beta_{37}^{\rightarrow}$ and $\beta_{100}^{\leftrightarrow}$ increase the level of conservatism and reduce the violation probability. $\beta_{37}^{\rightarrow}$ needs to be lower than approximately 0.6 to keep the violation probability within acceptable levels (i.e., $< 5\%$). We can also observe that for $\beta_{37}^{\rightarrow} > 0.4$, variations in $\beta_{100}^{\leftrightarrow}$ do not significantly influence the maximum violation probability. The middle and bottom plots depict the changes in generation cost of the CC-SOC-OPF z^{CC-SOC} and the recovered solution $z^{rCC-SOC}$, respectively. The behavior of the cost development in both cases is similar and leads to
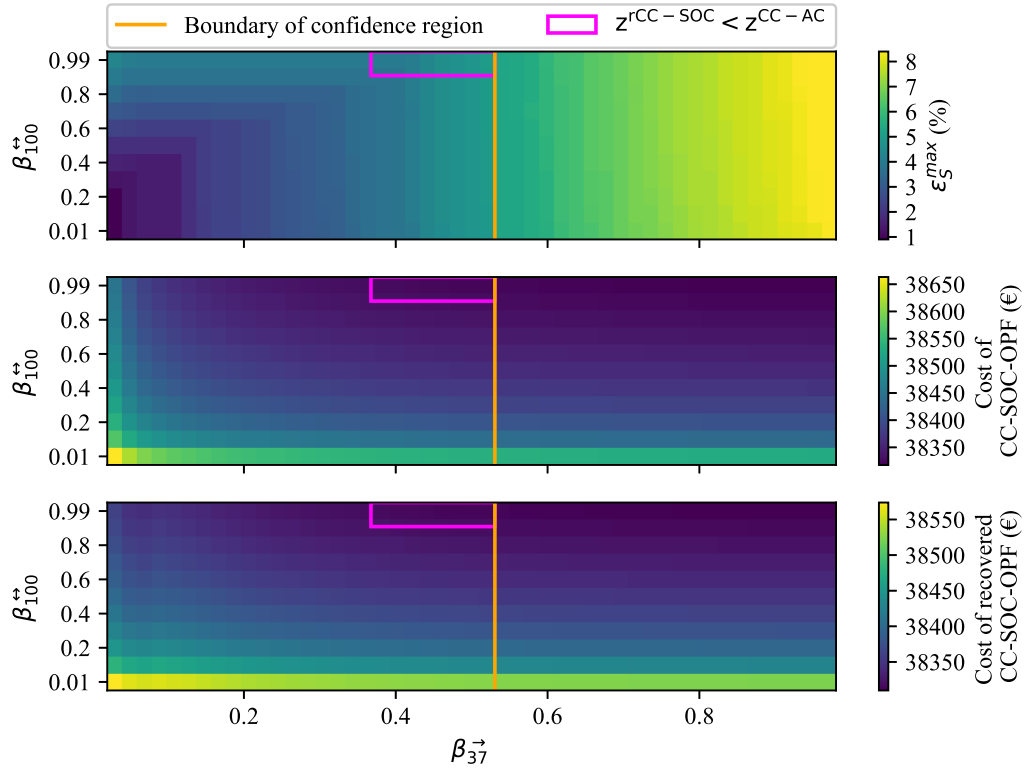
Figure 4.3: Maximum violation probability of apparent power flows ϵ_S^{max}, generation cost of the CC-SOC-OPF ($z^{\text{CC-SOC}}$) and the recovered CC-SOC-OPF solution ($z^{\text{rCC-SOC}}$) as functions of $\beta_{37}^{\rightarrow}$ and $\beta_{100}^{\leftrightarrow}$. The pink box indicates the region of operating points which are located inside the CR and are cheaper than the benchmark CC-AC-OPF solution. All operating points left of the boundary are located within the CR.

an increase in cost with lower weights. Counter-intuitively, the cost of the recovered AC feasible solution $z^{rCC-SOC}$ is lower than the cost of the CC-SOC-OPF z^{CC-SOC}. This is a consequence of the approximation of the chance constraints in order to make them tractable. As shown in the illustration of "cut 2" in Fig. 4.2, the linear cuts lead to some parts of the AC feasible space being cut off and not represented in the CC-SOC-OPF. However, our feasibility recovery procedure, not constrained by those linear cuts, is able to determine solutions inside the confidence region, which can have lower costs.

We use a finer sampling of $\beta_{37}^{\rightarrow}$ between 0.5 and 0.6 and evaluate the resulting operating points with $10\,000$ Monte Carlo simulations to determine its optimal value, which complies with the maximum violation probability but does not lead to unnecessarily high levels of conservatism and cost. We do not assume any weights for the chance constraints associated with line 100, as they are already met when enforced with the usual confidence level. Fig. 4.4 depicts the change in violation probabilities and cost for the finer sampling. A value of 0.555 for $\beta_{37}^{\rightarrow}$ has proven to just meet the maximum allowable 5% violation probability while still leading to lower operation cost at its recovered solution than the CC-AC-OPF. Note that the sensitivity analysis has only been performed for the CC-SOC-OPF, as the reformulation of the quadratic chance constraints are defined for convex quadratic constraints. In the CC-AC-OPF, where the apparent power flow limits are nonconvex, we use linear sensitivities of the apparent power flows to compute uncertainty
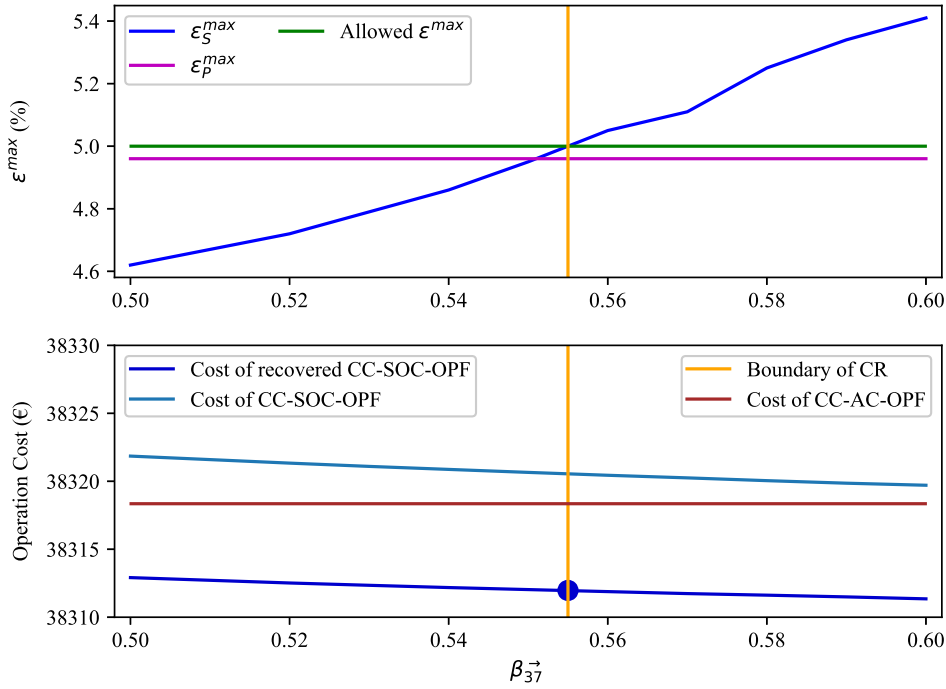
Figure 4.4: Operation cost and maximum violation probability of apparent power flow ϵ_S^{max} and active power generation ϵ_P^{max} limits for different values of $\beta_{37}^{\rightarrow}$ along line 37.

Table 4.2: Comparison of CC-AC-OPF and CC-SOC-OPF*.

	CC-AC-OPF	CC-SOC-OPF*
Cost	38 318.35 €	38 311.12 €
Iterations	4	4
Time	4.42 s	10.60 s

* Refers to the recovered SOC solution.

margins for the constraints, as proposed in [111]. Their derivation can be found in [111].

Comparison with CC-AC-OPF

The CC-SOC-OPF coupled with the AC feasibility recovery results in an operating point with lower cost as shown in Table 4.2 and is thus, less conservative. This is also reflected in less conservative violation probabilities shown in Table 4.1. The weights β on the quadratic chance constraints provide a significant additional degree of freedom in the CC-SOC-OPF. They can be used to, e.g., reduce the joint violation probability of the original OPF and increase its robustness without the need to explicitly account for joint chance constraints and use conservative sample-based scenario approaches to reformulate them. In this case study, joint violation probabilities of less than 10% can be achieved as depicted in Fig. 4.5.

The pink box in Fig. 4.3 highlights the recovered solutions of the CC-SOC-OPF, which are located within the CR and have lower generation cost $z^{rCC-SOC}$ than the CC-AC-OPF z^{CC-AC}. Apart from the operating points depicted in the pink box, 10 other points identified during the finer sampling of $\beta_{37}^{\rightarrow}$ (i.e., $0.5 \leq \beta_{37}^{\rightarrow} \leq 0.6$) also fulfill the original chance constraints and outperform
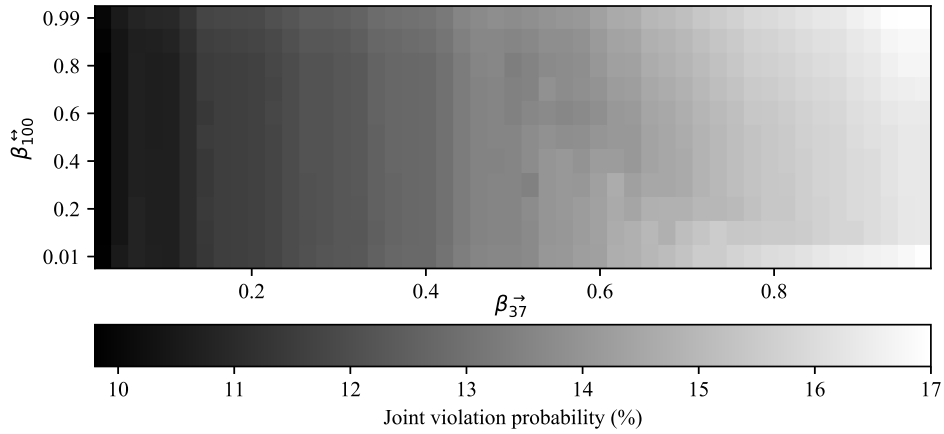
Figure 4.5: Joint violation probability for different values of $\beta_{37}^{\rightarrow}$ and $\beta_{100}^{\leftrightarrow}$.

the CC-AC-OPF in terms of operation cost. Thus, apart from the least-cost solution listed in Table 4.1 and 4.2, we find 18 other operating points, which are AC feasible, fulfill the original chance constraints and are still cheaper than the CC-AC-OPF solution of the nonlinear solver. This highlights (i) the potential of convex approximations to accurately determine the boundaries of the CR, and (ii) the importance of appropriate back-mapping procedures to translate the solution of the convex approximation back to the original domain. Despite the required tuning, β provides the flexibility to vary the shape of the convex approximation and direct the solution back into the original feasible space and the CR.

The need for computationally more efficient convex relaxations and approximations of (chance-constrained) AC-OPFs was identified in [93], where we developed a SDP relaxation of the chance-constrained AC-OPF based on rectangular and Gaussian uncertainty sets. Comparable instances to our case study may take up to 10 minutes to solve with the SDP relaxation (although the computational improvements proposed in [62] can reduce this time). Our proposed algorithm converges within 10.60 s. The solution time of the CC-SOC-OPF is mainly determined by the inner iteration loop for approximating the angle constraint (4.8), which accounts for 84% of the total solution time. More efficient approximations of the angle constraint, which can be implemented in an one-shot optimization, could significantly improve the performance of the proposed method. The CC-AC-OPF converges even faster after only 4.42 s, which again demonstrates its efficiency, when it converges. However, the discussion in Section 4.2.10 highlighted the need for more robust solution techniques not only for the CC-AC-OPF but also for the standard AC-OPF [17]. Another example is the work in [18], where the authors compared the performance of different solution techniques for the nonlinear AC-OPF. They demonstrated how the convergence behavior and solution quality in terms of costs for both small and large networks was highly sensitive to (i) the initialization of the various tested solvers (i.e., warm start) and (ii) the OPF problem formulation (i.e., rectangular, polar etc.). As a consequence, the authors strongly recommended not to rely on one solution technique only, but to employ a *multistart strategy* in real-life networks, where several solution techniques with different solver intializations are run in parallel to increase the robustness of the AC-OPF solution. In view of this, a *multistart strategy* could also be employed in case of the chance-constrained AC-OPF, where various instances of both the CC-SOC-OPF and the CC-AC-OPF are run in parallel to ensure robustness for the convergence and the lowest system

cost.

Still, the combination of the iterative algorithm and convex programming makes the method computationally very efficient, robust, and suitable for large-scale systems as demonstrated in our case study. Most current industrial tools integrate OPF calculations in iterative frameworks along with other functionalities, e.g., security assessments [11]. Consequently, the iterative solution algorithm with the decoupled uncertainty assessment is well aligned with this framework and has significant potential for application in already existing calculation procedures [59]. However, it must be noted that in case of infeasibility, our approach relies on the availability of a robust AC power flow tool to ensure a reliable AC feasibility recovery. AC power flow algorithms are usually based on an iterative numerical technique for solving a set of nonlinear equations and their convergence depends on an appropriate initialization. Nevertheless, we expect the solution of the CC-SOC-OPF to be a good initial guess, while the AC power flow algorithms are at a mature development stage. As a result, convergence issues, if any, are expected to be rare.

4.4   Summary

This chapter dealt with the impact of linear approximations for the unknown nonconvex confidence region of chance-constrained AC-OPF problems. The confidence region constitutes a major part of a power system's target operating region along with the static and dynamic security regions discussed in Chapter 3.

We introduced the first formulation of a chance-constrained second-order cone OPF. In contrast to existing approaches, our method offers the advantage of relying on convex formulations, thus providing convergence guarantees while being computationally more efficient than other convex formulations. Coupled with an AC feasibility recovery, we show that it can determine more cost-efficient solutions than chance-constrained nonconvex AC-OPF formulations and is guaranteed to provide a solution even in cases, where nonlinear solvers already fail for the standard deterministic AC-OPF [17].

To the best of our knowledge, this work is the first one to perform a rigorous analysis of the AC feasibility recovery for robust SOC-OPF formulations. Due to the approximation, a CC-SOC-OPF might determine AC infeasible operating points, while the linear reformulations of the chance constraints result in solutions which either lie outside the confidence region or are too conservative. Inaccurate approximations of the confidence region is an issue for all chance-constrained AC-OPF formulations. In this work, we introduce an approximation of the quadratic apparent power flow chance constraints with linear chance constraints using results proposed in [22]. Through that, we introduce new parameters able to reshape the approximation of the confidence region, offering a high degree of flexibility.

This chapter demonstrated that further work on more accurate and computationally more efficient approximations for the chance-constrained AC-OPF problem is necessary. The major challenge of the CC-SOC-OPF lies in the optimal selection of β for approximating the quadratic chance constraints. While we have proposed an ex ante screening to reduce the effort associated with the parameter tuning, more systematic procedures are necessary to ensure an optimal setting for realistic systems. One potential solution approach could be derived from the recent work in [112]. It defines a framework for optimizing the Bonferroni approximation, where the violation probabilities, which are aligned with β in our setting, are optimization variables and not known a priori.

CHAPTER 5

Approximating the target operating region: A unified OPF framework

*This chapter provides a unified framework for approximating the true target operating region in the optimal power flow problem, irrespective of how the power flow equations are modeled. The target operating region constitutes the intersection of the security and confidence regions, treated in Chapter 3 and Chapter 4, respectively. It provides a desired confidence level for both static and dynamic security against the uncertainty inherent in modern power system operations. We formulate the problem as a security- and chance-constrained OPF, for which we propose two tractable and efficient approximations. The first relies on a purely data-driven approach, which constructs the target operating region offline, whereas the second uses a combination of data-driven techniques and analytical reformulations. This chapter includes results from [**Paper D**] and compares the performances of both methods under different formulations of the power flow equations.*

5.1 Introduction

The optimal power flow (OPF) problem is increasing in importance and encompasses a growing number of decision processes as its application range is extending, from electricity markets, power system day-to-day operations to long-term planning. Generally, a broad consensus exists on the objective of the OPF to identify not only cost-optimal but above all *secure* decisions [11]. However, there still remains a lack of uniformity in the very problem definition on how to achieve this goal, which can trouble both developers and users of OPF tools [113]. This is mainly due to the immense complexity of the numerous operational requirements imposed by power systems, rooted in the highly nonlinear and nonconvex nature of the power flow equations.

The electricity industry mainly relies on simplified OPF formulations for which robust and reliable solution algorithms exist. Proxies in the form of transfer limits are used to deal with the high problem complexity while maintaining practicability. They capture all operational requirements and are imposed on the OPF to confine the solution space to a safe operating region. Nowadays, those proxies are determined by system operators through rather opaque procedures based on their estimation of the eventual market outcome and the future operating conditions. Both are increasingly difficult to predict. Market participants are becoming more flexible, responsive and strategic. Coupled with a growing share of volatile renewable generation, system conditions are changing more rapidly. These circumstances can lead to adverse repercussions. The transfer limits, determining the decision framework, are often inadequate – leading to decisions that are either very conservative or threaten system security and require expensive operator intervention. In both cases, unnecessary costs arise that are borne by the end consumer. Therefore, more transparent

approaches are needed that give access to the entire feasible decision space, respecting operational requirements, and do not rely on an initial estimate which severely limits it.

In order to improve the representation of the actual decision space, many approaches have been proposed to model various operational requirements in the OPF. The majority focuses on the static N-1 security criterion, which aims at maintaining voltage and equipment ratings in case of contingencies. Fewer approaches have been proposed that include dynamic security requirements. Recently, increasing uncertainty in system conditions such as from renewable energy generation has been recognized as a major threat to system security and prompted the development of probabilistic formulations. Hence, the scope of the operational requirements covered by OPF algorithms has become more diverse. Nevertheless, they usually account for a very limited share of the numerous requirements on power system security and adequacy; otherwise, it is very difficult to maintain tractability of the OPF. As a result, there is still a lack of consensus on a fundamental definition of the *true* target operating region (i.e., the feasible space), ensuring both power system security and adequacy.

There have been few attempts to derive a tractable constraint set for the true target operating region [64, 65]. However, they are still based on an initial estimate of the eventual operating conditions, and thus capture only one part of the target operating region. Moreover, the methods from [64, 65] are based on the nonlinear AC power flow equations, which still challenge current solution algorithms. How to ensure their solvability and what to do if no solution can be attained is left unaddressed. As a result, the methods are very application specific and not suited for the different formulations and algorithmic reliability requirements demanded by various OPF applications (e.g., linearized settings in electricity markets).

This work attempts to define a framework to give decision-makers access to the entire permissible decision space and eliminate the dependency on individual estimates. To do this, we use a data-driven approach, which has several benefits:

- it ensures tractability of all operational requirements in the OPF; we focus on those related to security and uncertainty;

- the reformulated security and uncertainty constraints can maintain linearity if needed; therefore, it is compatible with any formulation of the power flow equations and can fully exploit the efficiency and reliability of solvers for linear and convex programming;

- all security and uncertainty assessments can be carried out offline, significantly reducing the burden on the optimization;

- it allows to exploit the growing data volumes of an increasingly digitalized power system.

Specifically, we provide a general definition on the target operating region of power systems, accounting for both security and uncertainty. We propose efficient methods to approximate the region in the OPF, regardless of how the power flow equations are modeled. The target operating region constitutes the intersection between the secure and the confidence region, where static and dynamic security are probabilistically accounted for. We propose to do this through a combined security- and chance-constrained OPF (SC-CC-OPF), providing a desired confidence level for both static and dynamic security over the uncertainty range. It integrates the N-1 criterion and maintains the confidence level for all considered contingencies. In order to formulate the security-

and chance-constrained OPF, we propose two approaches. The first relies purely on data-driven techniques to approximate the target operating region offline and subsequently integrates it directly in the OPF. The second leverages the modular structure of the methods proposed in Chapter 3 and 4. It uses a combination of data-driven techniques for constructing the secure operating region offline and analytical reformulations to approach its intersection with the confidence region in the online OPF. While the first method is more efficient from the optimization perspective and possibly more accurate, the latter can serve as an alternative in case of insufficient data from the uncertainty space to reliably construct the confidence region.

5.2 The target operating region: A security- and chance-constrained OPF

Both proposed methods for the SC-CC-OPF rely on a combination of data-driven techniques, mixed integer programming (MIP) and disjunctive constraints to reformulate static and dynamic security constraints to tractable decision rules suitable for any OPF framework. The decision rules approximate the boundary between secure and insecure instances in the database. Thereby, they capture the secure operating region, which can be defined for any desired security criteria. As the data-driven SC-OPF serves as a starting point for both proposed formulations of the SC-CC-OPF, its derivation is briefly outlined for completeness. For more detailed information, the reader is referred to Chapter 3.

5.2.1 Data-driven SC-OPF

Our approach to formulate the basic data-driven SC-OPF consists of three major steps:

1. an offline database generation, discretizing the power flow solution space, and a subsequent security assessment to define the secure operating region within;

2. a feature selection and knowledge extraction, where we derive tractable decision rules based on selected features from the database using appropriate machine learning tools;

3. the implementation of the decision rules in an OPF to approximate the secure operating region in the optimization.

In this work, we focus on the N-1 criterion considering both static security and small-signal stability as part of the dynamic security. Thus, the security assessment in step 1 consists of a static security assessment and a small-signal stability assessment of all operating points in the database $\mathbf{\Psi}$. They are tested against each scenario in the contingency set $\mathcal{C}$. The static security assessment determines if an operating point i satisfies all equipment and voltage ratings under each scenario j. The small-signal stability assessment evaluates the corresponding damping ratio $\zeta_{i,j}$. We denote the damping ratio of an operating point ζ_i as the damping ratio associated with its lowest damped mode. The overall dynamic security performance of an operating point is defined based on its minimum damping ratio over the entire contingency set $\zeta_i^{\min} := \min\{\zeta_{i,j} \mid \text{for } j = 0, \ldots, c\}$, where 0 denotes the faultless system conditions and c the number of considered contingencies. A positive minimum damping ratio indicates that the operating point is small-signal stable under all conditions in $\mathcal{C}$. The secure operating region is thus given by the operating points that maintain all equipment ratings, voltage ratings and small-signal stability requirements over the contingency set. The small-signal stability requirements can be defined for the stability boundary $\zeta^{\min} > 0$ or a desired stability margin $\zeta^{\min} > \zeta^{\text{margin}}$ as usually done in practice.

Once the database is generated through a sequence of AC power flows and the secure operating region is defined, appropriate features from the database need to be selected, which are able to distinguish between secure and insecure operating points. The features are based on a subset $\hat{\psi}_i$ of the available data attributes (or combinations of them)

$$\psi_i := \{\mathbf{P}_i, \mathbf{Q}_i, \mathbf{V}_i, \boldsymbol{\theta}_i, \kappa_i\}, \quad \forall\, \psi_i \in \boldsymbol{\Psi}, \tag{5.1}$$

where κ_i is a Boolean parameter and equal to 1 if the operating point ψ_i is located in the secure operating region and 0 otherwise. $\mathbf{P}_i$, $\mathbf{Q}_i$, $\mathbf{V}_i$ and $\boldsymbol{\theta}_i$ refer to active and reactive nodal power injections as well as nodal voltage magnitudes and angles. They describe the state of the operating point i in the AC power flow solution space.

In this work, we aim at providing a comprehensive framework for translating security and uncertainty considerations, regardless of how the power flow equations are modeled. Therefore, we use active power flows as features, which are explicitly represented in any OPF formulation

$$\hat{\psi} := \Big\{ \mathbf{F} \mid F_l = f(V_i, V_j, \theta_i, \theta_j), \ \forall l = (i, j) \in \mathcal{L} \Big\}. \tag{5.2}$$

$\mathcal{L}$ denotes the set of network lines. In this chapter, we use the same features $\mathbf{F}$ for all OPF formulations, which are directly derived from the results of the AC power flows used to generate the database.

After the feature selection, we use decision trees (DTs) to derive rules based on active power line flows. They define the conditions for an operating point to be located in the secure or insecure operating region. The DT branches define upper and lower limits $\mathbf{F}^{\mathrm{max}}$ and $\mathbf{F}^{\mathrm{min}}$ on active power line flows, each of them characterizing a different subspace of the operating region. In doing so, the DT partitions the (secure) operating region into subspaces, which we then incorporate in the OPF using MIP and disjunctive constraints

$$\mathbf{F}^{\mathrm{min}}\mathbf{b} \leq \mathbf{P_{ij}} \leq \mathbf{F}^{\mathrm{max}}\mathbf{b}, \tag{5.3}$$

$$\sum_{p \in \mathcal{P}} b_p = 1. \tag{5.4}$$

$\mathbf{b}$ is a vector of binary variables associated with the DT branches $\mathcal{P}$, which lead to secure operating regions. $\mathbf{F}^{\mathrm{min}}$ and $\mathbf{F}^{\mathrm{max}}$ are matrices of size $(|\mathcal{L}| \times |\mathcal{P}|)$, where each column contains the limits on active power line flows defined by the corresponding DT branch. The decision rules are defined for the active power flows from their sending to their receiving nodes. $\mathbf{P_{ij}}$ denotes the $(|\mathcal{L}| \times 1)$ vector of directed active power flows and is formulated according to the considered power flow modeling framework. $\mathbf{P_{ij}}$ can be linear in case of a DC- or SOC-OPF or nonlinear in case of the AC-OPF. Augmenting the standard OPF with (5.3) – (5.4) results in the data-driven SC-OPF formulated as a MIP. However, in the current formulation, the data-driven SC-OPF does not account for the inherent uncertainty in power system operations. Consequently, its solution might violate security constraints if the system conditions deviate from their expectation.

5.2.2　Formulation of the security- and chance-constrained OPF

Therefore, the next step lies in identifying the target operating region, the part of the secure operating region which is also robust against the uncertainty impact and can maintain both static and dynamic security over a range of uncertainty realizations. This area truly ensures a secure operation of the power system with a desired confidence level. In general, confidence regions can

be represented in an optimization problem through chance constraints. They define the maximum allowable violation probability of inequality constraints and restrict the feasible space of the optimization problem to the confidence region by introducing an uncertainty margin [21]. As such, they are particularly well aligned with the preventive framework and the conditional security margins $\mathbf{F}^{\min}$ and $\mathbf{F}^{\max}$ from (5.3) of the data-driven SC-OPF.

We assume wind power forecast errors $\boldsymbol{\xi}$ to be the source of uncertainty and model the actual wind power realization $\tilde{P}_{W_i}$ as the sum of its expected value P_{W_i} and deviation ξ_i,

$$\tilde{P}_{W_i} = P_{W_i} + \xi_i, \qquad \forall i \in \mathcal{W}, \tag{5.5}$$

where $\mathcal{W} \subseteq \mathcal{N}$ denotes the set of nodes with wind generators. Subscript W indicates the contribution of wind generators to the nodal active power injection P_i.

The impact of the forecast errors $\boldsymbol{\xi}$ on the OPF decision variables $\mathbf{v}$ is modeled as

$$\tilde{\mathbf{v}}(\boldsymbol{\xi}) = \mathbf{v} + \boldsymbol{\Delta}\mathbf{v}(\boldsymbol{\xi}), \tag{5.6}$$

where $\tilde{\mathbf{v}}$ represents the decision variables' actual realizations, $\mathbf{v}$ their optimal setpoints at the forecasted wind infeed, where $\boldsymbol{\xi} = \mathbf{0}$, and $\boldsymbol{\Delta}\mathbf{v}(\boldsymbol{\xi})$ their reaction to a change in wind power injection. Note that we use $\mathbf{v}$ to denote the generalized set of OPF decision variables. In this work, it can refer to either the set of AC-OPF ($\mathbf{x}$), DC-OPF ($\mathbf{y}$) or SOC-OPF ($\mathbf{z}$) variables. In the event of a forecast error, conventional generators are assumed to compensate for deviations from the expected wind infeed and maintain active power balance according to the automatic generation control (AGC). Each generator's production is adjusted according to its AGC participation factor γ_i for the total active power mismatch $\Xi = \sum_{i \in \mathcal{W}} \xi_i$,

$$\tilde{P}_{G,i} = P_{G,i} - \gamma_i \Xi, \qquad \forall i \in \mathcal{G}, \tag{5.7}$$

where $\mathcal{G} \subseteq \mathcal{N}$ is the set of nodes connected to conventional generation. If $\sum_{i \in \mathcal{G}} \gamma_i = 1$ holds, the contribution of all generators ensures total active power balance over the entire continuous uncertainty range. In case losses are accounted for in the OPF, (5.7) includes an additional term for the generator at the slack bus, which represents its nonlinear output variation due to a change in system losses.

The general formulation of the security- and chance-constrained OPF (SC-CC-OPF) representing the target operating region can be formulated as

$$\min_{\mathbf{v}_0} \mathbf{c}_G^T \mathbf{P}_{G_0} \tag{5.8}$$

$$\text{s.t.} \quad f_i(\mathbf{v}_j) = 0, \qquad\qquad i = 1, \ldots, \text{n}, \quad j = 0, \ldots, \text{c}, \tag{5.9}$$

$$\mathbb{P}\left(\begin{array}{ll} g_i(\mathbf{v}_j + \boldsymbol{\Delta}\mathbf{v}_j(\boldsymbol{\xi})) \leq 0, & i = 1, \ldots, \text{m}, \quad j = 0, \ldots, \text{c}, \\ \zeta(\mathbf{v}_j) + \Delta\zeta(\boldsymbol{\Delta}\mathbf{v}_j(\boldsymbol{\xi})) \geq \zeta^{\text{margin}}, & j = 0, \ldots, \text{c}, \end{array} \right) \geq 1 - \epsilon. \tag{5.10}$$

Problem (5.8) – (5.10) seeks the optimal operating point $\mathbf{v}_0$ for the forecasted and faultless system conditions, which can maintain static and dynamic security under any contingency with confidence $1 - \epsilon$ even when deviating from its expected position. Note that an operating point is deemed secure if it can maintain equipment and voltage ratings as well as dynamic security requirements for all contingencies [13]. Extending this to a probabilistic framework, it requires an operating point to fulfill both static and dynamic security criteria, which by definition refer to all contingencies, with a certain confidence level. Hence, the probabilistic counterpart can be formulated as a joint

chance constraint (5.10). Both static ($\mathbf{g}(\tilde{\mathbf{v}}(\boldsymbol{\xi})) \leq \mathbf{0}$) and dynamic ($\tilde{\zeta}(\tilde{\mathbf{v}}(\boldsymbol{\xi})) \geq \zeta^{\mathrm{margin}}$) security criteria need to be met at the same time to ensure a secure operation and reduce the probability of insecure instances, which violate at least one of them, to the acceptable violation probability ϵ. All equality constraints (5.9) are enforced for the forecasted operating point and for all contingencies. They represent the link between the pre- and post-contingency variables. In a preventive security framework control variables, such as the active power output of generators at PV buses, are not allowed to change from pre- to post-contingency state. However, to compensate for active power imbalances due to forecast errors, conventional generators adjust their production according to (5.7). Hence, problem (5.8) – (5.10) allows for adjustments of active power generation at PV buses in reaction to a forecast error but not to a contingency.

The SC-CC-OPF (5.8) – (5.10) is intractable. First, due to the nonlinear nature of the AC power flows, the distribution of the OPF output variables $\tilde{\mathbf{v}}(\boldsymbol{\xi})$ cannot be inferred, even when the distribution of the uncertainty $\boldsymbol{\xi}$ is exactly known. Under a DC approximation, the variables depend linearly on the uncertainty, which means that its distribution also propagates linearly to the output variables. This allows for a tractable reformulation of the chance constraints. However, using full linearizations of both the power flow equations and the uncertainty impact usually results in AC infeasible solutions and/or the inability to maintain the confidence level when projected back into the true AC space [62]. Additionally, the highly nonlinear dynamic security requirements make it impossible to reformulate the chance constraint and also challenge the formulation of tractable approximations. In the following, we propose two tractable and efficient approximations of the SC-CC-OPF (5.8) – (5.10).

5.2.3   SC-CC-OPF: A purely data-driven approach

Our first method relies on an offline approximation of the target operating region similar to the approximation of the secure operating region for the data-driven SC-OPF in Section 5.2.1. We start from the operating points in the secure operating region and test each of them under all contingencies for different uncertainty realizations through Monte Carlo simulations of AC power flows. We sample the uncertainty vector $\boldsymbol{\xi}$ and assume that the forecast errors follow a normal distribution with zero mean and known covariance. We do this to allow for comparison with our alternative approximation of the SC-CC-OPF introduced in the next section, where the analytical reformulations require assumptions on at least the mean and the covariance of $\boldsymbol{\xi}$. However, the purely data-driven approach can accommodate any type of uncertainty or distribution in order to construct the target operating region. For the AC power flows, each operating point in the secure operating region is perturbed using the forecast error samples and the corresponding generation adjustments (5.7) provided by the AGC to compensate for the power imbalance. The Monte Carlo simulation allows us to identify the subset of operating points which maintain both static and dynamic security with probability of at least $1 - \epsilon$ over the tested samples. Their operating space finally constitutes our target operating region.

As for the approximation of the secure operating region, we again use decision trees (DTs) to formulate tractable rules based on active power lines flows. They are now derived for the target

operating region instead for the secure operating region. We formulate the DD-SC-CC-OPF as

$$\min_{\mathbf{v}_0} \mathbf{c}_G^T \mathbf{P}_{G_0} \tag{5.11}$$

$$\text{s.t. } f_i(\mathbf{v}_0) = 0, \qquad\qquad i = 1, \dots, n, \tag{5.12}$$

$$\mathbf{F}^{TR,min}\mathbf{b} \leq \mathbf{P}_{\mathbf{ij}_0} \leq \mathbf{F}^{TR,max}\mathbf{b}, \tag{5.13}$$

$$\sum_{p \in \mathcal{P}} b_p = 1, \tag{5.14}$$

$$\mathbf{P}_{G_0} \leq \mathbf{P}_G^{max} - \mathbf{R}_G^U, \tag{5.15}$$

$$\mathbf{P}_{G_0} \geq \mathbf{P}_G^{min} + \mathbf{R}_G^D, \tag{5.16}$$

$$\mathbf{v}^{min} \leq \mathbf{v}_0 \leq \mathbf{v}^{max}, \qquad\qquad \forall\, \mathbf{v}_0 \setminus \mathbf{P}_{G_0}, \tag{5.17}$$

where $\mathbf{F}^{TR,min}$ and $\mathbf{F}^{TR,max}$ denote the DT limits, which define the target operating region (TR). We derive the DTs from the discretized AC-OPF feasible space, such that they determine the boundary between the desired operating region and the remaining AC-OPF feasible space.

The DD-SC-CC-OPF aims at finding the least-cost secure solution for the forecasted and faultless system conditions, taking into consideration all contingencies and the possible uncertainty. The equality constraints are formulated for these conditions only, as all constraints related to the contingencies are already captured by (5.13). Note that we still need to ensure that enough generation capacity is available for balancing the forecast errors. As we already obtain the distribution of each generator's active power output from the Monte Carlo simulations, we can determine the probabilistic up- and down reserve requirements of a generator from the lower $\frac{\epsilon}{2}$ and upper $1 - \frac{\epsilon}{2}$ quantiles of its distribution

$$R_{G_i}^D = P_{G_i}^{init} - P_{G_i}^{\frac{\epsilon}{2}}, \tag{5.18}$$

$$R_{G_i}^U = P_{G_i}^{1-\frac{\epsilon}{2}} - P_{G_i}^{init}, \tag{5.19}$$

which is depicted in Fig. 5.1. $\mathbf{P}_G^{init}$ denotes the active power dispatch of the operating point under test, which can be interpreted as its "forecasted" value $\mathbf{P}_G$, before it is adjusted to the total power imbalance Ξ of the test sample according to (5.7). Since we use the same samples of $\boldsymbol{\xi}$ and the same AGC parameters $\boldsymbol{\gamma}$ for initializing the Monte Carlo simulations of all operating points in the secure region, the distance between the initial dispatch and the upper and lower quantiles remains unchanged for the generators at PV buses. It varies only for the generator at the slack bus, which adjusts its output according to the nonlinear variations in losses. In this case, we select the most stringent reserve capacity requirements on the slack generator imposed by any operating point in the target operating region. As our goal is to maintain overall secure operation with confidence $1 - \epsilon$, we use the $\frac{\epsilon}{2}$ and $1 - \frac{\epsilon}{2}$ quantiles to ensure that upper and lower generation limits are enforced jointly, i.e., $\mathbb{P}(\tilde{P}_{G_i} \leq P_{G_i}^{max}) \cup \mathbb{P}(\tilde{P}_{G_i} \geq P_{G_i}^{min}) \geq 1 - \epsilon$. The remaining equipment and voltage ratings are included in (5.17).

The major benefit of the purely data-driven approach is that we do not need to make any assumptions on the statistical behavior of the output variables. The Monte Carlo simulations based on the full nonlinear AC power flow equations already reveal their true distributions. It also allows us to define a tractable approximation for the full target operating region and as such, for the joint chance constraint (5.10) defining the confidence level for overall secure power system operation. Nevertheless, the DD-SC-CC-OPF depends on the availability of a sufficient number of high quality samples and adds an additional burden to the already demanding database generation.
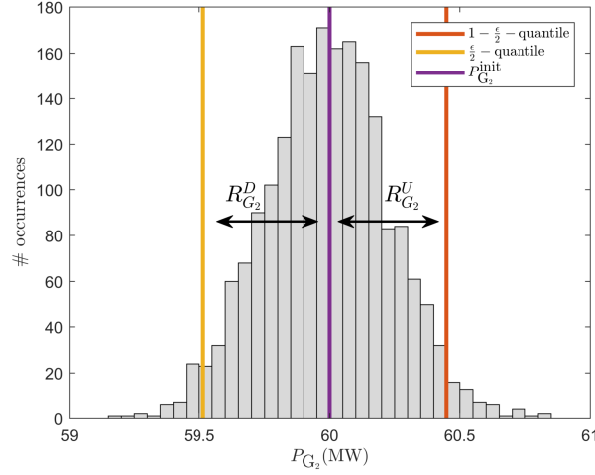
Figure 5.1: Determining probabilistic up- and down-reserve requirements for the DD-SC-CC-OPF.

Therefore, a combination of the data-driven approach for representing the security region, which can be constructed using data that operators often have available, and analytical reformulations to approximate the target operating region can serve as an alternative framework, whenever the information in the uncertainty space is sparse.

5.2.4   SC-CC-OPF: Combining data and analytical reformulations

In our second approach, we do not construct the target operating region offline but recast the deterministic data-driven SC-OPF representing the secure operating region to a probabilistic problem instead. To do this, we use single or univariate chance constraints, which we reformulate analytically to tractable constraints. The method is mainly based on the principles from Chapter 4 and this section highlights the key features for completeness. In the following, the abbreviation DA-SC-CC-OPF denotes the SC-CC-OPF based on a combination of data-driven methods and analytical reformulations, whereas DD-SC-CC-OPF refers to the purely data-driven approach from the previous section. We formulate the DA-SC-CC-OPF as

$$\min_{\mathbf{v}_0} \mathbf{c}_G^T \mathbf{P}_{G_0} \tag{5.20}$$

$$\text{s.t. } f_i(\mathbf{v}_0) = 0, \qquad\qquad i = 1, \ldots, \mathrm{n}, \tag{5.21}$$

$$\mathbb{P}\Big(\tilde{v}_{i_0}(\boldsymbol{\xi}) \leq v_i^{\max}\Big) \geq 1 - \epsilon, \qquad \forall\, \tilde{v}_{i_0}(\boldsymbol{\xi}) \in \tilde{\mathbf{v}}_0(\boldsymbol{\xi}), \tag{5.22}$$

$$\mathbb{P}\Big(\tilde{v}_{i_0}(\boldsymbol{\xi}) \geq v_i^{\min}\Big) \geq 1 - \epsilon, \qquad \forall\, \tilde{v}_{i_0}(\boldsymbol{\xi}) \in \tilde{\mathbf{v}}_0(\boldsymbol{\xi}), \tag{5.23}$$

$$\mathbb{P}\Big(\tilde{P}_{ij_0}(\boldsymbol{\xi}) \leq \mathbf{F}_{ij,*}^{\mathrm{SR,max}}\mathbf{b}\Big) \geq 1 - \epsilon, \qquad \forall\, l = (i,j) \in \mathcal{L}, \tag{5.24}$$

$$\mathbb{P}\Big(\tilde{P}_{ij_0}(\boldsymbol{\xi}) \geq \mathbf{F}_{ij,*}^{\mathrm{SR,min}}\mathbf{b}\Big) \geq 1 - \epsilon, \qquad \forall\, l = (i,j) \in \mathcal{L}, \tag{5.25}$$

$$\sum_{p \in \mathcal{P}} b_p = 1. \tag{5.26}$$

The objective function (5.20) as well as the equality constraints (5.21) referring to the power balance equations and the constraint setting the reference angle to zero are formulated for the forecasted operating point under faultless system conditions. The chance constraints (5.22) – (5.23) denote the usual probabilistic constraints in chance-constrained OPF formulations and limit the

probability of violating equipment or voltage ratings to a threshold ϵ. The probabilistic security constraints are represented by (5.24) – (5.25), where the conditional decision rules capturing the secure operating region over all contingencies are formulated as chance constraints. They contain binary variables. Constraint (5.26) ensures that only one set of security limits is selected, which can also accommodate the requirements imposed by the chance constraints. The DT matrices defining the secure operating region (SR) are denoted by $\mathbf{F}^{\text{SR,min}}$ and $\mathbf{F}^{\text{SR,max}}$, where $\mathbf{F}^{\text{SR,max}}_{ij,*}$ represents the row for line $l = (i, j)$.

When comparing the DA-SC-CC-OPF (5.20) – (5.26) and the DD-SC-CC-OPF (5.11) – (5.17), one has to keep in mind that they are not equivalent formulations but two different approximations of the target model (5.8) – (5.10). While the DD-SC-CC-OPF mimics the joint chance constraint (5.10), the DA-SC-CC-OPF enforces the confidence level for each system constraint individually. This means that its solution, despite fulfilling all security criteria for the forecasted operating point and all uncertainty requirements for each constraint individually, might still not maintain overall security with the desired confidence level over the entire uncertainty range. However, single chance constraints can also be used to effectively approximate joint chance constraints [56]. Most importantly, they offer the flexibility to target individual system constraints. Combined with a data-driven approach that identifies the dimensions susceptible to the uncertainty impact a priori, the violation probabilities of single chance constraints could then be tuned individually to ensure the desired overall performance. Additionally, the DT can be defined in a more conservative way by either increasing the required security margin or increasing the cost of misclassifications in order to compensate for the shortcomings of using individual chance constraints.

Reformulation of the chance constraints

In order to be able to reformulate the chance constraints (5.22) – (5.25) to tractable constraints suitable for implementation in an optimization environment, we use affine policies to model the system response

$$\tilde{\mathbf{v}}_0(\boldsymbol{\xi}) = \mathbf{v}_0 + \boldsymbol{\Delta}\mathbf{v}_0(\boldsymbol{\xi}) = \mathbf{v}_0 + \boldsymbol{\Upsilon}\boldsymbol{\xi}. \tag{5.27}$$

$\boldsymbol{\Upsilon} = \frac{\partial \mathbf{v}_0}{\partial \boldsymbol{\xi}}$ denotes the matrix of linear sensitivities describing the change in each optimization variable with respect to the uncertainty $\boldsymbol{\xi}$. We assume that the forecast errors $\boldsymbol{\xi}$ follow a normal distribution with zero mean and known covariance $\boldsymbol{\Sigma}$, which allows us to reformulate the linear chance constraint $\mathbb{P}(v_{i_0} + \boldsymbol{\Upsilon}^{\text{v}}_{i,*}\boldsymbol{\xi} \leq v_i^{\text{max}}) \geq 1 - \epsilon$ to

$$v_{i_0} \leq v_i^{\text{max}} - \Phi^{-1}(1 - \epsilon)\sqrt{\boldsymbol{\Upsilon}_{i,*}\boldsymbol{\Sigma}\boldsymbol{\Upsilon}^{\text{T}}_{i,*}}, \tag{5.28}$$

where $\Phi^{-1}(1 - \epsilon)$ denotes the inverse cumulative distribution function of the Gaussian distribution at the confidence level. The reformulation results in a deterministic constraint (5.28), where the introduced uncertainty margin $\Omega_i = \Phi^{-1}(1 - \epsilon)\sqrt{\boldsymbol{\Upsilon}_{i,*}\boldsymbol{\Sigma}\boldsymbol{\Upsilon}^{\text{T}}_{i,*}}$ tightens the original constraints and secures the system against the forecast error [21]. Note that the analytical reformulation is not dependent on the assumption of a Gaussian distribution but can also accommodate other behavior of the uncertainty by replacing $\Phi^{-1}(1 - \epsilon)$ and thus, changing the magnitude of the uncertainty margin accordingly (see [57] and Section 4.2.5 for a more detailed discussion).

The chance constraints on the conditional line flow limits (5.24) – (5.25) are binary chance constraints. We reformulate them by combining the uncertainty margin associated with the active power flow

on a line $l = (i, j)$, Ω_{ij}^F, directly with the conditional security margins defined by the DT

$$P_{ij_0} \leq (\mathbf{F}_{ij,*}^{\text{SR,max}} - \Omega_{ij}^F \mathbf{1})\mathbf{b}, \tag{5.29}$$

$$P_{ij_0} \geq (\mathbf{F}_{ij,*}^{\text{SR,min}} + \Omega_{ij}^F \mathbf{1})\mathbf{b}, \tag{5.30}$$

where $\mathbf{1}$ is an all-ones vector of size $(1 \times |\mathcal{P}|)$. Thus, the optimization determines the optimal subspace of the secure operating region (i.e., the optimal DT branch), which can accommodate the uncertainty requirements.

Under a DC approximation with the reduced variable set $\mathbf{y}_0 := \{\mathbf{P}_{\text{G}_0}, \boldsymbol{\theta}_0\}$, the matrix of sensitivities is a linear function of the generator participation factors and the power transfer distribution factors (PTDFs), i.e., $\boldsymbol{\Upsilon}^{\mathbf{y}} = \mathbf{f}(\boldsymbol{\gamma}, \mathbf{PTDF})$. PTDFs describe the change in active power flows due to a change in nodal active power injections [91]. Hence, the output variables $\mathbf{y}_0$ depend linearly on the uncertainty $\boldsymbol{\xi}$. This allows for a straightforward analytical reformulation of the DA-SC-CC-DC-OPF to a deterministic problem, if at least the mean and the covariance of the uncertainty are known. The set of chance constraints in the DC formulation is given by

$$\mathbb{P}(P_{\text{G}_{i,0}} - \gamma_i \Xi \leq P_{\text{G}_i}^{\max}) \geq 1 - \epsilon, \tag{5.31}$$

$$\mathbb{P}(P_{\text{G}_{i,0}} - \gamma_i \Xi \geq P_{\text{G}_i}^{\min}) \geq 1 - \epsilon, \tag{5.32}$$

for all generators and the two sets of probabilistic DT constraints (5.24) – (5.25). Since the total wind deviation $\Xi = \sum_{i \in \mathcal{W}} \xi_i$ is a sum of normally distributed random variables, it also follows a normal distribution with mean $\mu_\Xi = \sum_{i \in \mathcal{W}} \mu_{\xi_i}$ and variance $\sigma_\Xi^2 = \sum_{i \in \mathcal{W}} \sigma_{\xi_i}^2$, such that (5.31) – (5.32) can be reformulated according to (5.28).

The reformulation of the DA-SC-CC-OPF based on the nonlinear AC or SOC power flow equations to a nonlinear deterministic problem is more challenging as the optimization output variables are nonlinearly coupled with the uncertain input parameters. As a result, the sensitivity matrices $\boldsymbol{\Upsilon}^{\mathbf{x}}$ and $\boldsymbol{\Upsilon}^{\mathbf{z}}$ are nonlinear functions of $\boldsymbol{\gamma}$ and the optimization variables $\mathbf{x}$ or $\mathbf{z}$. To avoid additional nonlinearities in the OPF, we use the approach from Chapter 4, which was proposed in [59] and is a computationally efficient scheme for iteratively approximating the nonlinear chance-constrained AC-OPF. It alternates between (i) a deterministic nonlinear OPF and (ii) a computation of the sensitivity matrices and uncertainty margins. The computation in (ii) is based on a first-order Taylor series approximation linearizing the sensitivity matrices around the current optimal solution indicated with an asterisk, i.e., $\boldsymbol{\Upsilon}^{\mathbf{x}} = \mathbf{f}(\boldsymbol{\gamma}, \mathbf{x}^*)$ and $\boldsymbol{\Upsilon}^{\mathbf{z}} = \mathbf{f}(\boldsymbol{\gamma}, \mathbf{z}^*)$. The derivation of the linear sensitivities $\boldsymbol{\Upsilon}^{\mathbf{z}}$ can be found in Appendix A. The partial linearization allows for a tractable approximation of the nonlinear probabilistic OPF with a nonlinear deterministic OPF using the same reformulation principles as applied for linear chance-constrained programs. We adjust the iterative framework for the DA-SC-CC-OPF as outlined in Algorithm 2 and alternate between the deterministic data-driven SC-OPF and the computation of the uncertainty margins. The algorithm converges as soon as the change in uncertainty margins is small enough and the binary decisions do not change in two consecutive iterations.

However, in a nonconvex AC-OPF framework, the DA-SC-CC-OPF results in an iterative nonconvex mixed integer nonlinear program (MINLP), where the computational complexity associated with one single iteration is already impractical for realistic system sizes, let alone the entire iteration procedure. As in Chapter 3 and Chapter 4, we therefore, use the convex approximation of the AC-OPF starting from the alternative SOC power flow equations (2.10) – (2.13), relaxing the quadratic

---

Algorithm 2 DA-SC-CC-OPF: An iterative security- and chance-constrained OPF

1: Set iteration count: $\nu \leftarrow 0$
2: **while** $||\Omega^\nu - \Omega^{\nu-1}||_\infty > \rho$ **and** $\mathbf{b}^{\nu,*} \neq \mathbf{b}^{\nu-1,*}$ **do**
3:     **if** $\nu = 0$ **then**
4:         solve the DD-SC-OPF for the forecasted wind infeed $\mathbf{P_W}$ without considering uncertainty and obtain the secure operating point $\mathbf{v}_0^{\nu=0}$
5:         evaluate $\upsilon^{\nu=0}$ and $\Omega^{\nu=0}$ at $\mathbf{v}_0^{\nu=0}$
6:     **end if**
7:     include Ω^ν according to (5.28) for all variables $\mathbf{v}(\xi)$
8:     solve DD-SC-OPF to obtain $\mathbf{v}^{\nu+1}$
9:     evaluate $\Upsilon^{\nu+1}$ and $\Omega^{\nu+1}$ at $\mathbf{v}_0^{\nu+1}$
10:    $\nu \leftarrow \nu + 1$
11: **end while**.

---

equality constraint to a second order cone constraint, i.e., $c_l^2 + s_l^2 \leq u_i u_j$, and approximating the angle constraint $\theta_{ji} = \text{atan}(\frac{s_l}{c_l})$ with a Taylor series expansion as proposed in [42]. As a result, we avoid one level of nonconvexities associated with the power flow equations. As in previous chapters, we will refer to the OPF based on the relaxed and approximated alternative power flow equations (2.10) – (2.13) as *second order cone OPF* (SOC-OPF) throughout the remainder of this chapter. The resulting problem instance for the data-driven SC-OPF reduces to a convex mixed integer second order cone program (MISOCP), for which solvers have already reached a high level of maturity [28, 85].

5.3 Case study

We demonstrate how the target operating region can be efficiently approximated using the modified IEEE 14 bus test system from Section 3.5.3. In this case study, we assume 110 MVA line ratings for all lines and allow for 10% higher emergency line ratings after a contingency. The contingency set includes all line faults except for outages of lines 13 and 14, for which the system is not N-1 secure due to the introduced line ratings. Generator 4 is a wind power plant with an expected production level of 20 MW and its marginal cost is set to 0 €/MWh. The forecast errors are assumed to be normally distributed with zero mean and a standard deviation of 15% of the expected production level.

First, we will analyze the database in more detail and then show how we can gradually approach the target operating region for different power flow modeling frameworks by comparing

- the standard OPF, which does not include any security or uncertainty considerations

- the chance-constrained OPF (CC-OPF), which accounts for the stochastic nature of the wind generation

- the preventive security-constrained AC-OPF (SC-OPF) considering static but not dynamic security

- the data-driven SC-OPF (DD-SC-OPF) from Chapter 3 ensuring both static and dynamic security

- and finally, the proposed SC-CC-OPFs, which aim at providing a desired confidence level for both static and dynamic security over the uncertainty range.

We evaluate the performance of all OPF solutions through Monte Carlo simulations using AC power flows and a subsequent small-signal stability analysis. First, the optimal operating point at the forecasted wind infeed (i.e., the solution of any OPF) is tested for static and dynamic security against all contingencies. Then it is examined at the faultless base case and each contingency against 2000 samples randomly drawn from a normal distribution. As usual in power system operations, we require a minimum damping ratio of 3% for the base case and for the steady-states obtained after all contingencies as a measure for small-signal stability (i.e., dynamic security). The confidence level $1 - \epsilon$ is selected to be 0.95. This means that we require both static and dynamic security limits to be satisfied simultaneously with a probability of 95%.

In a preventive security framework, control variables are usually not allowed to change from pre- to post-contingency state. However, the test system is not N-1 secure under the current equipment and voltage ratings, if the voltage magnitudes at generator buses are enforced over the entire contingency set. This becomes obvious in the standard preventive SC-OPF, which resorts to infeasibility, if one tries to impose this requirement. Therefore, we enable a PV-PQ bus type switching in the Monte Carlo simulations to maintain the reactive power limits of generators, which, however, leads to a deviation from their voltage setpoints if the limits are reached. In the preventive security-constrained AC-OPF (SC-OPF) used as a benchmark, we incorporate the PV-PQ bus type switching and allow for deviations from the base case solution $\mathbf{V}_0$ in case of contingencies by adding

$$(\boldsymbol{\mathcal{I}}_{i,*}(\mathbf{V}_c - \mathbf{V}_0))(Q_{\mathrm{G}_{i,c}} - Q_{\mathrm{G}_{i,c}}^{\max})(Q_{\mathrm{G}_{i,c}} - Q_{\mathrm{G}_{i,c}}^{\min}) = 0, \qquad (5.33)$$

for each generator i and contingency c to the constraint set. $\boldsymbol{\mathcal{I}}_{i,*}$ denotes the row of the generator-to-node incidence matrix pertaining to generator i, while $\mathbf{V}$ denotes the vector of nodal voltage magnitudes. Constraint (5.33) enforces that a generator operates at either its AVR voltage setpoint (defined at the grid connection point) or at one of its reactive power limits. This essentially mimics the behavior of a generator's excitation limiter. Alternatively, (5.33) can be implemented using binary variables.

All simulations related to convex problems were carried out in Python with the Gurobi Optimizer. The nonconvex OPFs were implemented in Matlab using the YALMIP toolbox [114]. All AC power flow analyses, i.e., the database generation, the AC feasibility recovery and the Monte Carlo simulations, were carried out with MATPOWER [88].

5.3.1 Database analysis

We use a discretization interval of 1 MW for generating the database, which leads to more than 2.5 million operating points. The same database has already been used in the analysis of Section 3.6.3 for comparing the impact of different discretization intervals on the database and the resulting decision trees. Given that the data points were generated using AC power flows, not all of them satisfy all equipment and voltage ratings. Those are, therefore, not feasible to the AC-OPF. Approximately 675 000 operating points – 26.85% of the considered power flow solution space – fulfill all ratings and as such, constitute a discretization of the feasible space of the AC-OPF. A comparison of the simulated power flow solution space with its AC-OPF feasible subset is depicted in Fig. 5.2 on the left.

Data pre-processing and decision tree complexity reduction

The PV-PQ bus type switching was also enabled during the database generation, which means that the database contains many operating points, where generator voltage magnitudes slightly deviate from their setpoints in order to maintain generator reactive power limits. We will however, focus on the subset of the data which for the faultless base case maintains the generator voltage setpoints given in the case file. Note that this only refers to the base case and not the contingencies, where the voltage setpoints cannot be maintained as discussed above. Consequently, we also set the generator bus voltage magnitudes in all OPFs for the faultless base case to their specified setpoints. This serves primarily as an a priori measure to avoid unnecessarily complex decision trees and overfitting. When focusing on the subset of the data, which maintains the generator voltage setpoints at the base case, the entire database (i.e., the power flow solution space) reduces to only 59'772 operating points, out of which 49'615 are located in the AC-OPF feasible space. Thus, they represent 7.35% of the original discretized AC-OPF feasible space. While the reduction is substantial, the space spanned by the operating points maintaining the voltage setpoints in the base case still fairly well represents the operating region defined by all simulated AC-OPF feasible operating points as depicted in Fig. 5.2 on the right. Identifying the data points which best capture the collective behavior, and thereby, reducing the size of the database can significantly simplify the decision tree and avoid overfitting. Tree-simplification procedures are mainly based on a priori data reduction or a posteriori DT pruning techniques, the latter of which we applied in Chapter 3. However, if possible, data pre-processing prior to the decision tree construction is often favored. The decision tree size increases and overfitting tends to get worse as the size of the learning set grows meaning that the additional complexity does not usually yield an improvement in classification accuracy [115, 116].
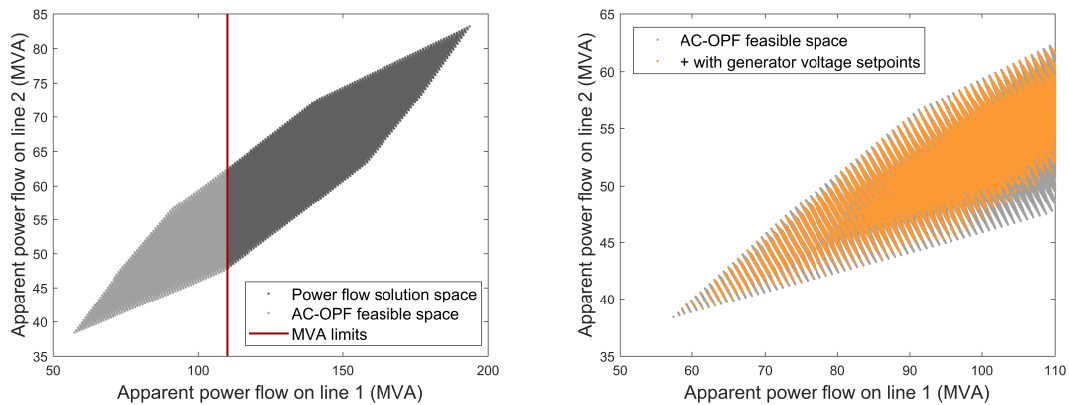
Figure 5.2: The figure on the left depicts the entire simulated power flow solution space with approximately 2.5 million operating points and compares it to its AC-OPF feasible subset, which covers 26.85% of the original space. The figure on the right zooms in on the operating region of interest (i.e., the AC-OPF feasible space). It shows the spaces spanned by the operating points, which do not maintain the generator voltage setpoints (in grey) and those that do (in orange).

Indeed, focusing on the selected data subset from the AC-OPF feasible space instead of the entire generated power flow solution space as we did in Chapter 3, results in a significantly less complex decision tree. Using active power line flows obtained from the AC power flow analyses as predictor variables and a subset from the AC-OPF feasible space for training, we obtain a decision tree for

the secure operating region with three leaf nodes. Its domain in the space of the active power line flows on lines 1 and 2 is depicted in Fig. 5.3. The left graph compares the DT domain to all data points in the AC-OPF feasible space and highlights the constituent parts of the security region (excluding the target operating region). When zooming in on the DT domain in the right figure, one can see that the DT captures all but one operating point fulfilling the security requirements and does not include any operating points deemed insecure. We use the same decision tree for the security region in the data-driven SC-OPF and the DA-SC-CC-OPF regardless of the power flow modeling framework. For the DD-SC-CC-OPF, we derive another decision tree based again on active power line flows, which captures the target operating region instead. Since the target operating region, derived based on 100 random samples of ξ, is smaller than the security region, the DT reduces to two leaf nodes only.
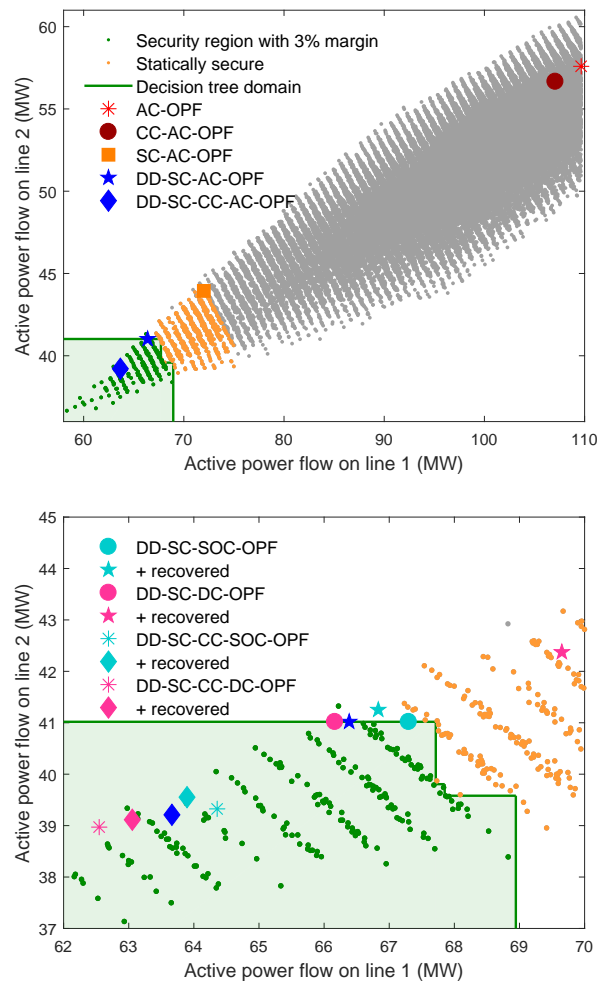
Figure 5.3: Locations of the OPF solutions compared to the secure decision tree domain.

Fig. 5.4 depicts the feasible operating range of each generator in the space of the active power generation and the minimum damping ratio, which is evaluated in security assessments after the database has been created (see Section 3.3.1). All dots represent generated data points and their alignment in the plots for generators 2 to 4 clearly indicates the 1 MW discretization interval. Note that we only vary the output of generators at PV buses uniformly. The output of generator 1 at the

slack bus is not a control variable but is automatically adjusted according to the system conditions to compensate for the power losses. This is also the reason why the feasible operating region of generator 1 in Fig. 5.4 has a distinct shape. Many more "unique" dispatch solutions of generator 1 occur during the database generation corresponding to the unique AC power flow initializations used.

The green and orange region in Fig. 5.4 comprises a total of 885 operating points (or 1.78% of the AC-OPF feasible space) that satisfy all equipment and voltage ratings under any considered contingency, and thus meet the static N-1 criterion. Here, all of the statically secure operating points also happen to be stable with $\zeta^{\min} > 0\%$ but do not necessarily meet the required minimum damping ratio of 3%. Only 218 operating points or 0.44% of the AC-OPF feasible space highlighted in green meet the dynamic security requirements in all contingencies. While the share of the secure operating region in the entire AC-OPF feasible space is very system specific, this still indicates (i) the importance of adequately representing security requirements in the OPF, and (ii) the excessive conservatism of the currently prevailing preventive security paradigm. Requiring lower damping ratios after a contingency could already considerably extend the secure operating region to include all remaining 667 operating points from the statically and dynamically secure region in orange increasing the area almost threefold. Note that many operating points share the same or very similar damping ratios and their corresponding data points overlap in Fig. 5.4. The actual feasible space of the AC-OPF is therefore, not drawn to scale. Despite achieving lower levels of conservatism by adjusting the preventive security criteria through e.g., lower post-contingency damping requirements, only appropriate corrective control actions could significantly extend the allowable secure operating region beyond the orange area and even beyond the black boundary. All operating points in the discretized AC-OPF feasible space actually fulfill the 3% stability margin and static security for the base case and most contingencies but cannot maintain it for the most critical contingency, which almost consistently corresponds to an outage of line 2. Post-contingency actions to mitigate the impact of a fault on line 2 have, therefore, enormous potential for extending the allowable operating region.

The data-driven approach also clearly helps in identifying the most critical contingencies and can possibly outline which controls under which operating conditions are most effective in alleviating their repercussions. This could avoid the need for explicitly incorporating the vast number of corrective control actions in corrective security-constrained OPF algorithms, instead focusing on optimizing the controls which actually have an impact and are truly at the disposal of the operator.

5.3.2 Approximating the target operating region

In this section, we compare our proposed security- and chance-constrained OPFs (DD-SC-CC-OPF and DA-SC-CC-OPF) in an AC, DC and SOC-OPF setting with the remaining OPF models listed earlier.

Approximation of losses in DC-OPF formulations

An approximation of the active power losses is fundamental to the accuracy of the DC-OPF [34]. We therefore determine a best guess operating point for each DC-OPF from the database considering the operating range, which the OPF formulation covers. Specifically, we consider the full AC-OPF feasible space at the forecasted wind infeed for the standard DC-OPF. For the CC-DC-OPF, we additionally take a reduction of the operating range of conventional generators
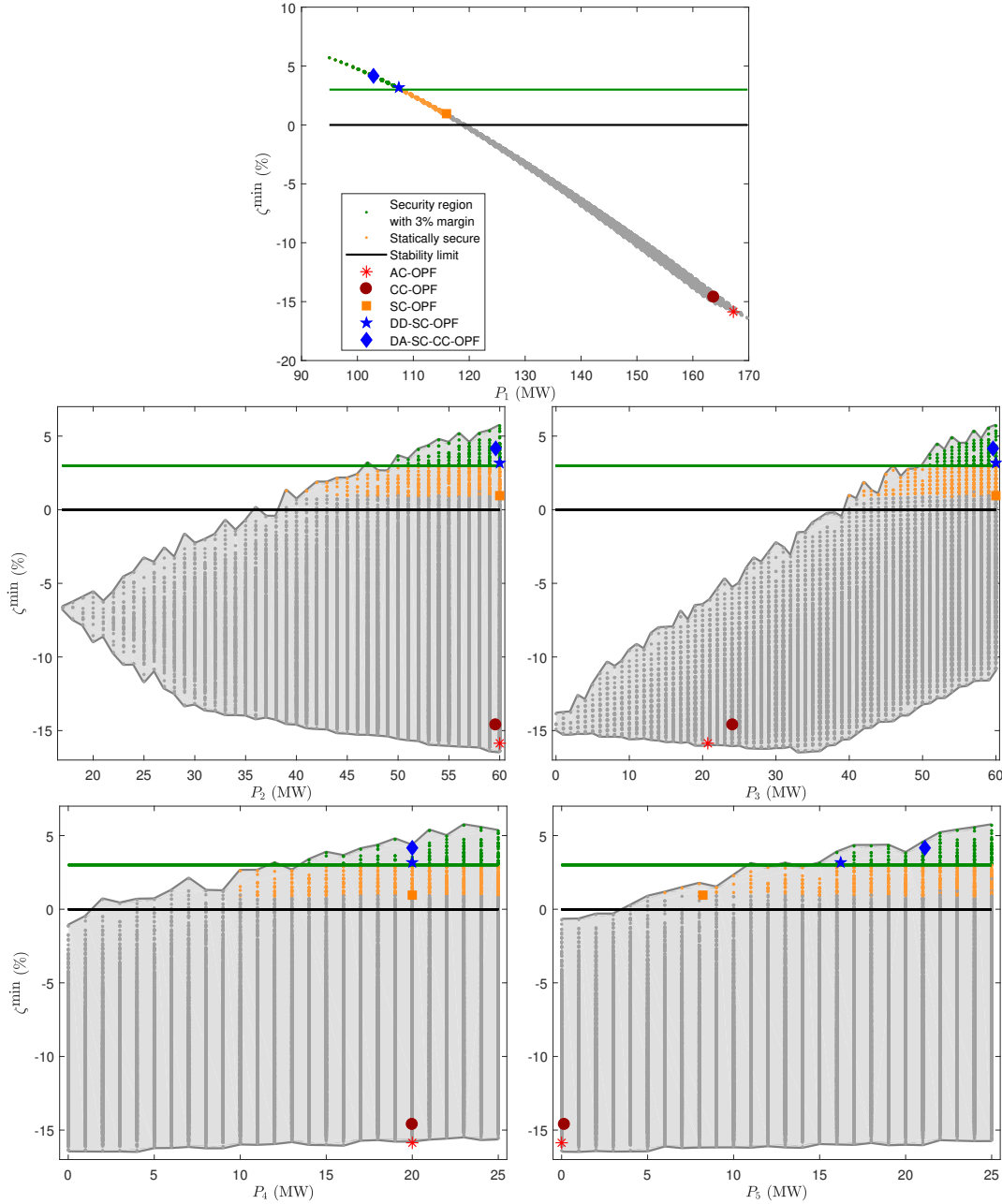
Figure 5.4: Operating regions of system generators. The dots represent all operating points in the database, which are feasible to the AC-OPF and hence, do not violate any equipment or voltage ratings. They depict the minimum damping ratio of an operating point for a specific generator dispatch. Operating points, which fulfill the static N-1 security criterion are depicted in orange, while those that additionally meet the 3% damping ratio are highlighted in green. All data-driven models are able to identify solutions in the secure operating region as opposed to the other tested OPF approaches. The results highlighted here were derived from the AC power flow variants of the optimization models. Note that the results of the DD-SC-CC-OPF are not depicted as they are very close to the DA-SC-CC-OPF solution and would hinder readability.

into account according to their participation in the automatic generation control γ_i. A part of the capacity is withheld to compensate for the total power imbalance, i.e., $P_i^{\mathrm{min}} + \Omega_i^{\mathrm{P}} \leq P_i \leq P_i^{\mathrm{max}} - \Omega_i^{\mathrm{P}}$, where $\Omega_i^{\mathrm{P}} = \gamma_i \sigma_\Xi \Phi^{-1}(1 - \epsilon)$. We do the same for obtaining the loss estimates of the data-driven

OPFs with the difference of searching the security region rather than the entire AC-OPF feasible space. Finally, the active power line losses of the corresponding best guess operating points are treated as additional loads in the DC-OPF variants and are equally shared between the sending and receiving nodes.

In order to determine the feasibility of the solution of any of the DC-OPF variants and obtain the required voltage magnitudes for its small-signal stability assessment, we use the operating point as an initialization to an ex-post AC power flow, which projects the solution back into the AC space. If no violations of equipment and voltage ratings occur at the power flow solution, the DC-OPF solution is also feasible to the AC-OPF. The feasibility of an SOC-OPF solution is determined in the same way. However, our SOC-OPF explicitly represents all original dimensions of the AC-OPF. Therefore, its feasibility can already be evaluated by simply computing the nodal active and reactive power mismatch based on the full nonlinear AC power flow equations at the SOC-OPF solution. If both active and reactive power mismatches are within tolerance (we use $||\mathbf{\Delta P}, \mathbf{\Delta Q}||_\infty \leq 10^{-5}$ p.u.), the ex-post power flow based recovery can be omitted.

Results

Table 5.1 lists the results of the tested OPFs. We omit the results of the standard OPFs as they do not meet any security or uncertainty requirements. However, they are depicted in Fig. 5.3, 5.4 and 5.7 along with the solutions of the other models for comparison. Fig. 5.4 clearly shows that the solutions of the standard AC-OPF and the CC-AC-OPF are located in regions far apart from the secure operating region. The standard preventive SC-OPF is naturally located in the N-1 secure region, which also happens to coincide with the small-signal stable operating region. However, as listed in Table 5.1 its minimum damping ratio ζ^{min} of 0.95% for the forecasted operating point does not fulfill the required margin of 3%. On the contrary, the solutions of all data-driven approaches are located in the secure operating region. Only the DD-SC-DC-OPF with a ζ^{min} of 2.98% violates the requirements slightly. This can be explained by the AC power flow based decision tree, which does not accurately map the security requirements to the DC space. When the DD-SC-DC-OPF solution is projected back into the AC space using an ex-post AC power flow, its solution is shifted out of the secure operating region as depicted in Fig. 5.3 on the right. Projecting the secure operating region first to the DC space and then deriving the decision tree directly from there could potentially alleviate this effect and lead to a better translation of the security requirements. Fig. 5.3 also indicates that the same happens to the solution of the DD-SC-SOC-OPF. The translation error is however, smaller and the solution remains within the vicinity of its starting point. Although it is no longer located within the limits imposed by the DT, it still remains within the desired operating region with a minimum damping ratio of 3.01%.

The results in Table 5.1 show that neither the CC-OPF, the standard preventive SC-OPF nor the DD-SC-OPF are able to maintain any of the security requirements with sufficient confidence over the tested uncertainty set. We use $\tilde{\epsilon}_J^{\mathrm{stat}}$ and $\tilde{\epsilon}_J^{\mathrm{dyn}}$ to indicate the empirically observed joint violation probabilities for static and dynamic security constraints, respectively. The overall joint security violation probability, when at least one constraint is violated, is denoted with $\tilde{\epsilon}_J = \tilde{\epsilon}_J^{\mathrm{stat}} \vee \tilde{\epsilon}_J^{\mathrm{dyn}}$. It can be seen that the DA-SC-CC-OPF using analytical reformulations, despite relying on single chance constraints, results in more secure but also more conservative solutions than the purely data-driven DD-SC-CC-OPF. As shown in Fig. 5.5, the introduced uncertainty margins reduce the security region and eventually, impose tighter constraints than the DT defined for the target

Table 5.1: Results of the security- and chance-constrained OPFs.

		CC-OPF			SC-OPF	DD-SC-OPF			DA-SC-CC-OPF			DD-SC-CC-OPF		
		DC[2]	SOC[1]	AC	AC	DC[2]	SOC[2]	AC	DC[2]	SOC[2]	AC	DC	SOC[1]	AC
Cost	(€)	2745	2747	2747	2953	3050	3004	3008	3045	3036	3038	3027	3031	3032
Time	(s)	0.22	1.96	1.97	14.34	0.50	1.84	4.00	0.34	8.42	12.50	0.70	4.26	2.81
ζ^{min}	(%)		unstable		0.95	2.98	3.01	3.17	4.34	4.07	4.16	3.79	3.93	3.89
						Monte Carlo analysis									
$\tilde{\epsilon}_J$	(%)		100		99.90	49.60	48.85	48.75		4.45		8.50	5.40	5.05
$\tilde{\epsilon}_J^{stat}$	(%)	13.90	10.10	9.95	48.75	48.75	48.85	48.75		4.45			2.30	
$\tilde{\epsilon}_J^{dyn}$	(%)		100		99.90	49.60	47.50	37.30	1.00	3.00	2.05	8.50	5.40	5.05
$\tilde{\zeta}^{min}$	(%)		unstable		unstable	0.66	0.69	0.88	2.25	1.93	2.03	1.59	1.71	1.75
$\tilde{\zeta}_{p5}^{min}$	(%)		unstable		unstable	1.96	1.99	2.17	3.44	3.14	3.24	2.84	2.94	2.99
$\tilde{\epsilon}_0^{single}$	(%)	8.25	4.50	4.25	47.30	47.30	47.35	47.30		4.45			2.30	

[1] SOC algorithm converged to the same solution as the AC-OPF or to another already AC feasible solution and does not require a feasibility recovery.

[2] The solutions from the OPF approximations were used to initialize an AC power flow for determining their feasibility.

Table 5.2: DD-SC-CC-DC-OPF results using a decision tree derived from DC power flows.

DD-SC-CC-DC-OPF								
Cost (€)	Time (s)	ζ^{min} (%)	$\tilde{\epsilon}_J$ (%)	$\tilde{\epsilon}_J^{stat}$ (%)	$\tilde{\epsilon}_J^{dyn}$ (%)	$\tilde{\zeta}^{min}$ (%)	$\tilde{\zeta}_{p5}^{min}$ (%)	$\tilde{\epsilon}_0^{single}$ (%)
3034	0.74	4.00	4.05	2.30	4.05	1.84	3.06	2.30

operating region. Despite slightly violating the dynamic security requirements by 1 sample out of 2000 (i.e., 0.05%), the DD-SC-CC-OPF using AC power flows still provides a more accurate representation of the target operating region. Its solution is closer to the true boundary of the target operating region than the solution of the DA-SC-CC-OPF. Additionally, the target operating region was constructed offline using a different and smaller test sample of ξ compared to the test set used for the Monte Carlo simulations to evaluate the OPF results. As such, errors naturally occur due to the discrepancies in the uncertainty representation. In this respect, analytical reformulations accounting for a continuous uncertainty range tend to be more robust than sample based reformulations, which are more sensitive to the choice of the test samples, if those deviate to a large extent from the initial set used for the reformulation.

Another indicator for the dynamic security performance is the 5th percentile of the minimum damping ratio observed in the test set, $\tilde{\zeta}_{p5}^{min}$, which can be regarded as more significant since it also indicates the magnitude of the constraint violation. The results for $\tilde{\zeta}_{p5}^{min}$ are listed in Table 5.1 and visualized in Fig. 5.6. An operating point is located in the target operating region if it satisfies the static security requirements and $\tilde{\zeta}_{p5}^{min}$ is above 3%. The results of $\tilde{\zeta}_{p5}^{min}$ for the DD-SC-CC-AC-OPF reveal that the security performance is actually quite accurate with a $\tilde{\zeta}_{p5}^{min}$ of 2.99%. Thus, the 0.05% violation of the maximum allowable threshold is most likely just a consequence of numerical inaccuracies.

Nevertheless, the sensitivity of any machine learning approach to its underlying training set and the feature selection is exemplified by the DD-SC-CC-OPF results based on a DC or SOC representation of the power flow equations. The DT for the target operating region was derived using results
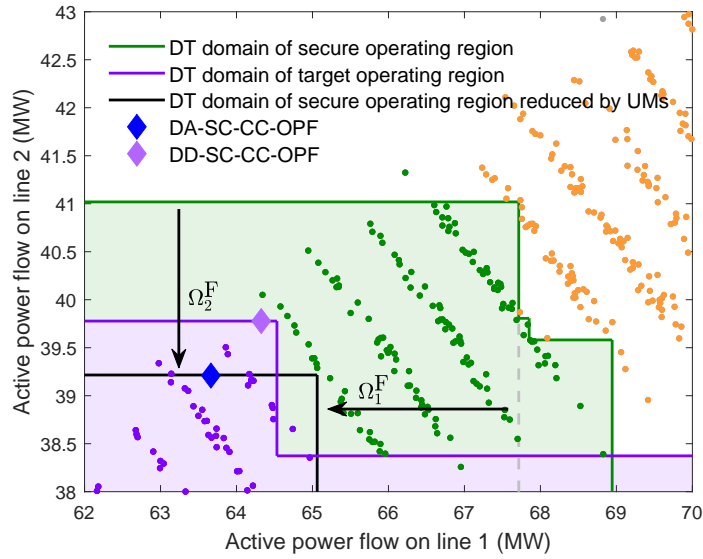
Figure 5.5: Comparison of the DA-SC-CC-OPF and DD-SC-CC-OPF using an AC power flow model. The graph contrasts the reduction of the secure operating region using uncertainty margins (i.e., analytical reformulations) against the domain covered by the decision tree for the target operating region (i.e., purely data-driven SC-CC-OPF).

from AC power analyses. While this was also the case in the DA-SC-CC-OPF, the analytical reformulations remedy the potential error of translating the security requirements to another power flow modeling framework. However, in the DD-SC-CC-OPF this is no longer the case and neither approximation meets the required confidence level. The more simplified the problem approximation, the larger its violation of the security requirements is, peaking under the DC formulation with a joint violation probability $\tilde{\epsilon}_J$ of 8.50%. This consequence was entirely prevented with a DT tailored to the DC power flows as indicated by the results listed in Table 5.2. As in Chapter 3, we first projected the power flows of the operating points in the target operating region to the lower dimensional DC space through DC power flow analyses. The DT was then derived based on the DC power flows instead of the original AC power flows leading to all security criteria being met at a lower cost than the DA-SC-CC-DC-OPF. In fact, the cost of DD-SC-CC-DC-OPF with $3034 \text{\euro}$ comes very close to the nonlinear AC solution with $3032 \text{\euro}$. The results confirm that a DC-OPF framework can achieve exceptionally good solutions and that a data-driven approach can provide very accurate approximations of the originally nonconvex feasible space.

Another benefit of the purely data-driven approach for the AC- and SOC-OPFs is its reduced computational cost. The DA-SC-CC-OPF for the AC- and SOC power flows requires an iterative procedure to derive the uncertainty margins, which usually converges very quickly but still requires at least four iterations for even the simplest cases with the constant risk of not converging at all [99]. Preventive measures to alleviate the risk of nonconvergence can be taken. Relying on convex problem formulations (e.g., SOC-OPF) provides increased robustness for the solution procedure of the OPF solved at each iteration. A branching algorithm as described in Section 4.2.10 can help avoid cycling behavior and the problem of constantly changing integer solutions and thus, constantly changing uncertainty margins between iterations. Alternatively, DTs with a manageable number of branches allow to leverage the structure of the disjunctive constraints by relaxing the
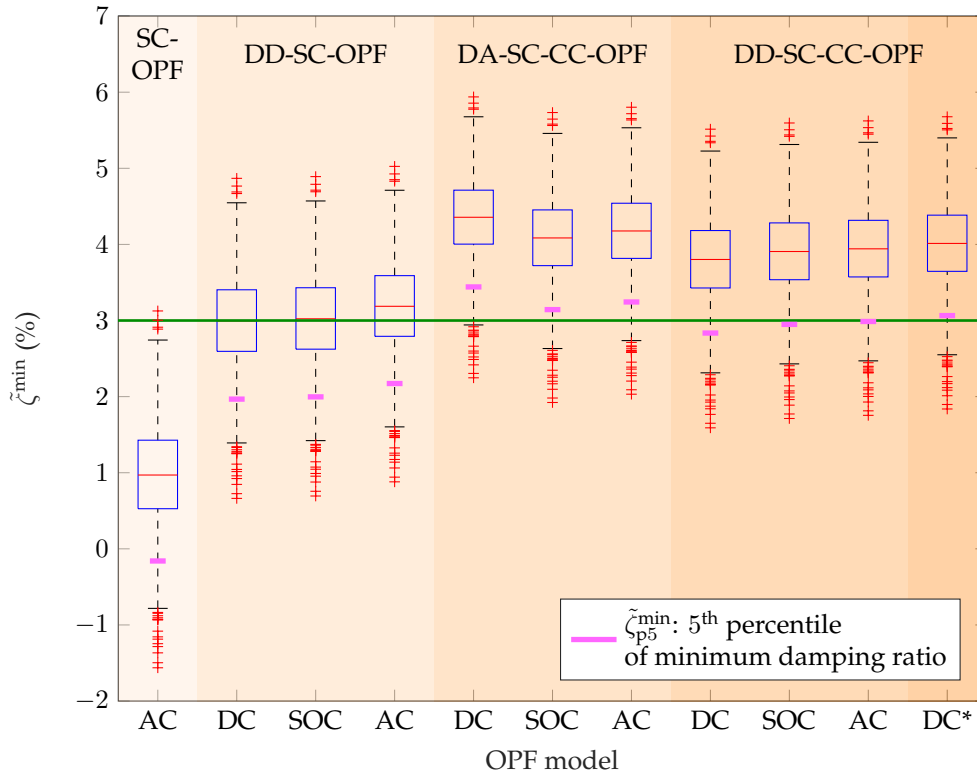
Figure 5.6: Distribution of minimum damping ratios for different OPF models obtained from Monte Carlo simulations. In addition to satisfying the static security requirements, the 5th percentile of all observations needs to be above the minimum required 3% damping ratio for an operating point to be located in the target operating region. "DC*" indicates the results of the DD-SC-CC-DC-OPF using a decision tree derived from DC power flows, as opposed to the remaining DD-SC-CC-OPFs based on AC power flows.

integrality and solving the problem for each binary solution (i.e., for each DT path) in parallel. Nevertheless, the computational complexity for the optimization remains higher compared to the purely data-driven approach. Furthermore, depending on the structure of the security region and the "degree" of its nonconvexity, it might happen that many smaller subregions with tighter DT limits are necessary to approximate it. They might not be able to accommodate the uncertainty margins, in which case the DA-SC-CC-OPF would result in infeasibility.

Fig. 5.7 depicts the minimum damping ratio of the OPF solutions in the discretized feasible space of the AC-OPF as a function of their total generation cost. It can be seen that all locally optimal OPF solutions are located along the outer left edge, where the generation cost is indeed the lowest for the corresponding ζ^{min}. Considering the relatively fine discretization interval of $1\,\mathrm{MW}$, we might be able to deduce that the locally optimal solutions are globally optimal for their specific problem formulation or at least very close to it. Note that the DC- and SOC-OPFs used in this work are approximations and not relaxations of the original problem. Therefore, they do not provide any information on the global optimality of the original problem.

The importance of providing a good loss estimate to any DC power flow based model is highlighted in Table 5.3. While all the OPFs listed perform reasonably well for their intended use when using a loss augmentation (i.e., results in Table 5.1), their performance deteriorates sharply without it. Particularly in case of the chance-constrained DC-OPF the maximum violation probability of
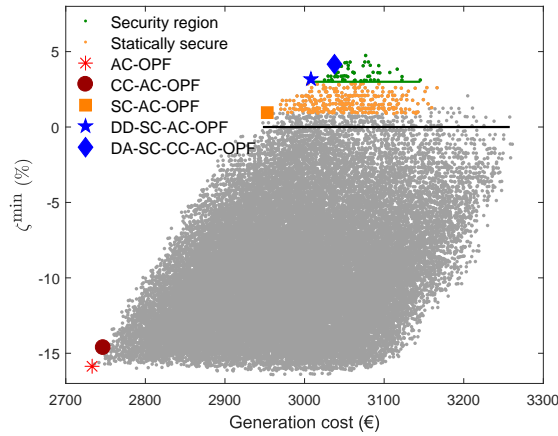
Figure 5.7: Minimum damping ratio $\zeta^{\min}$ vs. generation cost.

Table 5.3: DC results without loss estimates. Instances in bold mark the results of the target metrics, which the respective OPF aims at but fails to maintain when projected back into the AC space.

		CC-DC-OPF	DD-SC-DC-OPF	DA-SC-CC-DC-OPF
$\tilde{\epsilon}_J$	(%)	100	89.70	**13.20**
$\zeta^{\min}$	(%)	unstable	**2.18**	3.65
$\tilde{\epsilon}_0^{\text{single}}$	(%)	**98.90**	47.30	4.45

individual constraints, which it aims at reducing, increases from 8.25% to 98.90%. This again indicates that the full linearization of both the power flow equations and the uncertainty impact provides exceptionally good solutions in view of its simplicity and reduced dimensionality. Its performance, however, highly depends on an a priori estimate of the eventual operating region, which has a direct impact on the solution quality.

5.4   Summary

In this chapter, we proposed a general definition on the target operating region of power systems for an optimization environment. Our framework unifies static and dynamic security as well as uncertainty. It accommodates various formulations of the power flow equations and allows to fully exploit the robustness and efficiency of solvers for linear and convex programming. We formulate the problem as a security- and chance-constrained optimal power flow (SC-CC-OPF) and propose two tractable approximations. The first relies on a purely data-driven approach, which constructs the target operating region a priori, and subsequently incorporates it directly in the OPF. The security and uncertainty assessments are completely carried out offline, significantly reducing the burden on the optimization. The second uses a combination of data-driven techniques for the static and dynamic security regions and analytical chance constraint reformulations to approximate the target operating region. Even though the uncertainty assessment is performed online, the analytical reformulation maintains computational efficiency. Additionally, the online uncertainty assessment gives decision-makers the freedom to incorporate their proprietary uncertainty estimates, potentially improving the uncertainty modeling. Both methods combine machine learning, integer programming and disjunctive constraints to make the entire nonconvex target operating region tractable in the optimization and adaptable to any power flow environment.

We have shown that even the fully linearized SC-CC-DC-OPF can provide exceptionally good solutions, which meet the target metrics and come very close to the nonlinear SC-CC-AC-OPF solution. The results indicate that for practical purposes and when using data-driven techniques we can entirely avoid the nonlinear AC power flow equations in the OPF and the challenges related to their solvability. At the same time, we still preserve their benefits of having access to the entire solution space. However, the accuracy of any DC-OPF is highly dependent on an estimation of the losses. To address this issue, machine learning approaches can be easily augmented to provide loss estimates unique to each partition in the nonconvex space they create.

Through this work, we address the challenge of giving decision-makers access to the entire permissible decision space, improving decision-making processes in electricity markets and power system operations. We eliminate the dependency on system operators' estimates of the eventual market outcome and future system conditions, which determine the bounds on the decision space today. They are often perceived as overly restrictive and intransparent. Using a data-driven approach, we reduce the intervention of system operators in deriving those bounds, which can increase transparency of and trust in the derivation procedures. As such, data analytics and machine learning do not only provide tractability of complex problems but also benefits beyond their technical aspects, which further consolidates the role of data in power system optimization.

Out methods have proven to be accurate and efficient from an optimization perspective but several major challenges remain. The most challenging question concerns scalability related to the database generation and the definition of the target operating region itself. Theoretically, it would be possible to extend the database to any other security criteria including transient stability. This, however, would require extensive time-domain simulations of all operating points to identify if the transition from their pre- to any post-contingency state is secure. Furthermore, we have shown that the preventive security framework is overly conservative, severely limiting the allowable operating region of all generators. Enlarging the target operating region by incorporating corrective control is indispensable for an efficient system operation. How to accommodate the vast dimensionality of possible corrective control actions is a major challenge, which could also be addressed through sophisticated machine learning algorithms.

Enlarging the confidence region: A chance-constrained AC-OPF integrating corrective control

*The integration of large-scale renewable generation has major implications on the operation of power systems. Higher degrees of uncertainty due to forecast errors and frequent deviations from the expected system conditions entail that secure operation cannot always be maintained without resorting to corrective adjustments in real-time. Flexible system components, such as high voltage direct current (HVDC) transmission lines, provide increased controllability and are able to quickly react to changes in the operating conditions. In order to integrate the operation of HVDC lines in a cost-optimal and secure way, their corrective control strategies need to be accounted for in the OPF. In [**Paper E**], we formulate the first chance-constrained AC-OPF including HVDC lines and their corrective control capabilities in response to wind forecast errors. Both generator and HVDC control policies are optimized, leading to a significant reduction in cost.*

6.1 Introduction

Increasing shares of only partially predictable renewable energy generation and stochastic loads can lead to additional costs and jeopardize system security if uncertainty is not explicitly considered and addressed. In order to deal with uncertainty, operators carry out both preventive and corrective control actions in their systems [117]. The previous chapters have focused on preventive control for dealing with security and uncertainty. However, as already pointed out in Section 5.3.1, the prevailing preventive control paradigm is overly conservative and expensive. Remedial or corrective control actions, performed after an event has occurred, can substantially reduce operational costs and are in fact becoming inevitable as the degree of uncertainty in power system operations increases. More frequent deviations from the expected operating conditions have indeed led to an increased deployment of corrective control measures [4]. In practice, they are often based on haphazard and suboptimal ad-hoc decisions, such as expensive generation redispatch, which in some countries has incurred substantial costs [1, 2]. However, other more flexible system components, such as high-voltage direct current (HVDC) transmission lines or phase-shifting transformers, introduce additional degrees of freedom and can quickly react to changes in system conditions. They allow to selectively control power flows in real-time, which can reduce grid congestions. Corrective control actions in the form of power flow control have proven to substantially reduce the cost associated with an uncertain system operation if they are adequately planned and accounted for in operational tools [19].

In this regard, HVDC lines have gained increased attention. They incur very low losses and have, therefore, become the preferred technology for transmitting large amounts of renewable energy

over long distances, from remote generation locations (e.g., offshore) to load centers. Furthermore, HVDC lines offer remedial actions in the form of both active and reactive power flow control. In order to fully exploit their flexibility to quickly react to system changes and ensure that their corrective control will be sufficient in real-time, both the corrective control capabilities of HVDC lines and uncertainty need to be explicitly accounted for in optimal power flow (OPF) algorithms [19].

Previous work has already dealt with the incorporation of uncertainty and HVDC in a single optimization problem. For example, Refs. [19, 118–120] consider stochastic formulations incorporating HVDC lines and HVDC grids. However, they are all based on a simplified DC-OPF formulation. HVDC converters do not only offer corrective control for active power, but also reactive power, which enables them to assist in voltage support. In order to fully exploit the capabilities of HVDC lines, more accurate modeling environments accounting for reactive power and voltages are required.

The focus of this work is to avoid most of the simplifications used in previous work to the extent possible. To this end, we use the full AC power flow equations, as the DC-OPF can lead to substantial errors [33]. The AC-OPF formulation allows to fully utilize all corrective control capabilities of HVDC converters, including both active and reactive power control. In this work, we propose an iterative chance-constrained AC-OPF for AC grids with HVDC lines, based on the work from [59, 98]. The main contributions of our work are:

1. We integrate an HVDC line model and HVDC corrective control policies in a chance-constrained AC-OPF framework considering uncertainty in wind power.

2. We enable optimization of both generator and HVDC participation factors to react to forecast errors within a computationally efficient iterative solution algorithm.

3. Using realistic wind forecast data and Monte Carlo analyses, for a 10 and 39 bus system with HVDC lines and wind farms, we show that (i) not considering uncertainty leads to high constraint violation probabilities whereas our proposed approach achieves compliance with the target chance constraint violation probabilities and (ii) optimizing both generator and HVDC participation factors reduces the cost of uncertainty significantly.

6.2   Optimal power flow formulation

This section states the chance-constrained AC-OPF and presents a tractable reformulation of the chance constraints based on the work from [98] and [59]. The main characteristics of the chance-constrained AC-OPF were already thoroughly discussed in Chapter 4. Its key features are outlined below for completion followed by an extension for including HVDC lines and HVDC corrective control capabilities.

6.2.1   Chance-constrained AC optimal power flow

As in the previous chapters, we consider a power network that consists of a set of buses $\mathcal{N}$ and transmission lines $\mathcal{L}$. Each line $l \in \mathcal{L}$ is associated with a tuple (i, j) defining its sending and receiving node. The subset of nodes which have conventional generators connected to them is denoted with $\mathcal{G}$. $\mathcal{W}$ represents the set of nodes with uncertain wind power production.

The chance-constrained AC-OPF aims at determining the least-cost operating point which reduces the probability of violating the limits of system components to an acceptable level ϵ for a range of uncertainty realizations. Consequently, the AC-OPF variables $\mathbf{x} := \{\mathbf{P}, \mathbf{Q}, \mathbf{V}, \theta\}$ are not only subject to one possible set of realizations of the uncertain parameters but also depend on their forecast errors $\boldsymbol{\xi}$. $\mathbf{P}$, $\mathbf{Q}$, $\mathbf{V}$ and $\boldsymbol{\theta}$ denote vectors of nodal active and reactive power injections as well as nodal voltage magnitudes and angles, respectively. We assume wind power forecast errors $\boldsymbol{\xi}$ to be the the only source of uncertainty and to follow a multivariate Gaussian distribution with zero mean and known covariance. As explained in Section 4.2.1, we can model the actual wind power realization $\tilde{\mathbf{P}}_W$ as the sum of its expected value $\mathbf{P}_W$ and the forecast error $\boldsymbol{\xi}$,

$$\tilde{P}_{W_i} = P_{W_i} + \xi_i, \quad \forall i \in \mathcal{W}. \tag{6.1}$$

Note that our framework readily extends to consider other sources of uncertainty in power injections, e.g. of loads. We assume that wind power plants are operated with a constant power factor, which means that their reactive power output follows their active power output, i.e., $\tilde{Q}_{W_i} = \lambda(P_{W_i} + \xi_i)$, where the power ratio $\lambda = \sqrt{\frac{1-\cos^2\phi}{\cos^2\phi}}$ depends on the power factor $\cos\phi$ and can be a parameter or an optimization variable. The actual realizations of the OPF decision variables are modelled as the sum of their optimal setpoints at the forecasted wind infeed $\mathbf{x}$ and their reactions to a change in wind power injection $\boldsymbol{\Delta}\mathbf{x}(\boldsymbol{\xi})$, i.e., $\tilde{\mathbf{x}}(\boldsymbol{\xi}) = \mathbf{x} + \boldsymbol{\Delta}\mathbf{x}(\boldsymbol{\xi})$. This gives rise to the following formulation of the chance-constrained AC-OPF:

$$\min_{\mathbf{x}} \quad \frac{1}{2}\mathbf{P}_G^T\mathbf{C}_2\mathbf{P}_G + \mathbf{c}_1^T\mathbf{P}_G \tag{6.2}$$

$$\text{s.t.} \quad \mathbf{f}_i(\mathbf{x}) = 0, \qquad\qquad\qquad\qquad \forall i \in \mathcal{N}, \tag{6.3}$$

$$\mathbb{P}(P_{G_i} + \Delta P_{G_i}(\boldsymbol{\xi}) \leq P_{G_i}^{\max}) \geq 1 - \epsilon, \quad \forall i \in \mathcal{G}, \tag{6.4}$$

$$\mathbb{P}(P_{G_i}^{\min} \leq P_{G_i} + \Delta P_{G_i}(\boldsymbol{\xi})) \geq 1 - \epsilon, \quad \forall i \in \mathcal{G}, \tag{6.5}$$

$$\mathbb{P}(Q_{G_i} + \Delta Q_{G_i}(\boldsymbol{\xi}) \leq Q_{G_i}^{\max}) \geq 1 - \epsilon, \quad \forall i \in \mathcal{G}, \tag{6.6}$$

$$\mathbb{P}(Q_{G_i}^{\min} \leq Q_{G_i} + \Delta Q_{G_i}(\boldsymbol{\xi})) \geq 1 - \epsilon, \quad \forall i \in \mathcal{G}, \tag{6.7}$$

$$\mathbb{P}(V_i + \Delta V_i(\boldsymbol{\xi}) \leq V_i^{\max}) \geq 1 - \epsilon, \qquad \forall i \in \mathcal{N}, \tag{6.8}$$

$$\mathbb{P}(V_i^{\min} \leq V_i + \Delta V_i(\boldsymbol{\xi})) \geq 1 - \epsilon, \qquad \forall i \in \mathcal{N}, \tag{6.9}$$

$$\mathbb{P}(P_{ij} + \Delta P_{ij}(\boldsymbol{\xi}) \leq P_{ij}^{\max}) \geq 1 - \epsilon, \quad \forall (i,j) \in \mathcal{L}, \tag{6.10}$$

$$\mathbb{P}(P_{ij}^{\min} \leq P_{ij} + \Delta P_{ij}(\boldsymbol{\xi})) \geq 1 - \epsilon, \quad \forall (i,j) \in \mathcal{L}. \tag{6.11}$$

The chance-constrained AC-OPF (6.2) – (6.11) minimizes the total generation cost for the forecasted operating point. The terms $\mathbf{P}_G$ and $\mathbf{Q}_G$ denote active and reactive power dispatch of the generators. Linear cost factors are represented by $\mathbf{c}_1$, whereas $\mathbf{C}_2$ denotes the diagonal matrix capturing the quadratic cost coefficients. Active power line flows from node i to node j are denoted with $P_{ij} \in \mathbf{P_{ij}}$. Constraint (6.3) enforces active and reactive power balance for the forecasted operating point at each node in $\mathcal{N}$. Note that we do not explicitly enforce the power balance for $\boldsymbol{\xi} \neq \mathbf{0}$. Instead, as will be outlined in the following, our formulation ensures satisfaction of the linearized AC power flow equations around the forecasted operating point, which in combination with the chosen control policies has shown to perform well on the nonlinear system for reasonable levels of uncertainty [59]. The inequality constraints in (6.4) – (6.11) include upper and lower limits on active and reactive power generation, voltage magnitudes, as well as active power flows. They are formulated as individual chance constraints, enforced with a confidence level of $(1 - \epsilon)$. The chance constraints account for the entire range of $\boldsymbol{\xi}$. They can be analytically reformulated to tractable deterministic constraints, as discussed in Section 4.2.5 and briefly outlined in Section 6.2.1.

Affine policies

We model the control policies as affine functions of the uncertainty $\boldsymbol{\xi}$. Conventional generators are assumed to balance the total wind power deviation $\Xi = \sum_{i\in\mathcal{W}} \xi_i$ according to their generator participation factors $\boldsymbol{\gamma}$

$$\tilde{P}_{\mathrm{G}_i}(\boldsymbol{\xi}) = P_{\mathrm{G}_i} + \Delta P_{\mathrm{G}_i}(\boldsymbol{\xi}) = P_{\mathrm{G}_i} - \gamma_i \Xi + \Delta P_{\mathrm{U}_i}(\boldsymbol{\xi}), \tag{6.12}$$

where the term $\boldsymbol{\Delta P}_{\mathrm{U}}$ denotes the contribution to the compensation of the unknown changes in active power losses. This generator response mimics the automatic generation control (AGC) commonly used in power system operation. The generator participation factors $\boldsymbol{\gamma}$ are thus defined w.r.t. to the total wind deviation Ξ and can be either pre-determined (e.g., as a result of a reserve procurement) or optimized within the OPF. The condition $\sum_{i\in\mathcal{G}} \gamma_i = 1$ ensures balance of the total power mismatch, i.e., $\sum_{i\in\mathcal{G}} \gamma_i \sum_{j\in\mathcal{W}} \xi_j = \Xi$. Active power losses vary nonlinearly with the wind power deviation and are usually compensated by the generator at the reference bus; this results in the loss term $\boldsymbol{\Delta P}_{\mathrm{U}}$ being equal to zero for generators at PV and PQ buses. All other variables of interest $\boldsymbol{\Delta x}(\boldsymbol{\xi}) := \{\boldsymbol{\Delta Q}_{\mathrm{G}}, \boldsymbol{\Delta V}, \boldsymbol{\Delta \theta}, \boldsymbol{\Delta P_{ij}}\}$ are modeled similarly,

$$\tilde{x}_i(\boldsymbol{\xi}) = x_i + \boldsymbol{\Upsilon}^{x_i}\boldsymbol{\xi}, \tag{6.13}$$

where $\boldsymbol{\Upsilon}^{x_i}$ is a $(1 \times |\mathcal{W}|)$ vector defining the response of variable x_i to each wind power deviation. As in Chapter 4, the response is modeled as $\boldsymbol{\Delta x}(\boldsymbol{\xi}) = \frac{\partial \mathbf{x}}{\partial \boldsymbol{\xi}}\boldsymbol{\xi} = \boldsymbol{\Upsilon}\boldsymbol{\xi}$, where $\boldsymbol{\Upsilon}$ represents a matrix of linear sensitivities w.r.t. $\boldsymbol{\xi}$. The term $\boldsymbol{\Upsilon}$ also includes an expression for the unknown changes in active power losses ΔP_{U}, compensated by the reference generator, and is derived from the first order Taylor expansion of the AC power flow equations around the optimal forecasted operating point $\mathbf{x}^*$,

$$\begin{bmatrix} \boldsymbol{\Delta P} \\ \boldsymbol{\Delta Q} \end{bmatrix} = \mathbf{J}\Big|_{\mathbf{x}^*} \begin{bmatrix} \boldsymbol{\Delta \theta} \\ \boldsymbol{\Delta V} \end{bmatrix}. \tag{6.14}$$

The term $\mathbf{J}$ denotes the Jacobian matrix. The left-hand side of (6.14) can also be expressed in terms of the wind deviation $\boldsymbol{\xi}$, the power ratio $\boldsymbol{\lambda}$, the generator participation factors $\boldsymbol{\gamma}$ as well as the unknown nonlinear changes in active and reactive power (i.e., $\boldsymbol{\Delta P}_{\mathrm{U}}, \boldsymbol{\Delta Q}$),

$$\begin{bmatrix} \mathbf{I} \\ \mathrm{diag}(\boldsymbol{\lambda}) \end{bmatrix}\boldsymbol{\xi} + \begin{bmatrix} -\boldsymbol{\gamma}\mathbf{H} \\ \mathbf{0} \end{bmatrix}\boldsymbol{\xi} + \begin{bmatrix} \boldsymbol{\Delta P}_{\mathrm{U}} \\ \boldsymbol{\Delta Q} \end{bmatrix} = \boldsymbol{\Psi}\boldsymbol{\xi} + \begin{bmatrix} \boldsymbol{\Delta P}_{\mathrm{U}} \\ \boldsymbol{\Delta Q} \end{bmatrix}. \tag{6.15}$$

The terms $\mathbf{I}$, $\mathbf{H}$ and $\mathbf{0}$ denote $(|\mathcal{N}| \times |\mathcal{W}|)$ identity, all-ones and zero matrices, respectively. The matrix of generation distribution factors (GDF) $\boldsymbol{\Psi}$ depends linearly on $\boldsymbol{\gamma}$ and $\boldsymbol{\lambda}$ (for a detailed derivation refer to [16] or Appendix A based on the alternative power flow equations (2.10) – (2.13)). In accordance with common practices in power system operations, some variables are assumed not to change under different wind power realizations, such as the voltage magnitude at PV and reference buses, the voltage angle at the reference bus and the reactive power injection at PQ buses. We summarize the nonzero changes of unknown active and reactive power injections in $\boldsymbol{\Delta g} := [\Delta P_{\mathrm{U}_{\mathrm{ref}}} \ \Delta Q_{\mathrm{ref}} \ \boldsymbol{\Delta Q}_{\mathrm{PV}}^{\mathrm{T}}]^{\mathrm{T}}$. Analogously, $\boldsymbol{\Delta \hat{x}}$ denotes the nonzero changes in voltage magnitudes and angles, i.e., $\boldsymbol{\Delta \hat{x}} := [\boldsymbol{\Delta \theta}_{\mathrm{PV}}^{\mathrm{T}} \ \boldsymbol{\Delta \theta}_{\mathrm{PQ}}^{\mathrm{T}} \ \boldsymbol{\Delta V}_{\mathrm{PQ}}^{\mathrm{T}}]^{\mathrm{T}}$. Replacing the left-hand side in (6.14) with (6.15) and rearranging the resulting system of equations according to the groups of zero and nonzero elements, i.e.,

$$\begin{bmatrix} \boldsymbol{\Delta g} \\ \mathbf{0} \end{bmatrix} = \begin{bmatrix} \mathbf{J}_{\mathrm{mod}}^{\mathrm{I}} & \mathbf{J}_{\mathrm{mod}}^{\mathrm{II}} \\ \mathbf{J}_{\mathrm{mod}}^{\mathrm{III}} & \mathbf{J}_{\mathrm{mod}}^{\mathrm{IV}} \end{bmatrix} \begin{bmatrix} \mathbf{0} \\ \boldsymbol{\Delta \hat{x}} \end{bmatrix} - \begin{bmatrix} \boldsymbol{\Psi}_{\mathrm{mod}}^{\mathrm{I}} \\ \boldsymbol{\Psi}_{\mathrm{mod}}^{\mathrm{II}} \end{bmatrix}\boldsymbol{\xi}, \tag{6.16}$$
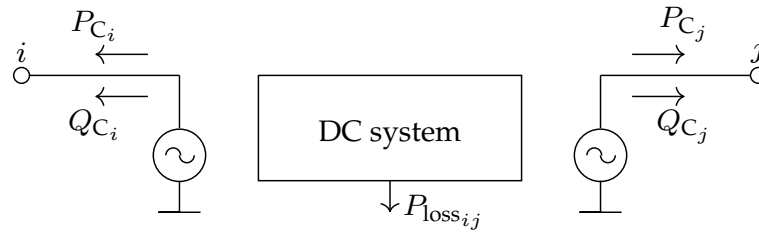
Figure 6.1: HVDC line model connecting AC bus i to AC bus j with active HVDC converter injections $\mathbf{P}_C$ and reactive HVDC converter injections $\mathbf{Q}_C$ at each bus. The loss term $P_{\text{loss}_{ij}}$ represents the lumped active power losses of the DC system.

allows us to derive expressions for the change in variables as a function of the uncertainty $\boldsymbol{\xi}$

$$\boldsymbol{\Delta}\hat{\mathbf{x}} = \left(\mathbf{J}_{\text{mod}}^{\text{IV}}\right)^{-1}\boldsymbol{\Psi}_{\text{mod}}^{\text{II}}\boldsymbol{\xi} = \boldsymbol{\Upsilon}_{\hat{\mathbf{x}}}\boldsymbol{\xi}, \tag{6.17}$$

$$\boldsymbol{\Delta}\mathbf{g} = \left(\mathbf{J}_{\text{mod}}^{\text{II}}(\mathbf{J}_{\text{mod}}^{\text{IV}})^{-1}\boldsymbol{\Psi}_{\text{mod}}^{\text{II}} - \boldsymbol{\Psi}_{\text{mod}}^{\text{I}}\right)\boldsymbol{\xi} = \boldsymbol{\Upsilon}_{\mathbf{g}}\boldsymbol{\xi}. \tag{6.18}$$

$\mathbf{J}_{\text{mod}}$ and $\boldsymbol{\Psi}_{\text{mod}}$ denote the modified Jacobian and GDF matrices, where the rows and columns have been rearranged according to $\boldsymbol{\Delta}\mathbf{g}$ and $\boldsymbol{\Delta}\hat{\mathbf{x}}$. Thus, the linear sensitivities $\boldsymbol{\Upsilon}$ depend on the GDF matrix $\boldsymbol{\Psi}$, which is a linear function of the generator participation factors $\boldsymbol{\gamma}$ and the power ratio $\boldsymbol{\lambda}$.

Reformulating the chance constraints

Given the linear dependency of the OPF variables on $\boldsymbol{\xi}$ in the region around the operating point and the assumption of a multivariate normal distribution for $\boldsymbol{\xi}$, we are able to reformulate the individual chance constraints (6.4)–(6.11) to tractable deterministic constraints. The linear chance constraint $\mathbb{P}(x_i + \boldsymbol{\Upsilon}^{x_i}(\boldsymbol{\Psi})\boldsymbol{\xi} \leq x_i^{\text{max}}) \geq 1 - \epsilon$ is reformulated to

$$x_i \leq x_i^{\text{max}} - \Phi^{-1}(1 - \epsilon)\sqrt{\boldsymbol{\Upsilon}^{x_i}\boldsymbol{\Sigma}(\boldsymbol{\Upsilon}^{x_i})^{\text{T}}}, \tag{6.19}$$

where Φ^{-1} denotes the inverse cumulative distribution function of the Gaussian distribution. It can be observed that the original constraint $x_i \leq x_i^{\text{max}}$ is tightened by an *uncertainty margin* $\Omega^{x_i} := \Phi^{-1}(1 - \epsilon)\sqrt{\boldsymbol{\Upsilon}^{x_i}\boldsymbol{\Sigma}(\boldsymbol{\Upsilon}^{x_i})^{\text{T}}}$, which secures the system against variations in wind infeed [98]. Given the dependency of $\boldsymbol{\Upsilon}$ on $\boldsymbol{\Psi}$, optimizing over the generation response $\boldsymbol{\gamma}$ explicitly represents its impact on the uncertainty margins of the remaining variables within the optimization.

6.3 HVDC line modeling

In this section, we present a model to include HVDC lines in the chance-constrained AC-OPF and to introduce HVDC participation factors to allow for corrective control.

We assume that the HVDC lines are modeled as presented in Fig. 6.1 with individual active and reactive power injections, $\mathbf{P}_C$ and $\mathbf{Q}_C$, at the two AC buses which the HVDC line connects. The loss term P_{loss} represents the aggregated losses of the whole DC system. Set $c \in \mathcal{C}$ denotes the set of converters. For each pair of HVDC converters comprising an HVDC line, the set $(i, j) \in \mathcal{L}_C$ denotes the AC buses which the two converters are connected to, respectively. Note that in the following, we use P_{C_c} to denote the active power setpoint of a converter, which is equivalent to its
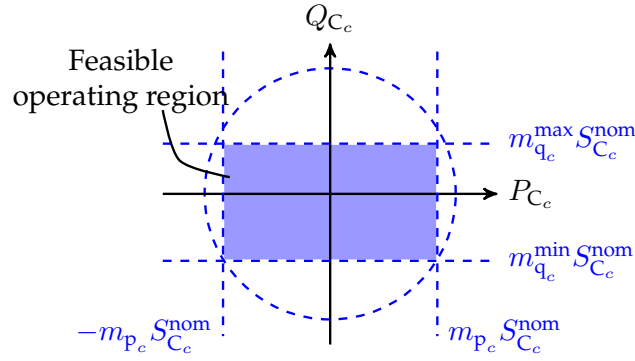
Figure 6.2: Active and reactive power capability curve of an HVDC converter c [121].

injection into the AC grid, i.e., $P_{C_c} = P_{C_i}$. We approximate the active and reactive power capability of the converter as a rectangular box with the following constraints

$$P_{C_c}^{\min} \leq P_{C_c} \leq P_{C_c}^{\max}, \quad \forall c \in \mathcal{C}, \tag{6.20}$$

$$Q_{C_c}^{\min} \leq Q_{C_c} \leq Q_{C_c}^{\max}, \quad \forall c \in \mathcal{C}. \tag{6.21}$$

Expressing the lower and upper active and reactive HVDC converter limits $\mathbf{P}_C^{\min}$, $\mathbf{P}_C^{\max}$, $\mathbf{Q}_C^{\min}$, $\mathbf{Q}_C^{\max}$ as a function of the nominal converter rated power $\mathbf{S}_C^{\mathrm{nom}}$ and assuming that the lower and upper bounds on active power are symmetric (i.e. $\mathbf{P}_C^{\min} = -\mathbf{P}_C^{\max}$) yields

$$-m_{P_c} S_{C_c}^{\mathrm{nom}} \leq P_{C_c} \leq m_{P_c} S_{C_c}^{\mathrm{nom}}, \quad \forall c \in \mathcal{C}, \tag{6.22}$$

$$m_{q_c}^{\min} S_{C_c}^{\mathrm{nom}} \leq Q_{C_c} \leq m_{q_c}^{\max} S_{C_c}^{\mathrm{nom}}, \quad \forall c \in \mathcal{C}. \tag{6.23}$$

The resulting feasible operating region is visualized in Fig. 6.2. For a more detailed modeling of the active and reactive power capability of HVDC converters the interested reader is referred to [122]. In order to link the active power injections at the two AC buses which the HVDC line connects, an active power balance constraint has to be included. To model the DC system losses $P_{\mathrm{loss}_{ij}}$, we use a constant loss term a defined as a share of the nominal apparent power rating of the converters. The active power balance constraint for each HVDC line $(i, j) \in \mathcal{L}_C$ is given by

$$P_{C_i} + P_{C_j} + P_{\mathrm{loss}_{ij}} = 0, \quad \text{with } P_{\mathrm{loss}_{ij}} = 2a S_{C_c}^{\mathrm{nom}}. \tag{6.24}$$

Note that we neglect the DC line losses. The reactive power injections at both AC buses $(i, j) \in \mathcal{L}_C$ can be chosen independently from each other within the HVDC converter limits. To allow for corrective control, we assign a participation factor β_c for each HVDC converter $c \in \mathcal{C}$ similar to the generator participation factors $\boldsymbol{\gamma}$. As the HVDC line itself cannot generate active power, the participation factor is positive at one end of the HVDC line and negative at the other end, i.e. $\beta_i = -\beta_j$ for buses $(i, j) \in \mathcal{L}_C$. This controllability can be used to e.g. reroute power to reduce congestion in case of forecast errors. The GDF matrix $\boldsymbol{\Psi}$ is modified as follows:

$$\boldsymbol{\Psi} = \begin{bmatrix} \mathbf{I} - (\boldsymbol{\gamma} + \boldsymbol{\beta})\mathbf{H} \\ \mathbf{diag}(\lambda) \end{bmatrix}. \tag{6.25}$$

In (6.25), $\boldsymbol{\beta}$ is a vector defined for all nodes $\mathcal{N}$. The HVDC participation factors are nonzero only for the converter connected AC buses and their signs depend on which end of the HVDC line they

are connected to. Similar to the engineering constraints of the AC grid, the converter limits need to be considered as chance constraints in order to ensure secure operation with sufficient probability throughout the uncertainty range, e.g.,

$$\mathbb{P}(-m_{\mathrm{p}_c} S_{\mathrm{C}_c}^{\mathrm{nom}} \leq P_{\mathrm{C}_c} + \beta_c \boldsymbol{\xi}) \geq 1 - \epsilon, \quad \forall c \in \mathcal{C}, \tag{6.26}$$

$$\mathbb{P}(m_{\mathrm{p}_c} S_{\mathrm{C}_c}^{\mathrm{nom}} \geq P_{\mathrm{C}_c} + \beta_c \boldsymbol{\xi}) \geq 1 - \epsilon, \quad \forall c \in \mathcal{C}. \tag{6.27}$$

These can be reformulated for each converter $c \in \mathcal{C}$:

$$-m_{\mathrm{p}_c} S_{\mathrm{C}_c}^{\mathrm{nom}} + \Phi^{-1}(1 - \epsilon)\sqrt{\beta_c \mathbf{1} \boldsymbol{\Sigma} \beta_c \mathbf{1}^{\mathrm{T}}} \leq P_{\mathrm{C}_c}, \tag{6.28}$$

$$m_{\mathrm{p}_c} S_{\mathrm{C}_c}^{\mathrm{nom}} - \Phi^{-1}(1 - \epsilon)\sqrt{\beta_c \mathbf{1} \boldsymbol{\Sigma} \beta_c \mathbf{1}^{\mathrm{T}}} \geq P_{\mathrm{C}_c}. \tag{6.29}$$

Note that the uncertainty margins $\Omega_c^{\mathbf{P_C}} = \Phi^{-1}(1 - \epsilon)\sqrt{\beta_c \mathbf{1} \boldsymbol{\Sigma} \beta_c \mathbf{1}^{\mathrm{T}}}$ introduced in (6.28) and (6.29) depend linearly on the HVDC participation factor β_c. The degree of controllability is determined by γ and β, both of which can be either pre-determined or optimized within the chance-constrained AC-OPF.

6.4 Iterative chance-constrained AC-OPF optimizing generator and HVDC control policies

The reformulated chance-constrained AC-OPF (6.30) – (6.34) considering HVDC lines extends the variable set $\mathbf{x} := \{\mathbf{P}, \mathbf{Q}, \mathbf{V}, \boldsymbol{\theta}\}$ to include the active and reactive power setpoints of the HVDC converters $\{\mathbf{P_C}, \mathbf{Q_C}\}$.

$$\min_{\mathbf{x}} \quad \frac{1}{2}\mathbf{P}_{\mathrm{G}}^{\mathrm{T}}\mathbf{C}_2\mathbf{P}_{\mathrm{G}} + \mathbf{c}_1^{\mathrm{T}}\mathbf{P}_{\mathrm{G}} \tag{6.30}$$

$$\text{s.t.} \quad \mathbf{f}^{\mathrm{ac}}(\mathbf{x}) = 0, \tag{6.31}$$

$$\mathbf{f}^{\mathrm{dc}}(\mathbf{P}_{\mathrm{C}}) = 0, \tag{6.32}$$

$$\mathbf{x} \leq \mathbf{x}^{\mathrm{max}} - \boldsymbol{\Omega}(\boldsymbol{\gamma}, \boldsymbol{\beta}), \tag{6.33}$$

$$\mathbf{x} \geq \mathbf{x}^{\mathrm{min}} + \boldsymbol{\Omega}(\boldsymbol{\gamma}, \boldsymbol{\beta}). \tag{6.34}$$

If the corrective control actions provided by conventional generators and HVDC lines are optimized within the same framework, then γ and β are added to the variable set $\mathbf{x}$ and the following additional equations are included

$$\beta_i = -\beta_j, \quad \forall (i, j) \in \mathcal{L}_C \tag{6.35}$$

$$\gamma_i \geq 0, \quad \forall i \in \mathcal{G} \tag{6.36}$$

$$\sum_{i \in \mathcal{G}} \gamma_i = 1. \tag{6.37}$$

Problem (6.30) – (6.34) introduces an additional power balance equation (6.32) for each HVDC line according to (6.24) considering the losses in the DC system. All inequality constraints are tightened with their corresponding uncertainty margins $\boldsymbol{\Omega}(\boldsymbol{\gamma}, \boldsymbol{\beta}) = [\boldsymbol{\Omega}^{\mathbf{P_G}}, \boldsymbol{\Omega}^{\mathbf{Q_G}}, \boldsymbol{\Omega}^{\mathbf{V}}, \boldsymbol{\Omega}^{\mathbf{P_{ij}}}, \boldsymbol{\Omega}^{\mathbf{P_C}}](\boldsymbol{\gamma}, \boldsymbol{\beta})$. The uncertainty margins do not only depend on the generator and HVDC participation factors but also on the Jacobian matrix of the AC power flow equations as can be observed in (6.17) and (6.18). Including the Jacobian terms as optimization variables would introduce even more nonlinearities in the AC-OPF and thus, substantially increase the complexity of the problem. To this end, the authors in [59] have introduced a computationally efficient iterative solution algorithm, which

decouples the uncertainty assessment (i.e., the derivation of the uncertainty margins) from the optimization.

To maintain computational efficiency, we extend the iterative framework of [59] and evaluate the Jacobian at each iteration for the current operating point. In [59], the uncertainty margins were constant and computed in an outer iteration. In our work, the sensitivity factors are constant, while γ and β are optimization variables, which allows us to optimize these at the expense of adding nonlinear (but convex) second order cone (SOC) terms. We define the steps in Algorithm 3, where subscript *opt* denotes the optimal solution of an OPF. The algorithm converges as the change in uncertainty margins between two consecutive iterations falls below a defined tolerance value ρ.

Algorithm 3 Iterative chance-constrained AC-OPF optimizing generator and HVDC corrective control policies

---

1: Set iteration count: $\nu \leftarrow 0$
2: initialize $\mathbf{\Omega}^{\nu=0} = \mathbf{0}$
3: **while** $||\mathbf{\Omega}^\nu - \mathbf{\Omega}^{\nu-1}||_\infty > \rho$ **do**
4:     **if** $\nu = 0$ **then**
5:         solve (6.30) – (6.34) for $\mathbf{x} \setminus \{\gamma, \beta\}$ and obtain $\mathbf{x}_{\text{opt}}^{\nu=0}$
6:         evaluate Jacobian at $\mathbf{x}_{\text{opt}}^{\nu=0}$
7:     **else**
8:         include $\mathbf{\Omega}^\nu(\gamma^\nu, \beta^\nu)$ according to (6.33) and (6.34)
9:         solve (6.30) – (6.34), (6.35) – (6.37) to obtain $\mathbf{x}_{\text{opt}}^\nu$
10:        evaluate Jacobian, $\mathbf{\Upsilon}_{\text{opt}}^\nu$ and $\mathbf{\Omega}_{\text{opt}}^\nu$ at $\mathbf{x}_{\text{opt}}^\nu$, γ_{opt}^ν and β_{opt}^ν
11:     **end if**
12:     derive expressions for $\mathbf{\Upsilon}^{\nu+1}$ and $\mathbf{\Omega}^{\nu+1}$ as functions of the optimization variables $\gamma^{\nu+1}$ and $\beta^{\nu+1}$
13:     $\nu \leftarrow \nu + 1$
14: **end while**.

6.5 Case study

We first test the proposed method on a 10 bus system. In the first part, we show the benefit of optimizing the generator participation factors for the proposed iterative chance-constrained AC-OPF. In the second part, we include an HVDC line to relieve congestion in the AC system and investigate the impact of optimizing both the generator and HVDC control policies on the total system cost and the convergence behaviour of the iterative solution algorithm. In the third part, we consider a 39 bus system and evaluate the benefit of controllability.

6.5.1 Simulation setup

To evaluate the performance of the proposed approaches we use two metrics. First, we compute the cost of uncertainty, which reflects the increase in generation cost as a result of including chance constraints, i.e. the difference in objective function value between an AC-OPF without considering uncertainty and a chance-constrained AC-OPF. Second, we perform an in- and out-of-sample analysis to compute the empirical individual chance constraint violation probability. They are based on Monte Carlo simulations of AC power flows performed with MATPOWER [88]. For the in-sample analysis we draw 10 000 samples from a Gaussian distribution, while for the out-of-sample analysis we use 10 000 samples from realistic forecast data. For the Monte Carlo analysis we assume a minimum violation limit of 0.1% to exclude numerical errors. Note that for each type
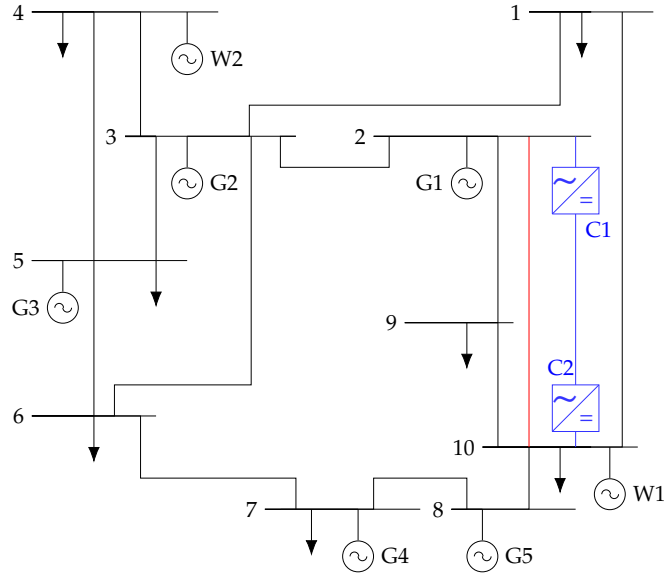
Figure 6.3: 10 bus system with two wind farms located at buses 4 and 10. An HVDC line (marked in blue) replaces the congested AC line (marked in red) between buses 2 and 10.

of individual chance constraint, we report the maximum observed empirical violation probability. The maximum allowable constraint violation limit is set to $\epsilon = 5\%$. We consider a convergence criterion of $\rho = 10^{-5}$. All simulations are carried out on a laptop with processor Intel(R) Core(TM) i7-7820HQ CPU @ 2.90 Ghz and 32GB RAM. The optimization problems are implemented with YALMIP [114] in MATLAB and are solved with IPOPT [123]. The wind farm power factor λ is set to 1.

The considered 10 bus system is shown in Fig. 6.3. The grid parameters are provided in [124]. The generator at bus 3 is selected to be the slack bus. Upper and lower voltage limits are set to 1.1 p.u. and 0.9 p.u., respectively. Since we consider active power flow limits on transmission lines, we set the maximum active power flow limit to 80% of the apparent power flow limit. In this system configuration, the power flows primarily from the upper left to the main load units at buses 7 to 10. This leads to a congestion of the transmission line connecting buses 2 and 10. Two wind farms are located at buses 10 and 4 with a maximum power of 1.0 GW and of 2.5 GW, respectively. To compute the covariance matrix Σ of the forecast errors, we use realistic day-ahead wind forecast scenarios from [125]. The forecasts are based on wind power measurements in the Western Denmark area from 15 different control zones collected by the Danish transmission system operator Energinet. We select control zone 7 and 9 at time step 4 to correspond to the wind farms at bus 2 and 10, respectively. In order to construct the covariance matrix we draw 100 random samples from this data. The forecasted wind infeed is computed as the mean of these 100 samples.

6.5.2 Optimization of generator participation factors

In this section, for a 10 bus test case, we demonstrate the benefit in terms of generation cost of optimizing the generator participation factors γ instead of assigning pre-determined participation factors as done in previous chapters. The fixed participation factors are $\gamma = [0.2\,0.2\,0.2\,0.2\,0.2]$, i.e. each generator equally compensates the deviation in wind power. We compare the performance

Table 6.1: Empirical constraint violation probability for the 10 bus test case without an HVDC line.

Constraint limits on	$\mathbf{P_G}$	$\mathbf{Q_G}$	$\mathbf{V}$	$\mathbf{P_{ij}}$
In-sample analysis with $10\,000$ samples (%)				
AC-OPF (w/o uncertainty)	49.0	0.0	6.7	49.7
CC-AC-OPF (fixed γ)	5.3	0.0	2.8	5.3
CC-AC-OPF (opt. γ)	4.9	0.0	2.9	4.9
Out-of-sample analysis with $10\,000$ samples (%)				
AC-OPF (w/o uncertainty)	43.2	0.0	4.6	49.2
CC-AC-OPF (fixed γ)	5.8	0.0	3.4	6.1
CC-AC-OPF (opt. γ)	5.8	0.0	3.4	5.6

of an AC-OPF without considering uncertainty to the iterative chance-constrained AC-OPF (CC-AC-OPF) with both fixed and optimized generator participation factors. For the 10 bus test case, the cost of uncertainty evaluates to 2.03% with fixed participation factors. This can be reduced to 0.39% by optimizing the participation factors. The number of iterations for fixed γ is 5 and for variable γ 6. The average solving time for the AC-OPF iteration is 0.4 seconds for fixed γ and 0.9 seconds for optimizing γ since the computational complexity is increased by including γ as optimization variables in the uncertainty margins (6.33)–(6.34).

The results of the Monte Carlo analysis for in- and out-of-sample testing are shown in Table 6.1. In both the in- and out-of-sample analyses the AC-OPF without considering uncertainty leads to large empirical violation probabilities for the active power generation limits and the active power line flow limits as the generation response to the wind power deviations is not considered. Voltage violations are observed as well. The proposed iterative chance-constrained AC-OPF with fixed and optimized generator participation factors reduces the empirical violation probability both in- and out-of-sample very close to the desired 5%. The remaining minor mismatch can be attributed to either a wrong estimation of the mean and covariance in the out-of-sample analysis or to the approximation we make by using the first-order Taylor expansion to linearize the system behaviour around the forecasted operating point. Note that the forecast errors drawn from the realistic forecast data are not Gaussian distributed and the observed violations out-of-sample can therefore be larger. However, we observe that they are still close to the desired 5% indicating good performance of the proposed algorithm.

If we optimize the generator participation factors, we obtain $\gamma^{\mathrm{opt}} = [0.0\ 0.30\ 0.57\ 0.0\ 0.13]$. In Fig. 6.4 we compare the generation dispatch and the uncertainty margins for the three formulations. We can observe that by optimizing the participation factors the generator response is shifted to the generators G2, G3 and G5 with mainly generator G3 compensating the wind power mismatch. The cheap generators G1 and G4 operate at their maximum power output for the forecasted system operating state. This significantly reduces the cost of uncertainty from 2.03% to 0.39%.

6.5.3 Including HVDC line and HVDC control policies

We replace the AC line between buses 2 and 10 in Fig.6.3 with an HVDC line of $S_C^{\mathrm{nom}} = 4\,\mathrm{GVA}$, and investigate the relief of congestion and the decrease of the cost of uncertainty. We assume the converters are of the multi-modular converter (MMC) technology and that the total losses per converter station are approximately $a = 1\%$ per HVDC converter according to [126]. The active
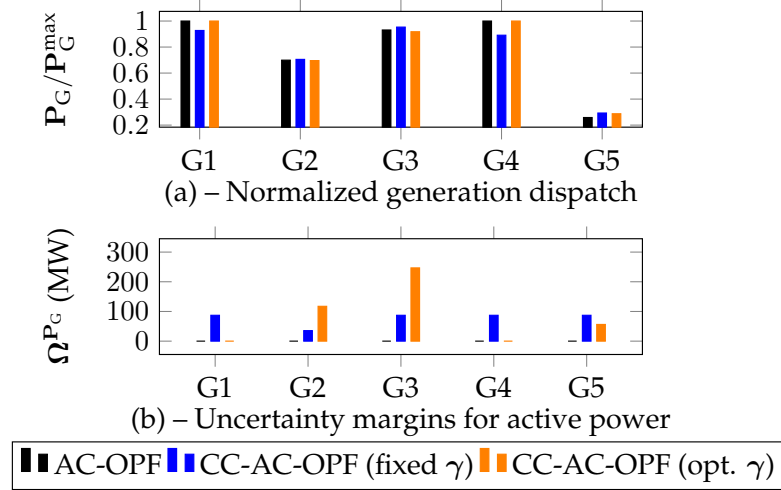
Figure 6.4: A comparison of (a) the normalized generation dispatch and (b) the uncertainty margins for active power generation without considering uncertainty (AC-OPF) and the chance-constrained AC-OPF with fixed and optimized generator participation factors. Note that the lower active power limits of all generators are zero.

Table 6.2: Empirical constraint violation probability for the 10 bus test case with one HVDC line.

Constraint limits on	$\mathbf{P_G}$	$\mathbf{Q_G}$	$\mathbf{V}$	$\mathbf{P_{ij}}$	$\mathbf{P_C}$
In-sample analysis with 10 000 samples (%)					
AC-OPF (w/o uncertainty)	50.5	0.0	45.3	12.4	0.0
CC-AC-OPF (fixed γ and β)	5.1	0.0	3.8	3.8	0.0
CC-AC-OPF (opt. γ and β)	0.9	0.0	3.9	3.5	0.0
CC-AC-OPF (mod.)	4.8	0.0	2.0	3.8	4.6
Out-of-sample analysis with 10 000 samples (%)					
AC-OPF (w/o uncertainty)	43.2	0.0	47.8	11.5	0.0
CC-AC-OPF (fixed γ and β)	5.8	0.0	3.4	3.9	0.0
CC-AC-OPF (opt. γ and β)	0.4	0.0	3.2	3.8	0.0
CC-AC-OPF (mod.)	5.7	0.0	1.0	4.6	4.0

and reactive power limits of the converter are determined by $m_P = 0.8$, $m_q^{min} = 0.4$, $m_q^{max} = 0.5$ [121]. The generation cost for the AC-OPF without considering uncertainty is decreased by 4.3% due to upgrading the AC to an HVDC line and thereby, reducing the congestion level of the system. In case of fixed generator participation factors $\gamma = [0.2\ 0.2\ 0.2\ 0.2\ 0.2]$ and HVDC participation factor $\beta = 0$, the cost of uncertainty amounts to 2.2%. By optimizing both generator and HVDC participation factors, the cost of uncertainty can be reduced to 0.0%, i.e. the available HVDC and generator controls are sufficient to absorb the uncertainty associated with the two wind farms without any cost increase. The number of iterations for both fixed and variable γ and β is 6. The average solving time for the AC-OPF iteration is 0.4 seconds for fixed γ and β and 1.6 seconds for optimizing γ and β, indicating that the computational complexity is further increased by considering β as an optimization variable.

Table 6.2 lists the empirical constraint violation probability for an AC-OPF without considering uncertainty, the iterative CC-AC-OPF with fixed γ and β and the iterative CC-AC-OPF with
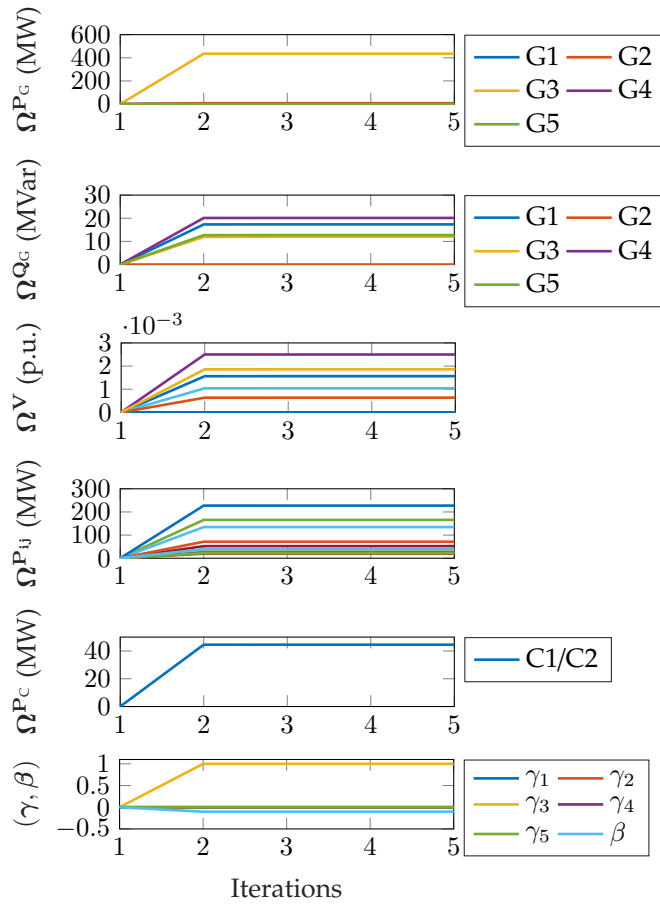
Figure 6.5: Uncertainty margins Ω and participation factors γ and β for each iteration of the chance constrained AC-OPF framework for the 10 bus test system with one HVDC line. The participation factors are optimization variables.

optimized γ and β. We observe again that without considering uncertainty, large violations of generator active power, voltage, and active branch flow limits occur. Both the CC-AC-OPF with fixed and optimized γ and β achieve a satisfactory performance in- and out-of-sample. For the considered test case, the optimized generator participation factors evaluate to $\gamma = [0.0\ 0.0\ 1.0\ 0.0\ 0.0]$ and the optimized HVDC participation factor β to 0.1032.

In Fig. 6.5 the uncertainty margins and participation factors for each iteration of the chance constrained AC-OPF framework are shown for the 10 bus test system with one HVDC line. The participation factors are optimization variables. Note that in the first iteration, the Jacobians are not available. We can observe that after the second iteration the uncertainty margins do not vary significantly showcasing the robustness of the iterative solution framework.

To investigate the ability of the introduced framework to comply with the chance constraints on the active HVDC converter setpoints (6.28) – (6.29), we consider a modified setup, where the HVDC line capability S_C^{nom} is reduced to 2 GVA, resulting in congestion on the HVDC line. We assign a fixed participation factor of $\beta = 0.25$ to this HVDC line, and allow for an optimization of the generator participation factors γ. The resulting empirical violation probability is shown in Table 6.2 with the entry CC-AC-OPF (mod.) and achieves satisfactory performance. Note, that
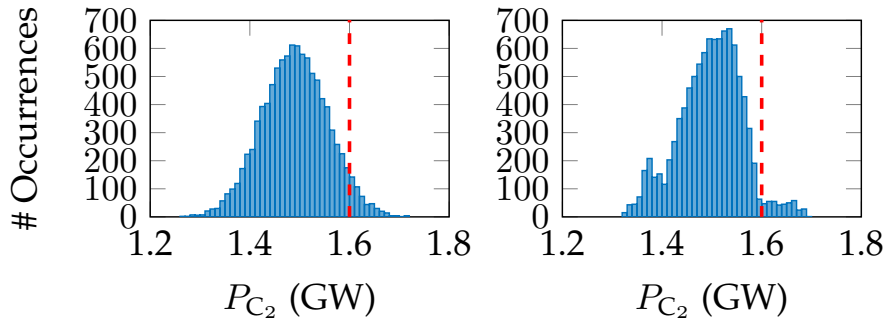
Figure 6.6: Histograms of the in-sample (left) and out-of-sample (right) Monte Carlo analysis for the active HVDC converter injection P_{C_2} at bus 2 for $10\,000$ samples. Note, that both in- and out-of-sample the empirical violation probability (4.6%, 4.0%) complies with the target value of 5%. The red dashed line indicates the maximum active power limit of the HVDC converter.

Table 6.3: Empirical constraint violation probability for the IEEE 39 bus test case with 2 HVDC lines and 2 wind farms.

Constraint limits on	$\mathbf{P}_G$	$\mathbf{Q}_G$	$\mathbf{V}$	$\mathbf{P}_C$
In-sample analysis with $10\,000$ samples (%)				
AC-OPF (w/o uncertainty)	49.0	50.0	5.4	0.0
CC-AC-OPF (fixed γ, β)	5.0	4.3	0.0	0.0
CC-AC-OPF (opt. γ, β)	5.1	3.2	0.0	5.0
Out-of-sample analysis with $10\,000$ samples (%)				
AC-OPF (w/o uncertainty)	41.6	58.0	1.4	0.0
CC-AC-OPF (fixed γ, β)	4.1	1.7	0.0	0.0
CC-AC-OPF (opt. γ, β)	4.2	1.2	0.0	4.2

both in- and out-of-sample the empirical violation probability of the HVDC chance constraints (4.6%, 4.0%) complies with the target value of 5%. This is confirmed in Fig. 6.6 which shows a histogram of the in- and out-of-sample analysis for the HVDC converter active power injection $P_{C,2}$ at bus 2.

6.5.4 IEEE 39 bus New England system

In the following, we investigate the performance of our proposed iterative chance constrained AC-OPF algorithm on an IEEE 39 bus New England system with 2 HVDC lines and 2 wind farms. We obtained the system data from the IEEE PES PGLib-OPF v19.01 benchmark library [127]. We place two farms at buses 4 and 16 with a maximum power of 0.5 GW and of 1.0 GW, respectively. The maximum wind power injection corresponds to 24.0% of the total system load. To compute the covariance matrix and forecast errors, we follow the same procedure as for the 10 bus system. We select control zones 7 and 9 at time step 4 to correspond to the wind farms at buses 4 and 16, respectively. We place two HVDC lines from bus 4 to bus 30 and from bus 16 to bus 38 with $S_C^{\mathrm{nom}} = 500$MVA, respectively. We assume that only the generators at buses 30, 32, and 36 have a non-zero participation factor γ. Note that we do not consider line limits for this test case.

First, we fix the participation factors to be equal in the chance constrained AC-OPF, i.e. $\gamma = [\frac{1}{3}\,\frac{1}{3}\,\frac{1}{3}]$, and set the HVDC participation factors to be zero, i.e. $\beta = [0\,0]$. The cost of uncertainty for fixed

participation factors evaluates to 1.7%. If both the generator and HVDC participation factors are optimization variables, for the considered test case, the optimized generator participation factors evaluate to $\gamma = [0.0\ 1.0\ 0.0]$ and the optimized HVDC participation factors evaluate to $\beta = [0.0\ 0.3675]$. The utilized controllability allows us to reduce the cost of uncertainty to 0.7%. The average solving time for the iterative AC-OPF is 0.8 seconds with 5 iterations for fixed γ and β and 1.6 seconds with 13 iterations for optimizing γ and β. Table 6.3 lists the empirical constraint violation probability for an AC-OPF without considering uncertainty and the iterative CC-AC-OPF with both fixed and optimized γ and β. We observe that without considering uncertainty, in this test case, large violations of the generator active and reactive power limits occur. Both CC-AC-OPFs with fixed and optimized γ and β achieve a satisfactory performance in- and out-of-sample.

6.6 Summary

In this work, we proposed an AC optimal power flow formulation that (i) considers uncertainty in wind power infeed, (ii) incorporates an HVDC line model and (iii) allows for an optimization of the generator and HVDC control policies in response to fluctuations in wind power production. For this purpose, we extend a computationally efficient iterative chance-constrained AC-OPF formulation introduced in [59, 98]. Using realistic wind forecast data and Monte Carlo analyses, we show for two test systems that our proposed chance-constrained OPF formulation achieves good in- and out-of-sample performance. Neglecting uncertainty, on the contrary, leads to high empirical constraint violation probabilities. In addition, we find that optimizing the control policies reduces the cost of uncertainty significantly.

Apart from forecast errors, corrective control can also be applied in response to contingencies and reduce the cost associated with an N-1 secure operation. Hence, appropriate modeling approaches that in addition to uncertainty and corrective control also account for security are required. The proposed framework could serve as a starting point. However, just like already existing corrective security-constrained OPF algorithms, it could quickly run into computational issues resulting from a large problem size caused by the vast number of contingencies and possible corrective control actions [9]. Consequently, a priori filtering techniques will be indispensable to identify only those contingencies and remedial actions which are truly relevant to the eventual operating conditions.

Additionally, HVDC converters and other electronic power flow control devices also have a significant impact on all aspects of dynamic security (i.e., small-disturbance, voltage and transient stability), which can sometimes even be detrimental [128]. Accounting for their dynamic behavior and the limits it imposes on the allowable static operating region is another aspect which has not yet been addressed in OPF algorithms. To this end, a data-driven approach similar to what has been proposed in Chapter 3 could be extended to account for power electronic system components and potentially to corrective control.

Enlarging the confidence region in multi-area AC and DC grids

*The previous chapter focused on integrating point-to-point high voltage direct current (HVDC) transmission lines in optimal power flow (OPF) algorithms. However, in the future, meshed DC grids are very likely to emerge from already existing point-to-point links. They are expected to offer the necessary controllability for integrating large amounts of intermittent renewable generation as they can offer preventive and corrective control of both active and reactive power. DC grids will interact with the underlying AC infrastructure and span multiple areas operated by different system and market operators. Market-clearing procedures, based on OPF algorithms, need to be revised to account for DC transmission, flexibility and privacy requirements. In [**Paper F**], we propose a decentralized two-stage stochastic market-clearing algorithm that incorporates meshed DC grids and allows the sharing of flexibility resources between areas. The benefit of this approach lies in its pricing mechanism used for coordinating the different area subproblems, requiring only a moderate exchange of information. Case studies are presented to illustrate the methodology and to demonstrate the benefits of additional controllability provided by DC grids.*

7.1 Introduction

The large scale integration of renewable energy sources (RES) has introduced significant uncertainties in power system planning and operation. This calls for flexibility and market setups that explicitly account for fluctuating and partially predictable generation [129]. In the future, in Europe, China, and the US, mixed AC and DC grids, spanning multiple areas controlled by different transmission system operators (TSO), are expected to offer the necessary controllability for integrating large amounts of RES. High voltage direct current transmission based on voltage source converter technology (VSC-HVDC) has significant benefits compared to AC and conventional HVDC technology. It can offer recourse actions, in the form of preventive and corrective control, and enables the formation of meshed HVDC grids which are very likely to evolve from already existing point-to-point connections [130]. To this end, optimal power flow algorithms (OPF), used in system and market operations, need to be revised in order to (i) optimally coordinate mixed AC and DC grids in a multi-area setting, (ii) avoid the disclosure of sensitive intraarea data, (iii) incorporate recourse actions offered by DC grids and (iv) provide a market for reserve capacity. Ideally, this coordination would be done by a central entity with access to all data, but the restriction imposed by (ii) calls for methods which decompose the OPF by area. This decentralization can be done by decomposition techniques that limit the amount of information shared between areas while ensuring system-wide optimality.

In [131] an OPF decomposition is performed using augmented Lagrangian relaxation with multiplier updates based on the auxiliary problem principle, whereas [132] decomposes the problem using Lagrangian relaxation (LR) combined with a subgradient method. Both methods

have the drawback of using multiplier updates whose convergence behavior is determined by parameters that must be tuned depending on the system. In [118] a multi-area OPF is solved using chance-constraints to account for wind power forecast errors. However, this setup only considers point-to-point HVDC interconnections and does not account for an explicit reserve capacity market that incentivizes the provision of regulating power. To complement these findings, we present a decentralized two-stage stochastic market-clearing algorithm that incorporates meshed DC grids and their flexibility while ensuring data privacy of each regional TSO. Flexibility resources are shared between areas and priced by a flexibility market. In contrast to the decomposition methods applied in [131, 132], we choose optimality condition decomposition (OCD), an LR based method, which does not require any parameter tuning or central coordination [133, 134]. Prices used for coordinating the different area subproblems, do not need to be estimated with auxiliary update methods that impact the performance of decomposition methods. Prices on power exports along tie-lines are provided by each area and can be used as costs in neighboring areas objective functions. This allows for a fully decentralized solution, but comes at a cost of requiring a higher information exchange, where primal and dual variables are exchanged. A reduced number of exchanged variables would enable a distributed solution but would require a coordinating entity. Reserve capacity markets are accounted for and make preventive and corrective control actions available across the entire system alleviating uncertainties arising from RES.

7.2 Mathematical formulation

The mathematical formulation of the centralized multi-area OPF for all areas $\mathcal{A}$ and its equivalent decomposed formulation are given in the following section. As opposed to the previous chapters, we now use a scenario based stochastic programming framework for modeling the uncertainty. The market-clearing model is formulated as a two-stage stochastic program optimizing the energy and reserve dispatch simultaneously [135]. The only source of uncertainty considered is wind power represented by a finite set of scenarios. The market is cleared in a single-period auction omitting intertemporal constraints, such as ramping limits. As usual in market applications, the network is modeled using a linear DC approximation. Conventional generators and loads are connected to AC nodes only. Wind farms are assumed to be located at AC and DC nodes.

7.2.1 Centralized OPF formulation

Objective function

The objective function to be minimized represents day-ahead and balancing costs in expectation

$$
\min_{\tilde{\mathbf{y}}} \quad \sum_{i \in \mathcal{A}} \left\{ \sum_{j \in \mathcal{G}_i} \left[c_{\mathrm{G}_j} P_{\mathrm{G}_j} + c_{\mathrm{G}_j}^{\mathrm{RU}} R_{\mathrm{G}_j}^{\mathrm{U}} + c_{\mathrm{G}_j}^{\mathrm{RD}} R_{\mathrm{G}_j}^{\mathrm{D}} \right] \right.
$$
$$
\left. + \sum_{s \in \mathcal{S}} \pi_s \left(\sum_{j \in \mathcal{G}_i} \left[c_{\mathrm{G}_j} (P_{\mathrm{G}_j} + r_{\mathrm{G}_{js}}^{\mathrm{U}} - r_{\mathrm{G}_{js}}^{\mathrm{D}}) \right] \right) + \sum_{j \in \mathcal{D}_i} V^{\mathrm{LOL}} p_{\mathrm{D}_{js}}^{\mathrm{shed}} \right\}, \tag{7.1}
$$

where $\tilde{\mathbf{y}}$ is the set of first- and second-stage decision variables. $\mathcal{G}$ and $\mathcal{D}$ denote the sets of generators and loads (demand). First-stage decisions are defined for the forecasted wind infeed. They comprise the active power generation $\mathbf{P}_{\mathrm{G}}$ of conventional generators, up- and down-reserve capacity $\mathbf{R}_{\mathrm{G}}^{\mathrm{U}}$ and $\mathbf{R}_{\mathrm{G}}^{\mathrm{D}}$, HVDC converter setpoints $\mathbf{P}_{\mathrm{C}}$ as well as intra- and interarea power flows. In the following, $\mathbf{F}$ denotes the internal power flows whereas $\mathbf{T}$ refers to the interarea tie-line flows.

Second-stage decisions depend on particular scenario realizations $s \in \mathcal{S}$ and are denoted with small letters.

Up- and down-reserve capacity costs, $\mathbf{c}_\mathrm{G}^\mathrm{RU}$ and $\mathbf{c}_\mathrm{G}^\mathrm{RD}$, are incorporated in the form of reserve capacity bids. Recourse actions include up- and down-reserve deployment ($\mathbf{r}_\mathrm{G}^\mathrm{U}$ and $\mathbf{r}_\mathrm{G}^\mathrm{D}$), load shedding ($\mathbf{p}_\mathrm{D}^\mathrm{shed}$), wind spillage ($\mathbf{p}_\mathrm{W}^\mathrm{spill}$), converter setpoint changes ($\mathbf{p}_\mathrm{C}$), and thus, real-time power flows on intra- and interarea DC links, denoted with $\mathbf{f}^\mathrm{DC}$ and $\mathbf{t}^\mathrm{DC}$, respectively. Out of these, costs are assigned to load shedding, in the form of penalties, and reserve deployment, which correspond to energy production costs. Other recourse actions are not penalized in the objective function.

Equality constraints

The set of equality constraints comprises power balance and the linearized power flow equations for the day-ahead and real-time stage, respectively. Power balance equations are given by

$$\mathcal{I}_{i,*}^\mathrm{G}\mathbf{P}_\mathrm{G} + \mathcal{I}_{i,*}^\mathrm{W}\mathbf{P}_\mathrm{W} - \mathcal{I}_{i,*}^\mathrm{C}\mathbf{P}_\mathrm{C} - \mathcal{I}_{i,*}^\mathrm{F}\mathbf{F} - \mathcal{I}_{i,*}^\mathrm{T}\mathbf{T} - \mathcal{I}_{i,*}^\mathrm{D}\mathbf{P}_\mathrm{D} = 0, \quad \forall i \in \mathcal{N}^\mathrm{AC}, \tag{7.2}$$

$$\mathcal{I}_{i,*}^\mathrm{W}\mathbf{P}_\mathrm{W} + \mathcal{I}_{i,*}^\mathrm{C}\mathbf{P}_\mathrm{C} - \mathcal{I}_{i,*}^\mathrm{F}\mathbf{F} - \mathcal{I}_{i,*}^\mathrm{T}\mathbf{T} = 0, \quad \forall i \in \mathcal{N}^\mathrm{DC}, \tag{7.3}$$

$$\mathcal{I}_{i,*}^\mathrm{G}(\mathbf{r}_{\mathrm{G}_s}^\mathrm{U} - \mathbf{r}_{\mathrm{G}_s}^\mathrm{D}) + \mathcal{I}_{i,*}^\mathrm{W}(\mathbf{p}_{\mathrm{W}_s} - \mathbf{p}_{\mathrm{w}_s}^\mathrm{spill} - \mathbf{P}_\mathrm{W}) - \mathcal{I}_{i,*}^\mathrm{C}(\mathbf{p}_{\mathrm{C}_s} - \mathbf{P}_\mathrm{C})$$
$$-\mathcal{I}_{i,*}^\mathrm{F}(\mathbf{f}_s - \mathbf{F}) - \mathcal{I}_{i,*}^\mathrm{T}(\mathbf{t}_s - \mathbf{T}) - \mathcal{I}_{i,*}^\mathrm{D}\mathbf{p}_\mathrm{D}^\mathrm{shed} = 0, \quad \forall i \in \mathcal{N}^\mathrm{AC}, \forall s \in \mathcal{S}, \tag{7.4}$$

$$\mathcal{I}_{i,*}^\mathrm{W}(\mathbf{p}_{\mathrm{W}_s} - \mathbf{p}_{\mathrm{w}_s}^\mathrm{spill} - \mathbf{P}_\mathrm{W}) + \mathcal{I}_{i,*}^\mathrm{C}(\mathbf{p}_{\mathrm{C}_s} - \mathbf{P}_\mathrm{C})$$
$$-\mathcal{I}_{i,*}^\mathrm{F}(\mathbf{f}_s - \mathbf{F}) - \mathcal{I}_{i,*}^\mathrm{T}(\mathbf{t}_s - \mathbf{T}) = 0, \quad \forall i \in \mathcal{N}^\mathrm{DC}, \forall s \in \mathcal{S}. \tag{7.5}$$

Day-ahead power balance equations of the AC (7.2) and DC grid (7.3) are coupled through controllable converter power flows $\mathbf{P}_\mathrm{C}$. Real-time power balance constraints (7.4) and (7.5) link recourse actions to day-ahead decisions depending on the actual wind power realization $\mathbf{p}_{\mathrm{W}_s}$. Incidence matrices are denoted with $\mathcal{I}$ and specify the location of generators, wind farms, converters, lines and loads with $\mathcal{I}_{i,*}$ indicating the row pertaining to node i.

Power flows in the DC grid are linearized and modeled according to [136]. Power flows on AC $\mathcal{T}^\mathrm{AC}$ and DC $\mathcal{T}^\mathrm{DC}$ tie-lines are given by

$$T_l = \frac{\Theta_i - \Theta_j}{x_l} : \quad \mu_l^\mathrm{AC}, \quad \forall l = (i,j) \in \mathcal{T}^\mathrm{AC}, \tag{7.6}$$

$$T_l = \frac{U_i - U_j}{r_l} : \quad \mu_l^\mathrm{DC}, \quad \forall l = (i,j) \in \mathcal{T}^\mathrm{DC}, \tag{7.7}$$

$$t_{ls} = \frac{\theta_{is} - \theta_{js}}{x_l} : \quad \nu_{ls}^\mathrm{AC}, \quad \forall l = (i,j) \in \mathcal{T}^\mathrm{AC}, \forall s \in \mathcal{S}, \tag{7.8}$$

$$t_{ls} = \frac{u_{is} - u_{js}}{r_l} : \quad \nu_{ls}^\mathrm{DC}, \quad \forall l = (i,j) \in \mathcal{T}^\mathrm{DC}, \forall s \in \mathcal{S}, \tag{7.9}$$

where Θ and U represent the day-ahead state variables – voltage angles and voltage magnitudes – of the AC and DC grid, respectively. Their corresponding second-stage variables are denoted with θ and u. Dual variables associated with tie-line flow constraints are indicated after the colon. Day-ahead and real-time intraarea AC and DC line flows, $\mathbf{F}$ and $\mathbf{f}$, are modeled in the same way and are not explicitly mentioned here.

Inequality constraints

Day-ahead and real-time inequality constraints comprise line capacity, converter power, DC voltage, generation and reserve capacity limits. Minimum and maximum voltage levels of DC buses are set to 0.9 and 1.1 p.u., respectively.

7.2.2 Decentralized OPF formulation

AC and DC tie-line flow constraints (7.6) – (7.9) contain variables from more than one area. They constitute complicating constraints and prevent the OPF of the interconnected power system to be decomposed per area. To tackle this, we use the optimality condition decomposition (OCD) technique, an iterative solution procedure, which is an extension to the common LR method and based on the decoupling of the first-order Karush-Kuhn-Tucker (KKT) conditions. The KKT conditions of the original problem correspond to the superposition of all subproblems' KKT conditions. A more detailed analysis of the method and conditions for convergence are provided in [137].

As opposed to LR, where all complicating constraints of the entire system are augmented as soft constraints to each area's objective function, OCD only augments complicating constraints belonging to neighboring areas (indicated with AA) [138]. As a result, each area can keep its own complicating constraints in the constraint set by treating neighboring areas' decision variables as parameters and setting them to the values obtained in the previous iteration. The benefit of this approach is that dual variables associated with tie-line flow constraints and used as cost parameters when augmenting the constraints to neighboring areas' objective functions, are readily available and do not need to be estimated with auxiliary methods, such as ADMM. Decomposition methods dependent on auxiliary update methods are prone to divergence, if their parameters are not properly selected. OCD allows for a fully decentralized solution, given that all computation is done within the scopes of the subproblems. Hence, the need for a central entity is avoided and a coordinated solution is achieved by exchanging only a moderate amount of information. Each area's OPF (A) is formulated as follows

$$
\min_{\bar{\mathbf{y}}^{\mathrm{A}}} \quad C^{\mathrm{DA,A}} + \mathbb{E}[C_s^{\mathrm{BA,A}}]
$$

$$
+ \sum_{l \in \mathcal{T}^{\mathrm{AC,A}}} \hat{\mu}_l^{\mathrm{AC,AA}} \Big(\frac{\hat{\Theta}_i^{\mathrm{AA}} - \Theta_j^{\mathrm{A}}}{x_l} - \hat{T}_l^{\mathrm{AA}} \Big)
$$

$$
+ \sum_{l \in \mathcal{T}^{\mathrm{DC,A}}} \hat{\mu}_l^{\mathrm{DC,AA}} \Big(\frac{\hat{U}_i^{\mathrm{AA}} - U_j^{\mathrm{A}}}{r_l} - \hat{T}_l^{\mathrm{AA}} \Big)
$$

$$
+ \sum_{s \in \mathcal{S}} \Bigg\{ \sum_{l \in \mathcal{T}^{\mathrm{AC,A}}} \hat{\nu}_{ls}^{\mathrm{AC,AA}} \Big(\frac{\hat{\theta}_{is}^{\mathrm{AA}} - \theta_{js}^{\mathrm{A}}}{x_l} - \hat{t}_{ls}^{\mathrm{AA}} \Big)
$$

$$
+ \sum_{l \in \mathcal{T}^{\mathrm{DC,A}}} \hat{\nu}_{ls}^{\mathrm{DC,AA}} \Big(\frac{\hat{u}_{is}^{\mathrm{AA}} - u_{js}^{\mathrm{A}}}{r_l} - \hat{t}_{ls}^{\mathrm{AA}} \Big) \Bigg\}
\tag{7.10}
$$

s.t.   Constraints in 7.2.1 for area A

$$
T_l^{\mathrm{A}} = \frac{\Theta_i^{\mathrm{A}} - \hat{\Theta}_j^{\mathrm{AA}}}{x_l} : \quad \mu_l^{\mathrm{AC,A}}, \qquad\qquad \forall l = (i,j) \in \mathcal{T}^{\mathrm{AC}}, \tag{7.11}
$$

$$
T_l^{\mathrm{A}} = \frac{U_i^{\mathrm{A}} - \hat{U}_j^{\mathrm{AA}}}{r_l} : \quad \mu_l^{\mathrm{DC,A}}, \qquad\qquad \forall l = (i,j) \in \mathcal{T}^{\mathrm{DC}}, \tag{7.12}
$$

$$
t_{ls}^{\mathrm{A}} = \frac{\theta_{is}^{\mathrm{A}} - \hat{\theta}_{js}^{\mathrm{AA}}}{x_l} : \quad \nu_{ls}^{\mathrm{AC,A}}, \qquad\qquad \forall l = (i,j) \in \mathcal{T}^{\mathrm{AC}}, \forall s \in \mathcal{S}, \tag{7.13}
$$

$$
t_{ls}^{\mathrm{A}} = \frac{u_{is}^{\mathrm{A}} - \hat{u}_{js}^{\mathrm{AA}}}{r_l} : \quad \nu_{ls}^{\mathrm{DC,A}}, \qquad\qquad \forall l = (i,j) \in \mathcal{T}^{\mathrm{DC}}, \forall s \in \mathcal{S}. \tag{7.14}
$$

$C^{\mathrm{DA,A}}$ and $C^{\mathrm{BA,A}}$ represent area A's day-ahead and balancing costs, respectively. Hatted terms are constants with values obtained from the neighboring areas' most recent iteration. Note that balancing tie-line flow constraints (i.e., stochastic complicating constraints) do not need to be

weighted by their probabilities when augmented to the objective function (7.10), since dual variables of stochastic constraints in the primal problem already contain information on their probability of occurrence. After each iteration border node state variables (i.e. voltage angles for AC tie-lines and voltage magnitudes for DC tie-lines) and dual variables associated with tie-line flow constraints are exchanged. The dual variables exchanged represent prices on power imports/exports along tie-lines. The algorithm is suitable for both sequential and parallel implementation. For systems with a low number of primal consensus variables, which connected areas need to agree on, tie-line flow mismatches can be used as convergence criteria. In this case, the algorithm converges as soon as all tie-line flow mismatches are within tolerance,

$$|T_l^{\text{A,k}} + T_l^{\text{AA,k}}| \le \rho, \quad \forall l \in \mathcal{T}^{\text{AC}} \cup \mathcal{T}^{\text{DC}}, \tag{7.15}$$

$$|t_{ls}^{\text{A,k}} + t_{ls}^{\text{AA,k}}| \le \rho, \quad \forall l \in \mathcal{T}^{\text{AC}} \cup \mathcal{T}^{\text{DC}}, \forall s \in \mathcal{S}, \tag{7.16}$$

where k represents the iteration counter. A large number of primal consensus variables significantly increases computation time. Instead, convergence criteria based on dual variables, which tend to converge faster, can be used. In this case, the algorithm converges, if the dual variables do not change significantly in two consecutive iterations

$$|\mu_l^{\text{k}} - \mu_l^{\text{k-1}}| \le \rho, \quad \forall l \in \mathcal{T}^{\text{AC}} \cup \mathcal{T}^{\text{DC}}, \tag{7.17}$$

$$\mathbb{E}[|\nu_{ls}^{\text{k}} - \nu_{ls}^{\text{k-1}}|] \le \rho, \quad \forall l \in \mathcal{T}^{\text{AC}} \cup \mathcal{T}^{\text{DC}}. \tag{7.18}$$

7.3   Case study

All simulations were carried out in Python using the Gurobi Optimizer [139].

7.3.1   IEEE two area RTS-96 test system with six-node DC overlay grid

The algorithm is tested on a modified version of the IEEE two area RTS-96 system [140] with an additional six-node DC overlay grid. The system is depicted in Fig. 7.1 with the DC grid highlighted in purple. The two areas are connected with two AC tie-lines and one DC tie-line. Each area contains three DC nodes, three internal DC lines, 12 conventional generators and six wind farms of 200 MW capacity each. AC tie-line parameters correspond to the ones of the original IEEE two area RTS-96 test system [141]. All DC lines have a resistance of 0.002 p.u. and a capacity of 300 MW. Power ratings of 500 MW are chosen for all converters. We consider a high demand snapshot with a total system load of 4770.9 MW for the single-period auction. Day-ahead wind power generation is set to its expected value. A set of 100 equally probable wind generation scenarios is used, which has been derived from wind measurement data of a location in western Denmark and made available online [125, 142]. The value of lost load V^{LOL} is chosen with 1000 €/MWh. The dual convergence criterion (7.17) – (7.18) is chosen with a tolerance ρ of 0.01 €. Quadratic cost functions are assumed for conventional generators. The area splitting is performed along geographical borders. TSOs are responsible for the operation of those parts of the interconnected AC and DC system that are located within their jurisdiction. The subproblems are solved sequentially. Alternatively, the algorithm is suitable for parallel implementation.

The decentralized algorithm converges after 19 iterations for the chosen tolerance. The results are listed in Table I. The cost difference between the centralized and the decentralized solution amounts to 0.04%. Fig. 7.2 depicts the convergence of the total system cost compared to the optimal centralized solution. The convergence behavior of the balancing tie-line flow prices for a particular
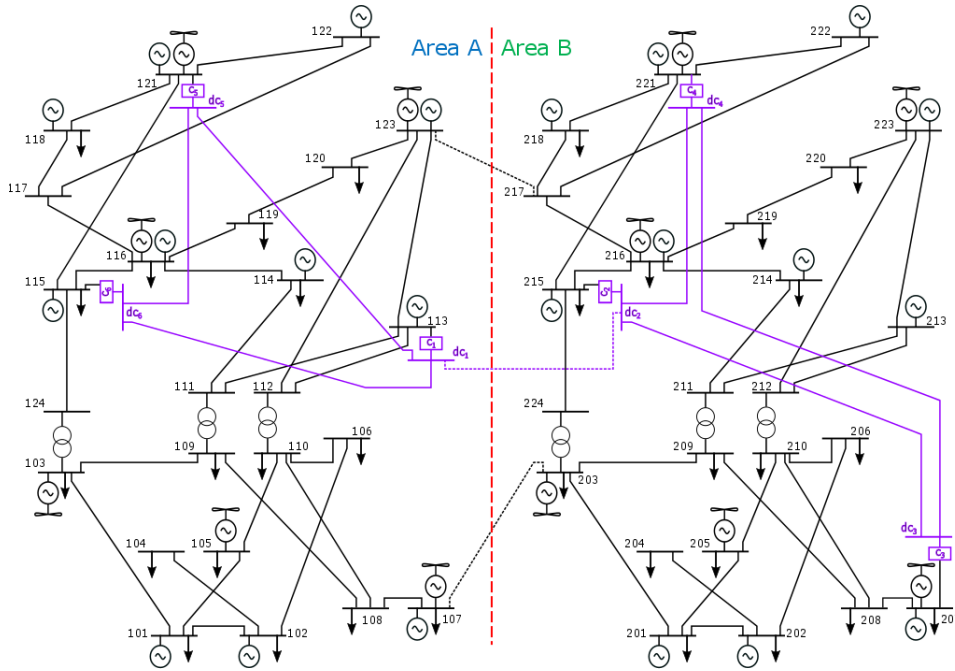
Figure 7.1: IEEE two-area RTS-96 system with six-node DC overlay grid.

scenario is illustrated in Fig. 7.3. It can be observed that the convergence behavior does not suffer from fluctuations as often seen in iterative solution procedures. Oscillations are quickly damped due to the availability of dual variables, which do not need to be estimated with auxiliary methods that determine the performance of the algorithm depending on the choice of parameters. Actual tie-line flow mismatches are below 1 MW for the day-ahead stage and at most 2.05 MW for the balancing stage in expectation, as shown in Table II. If necessary, tie-line flows would have to be adjusted by the two TSOs in agreement with each other to offset the minor mismatches. The price of avoiding the disclosure of sensitive intra-area data is the higher computation time of the decentralized case compared to the centralized solution. However, improvements can be achieved with a parallel implementation and by performing only single Newton-Raphson steps instead of solving the subproblems until optimality at each iteration. Nevertheless, it should be noted that this work focuses mainly on methods to preserve each area's independence, rather than increasing computational efficiency.

7.3.2   IEEE two area RTS-96 test system: HVAC vs. HVDC

To demonstrate the impact of increased controllability due to the DC grid, the overlay DC grid of the system used in Section III-A is replaced with AC transmission lines. Thus, the set of available recourse actions is reduced to reserve deployment, wind spillage and load shedding, and does not include converter setpoint changes and DC line flows. The line capacities of the overlay HVAC grid are set to 300 MW, corresponding to the values of the DC lines used in the previous section. The reactances of all new AC lines are chosen with 0.0628 p.u.. Note that buses 115 and 121 as well as 215 and 221 are already connected through AC lines in the original system. Their line parameters are adjusted to account for the new AC lines inserted in parallel. Table III lists the results for both HVAC and HVDC system configurations. The total system cost is higher for the HVAC case. Even though less reserve capacity is scheduled, day-ahead costs are higher, which
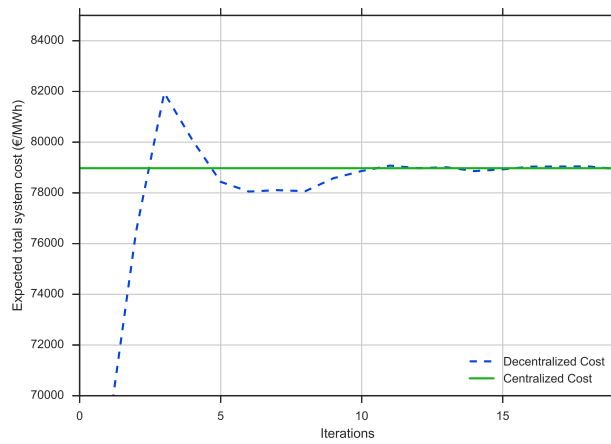
Figure 7.2: Convergence of expected total system cost for a single-period auction.
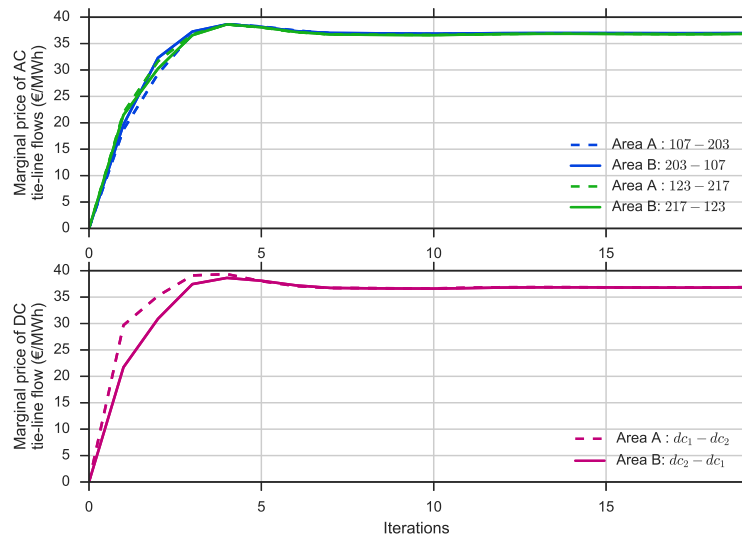
Figure 7.3: Convergence of marginal prices of balancing tie-line flow constraints for scenario 60.

indicates that more expensive generators need to be deployed for generation and reserve provision. In the HVDC case, more down-reserve capacity is scheduled allowing for more wind power to be accommodated by the system in scenarios with wind power surplus. This also leads to a lower amount of expected wind spillage resulting in cost savings due to the replacement of more expensive conventional generation by wind power. The DC grid for the case studies presented in this paper has not been chosen optimally and serves only the demonstration of the decentralized market-clearing algorithm. Thus, there is still room for improvement in the cost savings from DC grids, whose benefits are not fully captured here. As shown in table IV, the decentralized algorithm for the HVAC case converges after 20 iterations to a solution with a deviation of 0.02% from the centralized system cost.

Table 7.1: Results for the two area test system with an HVDC overlay grid.

Model	Total cost (€/h)	Number of iterations k	Cost difference (%)	Runtime (s)
Centralized	78 973.51	-	0.04	1.71
Decentralized	78 945.69	19		27.07

Table 7.2: Tie-line flow mismatches for the two area test system with a DC overlay grid.

Tie-line (-)	Day-ahead (MW)	Balancing (MW)
107-203	0.02	0.72
123-217	0.67	2.05
dc_1-dc_2	0.71	0.05

Table 7.3: Comparison of HVAC and HVDC overlay grid.

		HVAC	HVDC
Total system cost	(€/h)	79 160.03	78 973.50
Day-ahead system cost	(€/h)	73 275.20	73 199.50
Total up-reserve capacity $\mathbf{R}^U$	(MW)	1100	1100
Total down-reserve capacity $\mathbf{R}^D$	(MW)	202.30	209.40
Total expected wind spillage	(MW)	32.70	30.20

Table 7.4: Results for the two area test system with an HVAC grid.

Model	Total cost (€/h)	Number of iterations k	Cost difference (%)	Runtime (s)
Centralized	79 160.03	-	0.02	1.51
Decentralized	79 174.64	20		22.38

7.3.3   IEEE three area RTS-96 test system with seven-node DC overlay grid

In order to verify the adaptability of the algorithm to more than two areas, we have applied the method to a modified version of the IEEE three area RTS-96 test system. The two areas A and B of the system depicted in Fig. 7.1 are identical regarding their AC grids. A third area C with the same internal AC structure has been added to the system. A new DC node dc_7 is added to C and connected through a converter to the AC node 318. The set of interarea lines is extended to include one AC tie-line between B and C (i.e., from node 223 to node 317) and one DC tie-line between A an C (i.e., from node dc_5 to dc_7). The parameters of the new AC tie-line correspond to the ones of the original IEEE three area test system [141], while the parameters for the new DC tie-line have been chosen as in the previous section. As shown in table V, the algorithm converges after 27 iterations. The difference between the centralized and the decentralized solution amounts to 0.34%. This shows that the algorithm can be generalized to cases with more than two areas.

7.4   Summary

An iterative method to decentralize the market-clearing of mixed AC and DC grids by area has been presented. Flexibility resources are made available across the entire system and are more easily

Table 7.5: Results for the three area test system.

Model	Total cost (€/h)	Number of iterations k	Cost difference (%)
Centralized	120 343.25	-	0.34
Decentralized	120 753.87	27	

accessible due to the additional controllability provided by DC grids. Fast convergence is achieved while requiring only a moderate exchange of information between neighbors preserving each area's independence. The method has proven to be scalable and thus, applicable to large systems that cannot be solved centrally. In large networks with several areas we expect the computation of the decentralized solution to be equally good or even faster than in the centralized case. It has been shown in [143] that the performance of OCD largely depends on the splitting and coupling between areas.

Future work will investigate how to optimally split large interconnected systems comprising AC and DC grids, while allowing for an efficient decentralized solution. This could also give an indication on the operation of a future DC grid, whether it should be integrated in or decoupled from current AC grid operations. The algorithm presented in this paper could provide a framework for DC grid operators to offer preventive and corrective control as services to the AC grid using the pricing mechanism presented. Alternative ways to incorporate uncertainties and recourse actions in OCD algorithms will be studied.

CHAPTER 8

Conclusions and perspectives

8.1 Summary and conclusions

The growing share of renewable generation and the establishment of competitive electricity markets have significantly increased the volatility of power system operating conditions. The state of the system is less predictable, calling for new operational tools that will continue to ensure a reliable and affordable electricity supply under higher degrees of uncertainty. This thesis aimed at developing efficient reformulations of security and uncertainty constraints for power system optimization. As opposed to current practices, they give decision-makers – electricity market participants and power system operators – access to the entire permissible decision space, reducing cost without compromising system reliability in an increasingly uncertain environment.

First, we introduced a data-driven security-constrained optimal power flow (SC-OPF), addressing several major challenges of previous SC-OPF algorithms. It can consider any type of operational requirements, including any static and dynamic security criteria previously deemed intractable for an optimization framework. We focus on the N-1 security criterion with static and dynamic security. At the same time, we maintain a high computational efficiency in the optimization through linear formulations. They allow us to exploit powerful solvers for linear and general convex programming. To achieve this, we use decision trees to approximate the nonconvex secure operating region through partitions and translate them to an optimization framework using mixed integer programming (MIP). In combination with linear or convex AC-OPF approximations, the problem remains computationally robust and efficient. Yet, it preserves the benefits of the original nonconvex problem of having access to the entire decision space. Current approaches to include security requirements in the OPF usually consider one convex subspace, potentially neglecting more cost-efficient solutions in other areas. Our case study has shown how the security region represented in the OPF can be significantly increased when unifying traditional mathematical optimization with data-driven approaches.

This work is the first one to combine security assessments based on decision trees with traditional power system optimization. However, our framework extends to any other application of mathematical optimization beyond power systems. The combination of machine learning and binary programming, as we propose, can be used to accurately approximate any nonconvex space for an optimization framework through linear formulations. This also applies to nonconvex spaces that are difficult to parametrize, and have therefore been deemed intractable. All nonconvexities of the original problem can be dealt with offline, as demonstrated in our case study based on the fully linearized DC-OPF. We investigate necessary measures to ensure sufficient accuracy despite the dimensionality reduction and the linearization of the power flow equations. In this context, an estimation of the losses is essential, and we have shown how data can serve to provide high quality estimates. They ensure that the solution of the linearized and significantly simplified problem meets all security metrics at a very low additional cost. Alternatively, we avoid the

need for good loss estimates and reduce the cost of the linearization by using more accurate convex approximations of the power flow equations. Continuous and rapid improvements in solver technologies for general (mixed integer) convex programming reinforce the development of more accurate convex OPF approximations and relaxations. They can be solved rapidly and are becoming competitive with linear formulations in terms of computational efficiency while providing better solutions. Their application in both markets and system operations can further improve the cost-efficiency across the electricity industry.

In our second work, we demonstrated how convex approximations can identify even more cost-efficient solutions than similar approaches based on the nonlinear AC power flow equations. Here, we develop a tractable optimization framework for considering uncertainty through a chance-constrained second-order cone OPF (CC-SOC-OPF). Due to its convexity, the CC-SOC-OPF provides increased levels of robustness compared to nonconvex formulations of the chance-constrained AC-OPF (CC-AC-OPF). Generally, it is not possible to reformulate the original CC-AC-OPF to a tractable problem without a loss of accuracy. Some approximations are required, which might come at the expense of either feasibility (i.e., violations of the probabilistic constraints) or cost. We are the first to thoroughly investigate the impact of the required (linear) approximations for the probabilistic constraints in an SOC-OPF framework and have shown how they can be adjusted to compensate for modeling inaccuracies and ensure feasibility. In case of the CC-SOC-OPF, errors can occur due to the linearization of the uncertainty impact (which is also needed in the CC-AC-OPF) and the simplification of the power flow equations. Our analysis has shown that extended formulations of the convex quadratic chance constraints in the CC-SOC-OPF can more accurately approximate the feasible space of the original but intractable problem. More cost-efficient solutions are accessible, which would have otherwise been cut off. Through this work, we proved that convex approximations can serve as an intermediate approach between the prevailing optimization framework based on DC power flows and the true AC power flows. At the same time, they allow us to exploit the benefits of both worlds – using robust solution techniques while having access to the entire feasible space and indeed remaining feasible.

The benefits of convex AC-OPF approximations and relaxations are indisputable. However, there is little experience with their real-life deployment and system and market operators remain reluctant to adapt them. Therefore, the question that we addressed next was how under the current framework we could ensure that decision-makers at all levels get access to the entire permissible decision space without compromising reliability under increasingly uncertain conditions. To this end, we provided the first unified definition of the true target operating region of power systems for an optimization framework. It includes static and dynamic security as well as uncertainty, and accommodates various formulations of the power flow equations. We formulated the problem as a security- and chance-constrained OPF and proposed two tractable and efficient approximations. One relies on purely data-driven techniques, while the other uses a combination of data-driven and analytical reformulations. They mainly differ in their approximation accuracy, and thus their level of conservatism. Our results have confirmed that in both cases the security- and chance-constrained DC-OPF, formulated as an MILP, performs exceptionally well and comes close to the AC power flow based solution. This shows that decision-making processes at all levels can be significantly improved without requiring major changes of the status quo. In fact, current optimization software in both market and system operations is already equipped for integer programming (e.g., unit commitment decisions or "all-or-nothing" conditions of block orders). Additionally, we reduce the dependency of the market outcome on system operators and their estimates for determining the

bounds on the decision space. Today, these bounds are often perceived as overly restrictive and opaque. Using a data-driven approach and thereby, reducing the involvement of system operators in their derivation can increase transparency and trust in the derivation procedures. Thus, data analytics and machine learning do not only provide tractability of complex problems but also benefits beyond their technical aspects. This further consolidates the role of data in power system optimization.

We have also demonstrated that the prevailing preventive security paradigm significantly limits the allowable operating region. In our case study, barely 0.44% of the entire discretized AC-OPF feasible space were located in the secure operating region. Most of the remaining operating points – some having significantly lower generation costs – did not meet the security requirements for just one contingency. Here, appropriately planned corrective control actions could significantly extend the allowable operating region and reduce costs. To enlarge the target operating region, we developed two efficient frameworks for considering corrective control in response to forecast errors. The first is an operational tool and integrates both HVDC lines and the AC power flow equations in a chance-constrained OPF. We fully exploit the capability of HVDC converters to independently control active and reactive power. The second is a market tool for optimally coordinating flexibility resources in interconnected AC and HVDC grids and is based on DC power flows. In both cases, an optimization of generator and HVDC corrective controls significantly reduces the cost of securing the system against the uncertainty. However, more controllable devices also increase the computational complexity. To cope with this in large-scale systems, we propose to use decomposition procedures, which solve the optimization problem in a distributed, yet coordinated way. Such procedures will gain in importance as the amount of available controls and the level of coordination between different entities operating the system increase. Additionally, our method accommodates privacy requirements of the involved parties. Regulations for data protection are becoming more stringent, requiring also algorithms to adapt accordingly.

8.2 Perspectives for future work

The work in this thesis has opened up a number of different directions for future research, some of which are discussed below.

The most fundamental question raised by the work in this thesis revolves around the creation of the database and the amount of data necessary to reliably construct the feasible space. Recent approaches focusing on the boundary of the feasible space (and the high information content region around it) achieve significant speed-ups for generating such a database. Nevertheless, it is difficult to ensure that the entire boundary has been explored. "Gaps" in the boundary can still lead to infeasible solutions when transferred to an optimization framework. Avoiding unexplored regions along the boundary is of utmost importance. How to use historical observation data in this context and how to filter out noise are other key considerations.

Since the MILP framework based on the DC power flow equations worked very well in our simulations, another direction would be to include linearizations of the reactive power flows. Such an extension would allow for an optimization of, e.g., generator voltage setpoints as well. Many approaches exist that model reactive power and voltage magnitudes in the DC-OPF and could extend the immediate application range of our proposed data-driven framework.

Convex relaxations can abolish the need for approximations and the cost associated with them, potentially even identifying better (i.e., AC feasible and cheaper) solutions than current nonlinear

solvers for the nonconvex problem. They are a very promising direction for future work. The iterative approximation procedure for the second-order cone formulation of the power flow equations used in this work can be replaced by strengthening procedures, transforming the problem from an approximation to a relaxation. The impact of the relaxation on the solution quality of the proposed algorithms would have to be examined. Machine learning approaches could potentially strengthen the relaxation by learning the conditions for global optimality and the remedies to achieve a zero relaxation gap. Today, feasible solutions to inexact relaxations are recovered through heuristic procedures and manual tuning with no guarantees for either success or optimality. Through machine learning we might be able to systematically tune the relaxation to its global optimum.

Transforming the *optimal power flow* problem into an *optimal control* problem could entirely abolish the need for any power flow equations in the optimization. In the end, we are only interested in optimizing the controls that are at our disposal. All other variables are not true decisions but solely auxiliary variables to help define the permissible space of our decisions. Theoretically, it might be possible to define the partitions of the nonconvex feasible space such that any combination of the control variables in the individual subregions is AC feasible – essentially many small copper plates. The disjunctive inequality constraints, used to capture the nonconvex feasible space in our framework, would then have to be defined for the control variables instead of for the active power line flows, which are no longer represented.

The incorporation of the data-driven approach in electricity markets, where one entity is responsible for both system and market operations (e.g., the ISO model) is relatively straightforward. It is more challenging in interconnected power systems, operated by different system operators and where different markets are jointly cleared (as in Europe). Nowadays, transfer capacities on interconnectors are determined in mutual agreement between the two participating TSOs. Defining conditional transfer limits would require an increased amount of coordination, probably among all TSOs involved. Which kind of data and how much data would need to be shared to achieve this is another open issue. Alternatively, a centralized entity in charge of a common power system database, discretizing the solution space of the entire interconnected power system, could be formed. This entity would also be responsible for defining the conditional transfer limits and act as a link between system and market operators as well as regulating authorities. Beyond the traditional functionalities, it could also serve as an artificial intelligence hub, removing the barriers to a self-learning power system and ensuring that machine-driven decisions do not act against each other but are harmonized towards the global benefit. More sophisticated machine learning models could enable the system to continuously tune itself to an optimal state while anticipating possible deviations from the planned trajectory and keeping the optimal balance of preventive and corrective control measures. Eventually, this could entirely eliminate human intervention and reduce our tasks to monitoring purposes only.

A. Derivation of the linear sensitivity factors

The linear sensitivity factors used in Chapter 4 and 5 are calculated at each iteration of the CC-SOC-OPF based on a linearization around the iteration's current optimal operating point $\mathbf{z}^*$. The derivation of the sensitivity factors based on the most common power flow equations in polar coordinates (2.2) – (2.3) is given in [16]. The derivation based on the alternative formulation of the power flow equations (2.10) – (2.13) is described below, followed by an illustrative example.

The changes in nodal active and reactive power injections can be expressed in terms of the wind deviation $\boldsymbol{\xi}$, the generator participation factors $\boldsymbol{\gamma}$, the unknown nonlinear changes in active and reactive power (i.e., $\boldsymbol{\Delta P}_U$ and $\boldsymbol{\Delta Q}$) and the ratio $\boldsymbol{\lambda}$ between the reactive and active power injection of wind farms. Thus, the left-hand side of (4.16) can also be expressed as follows:

$$
\begin{bmatrix} -\boldsymbol{\gamma}\mathbf{1} \\ \mathbf{Z} \\ \mathbf{Z} \\ \mathbf{Z} \end{bmatrix} \boldsymbol{\xi} + \begin{bmatrix} \boldsymbol{\Delta P}_U \\ \boldsymbol{\Delta Q} \\ \mathbf{0} \\ \mathbf{0} \end{bmatrix} + \begin{bmatrix} \mathbf{I} \\ \mathbf{diag}(\boldsymbol{\lambda}) \\ \mathbf{Z} \\ \mathbf{Z} \end{bmatrix} \boldsymbol{\xi} = \begin{bmatrix} \boldsymbol{\Delta P}_U \\ \boldsymbol{\Delta Q} \\ \mathbf{0} \\ \mathbf{0} \end{bmatrix} + \begin{bmatrix} \boldsymbol{\Psi} \end{bmatrix} \boldsymbol{\xi},
\tag{8.1}
$$

where $\mathbf{Z}$, $\mathbf{1}$ and $\mathbf{I}$ denote $(|\mathcal{N}| \times |\mathcal{W}|)$ or $(|\mathcal{L}| \times |\mathcal{W}|)$ zero, all-ones and identity matrices, respectively. $\mathbf{0}$ is a vector of zeros. The system of equations (4.16) can finally be reformulated to:

$$
\begin{bmatrix} \boldsymbol{\Delta P}_U \\ \boldsymbol{\Delta Q} \\ \mathbf{0} \\ \mathbf{0} \end{bmatrix} + \begin{bmatrix} \boldsymbol{\Psi} \end{bmatrix} \boldsymbol{\xi} = \begin{bmatrix} \mathbf{J}^{SOC} \end{bmatrix} \Big|_{\mathbf{z}^*} \begin{bmatrix} \boldsymbol{\Delta u} \\ \boldsymbol{\Delta c} \\ \boldsymbol{\Delta s} \\ \boldsymbol{\Delta \theta} \end{bmatrix}.
\tag{8.2}
$$

$\boldsymbol{\Delta P}_U$ refers to the unknown changes in nonlinear active power losses, which are not accounted for by the generator participation factors. Following the assumptions outlined in Section 4.2.4, the nonzero elements of $\boldsymbol{\Delta P}_U$ and $\boldsymbol{\Delta Q}$ are summarized in $\boldsymbol{\Delta g} := [\Delta P_{U_{ref}} \ \Delta Q_{ref} \ (\boldsymbol{\Delta Q}_{PV})^T]^T$. Similarly, $\boldsymbol{\Delta \hat{z}}$ denotes the nonzero changes in the right-hand side of (8.2), i.e.,

$$
\boldsymbol{\Delta \hat{z}} := [\boldsymbol{\Delta u}_{PQ}^T \ \boldsymbol{\Delta c}^T \ \boldsymbol{\Delta s}^T \ \boldsymbol{\Delta \theta}_{PV}^T \ \boldsymbol{\Delta \theta}_{PQ}^T]^T.
\tag{8.3}
$$

Rearranging (8.2) by grouping the nonzero and zero elements separately, i.e.,

$$
\begin{bmatrix} \boldsymbol{\Delta g} \\ \mathbf{0} \end{bmatrix} = \begin{bmatrix} \mathbf{J}_x^{SOC,I} & \mathbf{J}_x^{SOC,II} \\ \mathbf{J}_x^{SOC,III} & \mathbf{J}_x^{SOC,IV} \end{bmatrix} \begin{bmatrix} \mathbf{0} \\ \boldsymbol{\Delta \hat{z}} \end{bmatrix} - \begin{bmatrix} \boldsymbol{\Psi}_x^I \\ \boldsymbol{\Psi}_x^{II} \end{bmatrix} \boldsymbol{\xi},
\tag{8.4}
$$

allows us to derive linear relationships between the changes in the variables of interest and the wind deviation $\boldsymbol{\xi}$,

$$
\boldsymbol{\Delta \hat{z}} = \left(\mathbf{J}_x^{SOC,IV} \right)^{-1} \boldsymbol{\Psi}_x^{II} \boldsymbol{\xi} = \boldsymbol{\Upsilon}_{\hat{z}} \boldsymbol{\xi},
\tag{8.5}
$$

$$
\boldsymbol{\Delta g} = \left(\mathbf{J}_x^{SOC,II} (\mathbf{J}_x^{SOC,IV})^{-1} \boldsymbol{\Psi}_x^{II} - \boldsymbol{\Psi}_x^I \right) \boldsymbol{\xi} = \boldsymbol{\Upsilon}_g \boldsymbol{\xi}.
\tag{8.6}
$$

Subscript $\mathbf{x}$ in $\mathbf{J}_{\mathbf{x}}^{\mathrm{SOC}}$ and $\mathbf{\Psi}_{\mathbf{x}}$ denotes that the columns and/or rows of the original matrices have been rearranged according to the grouping of zero and nonzero elements. The linear sensitivity factors $\mathbf{\Upsilon}$ are then used to calculate the uncertainty margins $\mathbf{\Omega}$.

Example

The derivation of the linear sensitivity factors is outlined in the following based on the two-bus system illustrated in Fig. 8.1. Bus 1 is the reference bus. The wind farm at bus 2 is associated with an uncertain forecast error ξ.
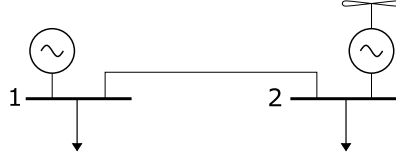

Figure 8.1: Two-bus system.

The $(2|\mathcal{N}| + 2|\mathcal{L}|)$ power flow equations for the two-bus system are given by

$$0 = -P_1 - G_{11}u_1 - G_{12}c_1 + B_{12}s_1, \tag{8.7}$$

$$0 = -P_2 - G_{22}u_2 - G_{21}c_1 - B_{21}s_1, \tag{8.8}$$

$$0 = -Q_1 + B_{11}u_1 - B_{12}c_1 - G_{12}s_1, \tag{8.9}$$

$$0 = -Q_2 + B_{22}u_2 - B_{21}c_1 + G_{21}s_1, \tag{8.10}$$

$$0 = c_1^2 + s_1^2 - u_1u_2, \tag{8.11}$$

$$0 = \theta_2 - \theta_1 - \arctan\left(\frac{s_1}{c_1}\right). \tag{8.12}$$

The system of equations (8.7) – (8.12) is linearized around an operating point $\mathbf{z}^*$,

$$0 = -\Delta P_1 - G_{11}\Delta u_1 - G_{12}\Delta c_1 + B_{12}\Delta s_1, \tag{8.13}$$

$$0 = -\Delta P_2 - G_{22}\Delta u_2 - G_{21}\Delta c_1 - B_{21}\Delta s_1, \tag{8.14}$$

$$0 = -\Delta Q_1 + B_{11}\Delta u_1 - B_{12}\Delta c_1 - G_{12}\Delta s_1, \tag{8.15}$$

$$0 = -\Delta Q_2 + B_{22}\Delta u_2 - B_{21}\Delta c_1 + G_{21}\Delta s_1, \tag{8.16}$$

$$0 = 2c_1^*\Delta c_1 + 2s_1^*\Delta s_1 - u_2^*\Delta u_1 - u_1^*\Delta u_2, \tag{8.17}$$

$$0 = \Delta\theta_2 - \Delta\theta_1 - \frac{c_1^*}{(c_1^*)^2 + (s_1^*)^2}\Delta s_1 + \frac{s_1^*}{(c_1^*)^2 + (s_1^*)^2}\Delta c_1. \tag{8.18}$$

The linear system (8.13) – (8.18) can equivalently be expressed in matrix notation in terms of the power flow Jacobian $\mathbf{J}^{\mathrm{SOC}}$,

$$
\begin{bmatrix}
\Delta P_1 \\
\Delta P_2 \\
\Delta Q_1 \\
\Delta Q_2 \\
0 \\
0
\end{bmatrix}
=
\underbrace{
\begin{bmatrix}
-G_{11} & 0 & -G_{12} & B_{12} & 0 & 0 \\
0 & -G_{22} & -G_{21} & -B_{21} & 0 & 0 \\
B_{11} & 0 & -B_{12} & -G_{12} & 0 & 0 \\
0 & B_{22} & -B_{21} & G_{21} & 0 & 0 \\
-u_2^* & -u_1^* & 2c_1^* & 2s_1^* & 0 & 0 \\
0 & 0 & \frac{s_1^*}{(c_1^*)^2+(s_1^*)^2} & \frac{c_1^*}{(c_1^*)^2+(s_1^*)^2} & -1 & 1
\end{bmatrix}
}_{\mathbf{J}^{\mathrm{SOC}}\big|_{\mathbf{z}^*}}
\begin{bmatrix}
\Delta u_1 \\
\Delta u_2 \\
\Delta c_1 \\
\Delta s_1 \\
\Delta\theta_1 \\
\Delta\theta_2
\end{bmatrix}. \tag{8.19}
$$

The changes in active and reactive power injections, $\mathbf{\Delta P}$ and $\mathbf{\Delta Q}$, can be expressed as the sum of known linear responses to ξ and unknown nonlinear responses,

$$\begin{bmatrix} \Delta P_1 \\ \Delta P_2 \\ \Delta Q_1 \\ \Delta Q_2 \\ 0 \\ 0 \end{bmatrix} = \underbrace{\begin{bmatrix} -\gamma_1 \\ 1 \\ 0 \\ \lambda^* \\ 0 \\ 0 \end{bmatrix}}_{\text{known}} \xi + \underbrace{\begin{bmatrix} \Delta P_{U_1} \\ 0 \\ \Delta Q_1 \\ 0 \\ 0 \\ 0 \end{bmatrix}}_{\text{unknown}}. \tag{8.20}$$

The generator at the reference bus adjusts its active power output according to the automatic generation control γ_1 in order to compensate the production imbalance caused by the wind power forecast error ξ. In addition to the known linear response, the active power adjustment also has to account for the unknown nonlinear change in active power losses ΔP_{U_1}. The reactive power output of the generator at the reference bus varies nonlinearly with ξ in order to keep the voltage magnitude at its grid connection point constant. This implies $\Delta u_1 = 0$ on the right-hand side of (8.19). Additionally, the voltage angle at the reference bus is always 0, such that $\Delta \theta_1 = 0$ in (8.19). Wind farms are assumed to operate with a constant power factor. Therefore, the reactive power output of the wind generator varies linearly with the forecast error ξ according to the current optimal power factor λ^*, i.e., $\Delta Q_2 = \lambda^* \xi$. Expressing the left-hand side of (8.19) with (8.20) and rearranging the system of linear equations according to known and unknown changes yields

$$\begin{bmatrix} 0 \\ 0 \\ 0 \\ 0 \\ \hline \Delta P_{U_1} \\ \Delta Q_1 \end{bmatrix} = \begin{bmatrix} \mathbf{J}_x^{\text{SOC,I}} & \mathbf{J}_x^{\text{SOC,II}} \\ \hline \mathbf{J}_x^{\text{SOC,III}} & \mathbf{J}_x^{\text{SOC,IV}} \end{bmatrix}\Bigg|_{\mathbf{z}^*} \begin{bmatrix} \Delta u_2 \\ \Delta c_1 \\ \Delta s_1 \\ \Delta \theta_2 \\ 0 \\ 0 \end{bmatrix} - \begin{bmatrix} 1 \\ \lambda^* \\ 0 \\ 0 \\ \hline -\gamma_1 \\ 0 \end{bmatrix} \xi, \tag{8.21}$$

where $\mathbf{J}_x^{\text{SOC}}$ denotes the Jacobian matrix with rearranged rows and columns. The response of the remaining unknown variables $\mathbf{\Delta \hat{z}} := [\Delta u_2 \; \Delta c_1 \; \Delta s_1 \; \Delta \theta_2]^{\mathrm{T}}$ can then be expressed in terms of the forecast error ξ,

$$\begin{bmatrix} \Delta u_2 \\ \Delta c_1 \\ \Delta s_1 \\ \Delta \theta_2 \end{bmatrix} = \left(\mathbf{J}_x^{\text{SOC,I}}\right)^{-1} \begin{bmatrix} 1 \\ \lambda^* \\ 0 \\ 0 \end{bmatrix} \xi = \mathbf{\Upsilon}_{\hat{\mathbf{z}}}\xi. \tag{8.22}$$

Finally, the changes in active and reactive power injections $\mathbf{\Delta g} := [\Delta P_{U_1} \; \Delta Q_1]^{\mathrm{T}}$ are given by

$$\begin{bmatrix} \Delta P_{U_1} \\ \Delta Q_1 \end{bmatrix} = \mathbf{J}_x^{\text{SOC,III}} \begin{bmatrix} \Delta u_2 \\ \Delta c_1 \\ \Delta s_1 \\ \Delta \theta_2 \end{bmatrix} - \begin{bmatrix} -\gamma_1 \\ 0 \end{bmatrix} \xi = \left(\mathbf{J}_x^{\text{SOC,III}} \left(\mathbf{J}_x^{\text{SOC,I}}\right)^{-1} \begin{bmatrix} 1 \\ \lambda^* \\ 0 \\ 0 \end{bmatrix} - \begin{bmatrix} -\gamma_1 \\ 0 \end{bmatrix}\right)\xi = \mathbf{\Upsilon}_{\mathbf{g}}\xi. \tag{8.23}$$

Bibliography

[1]   Bundesnetzagentur. Quartalsbericht zu Netz- und Systemsicherheitsmaßnahmen: Gesamtjahr und viertes Quartal 2017, 2018.

[2]   BDEW Bundesverband der Energie-und Wasserwirtschaft e.V. Redispatch in Deutschland, 2018.

[3]   P. H. Larsen, B. Boehlert, J. Eto, K. Hamachi-LaCommare, J. Martinich, and L. Rennels. Projecting future costs to U.S. electric utility customers from power interruptions. *Energy*, 147:1256–1277, 2018.

[4]   S. Garatti S.H. Low D.K. Molzahn A.X. Sun L. Wehenkel P. Panciatici, M.C. Campi. Advanced optimization methods for power systems. In *2014 Power Systems Computation Conference (PSCC)*, Aug. 2014.

[5]   R. Billinton and R. N. Allan. Power-system reliability in perspective. *Electronics and Power*, 30(3):231–236, March 1984.

[6]   Electric Consumer Research Council (ELCON). The economic impacts of the August 2003 blackout, 2004.

[7]   S. Küfeoğlu. *Economic impacts of electric power outages and evaluation of customer interruption costs*. PhD thesis, Aalto University, 2015.

[8]   M. B. Cain, R. P. O'Neill, and A. Castillo. History of optimal power flow and formulations - Optimal power flow paper 1. Technical report, Federal Energy Regulatory Commission, 2012.

[9]   F. Capitanescu, J.L. Martinez Ramos, P. Panciatici, D. Kirschen, A. Marano Marcolini, L. Platbrood, and L. Wehenkel. State-of-the-art, challenges, and future trends in security-constrained optimal power flow. *Electric Power Systems Research*, 81(8):1731–1741, 2011.

[10]   J. Carpentier. Contribution à l'étude du dispatching economique. *Bulletin de la Société Française des Electriciens*, 3(8):431–447, 1962.

[11]   B. Stott and O. Alsaç. Optimal power flow–Basic requirements for real-life problems and their solutions, 2012.

[12]   L. Papangelis, M. Debry, T. Prevost, P. Panciatici, and T. Van Cutsem. Stability of a voltage source converter subject to decrease of short-circuit capacity: A case study. In *2018 Power Systems Computation Conference (PSCC)*, June 2018.

[13]   P. Kundur, J. Paserba, V. Ajjarapu, G. Andersson, A. Bose, C. Canizares, N. Hatziargyriou, D. Hill, A. Stankovic, C. Taylor, T. Van Cutsem, and V. Vittal. Definition and classification of

power system stability IEEE/CIGRE joint task force on stability terms and definitions. *IEEE Transactions on Power Systems*, 19(3):1387–1401, Aug 2004.

[14] R. Zarate-Minano, F. Milano, and A. J. Conejo. An OPF methodology to ensure small-signal stability. *IEEE Transactions on Power Systems*, 26(3):1050–1061, Aug 2011.

[15] F. Capitanescu. Critical review of recent advances and further developments needed in AC optimal power flow. *Electric Power Systems Research*, 136:57–68, 2016.

[16] L. Roald. *Optimization methods to manage uncertainty and risk in power system operation*. PhD thesis, ETH Zurich, 2016.

[17] A. Eltved, J. Dahl, and M. S. Andersen. On the robustness and scalability of semidefinite relaxation for optimal power flow problems. *arXiv:1806.08620*, 2018.

[18] A. Castillo and R. P. O'Neill. Computational performance of solution techniques applied to the AC-OPF. Technical report, Federal Energy Regulatory Commission, 2013.

[19] L. Roald, S. Misra, T. Krause, and G. Andersson. Corrective control to handle forecast uncertainty: A chance-constrained optimal power flow. *IEEE Transactions on Power Systems*, 32(2):1626–1637, March 2017.

[20] K. V. d. Bergh, J. Boury, and E. Delarue. The flow-based market coupling in Central Western Europe: Concepts and definitions. *The Electricity Journal*, 29(1):24–29, 2016.

[21] L. Roald, F. Oldewurtel, T. Krause, and G. Andersson. Analytical reformulation of security-constrained optimal power flow with probabilistic constraints. In *2013 IEEE Grenoble Conference*, June 2013.

[22] M. Lubin, D. Bienstock, and J. P. Vielma. Two-sided linear chance constraints and extensions. *arXiv:1507.01995*, 2015.

[23] J. Duncan Glover, M. S. Sarma, and T. J. Overbye. *Power System Analysis and Design*. Brooks/Cole Publishing Co., Pacific Grove, CA, USA, 3rd edition, 2001.

[24] J. A. Taylor. *Convex Optimization of Power Systems*. Cambridge University Press, 2015.

[25] D. K. Molzahn and I. A. Hiskens. A survey of relaxations and approximations of the power flow equations. *Foundations and Trends in Electric Energy Systems*, 4(1-2):1–221, February 2019.

[26] H. Saadat. *Power System Analysis*. McGraw-Hill, 2009.

[27] A. Wigington. Application of advanced data processing, mathematical techniques, and computing technologies in control centers: Enhancing speed and robustness of power flow computation. Technical report, Electric Power Research Institute, 2012.

[28] P. Bonami, M. Kilinç, and J. Linderoth. Algorithms and software for convex mixed integer nonlinear programs. In Jon Lee and Sven Leyffer, editors, *Mixed Integer Nonlinear Programming*, pages 1–39, New York, NY, 2012. Springer New York.

[29] J. Lavaei and S. H. Low. Zero duality gap in optimal power flow problem. *IEEE Transactions on Power Systems*, 27(1):92–107, Feb 2012.

[30] A. Castillo and R. P. O'Neill. Survey of approaches for solving the AC-OPF - Optimal power flow paper 4. Technical report, Federal Energy Regulatory Commission, 2013.

[31] W. Murray, T. T. De Rubira, and A. Wigington. Improving the robustness of Newton-based power flow methods to cope with poor initial points. In *2013 North American Power Symposium (NAPS)*, Sep. 2013.

[32] F. Capitanescu and L. Wehenkel. Experiments with the interior-point method for solving large scale optimal power flow problems. *Electric Power Systems Research*, 95:276–283, 2013.

[33] K. Dvijotham and D. K. Molzahn. Error bounds on the DC power flow approximation: A convex relaxation approach. In *2016 IEEE 55th Conference on Decision and Control (CDC)*, Dec 2016.

[34] B. Stott, J. Jardim, and O. Alsac. DC power flow revisited. *IEEE Transactions on Power Systems*, 24(3):1290–1300, Aug 2009.

[35] S. Grijalva, P. W. Sauer, and J. D. Weber. Enhancement of linear ATC calculations by the incorporation of reactive power flows. *IEEE Transactions on Power Systems*, 18(2):619–624, May 2003.

[36] C. Coffrin and P. Van Hentenryck. A linear-programming approximation of AC power flows. *INFORMS J. on Computing*, 26(4):718–734, November 2014.

[37] Z. Yang, H. Zhong, Q. Xia, and C. Kang. Solving OPF using linear approximations: Fundamental analysis and numerical demonstration. *IET Generation, Transmission Distribution*, 11(17):4115–4125, 2017.

[38] A. Ott. Unit commitment in the PJM day-ahead and real-time markets, 2010.

[39] R. Madani, S. Sojoudi, and J. Lavaei. Convex relaxation for optimal power flow problem: Mesh networks. *IEEE Transactions on Power Systems*, 30(1):199–211, Jan 2015.

[40] C. Coffrin, H. L. Hijazi, and P. Van Hentenryck. The QC relaxation: A theoretical and computational study on optimal power flow. *IEEE Transactions on Power Systems*, 31(4):3008–3018, July 2016.

[41] A. Gomez Esposito and E. Romero Ramos. Reliable load flow technique for radial distribution networks. *IEEE Transactions on Power Systems*, 14(3):1063–1069, Aug 1999.

[42] R. A. Jabr. A conic quadratic format for the load flow equations of meshed networks. *IEEE Transactions on Power Systems*, 22(4):2285–2286, Nov 2007.

[43] D. K. Molzahn and I. A. Hiskens. Sparsity-exploiting moment-based relaxations of the optimal power flow problem. *IEEE Transactions on Power Systems*, 30(6):3168–3180, Nov 2015.

[44] H. L. Hijazi, C. Coffrin, and P. Van Hentenryck. Convex quadratic relaxations for mixed-integer nonlinear programs in power systems. *Math. Program. Comput.*, 9:321–367, 2017.

[45] D. Molzahn. *Application of semidefinite optimization techniques to problems in electric power systems*. PhD thesis, University of Wisconsin–Madison, 2013.

[46] R. A. Jabr. Radial distribution load flow using conic programming. *IEEE Transactions on Power Systems*, 21(3):1458–1459, Aug 2006.

[47] S. Huang, Q. Wu, J. Wang, and H. Zhao. A sufficient condition on convex relaxation of AC optimal power flow in distribution networks. *IEEE Transactions on Power Systems*, 32(2):1359–1368, March 2017.

[48] B. Kocuk, S. S. Dey, and X. A. Sun. Strong SOCP relaxations for the optimal power flow problem. *Operations Research*, 64(6):1177–1196, 2016.

[49] B. Kocuk, S. S. Dey, and X. Sun. New formulation and strong MISOCP relaxations for AC optimal transmission switching problem. *IEEE Transactions on Power Systems*, 2017. (in press).

[50] S. Delikaraoglou. *Harnessing and coordinating flexibility through market-based mechanisms*. PhD thesis, Technical University of Denmark, 2016.

[51] A. J. Conejo, M. Carrión, and J. M. Morales. *Stochastic Programming Fundamentals*, pages 27–62. Springer US, Boston, MA, 2010.

[52] N. V. Sahinidis. Optimization under uncertainty: State-of-the-art and opportunities. *Computers & Chemical Engineering*, 28(6):971–983, 2004. FOCAPO 2003 Special issue.

[53] K. Margellos, P. Goulart, and J. Lygeros. On the road between robust optimization and the scenario approach for chance-constrained optimization problems. *IEEE Transactions on Automatic Control*, 59(8):2258–2263, Aug 2014.

[54] D. Bertsimas and M. Sim. Tractable approximations to robust conic optimization problems. *Mathematical Programming*, 107(1):5–36, Jun 2006.

[55] G. C. Calafiore and M. C. Campi. The scenario approach to robust control design. *IEEE Transactions on Automatic Control*, 51(5):742–753, May 2006.

[56] A. Nemirovski and A. Shapiro. Convex approximations of chance-constrained programs. *SIAM J. on Optimization*, 17(4):969–996, December 2006.

[57] L. Roald, F. Oldewurtel, B. Van Parys, and G. Andersson. Security-constrained optimal power flow with distributionally robust chance constraints. *arXiv:1508.06061v1*, 2015.

[58] D. Bienstock, M. Chertkov, and S. Harnett. Chance-constrained optimal power flow: Risk-aware network control under uncertainty. *SIAM Review*, 56(3):461–495, 2014.

[59] L. Roald and G. Andersson. Chance-constrained AC optimal power flow: Reformulations and efficient algorithms. *IEEE Transactions on Power Systems*, 33(3):2906–2918, May 2018.

[60] J. R. Birge and F. Louveaux. *Introduction to stochastic programming*. Springer, 1997.

[61] M. Vrakopoulou, K. Margellos, J. Lygeros, and G. Andersson. A probabilistic framework for reserve scheduling and N-1 security assessment of systems with high wind power penetration. *IEEE Transactions on Power Systems*, 28(4):3885–3896, Nov 2013.

[62] A. Venzke and S. Chatzivasileiadis. Convex relaxations of security-constrained AC optimal power flow under uncertainty. In *2018 Power Systems Computation Conference (PSCC)*, June 2018.

[63] M. Vrakopoulou, M. Katsampani, K. Margellos, J. Lygeros, and G. Andersson. Probabilistic security-constrained AC optimal power flow. In *2013 IEEE Grenoble Conference*, June 2013.

[64] M. Perninge and C. Hamon. A stochastic optimal power flow problem with stability constraints—part ii: The optimization problem. *IEEE Transactions on Power Systems*, 28(2):1849–1857, May 2013.

[65] C. Hamon, M. Perninge, and L. Söder. Applying stochastic optimal power flow to power systems with large amounts of wind power and detailed stability limits. In *2013 IREP Symposium Bulk Power System Dynamics and Control - IX Optimization, Security and Control of the Emerging Power Grid*, Aug 2013.

[66] S. Xia, X. Luo, K. W. Chan, M. Zhou, and G. Li. Probabilistic transient stability-constrained optimal power flow for power systems with multiple correlated uncertain wind generations. *IEEE Transactions on Sustainable Energy*, 7(3):1133–1144, July 2016.

[67] I. J. Pérez-Arriaga. *Regulation of the Power Sector*. Springer, 2013.

[68] European Network of Transmission System Operators. Net transfer capacities (NTC) available transfer capacities (ATC), 2000.

[69] North American Electric Reliability Council. Available transfer capability – Definitions and determination, 1996.

[70] European Transmission System Operators. Definitions of transfer capacities in liberalised electricity markets, 2001.

[71] EPEX SPOT, Nord Pool, OMIE, OPCOM, GME, OTE, TGE. Euphemia public description – PCR market coupling algorithm, 2016.

[72] I. Dobson, S. Greene, R. Rajaraman, C.L. Demarco, Fernando L. Alvarado, R. Zimmerman, and M. Glavic. Electric power transfer capability: Concepts, applications, sensitivity and uncertainty. 2001.

[73] F. Capitanescu, M. Glavic, D. Ernst, and L. Wehenkel. Applications of security-constrained optimal power flows. 09 2006.

[74] John E. Condren and Thomas W. Gedra. Expected-security-cost optimal power flow with small-signal stability constraints. *IEEE Transactions on Power Systems*, 21(4):1736–1743, 2006.

[75] Y. Xu, Z.Y. Dong, R. Zhang, and K. P. Wong. A decision tree-based on-line preventive control strategy for power system transient instability prevention. *International Journal of Systems Science*, 2011, 10 2011.

[76] M. Chávez-Lugo, C. R. Fuerte-Esquivel, C. A. Canizares, and V. J. Gutierrez-Martinez. Practical security boundary-constrained DC optimal power flow for electricity markets. *IEEE Transactions on Power Systems*, 31(5):3358–3368, Sept 2016.

[77] F. Thams, A. Venzke, R. Eriksson, and S. Chatzivasileiadis. Efficient database generation for data-driven security assessment of power systems. *IEEE Transactions on Power Systems*, 2019.

[78] P. Kundur, N.J. Balu, and M.G. Lauby. *Power System Stability and Control*. Discussion Paper Series. McGraw-Hill Education, 1994.

[79] Operating security standards. Technical report, EirGrid, 2010.

[80] C. Y. Chung, Lei Wang, F. Howell, and P. Kundur. Generation rescheduling methods to improve power transfer capability constrained by small-signal stability. *IEEE Transactions on Power Systems*, 19(1):524–530, Feb 2004.

[81] F. Milano. *Power System Modelling and Scripting*. Springer Publishing Company, Incorporated, 1st edition, 2010.

[82] P.W. Sauer and M.A. Pai. *Power System Dynamics and Stability*. Prentice Hall, 1998.

[83] L. A. Wehenkel. *Automatic Learning Techniques in Power Systems*. Kluwer Academic Publishers, Norwell, MA, USA, 1998.

[84] FERC Joint Boards on Security-Constrained Economic Dispatch. Study and recommendations regarding security-constrained economic dispatch (SCED) in the Northeast by the joint board on economic dispatch for the northeast region, 2006.

[85] M. Lubin. *Mixed-integer convex optimization: outer approximation algorithms and modeling power*. PhD thesis, Massachusetts Institute of Technology, 2017.

[86] H. Hijazi, C. Coffrin, and P. V. Hentenryck. Convex quadratic relaxations for mixed-integer nonlinear programs in power systems. Technical report, NICTA, 2013.

[87] S. Kodsi and C. Canizares. Modeling and simulation of IEEE 14-bus system with FACTS controllers, 2003.

[88] R. D. Zimmerman, C. E. Murillo-Sanchez, and R. J. Thomas. MATPOWER: Steady-state operations, planning, and analysis tools for power systems research and education. *IEEE Transactions on Power Systems*, 26(1):12–19, Feb 2011.

[89] M. Lubin, E. Yamangil, R. Bent, and J. P. Vielma. Polyhedral approximation in mixed-integer convex optimization. *arXiv:1607.03566*, 2016.

[90] A. Bley, A. M. Gleixner, T. Koch, and S. Vigerske. Comparing MIQCP solvers to a specialised algorithm for mine production scheduling. In *Modeling, Simulation and Optimization of Complex Processes*, pages 25–39, Berlin, Heidelberg, 2012. Springer Berlin Heidelberg.

[91] R. D. Christie, B. F. Wollenberg, and I. Wangensteen. Transmission management in the deregulated environment. *Proceedings of the IEEE*, 88(2):170–195, Feb 2000.

[92] Amprion, APX, BelPEX, Creos, Elia, EnBW, EPEX, RTE, Tennet. CWE enhanced flow-based MC feasibility report. Technical report, 2011.

[93] A. Venzke, L. Halilbasic, U. Markovic, G. Hug, and S. Chatzivasileiadis. Convex relaxations of chance-constrained AC optimal power flow. *IEEE Transactions on Power Systems*, 33(3):2829–2841, May 2018.

[94] K. Baker, E. Dall'Anese, and T. Summers. Distribution-agnostic stochastic optimal power flow for distribution grids. In *2016 North American Power Symposium (NAPS)*, Sept 2016.

[95] C. Duan, W. Fang, L. Jiang, L. Yao, and J. Liu. Distributionally robust chance-constrained approximate AC-OPF with wasserstein metric. *IEEE Transactions on Power Systems*, pages 1–1, 2018.

[96] W. Xie and S. Ahmed. Distributionally robust chance-constrained optimal power flow with renewables: A conic reformulation. *IEEE Transactions on Power Systems*, 33(2):1860–1867, March 2018.

[97] Y. Guo, K. Baker, E. Dall'Anese, Z. Hu, and T. H. Summers. Data-based distributionally robust stochastic optimal power flow, part i: Methodologies. *arXiv:1804.06388*, 2018.

[98] J. Schmidli, L. Roald, S. Chatzivasileiadis, and G. Andersson. Stochastic AC optimal power flow with approximate chance-constraints. In *2016 IEEE Power and Energy Society General Meeting (PESGM)*, July 2016.

[99] L. Roald, D. Molzahn, and A. Tobler. Power system optimization with uncertainty and AC power flow: Analysis of an iterative algorithm. *10th IREP Symposium - Bulk Power Systems Dynamics and Control*, 2017.

[100] H. Zhang and P. Li. Chance-constrained programming for optimal power flow under uncertainty. *IEEE Transactions on Power Systems*, 26(4):2417–2424, Nov 2011.

[101] M. Lubin, Y. Dvorkin, and L. Roald. Chance constraints for improving the security of AC optimal power flow. *arXiv:1803.08754*, 2018.

[102] A. Lorca and X. A. Sun. The adaptive robust multi-period alternating current optimal power flow problem. *IEEE Transactions on Power Systems*, 33(2):1993–2003, March 2018.

[103] X. Bai, L. Qu, and W. Qiao. Robust AC optimal power flow for power networks with wind power generation. *IEEE Transactions on Power Systems*, 31(5):4163–4164, Sept 2016.

[104] Y. Zhou, Y. Tian, K. Wang, and M. Ghandhari. Robust optimisation for AC-DC power flow based on second-order cone programming. *The Journal of Engineering*, 2017(13):2164–2167, 2017.

[105] R. A. Jabr. Adjustable robust OPF with renewable energy sources. *IEEE Transactions on Power Systems*, 28(4):4742–4751, Nov 2013.

[106] M. Tsili and S. Papathanassiou. A review of grid code technical requirements for wind farms. *IET Renewable Power Generation*, 3(3):308–332, Sept 2009.

[107] Haoyuan Qu, L. Roald, and G. Andersson. Uncertainty margins for probabilistic AC security assessment. In *2015 IEEE Eindhoven PowerTech*, June 2015.

[108] W. A. Bukhsh, A. Grothey, K. I. M. McKinnon, and P. A. Trodden. Local solutions of the optimal power flow problem. *IEEE Transactions on Power Systems*, 28(4):4780–4788, Nov 2013.

[109] IEEE 118-bus, 54-unit, 24-hour system. Technical report, Electrical and Computer Engineering Department, Illinois Institute of Technology.

[110] A. J. Conejo, E. Castillo, R. M., and R. García-Bertrand. *Decomposition Techniques in Mathematical Programming: Engineering and Science Applications*. Springer-Verlag, 2006.

[111] J. Schmidli. Stochastic AC optimal power flow with approximate chance-constraints. *Semester Thesis, ETH Zurich*, 2015.

[112] W. Xie, S. Ahmed, and R. Jiang. Optimized Bonferroni approximations of distributionally robust joint chance constraints, 2017.

[113] J. A. Momoh, R. J. Koessler, M. S. Bond, B. Stott, D. Sun, A. Papalexopoulos, and P. Ristanovic. Challenges to optimal power flow. *IEEE Transactions on Power Systems*, 12(1):444–455, Feb 1997.

[114] J. Löfberg. YALMIP : A toolbox for modeling and optimization in MATLAB. In *In Proceedings of the CACSD Conference*, Taipei, Taiwan, 2004.

[115] M. Sebban, R. Nock, J. H. Chauchat, and R. Rakotomalala. Impact of learning set quality and size on decision tree performances. *International Journal of Computers, Systems and Signals*, 1:85–105, 2000.

[116] T. Oates and D. Jensen. The effects of training set size on decision tree complexity. In *Proceedings of the Fourteenth International Conference on Machine Learning*, ICML '97, San Francisco, CA, USA, 1997. Morgan Kaufmann Publishers Inc.

[117] E. Karangelos and L. Wehenkel. Probabilistic reliability management approach and criteria for power system real-time operation. In *2016 Power Systems Computation Conference (PSCC)*, June 2016.

[118] M. Vrakopoulou, S. Chatzivasileiadis, E. Iggland, M. Imhof, T. Krause, O. Mäkelä, J. L. Mathieu, L. Roald, R. Wiget, and G. Andersson. A unified analysis of security-constrained OPF formulations considering uncertainty, risk, and controllability in single and multi-area systems. In *Bulk Power System Dynamics and Control-IX Optimization, Security and Control of the Emerging Power Grid (IREP), 2013 IREP Symposium*. IEEE, 2013.

[119] M. Vrakopoulou, S. Chatzivasileiadis, and G. Andersson. Probabilistic security-constrained optimal power flow including the controllability of HVDC lines. In *IEEE PES ISGT Europe 2013*, Oct 2013.

[120] R. Wiget, M. Vrakopoulou, and G. Andersson. Probabilistic security-constrained optimal power flow for a mixed HVAC and HVDC grid with stochastic infeed. In *Power Systems Computation Conference*, 2014.

[121] M. C. Imhof. *Voltage Source Converter Based HVDC–Modelling and Coordinated Control to Enhance Power System Stability*. PhD thesis, ETH Zurich, 2015.

[122] J. Beerten, S. Cole, and R. Belmans. Generalized steady-state VSC MTDC model for sequential AC/DC power flow algorithms. *IEEE Transactions on Power Systems*, 27(2):821–829, May 2012.

[123] A. Wächter and L. T. Biegler. On the implementation of an interior-point filter line-search algorithm for large-scale nonlinear programming. *Mathematical Programming*, 106(1):25–57, Mar 2006.

[124] S. Chatzivasileiadis, T. Krause, and G. Andersson. Flexible AC transmission systems (FACTS) and power system security - A valuation framework. In *IEEE Power and Energy Society General Meeting*, Detroit Michigan, US, 2011.

[125] P. Pinson. Wind energy: Forecasting challenges for its operational management. *Statistical Science*, 28(4):564–585, 2013.

[126] P. S Jones and C. C. Davidson. Calculation of power losses for MMC-based VSC HVDC stations. In *Power Electronics and Applications (EPE), 2013 15th European Conference on*. IEEE, 2013.

[127] The IEEE PES Task Force on Benchmarks for Validation of Emerging Power System Algorithms. PGLib Optimal Power Flow Benchmarks, 2019.

[128] R. F. Mochamad and R. Preece. Impact of HVDC integration on the dynamic security of power systems. In *Mediterranean Conference on Power Generation, Transmission, Distribution and Energy Conversion (MedPower 2016)*, Nov 2016.

[129] R. Eriksson T. Weckesser S. Delikaraoglou, P. Pinson. Optimal dynamic capacity allocation of HVDC interconnections for cross-border exchange of balancing services in presence of uncertainty - Extended version. *arXiv:1503.00195*, 2015.

[130] E. Pierri, O. Binder, N. G.A. Hemdan, and M. Kurrat. Challenges and opportunities for a European HVDC grid. *Renewable and Sustainable Energy Reviews*, 70:427–456, 2017.

[131] B. H. Kim and R. Baldick. Coarse-grained distributed optimal power flow. *IEEE Transactions on Power Systems*, 12(2):932–939, May 1997.

[132] A. J. Conejo and J. A. Aguado. Multi-area coordinated decentralized DC optimal power flow. *IEEE Transactions on Power Systems*, 13(4):1272–1278, Nov 1998.

[133] F. J. Nogales, F. J. Prieto, and A. J. Conejo. A decomposition methodology applied to the multi-area optimal power flow problem. *Annals of Operations Research*, 120(1):99–116, Apr 2003.

[134] G. Hug-Glanzmann and G. Andersson. Decentralized optimal power flow control for overlapping areas in power systems. *IEEE Transactions on Power Systems*, 24(1):327–336, Feb 2009.

[135] H. Madsen P. Pinson M. Zugno J. M. Morales, A. J. Conejo. *Integrating Renewables in Electricity Markets: Operational Problems*. Springer, 2014.

[136] R. Wiget and G. Andersson. DC optimal power flow including HVDC grids. In *2013 IEEE Electrical Power Energy Conference*, Aug 2013.

[137] A. J. Conejo, F. J. Nogales, and F. J. Prieto. A decomposition procedure based on approximate Newton directions. *Mathematical Programming*, 93(3):495–515, Dec 2002.

[138] A. Ahmadi-Khatir, A. J. Conejo, and R. Cherkaoui. Multi-area energy and reserve dispatch under wind uncertainty and equipment failures. *IEEE Transactions on Power Systems*, 28(4):4373–4383, Nov 2013.

[139] Gurobi Optimization, LLC. Gurobi optimizer reference manual, 2018.

[140] C. Ordoudis, P. Pinson, J. M. Morales, and M. Zugno. An updated version of the IEEE RTS 24-bus system for electricity market and power system operation studies, 2016.

[141] C. Grigg, P. Wong, P. Albrecht, R. Allan, M. Bhavaraju, R. Billinton, Q. Chen, C. Fong, S. Haddad, S. Kuruganty, W. Li, R. Mukerji, D. Patton, N. Rau, D. Reppen, A. Schneider, M. Shahidehpour, and C. Singh. The IEEE reliability test system-1996. A report prepared by the reliability test system task force of the application of probability methods subcommittee. *IEEE Transactions on Power Systems*, 14(3):1010–1020, Aug 1999.

[142] W. A. Bukhsh, C. Zhang, and P. Pinson. An integrated multiperiod OPF model with demand response and renewable generation uncertainty. *IEEE Transactions on Smart Grid*, 7(3):1495–1503, May 2016.

[143] J. Guo, G. Hug, and O. Tonguz. Impact of partitioning on the performance of decomposition methods for AC optimal power flow. In *2015 IEEE Power Energy Society Innovative Smart Grid Technologies Conference (ISGT)*, Feb 2015.

Department of Electrical Engineering
Center for Electric Power and Energy (CEE)
Technical University of Denmark
Elektrovej, Building 325
DK-2800 Kgs. Lyngby
Denmark

www.elektro.dtu.dk/cee
Tel: (+45) 45 25 35 00
Fax: (+45) 45 88 61 11
E-mail: cee@elektro.dtu.dk